

special Issue: 27

Redalyc 3.0

ESCI Web of science

UNIVERSIDAD POLITÉCNICA SALESIANA ECUADOR

pISSN: 1390-650X

eISSN: 1390-860X

enero/ junio 2022

# INGENIUS

Revista de Ciencia y Tecnología



🇬🇧 Social distancing in the face of COVID-19: simulation of the maximum capacity of people through PHP

**Pag. 9**

🇬🇧 Characterization of DELUX: Ultraviolet light sterilization device for PFF2 / N95 masks against COVID-19

**Pag. 23**

🇬🇧 A review of the state-of-the-art of solar thermal collectors applied in the industry

**Pag. 59**

🇬🇧 A Deep Learning Approach to Estimate the Respiratory Rate from Photoplethysmogram

**Pag. 96**

**Subject Editors:** Ph.D. Teodiano Bastos-Filho, Ph.D. Sridhar Krishnan

# INGENIUS

INGENIUS • Special Issue 27 • january/june 2022. Journal of Science and Tecnology of the Universidad Politécnica Salesiana of Ecuador. Publication dedicated to studies related to the Sciences of Mechanical Engineering, Electrical Engineering, Electronic Engineering, Mechatronic Engineering, Systems Engineering and Industrial Engineering.

## Editors Board

RAFAEL ANTONIO BALART GIMENO, PHD, Universidad Politécnica de Valencia, España – Editor-in-chief.

JOHN IGNACIO CALLE SIGÜENCIA, PHD, Universidad Politécnica Salesiana, Ecuador – Editor-in-chief.

ESTEBAN MAURICIO INGA ORTEGA, PHD, Universidad Politécnica Salesiana, Ecuador – Associate Editor.

MARLON XAVIER QUINDE ABRIL, MSC, Universidad Politécnica Salesiana, Ecuador – Associate Editor.

TEODIANO FREIRE BASTOS FILHO, PHD, (Universidade Federal do Espírito Santo, Brasil – Associate Editor.

## Scientific board

JUAN LÓPEZ MARTÍNEZ, PHD, Universidad Politécnica de Valencia, España.

ELENA FORTUNATI, PHD, Universidad de Perugia, Italia.

GUSTAVO ROVELO RUIZ, PHD, Hasselt University, Diepenbeek, Bélgica.

FRANKLIN GAVILANEZ ALVAREZ, PHD, American University, Estados Unidos.

PIEDAD GAÑAN ROJO, PHD, Universidad Pontificia Bolivariana, Colombia.

JOSÉ ALEX RESTREPO, PHD, Universidad Simón Bolívar, Venezuela.

SERGIO LUJAN MORA, PHD, Universidad de Alicante, España.

MARTHA ZEQUERA DÍAZ, PHD, Pontificia Universidad Javeriana, Colombia.

GROVER ZURITA, PHD, Universidad Privada Boliviana, Bolivia.

VLADIMIR ROBLES, PHD, Universidad Politécnica Salesiana, Ecuador.

GERMÁN ARÉVALO, PHD, Universidad Politécnica Salesiana, Ecuador.

WILBERT AGUILAR, PHD, Universidad de las Fuerzas Armadas, ESPE, Ecuador.

JACK BRAVO TORRES, PHD, Universidad Politécnica Salesiana, Ecuador.

WALTER OROZCO, PHD, Universidad Politécnica Salesiana, Ecuador.

MARIELA CERRADA, PHD, Universidad Politécnica Salesiana, Ecuador.

JULIO CÉSAR VIOLA, PHD, Universidad Politécnica Salesiana, Ecuador.

SERGIO GAMBOA SÁNCHEZ, PHD, Universidad Nacional Autónoma de México, México.

ROGER ABDÓN BUSTAMANTE PLAZA, PHD, Universidad de Chile, Chile.

CHRISTIAN BLUM, PHD, Consejo Superior de Investigaciones Científicas, España.

SILVIA NOEMI SCHIAFFINO, PHD, Universidad Nacional del Centro de la Provincia de Buenos Aires, Argentina.

ANALÍA ADRIANA AMANDI, PHD, Universidad Nacional del Centro de la Provincia de Buenos Aires, Argentina.

RUBÉN DE JESÚS MEDINA MOLINA, PHD,

Universidad de Los Andes, Venezuela.

JOHNNY JOSUÉ BULLÓN TORREALBA, PHD, Universidad de Los Andes, Venezuela.

RODRIGO PALMA HILLERNS, PHD, Universidad de Chile, Chile.

GERARDO ESPINOZA PÉREZ, PHD, Universidad Nacional Autónoma de México, México.

ALEXANDRE MENDES ABRÃO, PHD, Universidad Federal de Minas Gerais, Brasil.

KAMLA ABDEL RADI ISMAIL, PHD, Universidad Estatal de Campinas Unicamp, Brasil.

ARNALDO DA SILVA, PHD, Universidad Estatal de Campinas Unicamp, Brasil.

ÁLVARO ROCHA, PHD, Universidad de Coimbra, Portugal.

JOSÉ ANTENOR POMILIO, PHD, Universidad Estatal de Campinas Unicamp, Brasil.

LUIS PAULO REIS, PHD, Universidad de Minho, Portugal.

LUÍS FERNANDES, PHD, Escuela Superior Náutica Infante d. Henrique, Portugal.

ANÍBAL TRAÇA DE ALMEIDA, PHD, Universidad de Coimbra, Portugal.

JORGE SÁ SILVA, PHD, Universidad de Coimbra, Portugal.

PEDRO MANUEL SOARES MOURA, PHD, Universidad de Coimbra, Portugal.

SÉRGIO MANUEL RODRIGUES LOPES, PHD, Universidad de Coimbra, Portugal.

RICARDO MADEIRA SOARES BRANCO, PHD, Universidad de Coimbra, Portugal.

CARLOS ALEXANDRE BENTO CAPELA, PHD, Universidad de Coimbra, Portugal.

FILIFE ARAUJO, PHD, Universidad de Coimbra, Portugal.

LUIS MANUEL GUERRA SILVA ROSA, PHD, Universidad de Lisboa, Portugal.

HÉLDER DE JESUS FERNANDES, PUGA, PHD, Universidad de Minho, Portugal.

FILIFE SAMUEL, PEREIRA DA SILVA, PHD, Universidad de Minho, Portugal.

CÉSAR SEQUEIRA, PHD, Universidad de Lisboa, Portugal.

JOSÉ TEIXEIRA ESTÊVÃO FERREIRA, PHD,

Universidad de Coimbra, Portugal.

NUNO LARANJEIRO, PHD, Universidad de Coimbra, Portugal.

LUÍS AMARAL, PHD, Universidad de Lisboa, Portugal.

JORGE HENRIQUES, PHD, Universidad de Coimbra, Portugal.

WILLIAM IPANAQUE, PHD, Universidad de Piura, Perú.

LORENZO LEIJA SALAS, PHD, Centro de Investigación y Estudios Avanzados del Instituto Politécnico Nacional, México.

VALERI KONTOROVICH MAZOVER, PHD, Centro de Investigación y de Estudios Avanzados del Instituto Politécnico Nacional, México.

ALEJANDRO ÁVILA GARCÍA, PHD, Centro de Investigación y de Estudios Avanzados del Instituto Politécnico Nacional, México.

PAOLO BELLAVISTA, PHD, Universidad de Bologna, Italia.

CARLOS RUBIO, PhD, Centro de Ingeniería y Desarrollo Industrial, México.

FERNANDO HERNÁNDEZ SÁNCHEZ, PhD, Centro de Investigación Científica de Yucatán, México.

EMILIO MUÑOZ SANDOVAL, PhD, Instituto Potosino de Investigación Científica y Tecnológica, México.

YASUHIRO MATSUMOTO KUWABARA, PhD, Centro de Investigación y de Estudios Avanzados del Instituto Politécnico Nacional, México.

DAVID ZUMOFFEN, PhD, Centro Internacional Franco Argentino de Ciencias de la Información y de Sistemas, Argentina.

VICENTE RODRÍGUEZ GONZÁLEZ, PhD, Instituto Potosino de Investigación Científica y Tecnológica, México.

ALEJANDRO RODRÍGUEZ ÁNGELES, PhD, Centro de Investigación y de Estudios Avanzados del Instituto Politécnico Nacional, México.

ALISTAIR BORTHWICK, PhD, Universidad de Edimburgo, Reino Unido.

## Reviewers board

FEDERICO DOMINGUEZ, PHD, Escuela Superior Politécnica del Litoral, Ecuador.

ENRIQUE CARRERA, PHD, Universidad de las Fuerzas Armadas, ESPE, Ecuador.

ANDRÉS TELLO, MSc, Universidad de Cuenca, Ecuador.

CRISTIAN GARCÍA BAUZA, PHD, Universidad Nacional del Centro de la Provincia de Buenos Aires, Argentina.

OSVALDO AÑÓ, PHD, Universidad Nacional de San Juan, Argentina.

THALÍA SAN ANTONIO, PHD, Universidad Técnica de Ambato, Ecuador.

VICTOR SAQUICELA, PHD, Universidad de Cuenca, Ecuador.

GONZALO OLMEDO, PHD, Universidad de las Fuerzas Armadas, ESPE, Ecuador.

ROMÁN LARA, PHD, Universidad de las Fuerzas Armadas, ESPE, Ecuador.

GUILLERMO SORIANO, PHD, Escuela Superior Politécnica del Litoral, Ecuador.

MARÍA FERNANDA GRANDA, PHD, Universidad de Cuenca, Ecuador.

RICARDO CAYSSIALS, PHD, Universidad Tecnológica Nacional, Argentina.

LEONARDO SOLAQUE GUZMAN, PHD, Universidad Militar Nueva Granada, Colombia.

JOSÉ DI PAOLO, PHD, Universidad Nacional de Entre Ríos, Argentina.

ASTRID RUBIANO FONSECA, PHD, Universidad Militar Nueva Granada, Colombia.

ROBINSON JIMÉNEZ, PHD, Universidad Militar Nueva Granada, Colombia.

ALFONSO ZOZAYA, PHD, Universidad de Carabobo, Venezuela.

MAURICIO MAULEDOUX, PHD, Universidad Militar Nueva Granada, Colombia.

LUIS MEDINA, PHD, Universidad Simón Bolívar, Venezuela.

ERNESTO CUADROS-VARGAS, PHD, Universidad Católica San Pablo, Perú.

SAMUEL SEPÚLVEDA CUEVAS, PHD, Universidad de la Frontera, Chile.

CARLOS CARES, PHD, Universidad de la Frontera, Chile.

RAFAEL SOTELO, PHD, Universidad de Montevideo, Uruguay.

OMAR LOPEZ, PHD, Universidad de Los Andes, Colombia.

JOB FLORES-GODOY, PHD, Universidad Católica del Uruguay, Uruguay.

LUIS MARIO MATEUS, PHD, Universidad de los Andes, Colombia.

AMADEO ARGÜELLES CRUZ, PHD, Instituto Politécnico Nacional, México.

SANTIAGO BENTANCOURT PARRA, PHD, Universidad Pontificia Bolivariana, Colombia.

GERMÁN ZAPATA, PHD, Universidad Nacio-

nal de Colombia, Colombia.

PEDRO GARCÍA, PHD, Universidad Autónoma de Barcelona, España.

ARTURO CONDE ENRÍQUEZ, PHD, Universidad Autónoma de Nuevo León, México.

ALBERTO CAVAZOS GONZÁLEZ, PHD, Universidad Autónoma de Nuevo León, México.

ERNESTO VÁZQUEZ MARTÍNEZ, PHD, Universidad Autónoma de Nuevo León, México.

MIGUEL DÍAZ RODRIGUEZ, PHD, Universidad de Los Andes, Venezuela.

EFRAÍN ALCORTA GARCÍA, PHD, Universidad Autónoma de Nuevo León, México.

LUIS CHIRINOS GARCIA, PHD, Pontificia Universidad Católica de Perú, Perú.

OSCAR AVILÉS, PHD, Universidad Militar Nueva Granada, Colombia.

DORA MARTÍNEZ DELGADO, PHD, Universidad Autónoma de Nuevo León, México.

DAVID OJEDA, PHD, Universidad Técnica del Norte, Ecuador.

IRENE BEATRÍZ STEINMANN, PHD, Universidad Tecnológica Nacional, Argentina.

MARIO SERRANO, Universidad Nacional de San Juan, Argentina.

CORNELIO POSADAS CASTILLO, PHD, Universidad Autónoma Nuevo León, México.

MARIO ALBERTO RIOS MESIAS, PHD, Universidad de Los Andes, Colombia.

YUDITH CARDINALE VILLARREAL, PHD, Universidad Simón Bolívar, Venezuela.

EDUARDO MATALLANAS, PHD, Universidad Politécnica de Madrid, España.

JOSE EDUARDO OCHOA LUNA, PHD, Universidad Católica San Pablo, Perú.

DANTE ANGEL ELIAS GIORDANO, PHD, Pontificia Universidad Católica de Perú, Perú.

MANUEL PELAEZ SAMANIEGO, PHD, Universidad de Cuenca, Ecuador.

JUAN ESPINOZA ABAD, PHD, Universidad de Cuenca, Ecuador.

PIETRO CODARA, PHD, Universidad de Milan, Italia.

ALBERTO SORIA, PHD, Centro de Investigación y de Estudios Avanzados del Instituto Politécnico Nacional, México.

JOSÉ M. ALLER, PHD, Universidad Politécnica Salesiana, Ecuador.

FERNEY AMAYA F., PHD, Universidad Pontificia Bolivariana, Medellín, Colombia.

SANTIAGO ARANGO ARAMBURO, PHD, Universidad Nacional de Colombia, Colombia.

DIEGO ARCOS-AVILÉS, PHD, Universidad de las Fuerzas Armadas, ESPE, Ecuador.

PABLO AREVALO, PHD, Universidad Politécnica Salesiana, Ecuador.

ROBERTO BELTRAN, MSc, Universidad de las Fuerzas Armadas, ESPE, Ecuador.

LEONARDO BETANCUR, PHD, Universidad Pontificia Bolivariana, Medellín, Colombia.

ROBERTO GAMBOA, PHD, Universidad de Lisboa, Portugal.

PAULO LOPES DOS SANTOS, PHD, Universidad do Porto, Portugal.

PEDRO ANDRÉ DIAS PRATES, PHD, Universidad de Coimbra, Portugal.

JOSÉ MANUEL TORRES FARINHA, PHD, Universidad de Coimbra, Portugal.

CELSO DE ALMEIDA, PHD, Universidad Estatal de Campinas Unicamp, Brasil.

RAMON MOLINA VALLE, PHD, Universidad Federal de Minas Gerais, Brasil.

CRISTINA NADER VASCONCELOS, PHD, Universidad Federal Fluminense, Brasil.

JOÃO M. FERREIRA CALADO, PHD, Universidad de Lisboa, Portugal.

GUILHERME LUZ TORTORELLA, PHD, Universidad Federal de Santa Catarina, Brasil.

MAURO E. BENEDET, PHD, Universidad Federal de Santa Catarina, Brasil.

ARTEMIS MARTI CESCHIN, PHD, Universidade de Brasilia, Brasil.

GILMAR BARRETO, PHD, Universidad Estatal de Campinas Unicamp, Brasil.

RICARDO EMILIO F. QUEVEDO NOGUEIRA, PHD, Universidad Federal de Ceará, Brasil.

WESLEY LUIZ DA SILVA ASSIS, PHD, Universidad Federal Fluminense, Brasil.

ANA P. MARTINAZZO, PHD, Universidad Federal Fluminense, Brasil.

JORGE BERNARDINO, PHD, Universidad de Coimbra, Portugal.

LUIS GERALDO PEDROSO MELONI, PHD, Universidad Estatal de Campinas Unicamp, Brasil.

FACUNDO ALMERAYA CALDERÓN, PHD, Universidad Autónoma de Nuevo León, México.

FREDDY VILLAO QUEZADA, PHD, Escuela Superior Politécnica del Litoral, Ecuador.

JOSE MANRIQUE SILUPU, MSc, Universidad de Piura, Perú.

GERMÁN ARIEL SALAZAR, PHD, Instituto de Investigaciones en Energía no Convencional, Argentina.

JOSÉ MAHOMAR JANANIÁS, PHD, Universidad del BIOBIO, Chile.

ARNALDO JÉLVEZ CAAMAÑO, PHD, Universidad del BIOBIO, Chile.

JORGE ANDRÉS URIBE, MSc, Centro de Ingeniería y Desarrollo Industrial, México.

RICARDO BELTRAN, PHD, Centro de Investigación en Materiales Avanzados, México.

ADI CORRALES, MSc, Centro de Ingeniería y Desarrollo Industrial, México.

JORGE URIBE CALDERÓN, PHD, Centro de Investigación Científica de Yucatán, México

JOSÉ TRINIDAD HOLGUÍN MOMACA, MSc, Centro de Investigación en Materiales Avanzados, México.

JUAN MANUEL ALVARADO OROZCO, PhD, Centro de Ingeniería y Desarrollo Industrial, México.

ARNALDO JÉLVEZ CAAMAÑO, PhD, Universidad del BIOBIO, Chile.

JAVIER MURILLO, PhD, Centro Internacional Franco Argentino de Ciencias de la Información y de Sistemas, Argentina.

LUCAS DANIEL TERISSI, PhD, Universidad Nacional de Rosario, Argentina.

RENE VINICIO SANCHEZ LOJA, MSc, Universidad Politécnica Salesiana, Ecuador.

FREDDY LEONARDO BUENO PALOMEQUE, MSc, Universidad Politécnica Salesiana, Ecuador.

DIEGO CABRERA MENDIETA, MSc, Universidad Politécnica Salesiana, Ecuador.

EDWUIN JESUS CARRASQUERO, PhD, Universidad Técnica de Machala, Ecuador.

CARLOS MAURICIO CARRILLO ROSERO, MSc, Universidad Técnica de Ambato, Ecuador.

DIEGO CARRION GALARZA, MSc, Universidad Politécnica Salesiana, Ecuador.

CARMEN CELI SANCHEZ, MSc, Universidad Politécnica Salesiana, Ecuador.

DIEGO CHACON TROYA, MSc, Universidad Politécnica Salesiana, Ecuador.

PAUL CHASI, MSc, Universidad Politécnica Salesiana, Ecuador.

JUAN CHICA, MSc, Universidad Politécnica Salesiana, Ecuador.

DIEGO MARCELO CORDERO GUZMÁN, MSc, Universidad Católica de Cuenca, Ecuador.

LUIS JAVIER CRUZ, PhD, Universidad Pontificia Bolivariana, Medellín, Colombia.

FABRICIO ESTEBAN ESPINOZA MOLINA, MSc, Universidad Politécnica Salesiana, Ecuador.

JORGE FAJARDO SEMINARIO, MSc, Universidad Politécnica Salesiana, Ecuador.

PATRICIA FERNANDEZ MORALES, PhD, Universidad Pontificia Bolivariana, Medellín, Colombia.

MARCELO FLORES VAZQUEZ, MSc, Universidad Politécnica Salesiana, Ecuador.

CARLOS FLORES VÁZQUEZ, MSc, Universidad Católica de Cuenca, Ecuador.

CARLOS FRANCO CARDONA, PhD, Universidad Nacional de Colombia, Colombia.

CRISTIAN GARCÍA GARCÍA, MSc, Universidad Politécnica Salesiana, Ecuador.

TEONILA GARCÍA ZAPATA, PhD, Universidad Nacional Mayor de San Marcos, Perú.

LUIS GARZÓN MÑOZ, PhD, Universidad Politécnica Salesiana, Ecuador.

NATALIA GONZALEZ ALVAREZ, MSc, Universidad Politécnica Salesiana, Ecuador.

ERNESTO GRANADO, PhD, Universidad Simón Bolívar, Venezuela.

ADRIANA DEL PILAR GUAMAN, MSc, Universidad Politécnica Salesiana, Ecuador.

JUAN INGA ORTEGA, MSc, Universidad Politécnica Salesiana, Ecuador.

ESTEBAN INGA ORTEGA, PhD, Universidad Politécnica Salesiana, Ecuador.

PAOLA INGAVÉLEZ, MSc, Universidad Politécnica Salesiana, Ecuador.

CESAR ISAZA ROLDAN, PhD, Universidad Pontificia Bolivariana.

NELSON JARA COBOS, MSc, Universidad Politécnica Salesiana, Ecuador.

RUBEN JERVES, MSc, Universidad Politécnica Salesiana, Ecuador.

VICTOR RAMON LEAL, PhD, Investigador de PDVSA, Venezuela

GABRIEL LEON, MSc, Universidad Politécnica Salesiana, Ecuador.

EDILBERTO LLANES, PhD, Universidad Internacional SEK, Ecuador.

LUIS LÓPEZ, MSc, Universidad Politécnica Salesiana, Ecuador.

CARLOS MAFLA YÉPEZ, MSc, Universidad Técnica del Norte, Ecuador.

HADER MARTÍNEZ, PhD, Universidad Pontificia Bolivariana, Medellín, Colombia

JAVIER MARTÍNEZ, PhD, Instituto Nacional de Eficiencia Energética y Energías Renovables, Ecuador.

ALEX MAYORGA, MSc, Universidad Técnica de Ambato, Ecuador.

JIMMY MOLINA, MSc, Universidad Técnica de Machala, Ecuador.

ANDRES MONTERO, PhD, Universidad de Cuenca, Ecuador.

VICENTE MORALES, MSc, Universidad Técnica de Ambato, Ecuador.

FABIÁN MORALES, MSc, Universidad Técnica de Ambato, Ecuador.

DIEGO MORALES, MSc, Ministerio de Electricidad y Energías Renovables del Ecuador.

YOANDRYS MORALES TAMAYO, PhD, Universidad Técnica de Cotopaxi, Cotopaxi

OLENA LEONIDIVNA NAIDIUK, MSc, Universidad Politécnica Salesiana, Ecuador.

OSCAR NARANJO, MSc, Universidad del Azuay, Ecuador.

PAUL NARVAEZ, MSc, Universidad Politécnica Salesiana, Ecuador.

HERNÁN NAVAS OLMEDO, MSc, Universidad Técnica de Cotopaxi, Ecuador.

CESAR NIETO, PhD, Universidad Pontificia Bolivariana, Medellín, Colombia

FABIO OBANDO, MSc, Universidad Politécnica Salesiana, Ecuador.

LUIS ORTIZ FERNANDEZ, MSc, Universidade Federal de Rio Grande del Norte, Brasil

PABLO PARRA, MSc, Universidad Politécnica Salesiana, Ecuador.

PAULO PEÑA TORO, PhD, Ministerio de Productividad, Ecuador.

PATSY PRIETO VELEZ, MSc, Universidad Politécnica Salesiana, Ecuador.

DIEGO QUINDE FALCONI, MSc, Universidad Politécnica Salesiana, Ecuador.

DIANA QUINTANA ESPINOZA, MSc, Universidad Politécnica Salesiana, Ecuador.

WILLIAM QUITIAQUEZ SARZOSA, MSc, Universidad Politécnica Salesiana, Ecuador.

FLAVIO QUIZHPI PALOMEQUE, MSc, Universidad Politécnica Salesiana, Ecuador.

WASHINGTON RAMIREZ MONTALVAN, MSc, Universidad Politécnica Salesiana, Ecuador.

FRAN REINOSO AVECILLAS, MSc, Universidad Politécnica Salesiana, Ecuador.

NÉSTOR RIVERA CAMPOVERDE, MSc, Universidad Politécnica Salesiana, Ecuador.

JORGE ROMERO CONTRERAS, MSc, Universidad de Carabobo, Venezuela

FABIAN SAENZ ENDERICA, MSc, Universidad de las Fuerzas Armadas, ESPE, Ecuador.

LUISA SALAZAR GIL, PhD, Universidad Simón Bolívar, Venezuela

GUSTAVO SALGADO ENRÍQUEZ, MSc, Universidad Central del Ecuador., Ecuador.

JUAN CARLOS SANTILLÁN LIMA, MSc, Universidad Nacional de Chimborazo

JONNATHAN SANTOS BENÍTEZ, MSc, Universidad Politécnica Salesiana, Ecuador.

ANDRÉS SARMIENTO CAJAMARCA, MSc, Universidad Federal de Santa Catarina, Brasil

LUIS SERPA ANDRADE, MSc, Universidad Politécnica Salesiana, Ecuador.

CRISTIAN TIMBI SISALIMA, MSc, Universidad Politécnica Salesiana, Ecuador.

MILTON TIPAN SIMBAÑA, MSc, Universidad Politécnica Salesiana, Ecuador.

PAUL TORRES JARA, MSc, Universidad Politécnica Salesiana, Ecuador.

RODRIGO TUFIÑO CÁRDENAS, MSc, Universidad Politécnica Salesiana, Ecuador.

FERNANDO URGILES ORTÍZ, MSc, Universidad Politécnica Salesiana, Ecuador.

JUAN VALLADOLID QUITOISACA, MSc, Universidad Politécnica Salesiana, Ecuador.

EFRÉN VÁZQUEZ SILVA, PhD, Universidad Politécnica Salesiana, Ecuador.

JULIO VERDUGO, MSc, Universidad Politécnica Salesiana, Ecuador.

MARY VERGARA PAREDES, PhD, Universidad de los Andes, Merida, Venezuela

JENNIFER YEPEZ ALULEMA, MSc, Universidad Politécnica Salesiana, Ecuador.

JULIO ZAMBRANO ABAD, MSc, Universidad Politécnica Salesiana, Ecuador.

PATRICIA ZAPATA MOLINA, MSc, Universidad Politécnica Salesiana, Ecuador.

### **Publications board**

JUAN CÁRDENAS TAPIA, SDB, PHD  
JAVIER HERRÁN GÓMEZ, SDB, PHD  
JOSÉ JUNCOSA BLASCO, PHD  
JUAN PABLO SALGADO GUERRERO, PHD  
ANGLE TORRES TOUKOUMIDIS, PHD  
JAIME PADILLA VERDUGO, PHD  
SHEILA SERRANO VINCENTI, MSC  
JORGE CUEVA ESTRADA, MSC  
JOHN CALLE SIGÜENCIA, PHD  
FLORALBA AGUILAR GORDÓN, PHD  
BETTY RODAS SOTO, MSC  
MÓNICA RUIZ VÁSQUEZ, MSC  
JORGE ALTAMIRANO SÁNCHEZ, MSC  
DAVID ARMENDÁRIZ GONZÁLEZ, MSC  
LUIS ÁLVAREZ RODAS, PHD

### **General Editor**

LUIS ÁLVAREZ-RODAS, PHD

### **Technical board**

ÁNGEL TORRES-TOUKOUMIDIS, PHD  
DRA. MARCIA PEÑA, Style Reviewer,  
Centro Gráfico Salesiano - Editorial Don Bosco  
MARLON QUINDE ABRIL, MSC, Diagramming and layout  
JOEL MONTERO GALÁN

### **Publications Service**

HERNÁN HERMOSA (General Coordination)  
MARCO GUTIÉRREZ (OJS Layout)  
PAULINA TORRES (Style Editing)  
RAYSA ANDRADE (Layout)  
MARTHA VINUEZA (Layout)  
ADRIANA CURIEL AVILA, (Translation)

### **Editorial**

Editorial Abya Yala (Quito-Ecuador),  
Av. 12 de octubre N422 y Wilson,  
Bloque A, UPS Quito, Ecuador.  
Casilla 17-12-719 Teléfonos: (593-2) 3962800 ext. 2638  
email: editorial@abyayala.org

Printing: 800 copies

Typographic system used in the composition of this document L<sup>A</sup>T<sub>E</sub>X.

# INGENIUS

REVISTA DE CIENCIA Y TECNOLOGIA

Special Issue 27: Use of Engineering Techniques to Fight COVID-19

january – june 2022

ISSN impreso 1390-650X / ISSN electrónico 1390-860X

The administration of the journal is done through the following parameters:

The journal uses the academic anti-plagiarism system  

The articles have an identification code (Digital Object Identifier) 

The editorial process is managed through the Open Journal System 

It is an open access publication (Open Access) licensed Creative Commons



The politics copyright of use postprint, are published in the Self-Archive Policy Repository

Sherpa/Romeo. 

The articles of the present edition can be consulted in

<http://revistas.ups.edu.ec/index.php/ingenius>



UNIVERSIDAD POLITÉCNICA SALESIANA DEL ECUADOR

INGENIUS Journal, is indexed in the following Databases and scientific information systems:

### SELECTIVE DATABASES



### REVIEWS EVALUATION PLATFORMS



### SELECTIVE DIRECTORIES



### SELECTIVE SERIAL LIBRARY



### SCIENTIFIC LITERATURE SEARCHERS OPEN ACCESS



### OTHER BIBLIOGRAPHICAL DATABASES



# CATALOG OF INTERNATIONAL UNIVERSITY LIBRARIES



Dear readers:

COVID-19 has affected more than 280 million people, killing more than 5.4 million worldwide, since the first case reported of SARS-CoV-2 in Wuhan, China, in 2019, followed by its variants, such as the United Kingdom variant (B.1.1.7), the Brazilian variants (P.1, P.2 and N.9), the South Africa variant (B.1.325), and the recent variant Omicron (B.1.1.529), firstly detected in Africa. COVID-19 is still strongly affecting some countries, as is the case of Russia, with currently more than 1,000 deaths per day.

This thematic issue brings articles on multidisciplinary techniques of Engineering to fight COVID-19, addressing all its aspects, including source and detection technologies for the study, treatment, and prevention of COVID-19; biomedical sensor design and fabrication, performance, processing approaches, and applications; new developments and recent improvements in designs; and the electronics, data processing, and materials of biomedical sensors.

Five contributions have been accepted for this issue, which were reviewed through the corresponding editorial process conducted by experts in this field. The contributions published here correspond to thirty-three researchers from different countries (Brazil, Ecuador, El Salvador, and Peru).

The first work “Social Distancing in the Face of COVID-19: Simulation of the Maximum Capacity of People Through PHP” makes use of programming techniques, using the PHP language, for the development of a web application that simulates the maximum capacity of people who can enter a place in an internal or external area, complying with the social distancing of 2 m required in this time of COVID-19. The work “Design and Construction of Automated Mechanical Ventilation Equipment to Assist Respiratory Failure” presents the requirements for the design (using Computer Aided Design – CAD), construction and validation of a mechani-

cal ventilation system, to be used in patients with respiratory failure, mainly due to the COVID-19 pandemic, followed by measurements of the conditions of the supplied air conducted with the help of professionals dedicated to the maintenance of medical equipment and with the approval of internist doctors.

The following article, entitled “Characterization of Delux: Ultraviolet Light Sterilization Device for PFF2 / N95 Masks Against COVID-19”, presents a characterization of the sterilization device, called DELUX, utilizing UVC (Ultraviolet C light spectra), for sterilization of PFF2/N95 masks, allowing to extend the time of safe use of these masks in emergency conditions. The work addresses the fact of the world population is still forced to wear facemasks in public, as they continue being the most effective protocol to avoid and prevent COVID-19 spread. Thus, the article “Evaluation of AIoT Performance in Cloud and Edge Computational Models for Mask Detection”, describes an automatic facemask detection system, using concepts of Artificial Intelligence of Things (AIoT), to remind people the importance of wearing them appropriately. The system allows detecting correct, inappropriate, and non- facemask wearing, based on two computational models: Cloud and Edge.

Finally, the work entitled “Prototype of a Device for the Automatic Physiological Measurement to Assist the Diagnosis and Monitoring of patients with COVID-19” describes the design, construction and preliminary results of a device to automate the measurement of physiological signals (temperature, oxygen, pressure and heart rate) to assist in the diagnosis and monitoring of COVID-19. The system includes also a mobile application, which receives measurements data in real time and create a database for medical evaluation.

Enjoy all these works! We hope in 2022 to be free of this pandemic!

Teodiano Bastos-Filho, PhD  
Associate Editor

# TABLE OF CONTENTS

<b>Social distancing in the face of COVID-19: simulation of the maximum capacity of people through PHP</b> .....	9
Distanciamiento social ante la COVID-19: Simulación del aforo máximo de personas mediante PHP	
Oscar J. M. Peña Cáceres, Manuel A. More More, Ruth E. Cornejo Sojo, Elvis R. Garay Silupu	
<b>Design and construction of automated mechanical ventilation equipment to assist respiratory failure</b> .....	17
Diseño y construcción de equipo de ventilación mecánica automatizada para asistir insuficiencia respiratoria	
Gilberto Carrillo, Mauricio Gómez, Jaime Rodas, Rafael Pimentel	
<b>Characterization of DELUX: Ultraviolet light sterilization device for PFF2 / N95 masks against COVID-19</b> .....	23
Caracterización de DELUX: Dispositivo de esterilización por luz ultravioleta para máscaras PFF2/N95 contra COVID-19	
Christiane Bertachini Lombello, Nasser Ali Daghashtanli, Hermann Windisch Neto, Fernando Luiz Affonso Fonseca, Felipe Nogueira Ambrosio, Raquel Arbex, Isabella Kobb Fernando, Victor Allisson da Silva, Luisa Pataquini dos Santos, Patricia Aparecida da Ana	
<b>Evaluation of AIoT performance in Cloud and Edge computational models for mask detection</b> .....	32
Evaluación de AIoT en modelos computacionales en la nube y en el borde aplicado a la detección de mascarillas	
Felipe Quiñonez-Cuenca, Cristian Maza-Merchán, Nilvar Cuenca-Maldonado, Manuel Quiñones-Cuenca, Rommel Torres, Francisco Sandoval, Patricia Ludeña-González	
<b>Prototype of a Device for the Automatic Measurement of Physiological Signals to Assist the Diagnosis and Monitoring of patients with COVID-19</b> .....	49
Prototipo de un dispositivo para la medición automática de señales fisiológicas para asistir al diagnóstico y seguimiento de pacientes con COVID-19	
Karla Llanos, Christian Landi, Fernando Yupa, Paola Vasquez, Ismael Criollo, John Calle-Siguencia, Fernando Urgilés-Ortiz, Ana Cecilia Villa-Parra	
<b>A review of the state-of-the-art of solar thermal collectors applied in the industry</b> ...	59
Una revisión de los últimos avances de los colectores solares térmicos aplicados en la industria	
Willian Carrión-Chamba, Wilson Murillo-Torres, Andrés Montero-Izquierdo	
<b>Design and construction of a friction welding equipment with laser assistance for the joint of AISI 1045 steel and aluminum 2017-T4 shafts</b> .....	74
Diseño y construcción de un equipo de soldadura por fricción con asistencia láser para la unión de ejes de acero AISI 1045 y aluminio 2017-T4	
José Luis Mullo, Jorge Andrés Ramos-Grez, Germán Omar Barrionuevo	
<b>Pedestrian detection at daytime and nighttime conditions based on YOLO-v5</b> .....	85
Detección de peatones en el día y en la noche usando YOLO-v5	
Bryan Montenegro, Marco Flores-Calero	
<b>A Deep Learning Approach to Estimate the Respiratory Rate from Photoplethysmogram</b> .....	96
Un enfoque de aprendizaje profundo para estimar la frecuencia respiratoria del fotoplethysmograma	
Lucas C. Lampier, Yves L. Coelho, Eliete M. O. Caldeira, Teodiano F. Bastos-Filho	
<b>D-BLAST MIMO Performance Analysis over SDR-USRP</b> .....	105
Análisis del Rendimiento de D-BLAST MIMO sobre SDR-USRP	
Freddy Cárdenas, Jairo Otáñez, Juan Inga, Esteban Inga, Andrés Ortega	
<b>Normas editoriales</b> .....	117
Guidelines	



# SOCIAL DISTANCING IN THE FACE OF COVID-19: SIMULATION OF THE MAXIMUM CAPACITY OF PEOPLE THROUGH PHP

## DISTANCIAMIENTO SOCIAL ANTE LA COVID-19: SIMULACIÓN DEL AFORO MÁXIMO DE PERSONAS MEDIANTE PHP

Oscar J. M. Peña Cáceres<sup>1,\*</sup> , Manuel A. More More<sup>2</sup> 

Ruth E. Cornejo Sojo<sup>1</sup> , Elvis R. Garay Silupu<sup>3</sup> 

Received: 03-11-2021, Received after review: 06-12-2021, Accepted: 13-12-2021, Published: 01-01-2022

### Abstract

Confluence of people in internal or external areas considerably increases transmission of COVID-19, because the social distancing established by the health system is not observed. The objective of this work was to use programming techniques with the PHP language (hypertext preprocessor), for developing an application that simulates the maximum number of people who can enter an internal or external area. The methodology enabled recognizing common internal and external areas, configuring the development environment, coding, simulation proposal and simulator execution where a practical case and ten places were evaluated to determine its reliability. The simulator provided the maximum people capacity of an internal or external area, honoring a social distancing of 2 m. Results enabled to know that using information technologies through programming techniques and the PHP language constitutes a technological alternative to fight against the spread of the virus.

**Keywords:** social distancing, PHP, programming techniques

### Resumen

La confluencia poblacional en áreas internas o externas incrementa considerablemente la trasmisión de la COVID-19, por no respetar el distanciamiento social que establece el sistema de salud. El objetivo de este trabajo fue hacer uso de técnicas de programación, empleando el lenguaje PHP (preprocesador de hipertexto), para el desarrollo de una aplicación que simule el aforo máximo de personas que pueden ingresar a un área interna o externa. La metodología permitió el reconocimiento de áreas internas y externas comunes, configuración al entorno de desarrollo, codificación, propuesta de simulación y ejecución del simulador donde se ha evaluado un caso práctico y diez lugares para determinar su confiabilidad. El simulador brindó el aforo máximo de personas que pueden ingresar a un lugar de área interna o externa cumpliendo el distanciamiento social de 2 m. Los resultados permitieron conocer que el uso de las tecnologías de información a través de las técnicas de programación y el lenguaje PHP contribuyó en ser una alternativa tecnológica para la lucha contra la propagación del virus.

**Palabras clave:** distanciamiento social, PHP, técnicas de programación

<sup>1,\*</sup>Escuela de Posgrado, Universidad Nacional de Piura – Perú.

Corresponding author : [openac@posgrado.unp.edu.pe](mailto:openac@posgrado.unp.edu.pe)

<sup>2,\*</sup>Departamento de Física, Universidad Nacional de Piura – Perú

<sup>3</sup>Área de Tecnologías de la Información, Centro de Reposo San Juan de Dios – Perú.

Suggested citation: Peña Cáceres, O. J. M.; More More, M. A.; Cornejo Sojo, R. E. and Garay Silupu, E. R. "Social distancing in the face of COVID-19: simulation of the maximum capacity of people through PHP," *Ingenius, Revista de Ciencia y Tecnología*, N.º 27, pp. 9-16, 2022, DOI: <https://doi.org/10.17163/ings.n27.2022.01>.

## 1. Introduction

Due to the presence of COVID-19, the world has taken different control measures, such as social distancing in public and private spaces, which has led to new communication ways and characteristics in which human beings cannot interact until the advent of a new normality [1]. Commercial places, financial institutions, recreation areas and governmental institutions, after closing their doors have resumed their business and commercial activities where one of the fundamental criteria for reopening is to determine the maximum people capacity. Such control measure converges with the appropriate use of masks and rational hand wash with water and soap or alcohol [2]. In this scenario it is important to manage areas of interaction, as well as knowing the number of people that can enter a public or private place according to the diameter of each infrastructure taking into consideration biosecurity regulations associated with the social distancing between one person and the other.

This information may be known through a simulation that provides the maximum capacity of people that can access and interact in open or closed spaces honoring biosecurity measures. The present research work intended to demonstrate that programming techniques are one of the means available to evaluate and simulate the maximum capacity of people in places of low, medium and high confluence of people. This exercise helped public and private sectors in a more agile and optimal way, to honor biosecurity regulations and to reduce possible infections of COVID-19 that may propagate due to typical people activities. Such activity contributes with the socio-economic sector and to a government-citizen transformation, developing better proximity and reliability links, mainly in the economic sphere and in the attention of essential services that people permanently use [3].

Research works about social distancing between one person and another to prevent COVID-19 infection were analyzed to address this study. Detection of people and identification of objects and the distance between them was revised, with the purpose of developing an application that involves detection and estimation of the people that would be more exposed to become infected by this virus [4]. However, this cannot be possible without analyzing it from a wide and dynamical context, and with a socioeconomic focus where the use of the resources available and the engineering cosmovision gets involved in the solution of common problems, thus contributing to strengthen productive and economic sectors. Consequently, the use of information technologies (IT) has become a daily means where people have a fundamental role in organizations which enable them to adapt to new changes, generate proposals and provide immediate solutions [5].

Humans may develop a cross-sectional view of world's reality, with the existing solutions to face COVID-19, with resilient characteristics and horizons, encouraging new proposals, context, collaborative ways and techniques that safeguard the integrity of population. ICTs may provide solutions to this new scenario [6]. Even though the COVID-19 pandemics paralyzed access to global systems, it focused on health care through unprecedented blockades and forced social distancing, quickly accelerating the development of these digital technologies to fulfill different worldwide requirements for health attention [7]. For this reason, it is intended to use emerging technologies to prevent its propagation [8]. Control and mitigation of COVID-19 requires involvement of many sectors, including general public. On the other hand, application technologies provide the means through which these different sectors may innovate, communicate and act quickly [9].

If control measures are not applied to reduce the number of contacts at particular places, this may have influence in the evolution of the pandemics. Consequently, it was important to identify the places of greater contact and determine the weight of propagation that has influence on the possibility to have available and make appropriate use of the resources. In this sense, the use of simulation models, as detailed in the current research work, may contribute to decision-making [10]. The findings from a systematic review of 172 studies (44 comparative studies;  $n = 25,697$  patients) about COVID-19, severe acute respiratory syndrome (SARS) and Middle East respiratory syndrome (MERS) provide the best available evidence that current policies of at least 1 m of physical distance are associated with a great reduction in case of infection, but distances of 2 m may be more effective [11].

In view of the above, the general objective of this research study is to use programming techniques with the PHP language, by means of reference variables such as the length and width of an internal or external area, which enables simulating and knowing the number of people that may be admitted honoring social distancing.

## 2. Materials and methods

Figure 1 illustrates the methodology considered for developing the web application, to enable knowing the maximum people capacity that may access internal or external areas honoring social distancing.

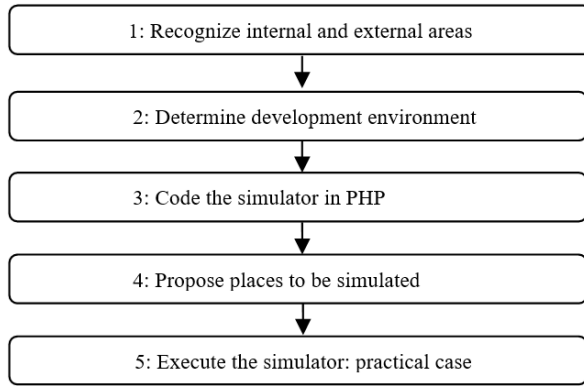


Figure 1. Methodology

### 2.1. Recognize internal and external areas

Internal areas are closed spaces or spaces with limited reduced surface, while external areas have larger dimensions and more access to people. Those spaces are known as indoor or outdoor environments. At present, the access to this type of areas or environments is subject to recommendations to mitigate the propagation of COVID-19. These are based on social distancing, which implies not having close contact with another person; a distance between 1 and 2 m is recommended, as defined in different countries [12].

Throughout all the different activities carried out by humans, they visit indoor places such as restaurants, shopping malls [13], transportation terminals, academic institutions, public-private institutions, bars, cafeterias, libraries, museums or cultural centers, a movie or a theater, a church or spiritual center, their house (or one of its rooms), the home of another person (or one of its rooms), a covered sport facility; they also visit outdoor (external) places such as a square, a urban forest, a viewpoint, a sport field, a street or a section of it, a park, a neighborhood and the terrace of a bar / cafeteria / restaurant [14].

Dispersed population that converges at the aforementioned places is linked to they type of geographical area. Indeed, residents of rural communities show greater levels of identity with the place they live in than residents of cities [15], behavior which is reflected in a high access traffic to shopping malls, restaurants and public institutions. This scenario is significantly affected by a weak and not moderate calculation of the maximum people capacity; this situation represents a lack of identification and evaluation of the available spaces that fulfill biosecurity regulations.

At a local level, the Government should establish control measures that foresee and contribute to the orientation of public and private places, strengthening management of its operations to enable ensuring social distancing and implementing cleaning, disinfection and personal protection actions [16].

### 2.2. Development environment

At present, PHP is one of the most popular programming languages, commonly used by the open-source community because it is an industry for constructing big web applications [17]. It is a compatible, scalable, secure and multidisciplinary programming language that enables developing agile, optimal and immediate applications based on the requirements of society.

Appserv 8.5.0 is used as an interpreter; it is an open-source tool for the Windows operating system that integrates Apache, MySQL and PHP, taking into account the 5.6.26 version of PHP. For coding, the SublimeText [18] text editor enables developing a web application to simulate and determine the maximum people capacity of an internal or external area honoring the mandatory social distancing.

### 2.3. Coding of the simulator in PHP

At the coding stage, programming techniques are used to exploit their expression, order and sequence when writing instructions and sentences. Priority rules [19] are also known for achieving optimal results and solving common problems [20], which contributes in the development of a web application to simulate the maximum people capacity of internal or external areas, honoring biosecurity regulations.

Table 1 describes the use of the five variables created, as well as the operationalizations that specify how these variables interact to give the inputs and outputs that define the behavior of the simulator according to the dimensions entered, as seen in Figure 2.

Table 1. Description of the variables used in simulator coding

N°	Variables	Description
1	\$area_lg	Width of the surface/area.
2	\$area_an	Length of the surface/area.
3	\$area_m2	Operationalization between variables 1 and 2 (product).
4	\$distanciamiento	Variable with an assigned value of "2" m.
5	\$operacion	Operationalization between variables 3 and 4, where variable 4 is divided by "2".

Table 2 explains the predominant instructions, sentences and labels for coding the simulator.

Table 2. Predominant instructions (I), sentences (S) and labels (L) for coding the simulator

Index	Type	Description
for	I	Loop that self-generates the results of the operationalization of the defined variables
if	S	Sentence that conditions the result
else	S	Sentence that is executed when one or more conditions are not met
table	E	Label that shows a table
img	E	Label that shows an image

```

1: <?php
2: $area_lg=20;
3: $area_an=8;
4: $area_m2=$area_lg*$area_an;
5: $distanciamiento=2;
6: $operacion=0;
7: $operacion=$area_m2/($distanciamiento*2);
8: ?>
9: <h2> Simular el Aforo Máximo de Personas</h2>
10: <h2>El aforo para un Área de
11: <?php echo $area_m2; ?> m2 es de
12: <?php echo $operacion; ?> Personas.</h2>
10: <table border="1" cellpadding="0"
11: cellspacing="0" width="60%">
12: <?php for ($j=0; $j <$area_lg ; $j++) {
13: if($j%2==0){
14: ?>
15: <tr>
16: <?php for ($x=0; $x <$area_an ; $x++) { ?>
17: <?php if($x%2==0){ ?>
18: <td align="center"></td>
20: <?php
21: }else{ ?>
22: <td align="center">&nbsp;&nbsp;&nbsp;</td>
23: <?php } } ?>
24: </tr>
25: <?php
26: }else{
27: ?>
28: <tr>
29: <?php for ($i=0; $i <$area_an ; $i++) {
30: if($i%2==0){
31: ?>
32: <td align="center"></td>
34: <?php
35: }else{
36: ?>
37: <td align="center"></td>

```

Figure 2. Coding of the simulator in PHP

The images shown in Figure 3, namely, *distance90*, *distance* and *person*, are used for the operation of the *img* label.

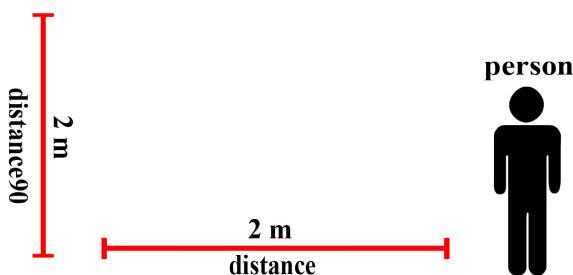


Figure 3. Images used in the coding

## 2.4. Places proposed for simulation

A simulation is an artificial representation of a real process [21], where it is simulation and not reality, and a special objective is sought [22]. In this context, ten places with the internal and external areas most commonly and recurrently visited by the people residing in the Region, Province and District of Piura – Peru, to know the maximum people capacity that may be admitted to each of the places shown in Table 3, honoring the biosecurity regulations.

Table 3. Places with simulated internal and external areas

Nº	Place	Area	Width m2	Length m2
1	Restaurant	Internal	8	15
2	Church	Internal	10	100
3	Cafeteria	Internal	5	20
4	Bar	Internal	6	20
5	Commercial store	Internal	4	8
6	Square	External	85	82
7	Park	External	72	225
8	Sport field	External	26	34
9	Recreational center	External	50	400
10	Avenue	Externa	12	100

## 2.5. Execution of the simulator: practical case

In this stage, initial tests were carried out involving execution of the simulator, where it was sought to know the maximum people capacity that may be admitted to the waiting area of the COVID-19 vaccination facility of the Universidad de Piura, identified as an external outdoor area, with a length of 12 m and a width of 10 m.

The results of the simulation for this first test case indicate that there is an area of 120 m<sup>2</sup>, and that the maximum people capacity is 30 people honoring a social distancing of 2 m, as shown in Figure 4.

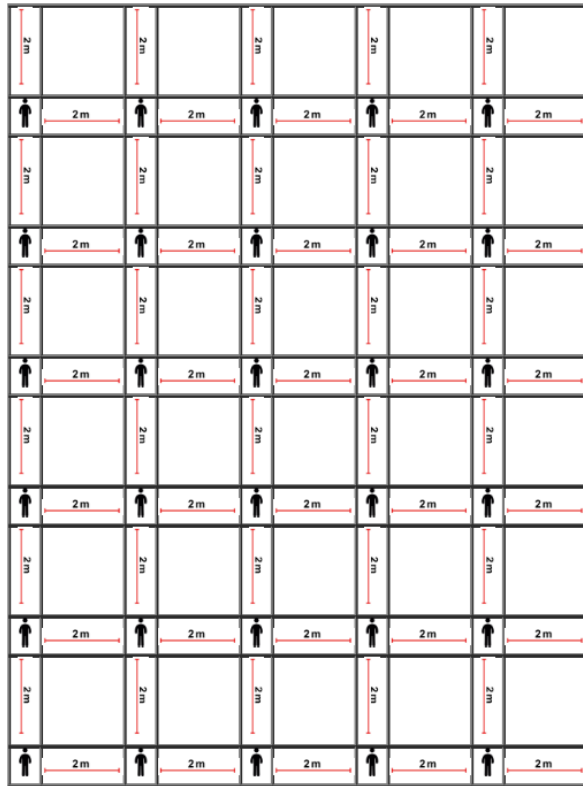


Figure 4. Simulation results

It may be seen that the parametrization of the admission variables is not absolute, as well as the diameter for honoring the social distancing; the composition and form of the results will depend on the admission data.

### 3. Results and discussion

Table 4 shows the results of the ten places identified, and it may be observed in the column Maximum available people capacity that results are favorable, considering the percentage of available area, which enables obtaining real results and knowing the reliability of the web application, provided it is clear that 100 % of the space is not always available in internal or external areas for free access of people.

According to the results of Table 4, it can be also seen that places with external areas exhibit better predominance in the use of the simulator that enables determining the maximum people capacity honoring social distancing; however, for places with internal areas it can be seen that there are some limitations due to the presence of objects, accessories and others, where it should be first obtained the occupied and available area to achieve more reliable results.

Table 4. Results of maximum people capacity in places with internal and external areas

N°	Place	Type of area	Width m	Length m	Area m <sup>2</sup>	Simulated maximum people capacity	Available area	Maximum people capacity
1	Restaurant	Internal	8	15	120	30	50%	15
2	Church	Internal	10	100	1000	250	80%	200
3	Cafeteria	Internal	5	20	100	25	65%	16
4	Bar	Internal	6	20	120	30	60%	18
5	Commercial store	Internal	4	8	32	8	60%	5
6	Square	External	85	82	6970	1742	85%	1481
7	Park	External	72	225	16 200	4050	85%	3443
8	Sport field	External	26	34	884	221	90%	199
9	Recreational center	External	50	400	20 000	5000	90%	4500
10	Avenue	External	12	100	120	30	95%	29

Recall that in places such as restaurants, cafeterias, bars and commercial stores there are spaces where people should wait to access the service or request being made. In this context, the simulator represents a contribution suitable to be used to know the maximum people capacity that may be admitted to places with internal and external areas, making available for entrepreneurs and public sector technological tools that promote honoring biosecurity protocols, articulated with the socioeconomic sector that provides people's source of livelihood.

It is deduced that the use and application of the simulator will contribute and boost the identification of places with internal areas due to the lack of pipes in these places of population recurrence.

The results obtained regarding the simulated maximum people capacity and the available maximum people capacity show a variation of the available area which depends on the place where the simulator is used to determine the maximum people capacity, as seen in Figure 5.

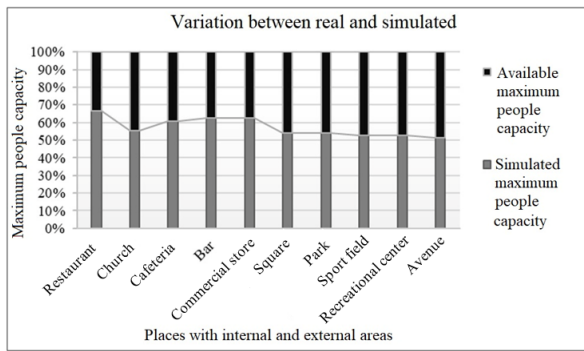


Figure 5. Simulation results

In this sense, to obtain reliable results it is important to know the available area, ignoring factors that limit access to people that seek to interact inside or outside a place, with the purpose of honoring social distancing according to biosecurity regulations.

#### 4. Conclusions

The results given by the simulator for the practical case stated and the ten places evaluated enabled knowing the maximum people capacity that may be admitted to a place with internal and external areas, honoring the social distancing of 2 m. For effective use of the simulator, it is necessary to know the area occupied by objects, accessories and others in the place being evaluated.

The simulator visually shows the certainty, order and security of knowing how to calculate the maximum people capacity that may be admitted in places with external or internal areas, taking into account that places with external areas are the most appropriate for convergence of people since they have a greater available area and smaller number of obstacles that might reduce the maximum number of people that may be in an environment.

The present research work may be strengthened locating a system of video cameras inside or outside places with greater recurrence of people, to know the number of people that have come in or gone out, and those how are in the place. This product may be developed using the PHP programming language and, as an alternative, Python with artificial vision techniques.

Therefore, it is demonstrated that the application of the techniques and the PHP programming language provides a promising route to fight against COVID-19, through easy handling, stability, compatibility and reliability of the results.

#### References

[1] B. L. Valle Canales and J. C. Chavarría Hernández, “Communicative habitus and social distancing. Effects on the modes of sign production

during the COVID-19 pandemic,” *Comunicación y Sociedad*, vol. 18, pp. 1–27, 2021. [Online]. Available: <https://doi.org/10.32870/cys.v2021.7953>

- [2] C. Maguiña Vargas, “El COVID-19 en el Perú,” *Revista de la Sociedad Peruana de Medicina Interna*, vol. 33, no. 4, pp. 129–131, 2020. [Online]. Available: <https://doi.org/10.36393/spmi.v33i4.558>
- [3] A. Ziccardi and D. Figueroa, “Mexico City: Housing conditions and social distancing imposed, COVID-19,” *Revista mexicana de sociología*, vol. 83, pp. 31–60, 2021. [Online]. Available: <https://doi.org/10.22201/iis.01882503p.2021.0.60068>
- [4] C. V. Niño Rondón, S. A. Castro Casadiego, B. Medina Delgado, D. Guevara Ibarra, and J. Gómez Rojas, “Procesamiento a imágenes de video para verificación de distanciamiento social durante la pandemia de la COVID-19,” *Revista Logos Ciencia & Tecnología*, vol. 13, pp. 116–127, 2021. [Online]. Available: <https://doi.org/10.22335/rlct.v13i1.1305>
- [5] C. L. Vidal-Silva, A. Sánchez-Ortiz, J. Serrano, and J. M. Rubio, “Experiencia académica en desarrollo rápido de sistemas de información web con Python y Django,” *Formación universitaria*, vol. 14, pp. 85–94, 2021. [Online]. Available: <http://dx.doi.org/10.4067/S0718-50062021000500085>
- [6] M. Guisado-Clavero, S. Ares-Blanco, and L. D. Ben Abdellah, “Using mobile applications and websites for the diagnosis of COVID-19 in Spain,” *Enfermedades infecciosas y microbiología clínica (English ed.)*, vol. 39, no. 9, pp. 454–457, 2021. [Online]. Available: <https://doi.org/10.1016/j.eimce.2021.08.003>
- [7] W. Y. Ng, T.-E. Tan, P. V. H. Movva, A. H. S. Fang, K.-K. Yeo, D. Ho, F. S. S. Foo, Z. Xiao, K. Sun, T. Y. Wong, A. T.-H. Sia, and D. S. W. Ting, “Blockchain applications in health care for COVID-19 and beyond: a systematic review,” *The Lancet Digital Health*, vol. 3, no. 12, pp. e819–e829, 2021. [Online]. Available: [https://doi.org/10.1016/S2589-7500\(21\)00210-7](https://doi.org/10.1016/S2589-7500(21)00210-7)
- [8] M. Adil and M. K. Khan, “Emerging IoT Applications in Sustainable Smart Cities for COVID-19: Network Security and Data Preservation Challenges with Future Directions,” *Sustainable Cities and Society*, vol. 75, pp. 1–12, 2021. [Online]. Available: <https://doi.org/10.1016/j.scs.2021.103311>
- [9] K. Intawong, D. Olson, and S. Chariyalertsak, “Application technology to fight the COVID-19 pandemic: Lessons learned in Thailand,” *Biochemical and Biophysical Research Communications*,

- vol. 538, pp. 231–237, 2021. [Online]. Available: <https://doi.org/10.1016/j.bbrc.2021.01.093>
- [10] N. Morando, M. Sanfilippo, F. Herrero, M. Iturburu, A. Torti, D. Gutson, M. A. Pando, and R. D. Rabinovich, “Evaluación de intervenciones durante la pandemia COVID-19: desarrollo de un modelo basado en subpoblaciones con distintas tasas de contacto,” *Revista Argentina de Microbiología*, 2021. [Online]. Available: <https://doi.org/10.1016/j.ram.2021.04.004>
- [11] D. K. Chu, E. A. Akl, S. Duda, K. Solo, S. Yaacoub, H. J. Schunemann, D. K. Chu, E. A. Akl, A. El-harakeh, A. Bognanni, T. Lotfi, M. Loeb, A. Hajizadeh, A. Bak, A. Izcovich, C. A. Cuello-Garcia, C. Chen, D. J. Harris, E. Borowiack, F. Chamseddine, F. Schnemann, G. P. Morgano, G. E. U. Muti Schunemann, G. Chen, H. Zhao, I. Neumann, J. Chan, J. Khabsa, L. Hneiny, L. Harrison, M. Smith, N. Rizk, P. Giorgi Rossi, P. AbiHanna, R. Elkhoury, R. Stalteri, T. Baldeh, T. Piggott, Y. Zhang, Z. Saad, A. Khamis, M. Reinap, S. Duda, K. Solo, S. Yaacoub, and H. J. Schunemann, “Physical distancing, face masks, and eye protection to prevent person-to-person transmission of SARS-CoV-2 and COVID-19: a systematic review and meta-analysis,” *The Lancet*, vol. 395, no. 10242, pp. 1973–1987. [Online]. Available: [https://doi.org/10.1016/S0140-6736\(20\)31142-9](https://doi.org/10.1016/S0140-6736(20)31142-9)
- [12] B. R. Rowe, A. Canosa, J. M. Drouffe, and J. B. A. Mitchell, “Simple quantitative assessment of the outdoor versus indoor airborne transmission of viruses and COVID-19,” *Environmental Research*, vol. 198, p. 111189, 2021. [Online]. Available: <https://doi.org/10.1016/j.envres.2021.111189>
- [13] F. Zhang, J. Zu, M. Hu, D. Zhu, Y. Kang, S. Gao, Y. Zhang, and Z. Huang, “Uncovering inconspicuous places using social media check-ins and street view images,” *Computers, Environment and Urban Systems*, vol. 81, p. 101478, 2020. [Online]. Available: <https://doi.org/10.1016/j.compenvurbsys.2020.101478>
- [14] M. Subiza-Pérez, T. Pasanen, E. Ratcliffe, K. Lee, A. Bornioli, J. de Bloom, and K. Korpela, “Exploring psychological restoration in favorite indoor and outdoor urban places using a top-down perspective,” *Journal of Environmental Psychology*, vol. 78, p. 101706, 2021. [Online]. Available: <https://doi.org/10.1016/j.jenvp.2021.101706>
- [15] D. Belanche, L. V. Casaló, and M. A. Rubio, “Local place identity: A comparison between residents of rural and urban communities,” *Journal of Rural Studies*, vol. 82, pp. 242–252, 2021. [Online]. Available: <https://doi.org/10.1016/j.jrurstud.2021.01.003>
- [16] L. Pan, J. Wang, X. Wang, J. S. Ji, D. Ye, J. Shen, L. Li, H. Liu, L. Zhang, X. Shi, and L. Wang, “Prevention and control of coronavirus disease 2019 (COVID-19) in public places,” *Environmental Pollution*, vol. 292, p. 118273, 2022. [Online]. Available: <https://doi.org/10.1016/j.envpol.2021.118273>
- [17] M. Hills, P. Klint, and J. J. Vinju, “Enabling PHP software engineering research in Rascal,” *Science of Computer Programming*, vol. 134, pp. 37–46, 2017. [Online]. Available: <https://doi.org/10.1016/j.scico.2016.05.003>
- [18] K. Alrashedy, D. Dharmaretnam, D. M. German, V. Srinivasan, and T. Aaron Gulliver, “Scc++: Predicting the programming language of questions and snippets of stack overflow,” *Journal of Systems and Software*, vol. 162, p. 110505, 2020. [Online]. Available: <https://doi.org/10.1016/j.jss.2019.110505>
- [19] O. D. Castrillón, W. Sarache, and S. Ruiz, “Desempeño de técnicas tradicionales de programación de la producción frente a un algoritmo evolutivo,” *Información tecnológica*, vol. 29, pp. 141–154, 2018. [Online]. Available: <http://dx.doi.org/10.4067/S0718-07642018000200141>
- [20] W. Auccahuasi, G. Bernardo, M. Bernardo, D. Vega, R. Urbano, and E. Oré, “Herramienta interactiva en línea como instrumento para el aprendizaje de las matemáticas mediante las técnicas de programación, dirigido a alumnos de educación secundaria,” in *16th LACCEI International Multi-Conference for Engineering, Education, and Technology: Innovation in Education and Inclusion*, 2018, pp. 19–21. [Online]. Available: <https://doi.org/10.18687/LACCEI2018.1.1.573>
- [21] L. Gómez-López, B. Tena-Blanco, R. Bergé-Ramos, M. Coca-Martínez, C. Forero-Cortés, and C. Gomar-Sancho, “Nueva plantilla para diseñar escenarios de simulación: interrelación de elementos en un vistazo,” *Educación Médica*, vol. 19, pp. 350–359, 2018. [Online]. Available: <https://doi.org/10.1016/j.edumed.2017.12.001>
- [22] M. L. Alfonso-Mora, A. L. Castellanos-Garrido, A. del Pilar Villarraga Nieto, M. L. Acosta-Otálora, C. Sandoval-Cuellar, R. del Pilar Castellanos-Vega, R. L. Goyeneche-Ortegón, and E. A. Cobo-Mejía, “Aprendizaje basado en simulación: estrategia pedagógica en fisioterapia. revisión integrativa,” *Educación Médica*, vol. 21, no. 6, pp. 357–363, 2020. [Online]. Available: <https://doi.org/10.1016/j.edumed.2018.11.001>





# DESIGN AND CONSTRUCTION OF AUTOMATED MECHANICAL VENTILATION EQUIPMENT

## DISEÑO Y CONSTRUCCIÓN DE EQUIPO DE VENTILACIÓN MECÁNICA AUTOMATIZADA

Gilberto Carrillo<sup>1</sup> , Mauricio Gómez<sup>2,\*</sup> 

Jaime Rodas<sup>1</sup> , Rafael Pimentel<sup>1</sup> 

Received: 11-10-2021, Received after review: 06-12-2021, Accepted: 15-12-2021, Published: 01-01-2022

### Abstract

This document presents the requirements met for the design, construction and initial validation of a mechanical ventilation system to be used in patients with respiratory insufficiency, which in the initial context was due to the COVID-19 pandemics. The design required the use of computer aided drawing software (Computer Aided Design) CAD and the construction required the use of installed capabilities in mechanical, electropneumatic, electronic, biomedical and automation manufacturing of institutes and centers of the Universidad Don Bosco (El Salvador). The adjustment, configuration and programming tasks were in charge of research professors specialized in these disciplines. The elements used for its construction were available in the Salvadoran market, considering the closure of borders as a government measure to face the expansion of the pandemics. After the design, manufacturing and commissioning stage, conditions of the supplied air were measured with the help of professionals dedicated to the maintenance of medical equipment and with the approval of internist doctors. The results achieved are those obtained with paramedical equipment and with first aid equipment, and consequently it has been foreseen that the equipment can be tested in a subsequent instance with the certified medical union.

**Keywords:** Mechanical ventilation, assisted respiration, COVID-19, respiratory insufficiency

### Resumen

Este documento presenta los requerimientos cumplidos para el diseño, construcción y primera validación de un sistema de ventilación mecánica para ser utilizado en pacientes con insuficiencia respiratoria, que en el contexto inicial fuera a causa de la pandemia de COVID-19. El diseño requirió el uso de *software* de dibujo asistido por computadora (*Computer Aided Design*) CAD y la construcción necesitó el uso de las capacidades instaladas en manufactura mecánica, electroneumática, electrónica, biomédica y automatización de los institutos y centros de la Universidad Don Bosco (El Salvador). Los trabajos de ajuste, configuración y programación estuvieron a cargo de docentes investigadores especialistas en dichas disciplinas. Los elementos empleados para su construcción estaban disponibles en el mercado salvadoreño, considerando el cierre de las fronteras como medida gubernamental ante la expansión de la pandemia. Luego de la etapa de diseño, fabricación y puesta en funcionamiento, se realizaron mediciones de las condiciones del aire suministrado con la ayuda de profesionales dedicados al mantenimiento de equipo médico y con el visto bueno de doctores internistas. Los resultados conseguidos son los que se obtienen con equipos paramédicos y con equipos de primera asistencia, por lo cual se ha previsto que el equipo pueda ser probado en una siguiente instancia con el gremio médico certificado.

**Palabras clave:** ventilación mecánica, respiración asistida, COVID-19, insuficiencia respiratoria

<sup>1</sup>Centro de Innovación en Diseño Industrial y Manufactura, Universidad Don Bosco, El Salvador.

<sup>2,\*</sup>Instituto de Investigación e Innovación en Electrónica, Universidad Don Bosco, El Salvador.

Corresponding author ✉: mauricio.gomez@udb.edu.sv

## 1. Introduction

At the beginning of 2020, America becomes the epicenter of the SARS CoV-2 (Severe acute respiratory syndrome coronavirus-2) [1,2], and in March it is declared a worldwide pandemics due to the ease of propagation because of the globalization phenomenon [3]. The first confirmed case in El Salvador was registered that same month. At that time, different protocols were activated to prevent massive infections in the population. However, hospitals were getting prepared for the attention of future patients.

With the purpose of visualizing the possible impact of the pandemics in the country, different scenarios were considered such as the construction of a specialized hospital for the attention of patients with COVID-19 (Corona Virus Disease - 2019), strengthening the installed capacity of existing hospitals, oxygen supply, possible medication for treating patients, training and hiring of medical staff for attention of patients, among other actions. In this last case, it is evident that when a patient requires personalized attention with an equipment for manual assistance of respiration, the medical or auxiliary staff assisting him/her cannot care other patients, thus becoming a human resource unavailable for assisting people; this impact may be reduced if an automated equipment easy to install and easy to use in emergencies is supplied.

The expectation of a possible shortage of equipment for respiratory assistance motivated researchers to propose alternative systems of mechanical ventilation [4,5] from auxiliary manual breathing units (AMBU) [6,7]. This initiative sought the collaboration between the Industrial Design and Manufacturing Innovation Center (CIDIM, Centro de Innovación en Diseño Industrial y Manufactura) and the Research and Innovation Institute in Electronics (IIIE, Instituto de Investigación e Innovación en Electrónica), with the management of special resources of the Energy Research Institute (IIE, Instituto de Investigación en Energía) and the support from the collaboration of the United States Embassy in El Salvador.

To determine the best design of the system, and considering the strengths and capacity of the centers and institutes, it was stated that it fulfilled the following requirements:

- Take advantage of the existence of a manual reviver [8] used by paramedics and internist doctors.
- The reviver should be operated using two systems, one electropneumatic and another electronic.
- Structural accessories should be easy to manufacture in metal-mechanic shops.

- The acquisition of the specialized monitoring sensors would be handled through the American Space UDB of the IIE [9], due to the national quarantine that made difficult the imports by local industries.

## 2. Materials and methods

The basic fundamental of the designed system is an electropneumatic control system that drives a manual reviving equipment. The operation signals are controlled by a programmable logical controller, that receives electric signals from sensors that monitor the heart rate and the level of oxygen concentration in the air supplied.

The first design stage consisted of meetings between technical researchers and intensive care doctors from the Hospital San Rafael. The control variables that should be monitored in patients were determined in these meetings; these variables include the air volume according to the consistency of the patient, the number of cycles per minute required by patients according to their clinical picture, the ventilation pressure, the positive end-expiratory pressure (PEEP) [4], [10], the air flow, and the inspiratory-to-expiratory (I/E) ratio. Another important requirement is that the system should operate in three types of cycles: volume-cycled, pressure-cycled and combination of both. However, with the approval of the intensive care doctor it was chosen the volume-cycled, since it is a simple and effective operation mode, always taking into account that it is an emergency measure [11].

The design should provide appropriate ventilation for patients prior to releasing a specific ventilator [12], and thus it was considered the tidal volume and the respiratory rate that would maintain patients stable [13]. The tidal volume was determined based on a ratio with the ideal weight of patients and it is calculated taking as reference the weight of the person:

IBW (ideal body weight, kilograms) men [14]:

$$50 + 2.3 * (\text{size in inches} - 60) \text{ or}$$

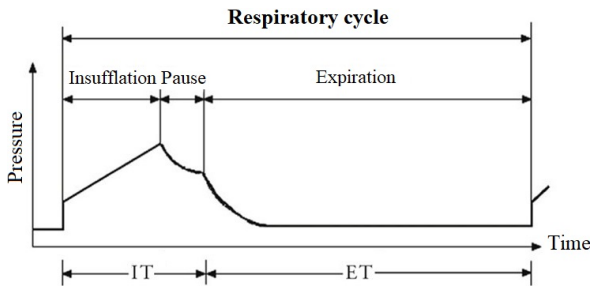
$$50 + 0.9 * (\text{size in cm} - 152,4)$$

IBW (ideal body weight, kilograms) women:

$$45.5 + 2.3 * (\text{size in inches} - 60) \text{ o}$$

$$45.5 + 0.9 * (\text{size in cm} - 152,4)$$

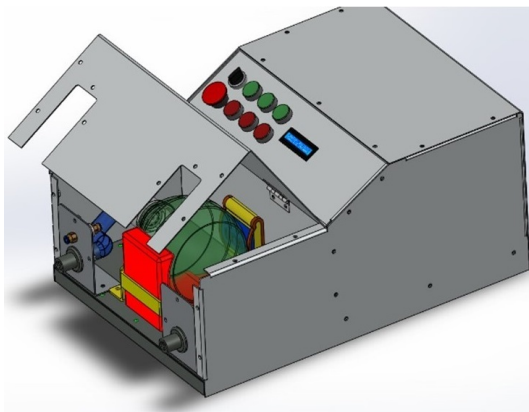
With respect to respiratory rate, the inspiration and expiration cycle is related to the age of patients, according to the behavior shown in the curve of Figure 1.



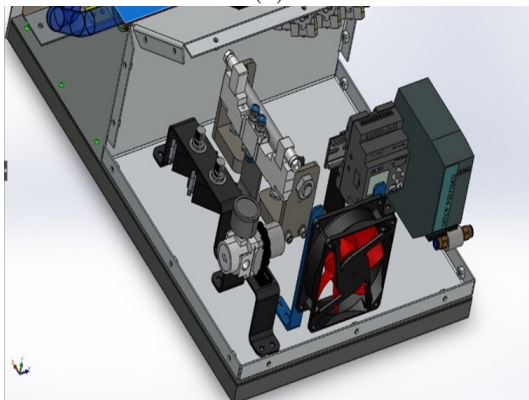
**Figure 1.** Respiratory cycle

Figure 1 shows the I/E ratio [15], inspiration [16] (insufflation) and expiration (exhalation), which may be adjusted to 1:3. But if the patient condition is preexisting asthma [17] or exacerbation of chronic obstructive pulmonary disease, it may be adjusted to 1:4.

After obtaining the operation requirements, the structural design was carried out with the aid of CAD software [18] and 3D printing light manufacturing [19], with the result presented in Figure 2.



(a)



(b)

**Figure 2.** Design of the system with the aid of CAD software

Figure 2 shows the design obtained of the structural system and of the electropneumatic system. Figure 2(a) shows the structural distribution to hold the reviver,

the location of the access points to the inlet and outlet air connections, together with the valves that regulate the reviver pressure, the mobile door, the cover with the set of buttons and the information display. Figure 2(b) shows the distribution of the electropneumatic control system constituted by the 5/3 bistable electropneumatic valve, unidirectional flow regulators, pressure regulator, programmable logic controller (PLC), ventilator, electric and pneumatic adapters, supports and configuration of the structural base.



(a)



(b)

**Figure 3.** Construction of the electropneumatic system

Figure 3 shows the finalized structural (a) and electropneumatic (b) systems, ready to carry out tests and measurements. It is important to remark that all control system elements installed were found at the place, since imports to El Salvador were not possible as a consequence of the confinement due to COVID-19 pandemics. This enables replicating the system without difficulty, in case it is required.

A SIEMENS LOGO version 8.0 micro-PLC was used to control the process. It can handle 4 digital outputs, better known as output to relays, which are used to govern the valves and electrovalves required by the system. Similarly, the buttons enable to control the number of repetitions per minute demanded by the patient and according to the criterion of the treating physician.

The control system was designed according to the plot of the respiration process shown in Figure 1, where

the specialist may determine if the patient requires 12, 14, 16 or more repetitions per minute for his/her treatment. It should be mentioned that the code is versatile enough to be modified at any moment, and configure it in the cadences required by internist doctors.

The PLC has a display where the specialist may see the selected value of repetitions and the buttons are marked to avoid confusions. The electropneumatic system is prepared to receive compressed air from the hospital infrastructure, and thus it has been anticipated that this air is used as pneumatic supply to the control electrovalves.

The system design was prepared to place programmed control processes in the PLC, to enable specialists to be certain about the number of repetitions that they are selecting for the patient. At this moment the system is open-loop, because the sensors required to implement the corresponding control loops are not available. However, appropriate sensors may be installed in a subsequent version such that the system self-regulates based on the information provided by the sensors, thus transforming it into a close-loop system.

Figure 4 shows the connections between the PLC and the different parts of the respirator.

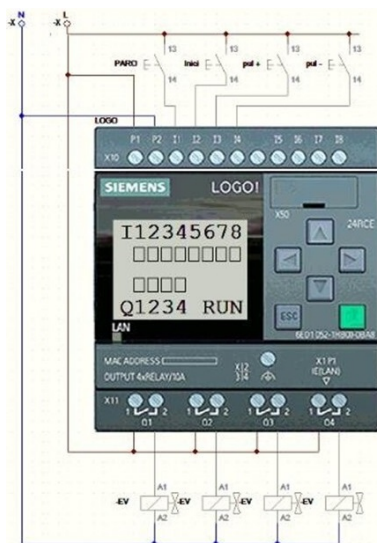


Figure 4. Configuration of the PLC

### 3. Results and discussion

Due to the agreement between the diagrams and the final equipment, it is considered that the conceptual prototype may be easily reproduced, both its structural and electropneumatic components.

Measurements were carried out by the INFRA personnel in El Salvador, to conduct operation tests and verify that it complies with the parameters indicated by the internist doctor. They are responsible of per-

forming maintenance of assisted mechanical ventilation equipment, with the use of specialized equipment.



(a)



(b)

Figure 5. Equipment for measuring operational parameters

Figure 5 presents the measurement equipment: (a) verifies that it is a Certifier FA TSI High Flow Module [20] and (b) presents the detected value of 0.301 liters of air and 15.2 blows per minute (BPM). The values shown are in agreement with the ones indicated by internist doctors for patients with ages between 25 and 40 years, with 15 to 19 inspirations per minute, values that can be regulated through PLC programming and varying the flow regulator, establishing predefined pushbuttons for such parameters and for medical conditions of patients. In addition, measurements were carried out with the NI ELVIS [21] equipment of the University Biomedical Laboratory, which was used to build a plot from the signals detected by sensors, that coincides with the data obtained by the INFRASAL specialists.

Table 1 shows the data measured with the TSI equipment, indicating the respirations per minute (RPM), the minimum and maximum air volume given in milliliters, the minimum and maximum air flow in liters per second, the minimum and maximum air pressure in  $\text{cm H}_2\text{O}$ . The equipment was configured for 15 and 19 RPM, es requested by specialists. When configured for 15 RPM, the volume transfer obtained was between 290 and 330 ml, the flow varied from 2.5

to 3 l/s and the pressure reached a value of 42 cm H<sub>2</sub>O. On the other hand, when the equipment was configured for 19 RPM, a volume transfer between 270 and 320 ml was obtained, the flow varied from 2.5 to 3 l/s and the pressure reached a value of 40 cm H<sub>2</sub>O [22, 23]. In both cases, the values obtained are considered appropriate.

**Table 1.** Measurements carried out with the TSI equipment

	RPM	Volume (ml)		Flow (l/s)		Pressure (cm H <sub>2</sub> O)	
		Min.	Max.	Min.	Max.	Min.	Max.
<b>1</b>	15	290	330	2,5	3	-	42
<b>2</b>	19	270	320	2,5	3	-	40

#### 4. Conclusions

Some of the strong proficiencies of the Universidad Don Bosco are in the areas of electronics, automation and manufacturing, and thus this work proposes the design of a mechanical ventilation system assisted by automatic control systems.

The support provided by the American Space UDB was key to obtain electronic elements that were not available at the moment due to the closure of borders as a consequence of the pandemics, but that are necessary for developing automatic and medical equipment, which enables to give a fast response to face worldwide challenges.

Improvements may be implemented in the design and the prototype which makes it more complex, efficient, precise, but which enables applying it to a larger number of cases that arise at the medical level.

The systems designed and constructed are versatile, because they may be configured according to the requirements of doctors and patients in short time, both face-to-face and remotely. Different programs may be simultaneously loaded in the PLC, such that pressing different buttons or changing the position of a knob, different programs may be called for the operation of the pneumatic cylinder (cycles, stroke length) according to the requirement of each patient.

Another advantage of the PLC is that different clinical sensors may be connected to it, and with the interpretation of such signals changes in the operating conditions of the pneumatic control system are automatically activated.

The system constructed may be used for studies in medicine, manufacturing, electronics, automation, both in continuous training of specialists, and in graduate and undergraduate studies. The objective is always to provide humanitarian aid.

The physical model constructed may be a reference for future development of mathematical and simulation

models, in the medical and engineering areas, among others.

#### References

- [1] M. Ciotti, M. Ciccozzi, A. Terrinoni, W.-C. Jiang, C.-B. Wang, and S. Bernardini, "The COVID-19 pandemic," *Critical Reviews in Clinical Laboratory Sciences*, vol. 57, no. 6, pp. 365–388, 2020, pMID: 32645276. [Online]. Available: <https://doi.org/10.1080/10408363.2020.1783198>
- [2] S. A. Lone and A. Ahmad, "COVID-19 pandemic an African perspective," *Emerging Microbes & Infections*, vol. 9, no. 1, pp. 1300–1308, 2020, pMID: 32458760. [Online]. Available: <https://doi.org/10.1080/22221751.2020.1775132>
- [3] J. Watkins, "Preventing a COVID-19 pandemic," *BMJ*, vol. 368, 2020. [Online]. Available: <https://doi.org/10.1136/bmj.m810>
- [4] M. Mittermaier, P. Pickerodt, F. Kurth, L. B. de Jarcy, A. Uhrig, C. Garcia, F. Machleidt, P. Pergantis, S. Weber, Y. Li, A. Breitbart, F. Bremer, P. Knape, M. Dewey, F. Doellinger, S. Weber-Carstens, A. S. Slutsky, W. M. Kuebler, N. Suttorp, and H. Müller-Redetzky, "Evaluation of PEEP and prone positioning in early COVID-19 ARDS," *EClinicalMedicine*, vol. 28, p. 100579, 2020. [Online]. Available: <https://doi.org/10.1016/j.eclinm.2020.100579>
- [5] P. d. F. Chambergo Ruiz, "Diseño, simulación y control de un resucitador para respiratoria," 2017. [Online]. Available: <https://bit.ly/3IWbTBO>
- [6] L. Fiorineschi, F. S. Frillici, and F. Rotini, "Challenging COVID-19 with Creativity: Supporting Design Space Exploration for Emergency Ventilators," *Applied Sciences*, vol. 10, no. 14, 2020. [Online]. Available: <https://doi.org/10.3390/app10144955>
- [7] A. Jumlongkul, "Automated AMBU Ventilator With Negative Pressure Headbox and Transporting Capsule for COVID-19 Patient Transfer," *Frontiers in Robotics and AI*, vol. 7, p. 221, 2021. [Online]. Available: <https://doi.org/10.3389/frobt.2020.621580>
- [8] F. Pasquevich, A. Patanella, G. Garaventa, and M. Actis, "Respirador mecánico de emergencia," *Innovación y Desarrollo Tecnológico y Social*, vol. 2, no. 2, pp. 134–166, 2020. [Online]. Available: <https://doi.org/10.24215/26838559e020>
- [9] IUS. (2020) Embajada de Estados Unidos dona a la UDB equipo tecnológico para el impulso

- de proyectos formativos. Instituciones Salesianas de Educación Superior. [Online]. Available: <https://bit.ly/3mmDqCG>
- [10] O. Heredia, X. Chunga, L. De la Cruz, and M. Zimic, “Diseño y evaluación de un ventilador mecánico,” *SciELO*, 2021. [Online]. Available: <https://bit.ly/3dZdWqu>
- [11] F. Aranda, J. Aliste, F. Altermatt, F. Alvarez, JP Bernucci, A. Bruhn, M. C. Cabrera, E. Carrasco, R. Castillo, R. De la Fuente, R. Díaz, J. I. Egaña, R. González, T. Honorato, H. J. Lacassie, M. López, W. Merino, A. Penna, F. Pizarro, D. Torres, R. Cristián, A. Bruhn, D. Acuña, and T. Regueira, “Recomendaciones para el manejo de pacientes con COVID-19 con indicación terapéutica de ventilación mecánica que eventualmente son conectados a máquinas de anestesia,” *Revista Chilena de Anestesia*, vol. 49, no. 3, 2020. [Online]. Available: <https://doi.org/10.25237/revchilanstv49n03.09>
- [12] G. Tusman, M. Campos, and E. Gogniat, “COVID-19: Cómo transformar un ventilador de no invasiva en un ventilador de críticos,” *Revista Española de Anestesiología y Reanimación*, vol. 67, no. 7, pp. 367–373, 2020. [Online]. Available: <https://doi.org/10.1016/j.redar.2020.05.002>
- [13] W. Mazzotti, “Prácticas de enseñanza medidas por la tecnología. Cómo enseñan los docentes en los foros de discusión de cursos que se desarrollan en modalidad a distancia,” *Cuadernos de Investigación Educativa*, vol. 2, no. 16, pp. 25–45, 2018. [Online]. Available: <https://doi.org/10.18861/cied.2009.2.16.2721>
- [14] F. Gutiérrez Muñoz, “Ventilación mecánica,” *Acta Médica Peruana*, vol. 28, pp. 87–104, 2011. [Online]. Available: <https://bit.ly/3mbefTB>
- [15] B. A. Rozas, J. V. Urra, and J. G. Garzón, “Características de la ventilación mecánica invasiva en COVID-19 para médicos no especialistas,” *Revista Chilena de Anestesia*, vol. 49, no. 4, 2020. [Online]. Available: <https://doi.org/10.25237/revchilanstv49n04-06>
- [16] T. H. Barnes and M. Singer, “Low cost devices to help in COVID-19,” *Trends in Anaesthesia and Critical Care*, vol. 38, pp. 21–23, 2021. [Online]. Available: <https://doi.org/10.1016/j.tacc.2021.03.011>
- [17] H. Kitazawa, N. Hizawa, Y. Nishimura, T. Fujisawa, T. Iwanaga, A. Sano, H. Nagase, H. Matsumoto, T. Horiguchi, S. Konno, and K. Asano, “The impact of the COVID-19 pandemic on asthma treatment in Japan: Perspectives based on doctors’ views,” *Respiratory Investigation*, vol. 59, no. 5, pp. 670–674, 2021. [Online]. Available: <https://doi.org/10.1016/j.resinv.2021.06.004>
- [18] R. Prabhu, J. S. Masia, J. T. Berthel, N. A. Meisel, and T. W. Simpson, “Design and manufacturability data on additively manufactured solutions for COVID-19,” *Data in Brief*, vol. 36, p. 107012, 2021. [Online]. Available: <https://doi.org/10.1016/j.dib.2021.107012>
- [19] M. Larriba, D. Rodríguez-Llorente, A. C. nada Barcala, E. Sanz-Santos, P. Gutiérrez-Sánchez, G. P.-M. noz, S. Álvarez-Torrellas, V. I. Águeda, J. A. Delgado, and J. García, “Lab at home: 3D printed and low-cost experiments for thermal engineering and separation processes in COVID-19 time,” *Education for Chemical Engineers*, vol. 36, pp. 24–37, 2021. [Online]. Available: <https://doi.org/10.1016/j.ece.2021.02.001>
- [20] TSI. (2021) Certifier flow analyzer plus high flow module kit 4081. TSI Incorporated. [Online]. Available: <https://bit.ly/32k6a82>
- [21] NI. (2021) NI Educational Laboratory Virtual Instrumentation Suite (NI ELVIS). National Instruments. [Online]. Available: <https://bit.ly/3spEIAQ>
- [22] F. Ruza Tarrío, *Tratado de cuidados intensivos pediátricos*. Capitel Editores, 2002. [Online]. Available: <https://bit.ly/3p0DXvH>
- [23] S. H. Ochoa, M. I. Martínez, and G. E. J. Díaz, “Ventilación mecánica en pacientes con COVID-19 de acuerdo a los fenotipos de gattinoni,” *Acta Médica Grupo Ángeles*, vol. 18, no. 3, pp. 336–340, 2020. [Online]. Available: <https://dx.doi.org/10.35366/95421>



# CHARACTERIZATION OF DELUX: ULTRAVIOLET LIGHT STERILIZATION DEVICE FOR PFF2 / N95 MASKS AGAINST COVID-19

## CARACTERIZACIÓN DO DELUX: DISPOSITIVO DE ESTERILIZACIÓN POR LUZ ULTRAVIOLETA PARA MÁSCARAS PFF2/N95 CONTRA COVID-19

Christiane Bertachini Lombello<sup>1,\*</sup> , Nasser Ali Daghashtanli<sup>1</sup> ,  
 Hermann Windisch Neto<sup>1</sup> , Fernando Luiz Affonso Fonseca<sup>2</sup> ,  
 Felipe Nogueira Ambrosio<sup>1</sup> , Raquel Arbex<sup>1</sup> ,  
 Isabella Kobb Fernando<sup>1</sup> , Victor Allisson da Silva<sup>1</sup> ,  
 Luisa Pataquini dos Santos<sup>1</sup> , Patricia Aparecida da Ana<sup>1</sup> 

Received: 15-11-2021, Received after review: 20-12-2021, Accepted: 26-12-2021, Published: 01-01-2022

### Abstract

The World Health Organization (WHO) has declared a public health pandemic state due to the transmission of the new coronavirus on March 11th, 2020. COVID-19, that is caused by SARS-CoV-2, has a very broad clinical spectrum, with predominantly respiratory symptoms developments. The role of the health professionals in fighting the pandemic requires the use of Personal Protective Equipment (PPE). PFF2 / N95 masks are suitable PPEs for this purpose. Due to the high demand for PFF2 / N95 masks to fight the pandemic, there was a shortage of this PPE worldwide. This work aims to present a characterization of the device called DELUX, utilized for UVC (ultraviolet C light spectra) sterilization of PFF2 / N95 masks, and allowing to extend the time of safe use of this PPE in emergency conditions. The photometric validation of the device resulted in the verification of the emission spectrum of the lamps used in the device, and the measurement of the optical power, demonstrating the adequacy of irradiation with UVC light, with a 15-minute cycle, and safely. Biological validation showed that DELUX is capable of inactivating SARS-CoV-2 present on the surface of PFF2 / N95 masks, thus being efficient for their sterilization. The safety offered by the sterilization cycle allows to extend the safe use of those masks.

**Keywords:** COVID-19, equipment, protective, radiation, sterilization, ultraviolet

### Resumen

La Organización Mundial de la Salud (OMS) declaró un estado pandémico de salud pública debido a transmisión del nuevo coronavirus el 11 de marzo de 2020. La COVID-19, causada por el SARS-CoV-2, tiene un espectro clínico muy amplio, con predominio de desarrollos sintomáticos respiratorios. El papel de los profesionales de salud en la lucha contra pandemia requiere el uso de Equipo de Protección Personal (EPP). Las máscaras PFF2 / N95 son EPP adecuados para este propósito. Debido a gran demanda de máscaras PFF2 / N95 para combatir la pandemia, hubo escasez en el mercado. Este trabajo tiene como objetivo caracterizar un dispositivo denominado DELUX para la esterilización por UVC (espectros de luz ultravioleta C) de mascarillas PFF2 / N95, ampliando el tiempo de uso seguro de este EPP en condiciones de emergencia. La validación fotométrica del dispositivo permitió la verificación del espectro de emisión de las lámparas utilizadas en el dispositivo y la medición de la potencia óptica, demostrando la idoneidad de la irradiación con luz UVC, en ciclos de 15 minutos, de forma segura. La validación biológica mostró que DELUX es capaz de inactivar el SARS-CoV-2 presente en la superficie de las mascarillas PFF2 / N95, siendo así eficiente para su esterilización. La seguridad que ofrece el ciclo de esterilización permite extender el tiempo de uso seguro de estas mascarillas.

**Palabras clave:** COVID-19, equipo, esterilización, protección, radiación, ultravioleta

<sup>1,\*</sup>CECS, Federal University of ABC, UFABC, Brazil. Corresponding author ✉: [christiane.lombello@ufabc.edu.br](mailto:christiane.lombello@ufabc.edu.br).

<sup>2</sup>ABC Medical School, FMABC, Brazil

Suggested citation: Lombello, C. B.; Ali Daghashtanli, N.; Windisch Neto, H.; Affonso Fonseca, F. L.; Nogueira Ambrosio, F.; Arbex, R.; Kobb Fernando, I.; da Silva, V. A.; Pataquini dos Santos, L. and Aparecida da Ana, P. "Characterization of DELUX: Ultraviolet light sterilization device for PFF2 / N95 masks against COVID-19," *Ingenius, Revista de Ciencia y Tecnología*, N.º 27, pp. 23-31, 2022, DOI: <https://doi.org/10.17163/ings.n27.2022.03>.

## 1. Introduction

Viruses known as coronaviruses belong to the order Nidovirales, family Coronaviridae, subfamily Coronavirinae, genus Coronavirus (CoVs) [1]. They were first identified in poultry in the 1930s and many of them have been associated with respiratory, gastrointestinal, liver and neurological diseases in animals. Some coronaviruses are known to cause disease in humans [2]. Of these, four species (229E, OC43, NL63 and HUK1) usually cause symptoms of a common cold in humans, and only rarely can result on a severe lower respiratory tract infection, such as pneumonia. These cases are particularly important in children, the elderly and immunodepressed patients [3–5].

However, three other species considered zoonoses (SARS-CoV, MERS-CoV and SARS-CoV-2) are associated with more severe respiratory infections in humans, and can be fatal [3,4]. SARS-CoV was identified in 2002 as the cause of Severe Acute Respiratory Syndrome (SARS), while MERS-CoV was identified in 2012 as the cause of Middle Eastern Respiratory Syndrome (MERS) [4]. More recently, SARS-CoV-2 (Figure 1), known as the new coronavirus, was first detected on December 2019 in the city of Wuhan (China), and identified as the etiologic agent of the disease capable of aggravating the respiratory system [3], [6] with an important impact on global public health due to consequent morbidity and mortality worldwide [7,8]. According to the World Health Organization (WHO), the official nomenclature for the disease caused by this virus was defined as Coronavirus Disease-2019 (COVID-19) and, on March 11, 2020, WHO declared a state of pandemic in public health, due to the transmission of the new coronavirus [9,10].

COVID-19 disease, caused by SARS-CoV-2, has a very broad clinical spectrum. There are asymptomatic variations or diverse clinical symptoms, such as sore throat, diarrhea, anosmia or hyposmia, myalgia, tiredness, fatigue, and skin manifestations, like dermatoses and urticaria were also recorded [8], [11,12]. However, mainly respiratory symptoms such as dry cough and shortness of breath, associated with fever, and other symptoms mentioned above are directly related to the high rates of hospitalization and death resulting from the disease [8], [12].

The health professionals work is fundamental during the infection combat, in prevention, detection, patient treatment and recovery, and these professional efforts are recognized worldwide [13]. During the professional activities the use of Personal Protective Equipment (PPE) can provide safety, preventing accidents or occupational diseases. The Brazilian Health Regulatory Agency (*Agência Nacional de Vigilância Sanitária*, Anvisa) determines that the PPE required during the activities performed by health professionals with possible exposition to SARS-CoV-2 include: cap, protection

glasses or face shield, mask (surgical or respiratory protection mask), long-sleeved coat and gloves [14].

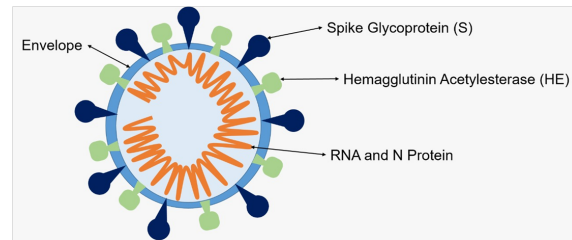


**Figure 1.** Structure of the coronavirus. The envelope, capsid proteins (S and HE), N protein and viral RNA are represented

As this is a disease with preferential transmission through the air, masks are essential PPE in controlling the spread of the disease. These devices are also called Respiratory Protection Equipment (RPE). Surgical masks are indicated to prevent the contamination of the professionals' airways by respiratory droplets (particles larger than 5  $\mu\text{m}$ ) when acting less than 1 meter from the patient. However, not all the masks provide protection against aerosols [14,15]. Although these masks, as well as fabric masks, are not considered PPE by Anvisa, their use by the population was mandatory in several countries, like Brazilian one, in order to contain the transmission of COVID-19. In health services, masks must be used by asymptomatic patients, visitors, companions and professionals in administrative areas who do not have contact with patients at distances of less than 1 meter [14], [16].

The masks called semi-facial filtering piece (PFF) are PPEs with a minimum efficiency of 95% in the filtration of particles up to 0.3  $\mu\text{m}$ . The classification of masks occurs according to the level of penetration and breathing resistance, which can be PFF1, PFF2 and PFF3 in Brazil. For the protection of aerosols (that is, particles smaller than droplets) containing biological agents, PFF2 must be used, equivalent to the N95 mask adopted in the United States [14], [16–18].

These RPEs should be used by healthcare professionals who work in procedures with risk of generating aerosols, such as collection of nasotracheal secretions, bronchoscopy, non-invasive ventilation, manual ventilation before intubation, intubation or tracheal aspiration, and cardiopulmonary resuscitation. In addition, they are also recommended to support professionals who develop their activities in areas of carrying out procedures that generate aerosols [14], [16]. However, in cases of prolonged use, it is important that this equipment remains adjusted in the face, and functional. In this context, the Brazilian Institute for Patient Safety (IBSP) warns that these masks remain effective when used for up to 8 consecutive hours [19]. PFF2/N95 masks are formed by superimposed layers of fabric-non-woven (TNT) polypropylene, which filter the air

and trap particles in the order of 0.3  $\mu\text{m}$ , including microorganisms such as the SARS-CoV-2 virus [20].

The impact of the COVID-19 pandemic on healthcare services included the high demand for PPE used by healthcare professionals in the combat of the coronavirus, resulting in a shortage of supply of this equipment. Although not ideal, the lack of availability of PFF2/N95 masks on the market makes the reuse of these PPEs necessary. The Anvisa agency states that respiratory protection masks may, exceptionally, be used for a longer period or for several times greater than that foreseen by the manufacturer. However, the reuse of these PPE for a time beyond what is considered safe exposes health professionals to contamination by the virus, due to the conditions of prolonged use, handling and storage. Some Anvisa recommendations described in the Technical Note GVIMS/GGTES/ANVISA N. 04/2020 [16] indicates the proper use of this PPE that must be followed. The reprocessing of a PPE regularized at Anvisa as disposable must ensure that it is as safe as a new PPE, in addition to not affecting the performance characteristics. Possible reprocessing protocols must be validated in order to guarantee the sterilization of the product as well as its integrity and functionality [16].

Among the alternatives developed to ensure safety in the extension of the useful life and reuse of these masks, the sterilization of these equipments with UVC radiation has shown to be promising. This technique, in addition to enabling the reuse of masks quickly, does not require large infrastructure and elaborate spaces, as well as the frequent replacement of supplies. Thus, the use of a sterilization device with such a function guarantees a versatile possibility so that, at first, healthcare workers can sterilize their PPE safely and quickly [21].

This paper aims to characterize a low-cost and fast production equipment, developed in the ABC region of São Paulo, for the sterilization of PFF2/N95 masks, with the proposal to extend the time of use of this PPE in emergency conditions of shortages in the market due to the current COVID-19 pandemic.

## 2. Materials and methods

### 2.1. Emission of UVC lamps

The characterizations of the emission spectrum of the UVC lamps (PURITEC 15W, Osram, Brasil) used in the DELUX device was carried out using three different devices.

#### 2.1.1. Ultraviolet-visible photodiode spectrophotometer (Cary 50, Varian)

Measurements were taken to obtain the emission spectrum of UVC lamps (PURITEC 15W, Osram, Brasil).

#### 2.1.2. OCEAN OPTICS spectrometer (UV-VIS-NIR spectrometer)

This spectrometer is coupled to an optical fiber ( $\varphi=400$  nm) to measure the emission of the UVC lamp in loco, that is, inside the sterilization and measurement equipment of the internal environment of the irradiation chamber.

#### 2.1.3. FieldMaxII-TO optical powermeter (Coherent-USA)

Powermeter was coupled to the PM10 sensor (Coherent-USA) to measure the power values per area ( $\text{mW}/\text{cm}^2$ ) through the PM10 semiconductor sensor in the desired spectral region.

## 2.2. Biological Tests

Validation of efficacy was carried out together with the ABC Medical School (FMABC). To ensure the correct PFF2/N95 mask sterilization through the DELUX system, a methodology was proposed to assess the effectiveness against the presence of viruses after the sterilization cycle. For this study the virus were detected using RT-PCR (polymerase chain reaction) [22, 23].

Three N95 masks of the same type used by health professionals during their daily activities were used (in particular the respiratory mask 8801H 9 PFF-2 Respirators for biological risks (Brand: 3M®, Brasil)) A control sample with the SARS-CoV-2 virus was used to mimic the contamination on the front of the mask, following the experimental procedures. Initially a swab containing a viral sample was used to spread the contents from bottom to top and left to right. The swab was used for 6 times for spreading in the anterior direction of each of the masks, and rested at room temperature for 3 minutes, in biosafety cabinet. The masks were then positioned in the DELUX device in order to maximize their complete illumination with UVC light. Irradiation of the masks with UVC light was carried out in a single 15-minute cycle.

After irradiation, samples were collected from the masks. For this purpose, the masks were kept for 1 minute in a biosafety cabinet, and using a sterile swab was rubbed on the surface of the mask in the anterior region from the bottom to the top and from the left to the right, repeated 6 times. The swab was placed in an extraction solution in order to obtain the viral RNA. RNA extraction and amplification followed the Centers for Disease Control and Prevention (CDC) protocol.

## 3. Results and discussion

For the sterilization of PFF2/N95 masks, one of the possible measures adopted worldwide is sterilization

with UVC radiation, a physical agent. Ultraviolet light is in the electromagnetic spectrum, and UVC radiation comprises wavelengths between 190 and 280 nm, located within the spectrum of UV light (electromagnetic spectrum between 100 and 390 nm). However, wavelengths below 200 nm have no biological significance, as they are intensely absorbed by air [24].

UVC radiation lamps used for germicidal action usually have peak emission at a wavelength of 254 nm. This parameter is suitable for the inactivation of several microorganisms, including coronaviruses, as stated in previous studies with SARS-CoV and MERS-CoV [25, 26]. The photolytic effect of UVC radiation is capable of destroying or inactivating the microorganism, preventing it from multiplying. It is intensely absorbed by nucleic acids and proteins, causing the disruption of nucleic acid bases and the inactivation of enzymes. Unlike other techniques, its photolytic action rarely produces potentially dangerous by-products [27–29].

The device called DELUX (Figure 2) was developed in partnerships with the ABC School of Medicine, FMABC, and with the company based in the ABC region of São Paulo (named Ecosan). The device was made with materials compatible with the purpose and use, mainly using 304 stainless steel sheets, carrying handle, electrical system to drive 4 ultraviolet light lamps (PURITEC 15W, Osram, Brasil), automated timer system, lamp activation indicator LED and safety system to prevent the activation of the lamps with the equipment open.

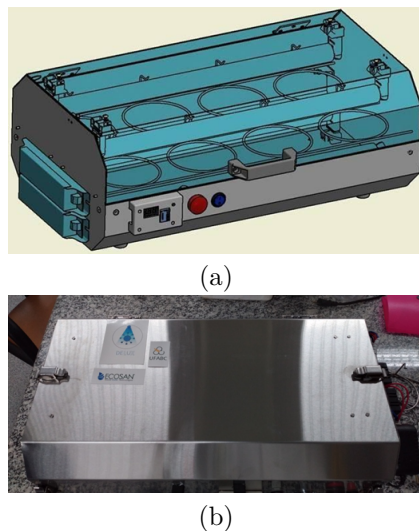


**Figure 2.** DELUX. (a) prototype, (b) device

The device allows the simultaneous accommodation of up to 16 masks, in niches that allow the identification of each mask. It was carried out with the validation of the photometric efficacy of the device and the verification of the biological efficacy against the coronavirus.

### 3.1. Photometric Measures

Ultraviolet light (UV) is part of the electromagnetic spectrum characterized by wavelengths ( $\lambda$ ) smaller than those of the visible light (VIS) spectrum, which varies between 400nm - 800nm. The spectral range of UV light is between 100 - 400 nm, and it is divided into 3 different regions: UVA (long-wave) between 315 - 400 nm; UVB (medium-wave) between 280-315 nm, and UVC (short-wave) between 100 - 280 nm [24]. UVC light has a germicidal effect compared to visible light [24], [28, 29].

Regarding safety, exposure to UVC can cause several adverse biological effects, such as acute inflammation of human tissues, conjunctivitis, erythema, in addition to being associated with chromosomal alterations that can even cause some types of cancer [24]. Thus, the use of UV light must be carried out carefully to prevent possible adverse effects. The biological effects of the action of UV light can be evaluated as a function of damage through the parameter of Relative Spectral Effectiveness,  $S(\lambda)$ , thus when exposure to UV light occurs, care must be taken [24], [26], [28, 29].

The measurements of the optical power of the lamps used in the DELUX prototype were started with the photometric characterization of the PURITEC 15W, (Osram, Brasil), by measuring the emission spectrum in the UV-VIS region (Varian spectrophotometer), as shown in Figure 3. Typical emission peaks at specific wavelengths were observed.

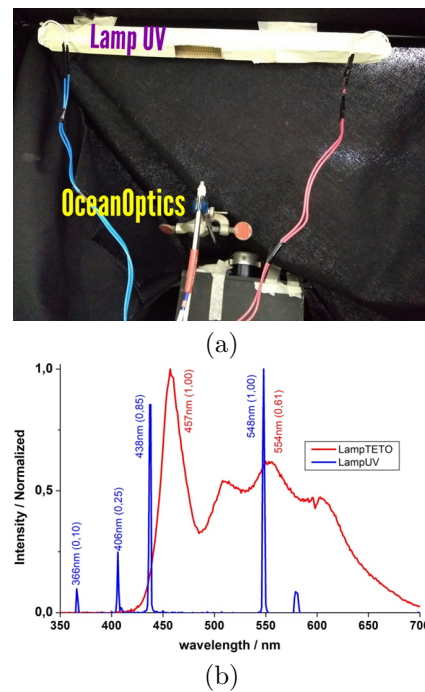


**Figure 3.** (a) Experimental setup with the light probe (Ocean Optics). (b) Emission spectra of a white light lamp (LampTETO) and UVC light (LampUV). Emission peaks in the region of interest, below 400 nm.

The measurements of the power emission intensities were complemented with the optical powermeter. Measurements of the power emitted by the UVC lamp were performed using peak emission at  $\lambda = 256 \text{ nm}$ , and  $\lambda = 438 \text{ nm}$ , shown in Figure 4. These data allowed us to evaluate the emission of the UVC lamps used in DELUX at the relevant wavelengths ( $\lambda$ ) (Figure 4).

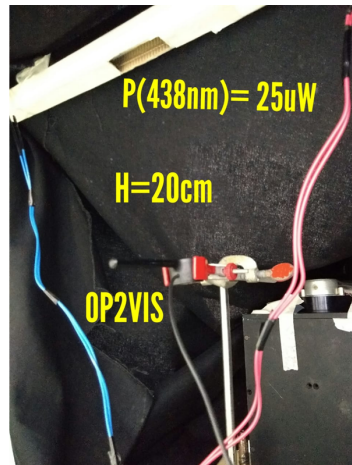


**Figure 4.** Assembly for measuring the power of UV light emitted by UV lamps. Measurements were performed with two different power probes (Coherent), OP2-VIS and PM10 (for UVC). Height (H), optical power (P)

Temporal measurements of UVC light emission (at 256 nm) were performed from the moment the lamps were turned on at an interval of 800 s. Figure 4 shows the kinetic curve of the UV lamp emission. We observe that the power emission efficiency of the lamp increases from exponential-like transient to constant emission (Figure 5).

Measurements were performed using the UV lamps in the interior of the device, and possible leak of light to the exterior of the device was verified. The equipment has the installation of rubber blankets that were effective for the complete blocking of light. Measurements of light power were not obtained on the outside of the device, closed and turned on, with activation of the lamps, which is an important result to guarantee safety for users.

For sterilization to be effective, some factors must be taken into account. The dose (or intensity) of light delivered ( $\text{J}/\text{cm}^2$ ) is determined by the product between the irradiance of the light source ( $\text{mW}/\text{cm}^2$ ) and the irradiation time. The dose of light must be sufficient and adequate to penetrate the material to be sterilized. The penetration of light radiation is controlled by the material's absorption coefficient: the lower the coefficient, the greater the success of the application [28, 29].

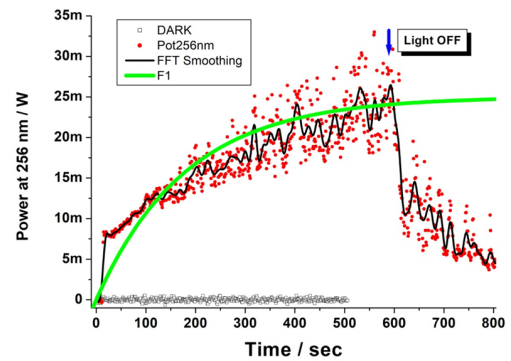


**Figure 5.** Kinetic curve of UV lamp emission. Temporal measurements. Red dots are the monoexponential fit of light emission at 256 nm (10Hz). Black line is dot smoothing (FFT - Origin). Solid green line is the monoexponential fit of the experimental data, UVC lamp emission reaches maximum value of 25mW after 400s. Minimum power emitted  $\sim 8 \text{ mW}$

The sterilization efficiency also depends on the regularity and exposed area on the material surface, as there is a minimum dose of UVC radiation to inactivate the microorganisms [20, 21], [28, 29]. Thus, a successful sterilization will only occur if the entire surface of the material is exposed to UVC radiation, as any shadows produced by the fabric layers of the masks can reduce the effectiveness of the sterilization. As the surface requires high intensity UV light, the lamps must be close to the material to be sterilized [30].

Different mask models may have different sterilization results [21]. Models with extra layers of outer protection can make it difficult or even prevent UVC light from penetrating the innermost layers. There are more studies that allow the standardization of this procedure, and individual tests are recommended for each type of mask that is used in a particular location [21], [31].

The recommended dose of UVC radiation to ensure effective sterilization is  $1 \text{ J}/\text{cm}^2$ . The dose between  $0.5\text{--}1.8 \text{ J}/\text{cm}^2$  was able to inactivate 99.9% of pathogens, such as some types of Influenza A, MERS-CoV, SARS-CoV and the MS2 bacteriophage. The mask's filtering capacity was maintained even with high doses of UVC radiation [20, 21], [28–31].

The use of UVC light is a possible solution for the sterilization of N95 masks in their reuse, as they have antimicrobial and antiviral effects and do not generate toxic residues that may remain in the masks. UVC radiation can promote the degradation of the polypropylene that makes up the filtering layers, but this is a slow process, in which doses lower than  $950 \text{ J}/\text{cm}^2$  do not present any significant loss of filtration efficiency [32, 33].

### 3.2. Biological Tests

Upon analyzing the results, all samples were classified as «Not Detected». It was possible to conclude that the samples tested after the SARS-CoV-2 scattering procedure and submitted to DELUX presented a «Not Detected» result, showing that the 15 minute UVC light cycle with the DELUX device was sufficient to sterilize the masks.

Due to high demand associated with production and logistical difficulties, the quantity of N95 masks was shown to be limited and insufficient to attend healthcare professionals during a pandemic situation [34, 35]. The Anvisa determines that, due to the public health emergency situations, exceptionally, these masks can be used for longer periods of time and for a several times greater than the specifications provided by the manufacturer, which must be followed by some precautions. These must include PPE protection, proper handling and inspection before each period of usage [36, 37]. The reuse limit is not stipulated by Anvisa, which must be recommended by each healthcare facility, and proper protocols related to the reuse of these PPE are encouraged, as well as, health professionals care with the PPE.

A review study demonstrated that an irradiation dose of 4 J/cm<sup>2</sup> resulted in a 3-log (99.9%) reduction in viral presence, which represents a total decontamination in models using Influenza virus [31]. In addition to the irradiation dose, the time elapsed after contamination also results in a decrease in the presence of microorganisms, with a reduction of 1 log (90%) occurring after 24 hours [31]. Studies consider a period of 60 seconds of irradiation for sterilization [38]. For the MERS-CoV virus, the appropriate time was 5 minutes [26]. Meanwhile for the H1N1 virus, the appropriate time was 15 minutes, and the distance between the UVC lamp and the masks was 25 centimeters [39]. The DELUX device was based on 15 minute cycle sterilization, proposing a unique cycle per day per mask.

In Brazil, due to lack of funds, many centers do not have space or equipment to implement or develop protocols regarding sterilization by ultraviolet radiation (UVC), and the lack of this PPE has been a persistent problem since the beginning of the pandemic. This study allowed the characterization of the DELUX device that can be used to sterilize PFF2/N95 masks using UVC radiation, in a standardized way, ensuring the extension of the time of use of these PPEs safely for health professionals, as shown by photometric and biological characterizations.

Another advantage of this UVC PFF2/N95 masks sterilization includes the reduction of potentially infectious waste generated by the disposal of the large amount of masks used in the COVID-19 pandemic [40].

### 4. Conclusions

The DELUX device is based on the UVC sterilization strategy for irradiating PFF2/N95 masks with a 15 minute cycle. It is a low-cost, fast and effective device to sterilize PFF2/N95 masks, allowing for its proper and safe reuse in order to alleviate the shortage of PPE during the COVID-19 pandemic. The photometric measurements show that the DELUX can make an adequate UVC-light irradiation, resulting in an efficient sterilization on masks. Additionally, photometric measurements allowed, guarantying a safe device to handle with. The biologic characterization resulted in inactivation of SARS-CoV-2 on the masks surface.

### Acknowledgments

The UFABC for financial support, UFABC Multiuser Center (CEM UFABC) for the equipment support, the ABC Medical School (FMABC) for the partnership and biological validation, and Ecosan for the development of the DELUX device.

### References

- [1] S. Payne, "Family coronaviridae," *Elsevier Public Health Emergency Collection*, pp. 149–158, 2017. [Online]. Available: <https://dx.doi.org/10.1016/B978-0-12-803109-4.00017-9>
- [2] J. S. M. Peiris, "Coronaviruses," *Elsevier Public Health Emergency Collection*, pp. 587–593. [Online]. Available: <https://dx.doi.org/10.1016/B978-0-7020-4089-4.00072-X>
- [3] M. D. S. Cespedes and J. C. R. P. Souza, "Sars-cov-2: A clinical update - ii," *Revista da Associação Médica Brasileira*, vol. 66, no. 4, pp. 547–557. [Online]. Available: <https://doi.org/10.1590/1806-9282.66.4.547>
- [4] M. Pal, G. Berhanu, C. Desalegn, and V. Kandi, "Severe Acute Respiratory Syndrome Coronavirus-2 (SARS-CoV-2): An Update," *Pal M, Berhanu G, Desalegn C, Kandi V. Severe Acute Respiratory Syndrome Coronavirus-2 (SARS-CoV-2): An Update. Cureus. 2020;12(3):e7423. Published 2020 Mar 26. doi:10.7759/cureus.7423*, vol. 12, no. 3, p. e7423, 2020. [Online]. Available: <https://dx.doi.org/10.7759/cureus.7423>
- [5] D. X. Liu, J. Q. Liang, and T. S. Fung, "Human coronavirus-229e, -oc43, -nl63, and -hku1 (coronaviridae)," *Elsevier Public Health Emergency Collection*, pp. 428–440. [Online]. Available: <https://dx.doi.org/10.1016/B978-0-12-809633-8.21501-X>

- [6] M. Wang, R. Cao, L. Zhang, X. Yang, J. Liu, M. Xu, Z. Shi, Z. Hu, W. Zhong, and G. Xiao, “Remdesivir and chloroquine effectively inhibit the recently emerged novel coronavirus (2019-nCoV) in vitro,” *Cell research*, vol. 30, no. 3, pp. 269–271, 2020. [Online]. Available: <https://doi.org/10.34172/jrcm.2020.005>
- [7] S. H. Alfaraj, J. A. Al-Tawfiq, A. Y. Asiri, N. A. Alzahrani, A. A. Alanazi, and Z. A. Memish, “Clinical predictors of mortality of Middle East Respiratory Syndrome Coronavirus (MERS-CoV) infection: A cohort study,” *Travel Medicine and Infectious Disease*, vol. 29, pp. 48–50. [Online]. Available: <https://doi.org/10.1016/j.tmaid.2019.03.004>
- [8] L. Piroth, J. Cottenet, A.-S. Mariet, P. Bonniaud, M. Blot, P. Tubert-Bitter, and C. Quantin, “Comparison of the characteristics, morbidity, and mortality of COVID-19 and seasonal influenza: a nationwide, population-based retrospective cohort study,” *The Lancet Respiratory Medicine*, vol. 9, no. 3, pp. 251–259, 2021. [Online]. Available: [https://doi.org/10.1016/S2213-2600\(20\)30527-0](https://doi.org/10.1016/S2213-2600(20)30527-0)
- [9] FIOCRUZ. (2021) Por que a doença causada pelo novo coronavírus recebeu o nome de Covid-19? Fundação Oswaldo Cruz. [Online]. Available: <https://bit.ly/3pwoiEE>
- [10] J. Zhang, W. Wu, X. Zhao, and W. Zhang, “Recommended psychological crisis intervention response to the 2019 novel coronavirus pneumonia outbreak in China: a model of West China Hospital,” *Precision Clinical Medicine*, vol. 3, no. 1, pp. 3–8, 02 2020. [Online]. Available: <https://doi.org/10.1093/pccmedi/pbaa006>
- [11] M. Relvas, J. C. ao, R. Oliveira, J. C. Cardoso, and M. Gonçalo, “Manifestações cutaneas associadas a COVID-19: Uma revisão narrativa,” *Revista Científica da Ordem dos Médicos*, vol. 34, no. 2, pp. 128–136, 2021. [Online]. Available: <https://doi.org/10.20344/amp.14574>
- [12] M. C. Grant, L. Geoghegan, M. Arbyn, Z. Mohammed, L. McGuinness, E. L. Clarke, and R. G. Wade, “The prevalence of symptoms in 24,410 adults infected by the novel coronavirus (SARS-CoV-2; COVID-19): A systematic review and meta-analysis of 148 studies from 9 countries,” *PLoS One*, vol. 15, no. 6, p. e0234765, 2020. [Online]. Available: <https://doi.org/10.1371/journal.pone.0234765>
- [13] E. A. S. Medeiros, “A luta dos profissionais de sade no enfrentamento da COVID-19,” *Acta Paul Enferm.*, p. 33, 2020. [Online]. Available: <http://dx.doi.org/10.37689/acta-ape/2020EDT0003>
- [14] Secretaria de Vigilância em Saúde. (2021) Recomendações de proteção aos trabalhadores do serviço de saúde no contexto da pandemia da Covid-19. Ministério da Saúde, Brasil. [Online]. Available: <https://bit.ly/3pvZ3lX>
- [15] C. D. Cappa, S. B. Sima Asadi, A. S. Wexler, N. M. Bouvier, and W. D. Ristenpart, “Expiratory aerosol particle escape from surgical masks due to imperfect sealing,” *Scientific Reports*, no. 11, p. 12110, 2021. [Online]. Available: <https://doi.org/10.1038/s41598-021-91487-7>
- [16] ANVISA, *Nota Técnica GVIMS/GGTES/ANVISA N° 04/2020. Orientações para serviços de saúde: medidas de prevenção e controle que devem ser adotadas durante a assistência aos casos suspeitos ou confirmados de infecção pelo novo coronavírus (SARS-CoV-2)*. Agência Nacional de Vigilância Sanitária, 2021. [Online]. Available: <https://bit.ly/3z12T9X>
- [17] ABNT, *Equipamento de proteção respiratória – Filtros para partículas*. Associação Brasileira de Normas Técnicas (ABNT), 2010. [Online]. Available: <https://bit.ly/3qwTiUF>
- [18] —, *Equipamento de proteção respiratória – Peça semifacial filtrante para partículas*. Associação Brasileira de Normas Técnicas (ABNT). [Online]. Available: <https://bit.ly/3qqm09z>
- [19] IBSP. (2020) Máscaras n95 – recomendações para uso prolongado e reutilização. Instituto Brasileiro Para Segurança Do Paciente. [Online]. Available: <https://bit.ly/3Jpfd8D>
- [20] S. Duncan, P. Bodurtha, and S. Naqvi, “The protective performance of reusable cloth face masks, disposable procedure masks, kn95 masks and n95 respirators: Filtration and total inward leakage,” *PLoS One*, vol. 16, no. 10, p. e0258191, 2021. [Online]. Available: <https://doi.org/10.1371/journal.pone.0258191>
- [21] C. C. Ontiveros, D. C. Shoults, S. MacIsaac, K. D. Rauch, C. L. Sweeney, A. K. Stoddart, and G. A. Gagnon, “Specificity of UV-C LED disinfection efficacy for three N95 respirators,” *Scientific Reports*, no. 11, p. 15350, 2021. [Online]. Available: <https://doi.org/10.1038/s41598-021-94810-4>
- [22] D. B. Larremore, B. Wilder, E. Lester, S. Shehata, J. M. Burke, J. A. Hay, T. Milind, M. J. Mina, and R. Parker, “Test sensitivity is secondary to frequency and turnaround time for covid-19 surveillance,” *medRxiv : the preprint server for health sciences*, vol. 20, p. 20136309, Sep 2020. [Online]. Available: <https://dx.doi.org/10.1101/2020.06.22.20136309>

- [23] CDC. (2020) Research Use Only 2019–Novel Coronavirus (2019-nCoV) Real-time RT-PCR Primers and Probes. Centers for Disease Control and Prevention. [Online]. Available: <https://bit.ly/3EBvJyF>
- [24] T. I. C. on Non-Ionizing Radiation Protection, “Guidelines on limits of exposure to ultraviolet radiation of wavelengths between 180 nm and 400 nm (incoherent optical radiation),” *Health Physics*, vol. 87, no. 2, 2004. [Online]. Available: <https://doi.org/10.1097/00004032-200408000-00006>
- [25] M. E. R. Darnell, K. Subbarao, S. M. Feinstone, and D. R. Taylor, “Inactivation of the coronavirus that induces severe acute respiratory syndrome, SARS-CoV,” *J Virol Methods*, vol. 121, no. 1, pp. 85–91, Oct. 2004. [Online]. Available: <https://doi.org/10.1016/j.jviromet.2004.06.006>
- [26] K. Bedell, A. H. Buchaklian, and S. Perlman, “Efficacy of an automated multiple emitter whole-room ultraviolet-c disinfection system against coronaviruses mhv and mers-cov,” *Infection Control & Hospital Epidemiology*, vol. 37, no. 5, pp. 598–599, 2016. [Online]. Available: <https://doi.org/10.1017/ice.2015.348>
- [27] F. A. Alexandre, J. A. F. Faria, and C. F. Cardoso, “Avaliação da eficiência da radiação ultravioleta na esterilização de embalagens plásticas,” *Ciência e Agrotecnologia*, vol. 32, no. 5, pp. 1524–1530, 2008. [Online]. Available: <https://bit.ly/3mAbDie>
- [28] J. S. Smith, H. Hanseler, J. Welle, R. Ratray, M. Campbell, T. Brotherton, T. Moudgil, T. F. Pack, K. Wegmann, S. Jensen, J. Jin, C. B. Bifulco, S. A. Prahl, B. A. Fox, and N. L. Stucky, “Effect of various decontamination procedures on disposable n95 mask integrity and sars-cov-2 infectivity,” *Journal of clinical and translational science*, vol. 5, no. 1, pp. e10–e10, Jun 2020. [Online]. Available: <https://dx.doi.org/10.1017/cts.2020.494>
- [29] M. Biasin, A. Bianco, G. Pareschi, A. Cavalleri, C. Cavatorta, C. Fenizia, P. Galli, L. Lessio, M. Lualdi, E. Tombetti, A. Ambrosi, E. M. A. Redaelli, I. Saulle, D. Trabattoni, A. Zanutta, and M. Clerici, “Uv-c irradiation is highly effective in inactivating sars-cov-2 replication,” *Scientific Reports*, vol. 11, no. 1, p. 6260, Mar 2021. [Online]. Available: <https://doi.org/10.1038/s41598-021-85425-w>
- [30] CDC. Implementing Filtering Facepiece Respirator (FFR) Reuse, Including Reuse after Decontamination, When There Are Known Shortages of N95 Respirators. Centers for Disease Control and Prevention. [Online]. Available: <https://bit.ly/3sD9ypQ>
- [31] K. O’Hearn, S. Gertsman, M. Sampson, R. Webster, A. Tsampalieros, R. Ng, J. Gibson, A. T. Lobos, N. Acharya, A. Agarwal, S. Boggs, G. Chamberlain, E. Staykov, L. Sikora, and J. D. McNally, “Decontaminating n95 and sn95 masks with ultraviolet germicidal irradiation does not impair mask efficacy and safety,” vol. 106, no. 1, pp. 163–175. [Online]. Available: <https://doi.org/10.1016/j.jhin.2020.07.014>
- [32] L. Liao, W. Xiao, M. Zhao, X. Yu, H. Wang, Q. Wang, S. Chu, and Y. Cui, “Can n95 respirators be reused after disinfection? how many times?” *ACS nano*, vol. 14, no. 5, pp. 6348–6356, May 2020. [Online]. Available: <https://dx.doi.org/10.1021/acsnano.0c03597>
- [33] W. G. Lindsley, S. B. Martin, Jr, R. E. Thewlis, K. Sarkisian, J. O. Nwoko, K. R. Mead, and J. D. Noti, “Effects of ultraviolet germicidal irradiation (UVGI) on N95 respirator filtration performance and structural integrity,” *J Occup Environ Hyg*, vol. 12, no. 8, pp. 509–517, 2015. [Online]. Available: <https://doi.org/10.1080/15459624.2015.1018518>
- [34] ABMT. 87 % das denúncias de falta de EPIs são sobre máscaras N95, diz AMB. Associação Brasileira de Medicina do Trabalho. [Online]. Available: <https://bit.ly/3JIBFj5>
- [35] J. Rose. (2020) Why can’t america make enough n95 masks? 6 months into pandemic, shortages persist. NPR. SPECIAL SERIES The Coronavirus Crisis. [Online]. Available: <https://n.pr/3mBjImT>
- [36] K. Seresirikachorn, V. Phoophiboon, T. Chobarporn, K. Tiankanon, S. Aeumjaturapat, S. Chusakul, and K. Snidvongs, “Decontamination and reuse of surgical masks and N95 filtering facepiece respirators during the COVID-19 pandemic: A systematic review,” *Infect Control Hosp Epidemiol*, vol. 42, no. 1, pp. 25–30, Jul. 2020. [Online]. Available: <https://doi.org/10.1017/ice.2020.379>
- [37] E. C. Toomey, Y. Conway, C. Burton, S. Smith, M. Smalle, X.-H. S. Chan, A. Adishes, S. Tanveer, L. Ross, I. Thomson, D. Devane, and T. Greenhalgh, “Extended use or reuse of single-use surgical masks and filtering face-piece respirators during the coronavirus disease 2019 (COVID-19) pandemic: A rapid systematic review,” *Infect Control Hosp Epidemiol*, vol. 42, no. 1, pp. 75–83, Oct. 2020. [Online]. Available: <https://doi.org/10.1017/ice.2020.1243>

- [38] NEVMS, *Descontaminação de máscaras de proteção respiratória modelo N95 (respirador particulado)*. Núcleo de Evidência de Mato Grosso do Sul, 2020. [Online]. Available: <https://bit.ly/345EmW1>
- [39] B. K. Heimbuch, W. H. Wallace, K. Kinney, A. E. Lumley, C.-Y. Wu, M.-H. Woo, and J. Wander, "A pandemic influenza preparedness study: use of energetic methods to decontaminate filtering facepiece respirators contaminated with H1N1 aerosols and droplets," *Am J Infect Control*, vol. 39, no. 1, pp. e1–9, Dec. 2010. [Online]. Available: <https://doi.org/10.1016/j.ajic.2010.07.004>
- [40] S. Sangkham, "Face mask and medical waste disposal during the novel covid-19 pandemic in asia," vol. 2, p. 100052. [Online]. Available: <https://doi.org/10.1016/j.cscee.2020.100052>



# EVALUATION OF AIOT PERFORMANCE IN CLOUD AND EDGE COMPUTATIONAL MODELS FOR MASK DETECTION

## EVALUACIÓN DE AIOT EN MODELOS COMPUTACIONALES EN LA NUBE Y EN EL BORDE APLICADO A LA DETECCIÓN DE MASCARILLAS

Felipe Quiñonez-Cuenca<sup>1,\*</sup> , Cristian Maza-Merchán<sup>1</sup> ,  
 Nilvar Cuenca-Maldonado<sup>1</sup> , Manuel Quiñones-Cuenca<sup>1</sup> , Rommel Torres<sup>1</sup> ,  
 Francisco Sandoval<sup>1</sup> , Patricia Ludeña-González<sup>1</sup>

Received: 15-11-2021, Received after review: 20-12-2021, Accepted: 27-12-2021, Published: 01-01-2022

### Abstract

COVID-19 has caused serious health damage, infecting millions of people and unfortunately causing the several deaths around the world. The vaccination programs of each government have reduced those rates. Nevertheless, new coronavirus mutations have emerged in different countries, which are highly contagious, causing concern with vaccination effectiveness. So far, wearing facemasks in public continues being the most effective protocol to avoid and prevent COVID-19 spread. In this context, there is a demand of automatic facemask detection services to remind people the importance of wearing them appropriately. In this work, a performance evaluation of an AIoT system to detect correct, inappropriate, and non-face-mask wearing, based on two computational models: Cloud and Edge, was conducted. Having as objective to determine which model better suits a real environment (indoor and outdoor), based on: reliability of the detector algorithm, use of computational resources, and response time. Experimental results show that Edge-implementation got better performance in comparison to Cloud-implementation.

**Keywords:** AIoT, COVID-19, Cloud Computing, Edge Computing, Face mask detection, YOLO

### Resumen

La COVID-19 ha provocado graves daños a la salud: centenas de millones de personas infectadas y varios millones de fallecidos en el mundo. Los programas de vacunación de cada Gobierno han influido en el decaimiento de estos índices, pero con la aparición de nuevas mutaciones del coronavirus más contagiosas, la preocupación sobre la efectividad de las vacunas se hace presente. Frente a esta situación el uso de mascarillas sigue siendo eficaz para prevenir la transmisión y contagio de la COVID-19. Lo que ha generado una creciente demanda de servicios de detección automática de mascarillas, que permita recordar a las personas la importancia del empleo de estas. En este trabajo se plantea un análisis del rendimiento de un sistema AIoT para la detección del uso correcto, incorrecto y sin mascarilla basado en dos modelos computacionales de Cloud y Edge, con la finalidad de determinar qué modelo se adecua mejor en un entorno real (interior y exterior) sobre la base de la confiabilidad del algoritmo, uso de recursos computacionales y tiempo de respuesta. Los resultados experimentales demuestran que el modelo computacional Edge presentó un mejor desempeño en comparación con el Cloud.

**Palabras clave:** AIoT, COVID-19, computación en la nube, computación de borde, detección de máscara facial, YOLO

<sup>1,\*</sup>Departamento de Ciencias de la Computación y Electrónica, Universidad Técnica Particular de Loja, Loja, Ecuador. Corresponding author ✉: fdquinones@utpl.edu.ec.

Suggested citation: Quiñonez-Cuenca, F.; Maza-Merchán, C.; Cuenca-Maldonado, N.; Quiñones-Cuenca, M.; Torres, R.; Sandoval, F. and Ludeña-González, P. (2022). «Evaluation of AIoT performance in Cloud and Edge computational models for mask detection». INGENIUS. N.º 27, (january-june). pp. 32-48. DOI: <https://doi.org/10.17163/ings.n27.2022.04>.

## 1. Introduction

Humanity is experiencing a health crisis due to COVID-19, caused by the new SARS-CoV-2 coronavirus strain [1], which has unexpectedly and dramatically affected people's health, economy and lifestyle worldwide. The origin of the virus was identified at the end of 2019 in the city of Wuhan, China. Subsequently, the virus spread worldwide and on March 11, 2020 it was declared by the World Health Organization (WHO) as a global COVID-19 pandemic [2]. SARS-CoV-2 attacks people's immune systems. Although most people who get infected with the virus have mild and moderate symptoms, another significant group of people need hospitalization, and even the use of ICU beds (Intensive Care Unit). This virus is transmitted mainly through microscopic droplets of cellular plasma expelled by the infected person when coughing, sneezing, or exhaling [3].

Twenty months of pandemic have marked the history of human health, which is evidenced by official statistical data. To date, December 3, 2021, globally, according to WHO statistics (2021), a little more than two hundred and sixty-three million cases have been confirmed, of which more than five million died. On the continental level, America has the highest rate of infection in relation to the other five continents, nearly 97 million confirmed cases have been reported, of which more than two million people died. While in Ecuador, more than five hundred and twenty-seven thousand confirmed cases are recorded and more than thirty-three thousand have died [4].

To neutralize the COVID-19 pandemic, world leaders made crucial decisions, leading to collateral problems from which humanity is still recovering. Measures include global confinement, implementation of safety protocols, and even the invention and distribution of vaccines.

At the local level, in mid-March 2020, the Ecuadorian government declared a state of emergency, which involved restrictions on mobility, isolation, and border closures, which severely affected the country's economy. Companies had to abruptly halt their production, and government, educational and financial institutions were forced to continue their activities online.

After four and a half months of confinement, the country's economy did not resist and confinement restrictions were gradually eliminated; but biosafety protocols had to be implemented by the community to work face-to-face. To prevent the spread of SARS-CoV-2 virus, each individual is required: compulsory use of masks, avoid conglomerations, keep distance, wash hands regularly with soap, and continuously disinfect commonly used surfaces with alcohol. Strict monitoring of biosafety protocols has been the key to preventing the virus, since initially, there was no specialized medicine and vaccine to protect people because

SARS-CoV2 was new. Several COVID-19 vaccines are currently available.

The Pan American Health Organization (PAHO) [5], on its official website, has made available to the general public information related to COVID-19 vaccines, including Pfizer/BioNTech, Moderna, AztraZeneca, Janssen, Sinopharm, and Sinovac. Although there are several vaccines, the vaccination process does not progress as planned. According to statistics [6], to date (December 2021) 54.9% of the world's population has received at least one dose of the COVID-19 vaccine. More than eight billion doses have been administered worldwide, and thirty-four million doses are administered each day.

Simultaneously with the global vaccination process, new variants of the COVID-19 virus have been identified in different regions of the world. The high number of infected people increases the risk of virus's mutations. The more the virus spreads, the smaller changes occur in its genetic code, allowing it to survive and reproduce. Multiple variants circulate globally, for example: the UK variant, known as Alpha; the South African variant, known as Beta; the Brazilian variant, known as Gamma, the Indian variant, known as Delta; and the last one known as Omicron detected in South Africa. According to experts, viruses mutate all the time, and most changes are irrelevant, but others can make the disease more infectious or threatening, and these mutations tend to dominate [7].

The goal of vaccination is to achieve global collective immunity to prevent SARS-CoV-2 from continuing to mutate, becoming more resistant to current vaccines and causing more periods of mass mortality. However, PAHO, at the end of the first week of August, due to a high rate of contagion of the variant (VOC) Delta, in several countries, inside and outside America, recommends reviewing contingency plans and be prepare for an eventual increase in cases and hospitalizations, emphasizing in that report that social distancing, the use of masks, and the use of antiseptic solutions continue to be the most effective measures to reduce transmission of this and all variants. From the above data, it can be deduced that COVID-19 pandemic has not yet ended, the future is uncertain. Research and innovation are therefore needed to provide technological contributions to society in the fight against COVID-19 pandemic.

This paper describes the design, implementation, and performance analysis of a system based on two cloud and edge computing models, applied to real-time mask usage detection by using artificial intelligence of things (AIoT). The importance of system development and evaluation lies in the fact that it analyzes response time, detection algorithm performance, and computational resources.

The article is organized as follows. Section II describes the proposed method, and details the computational designs and components used. Section III

presents the results of the analysis of computer models. Finally, Section IV shows the conclusions and future work.

## 2. Materials and methods

The research was divided into five phases (see Figure 1) through an experimental design and quantitative approach. Then, the activities that were carried out in each of the phases are detailed:

- State-of-the-art analysis of enabling technologies for AIoT, related works and detection algorithms to detect the use of masks in real time.
- Design of an architecture and determination of hardware and software components for deployment of computing models in the cloud and on the edge of the network.
- Development in the stage in which software and hardware components are integrated, and the real-time mask detection and execution algorithm implemented in both computational models.
- Evaluation of the stage in which a controlled scenario and real scenarios are determined to perform tests that allow validating the performance of the computational models.
- Analysis of results to determine the performance of resources used in both computer models. Metrics collected include the demand for computing resources (CPU, RAM, memory, and storage), and system response time. To analyze the performance of the detection algorithm, the accuracy, precision, revocation, harmonic mean, and mean of the average accuracy are evaluated.

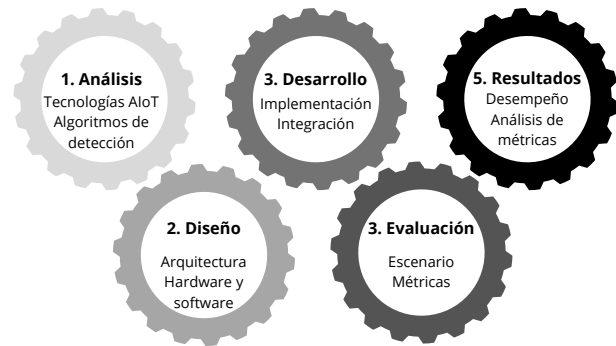


Figure 1. Methodology

### 2.1. Architecture

For developing the system, a comparison strategy was designed to allow the two computer models to be equipped with the same or similar capabilities. However, because each implementation has intrinsic characteristics that differentiate them from each other, the comparison strategy was designed with two structures, one common to both computational models and the one specific to each one. In Figure 2 can be observed the layout of each of the hardware and software components that are part of the system architecture, segmented into: scenario, sensors and actuators, computational models, and actuators.

The system architecture integrates an IP camera to obtain the video from the test scenario, which is sent via Real Time Transmission Protocol (RTSP) to the two computer models. Video processing is performed by applying the real-time object detection algorithm based on YOLOv3 («You only look once v3») to determine correct and incorrect use and no mask. The Edge computational model performs real-time inference and presents the results on a screen by ticking the faces depending on the result with «correct mask», «incorrect mask» and «no mask». Audible and visual alarms are generated, and it is then sent to a web platform in the cloud to store the processed images. While the processing is carried out in the Cloud computational model and the result can be visualized through a device and the inference is stored as detailed in the Edge model.

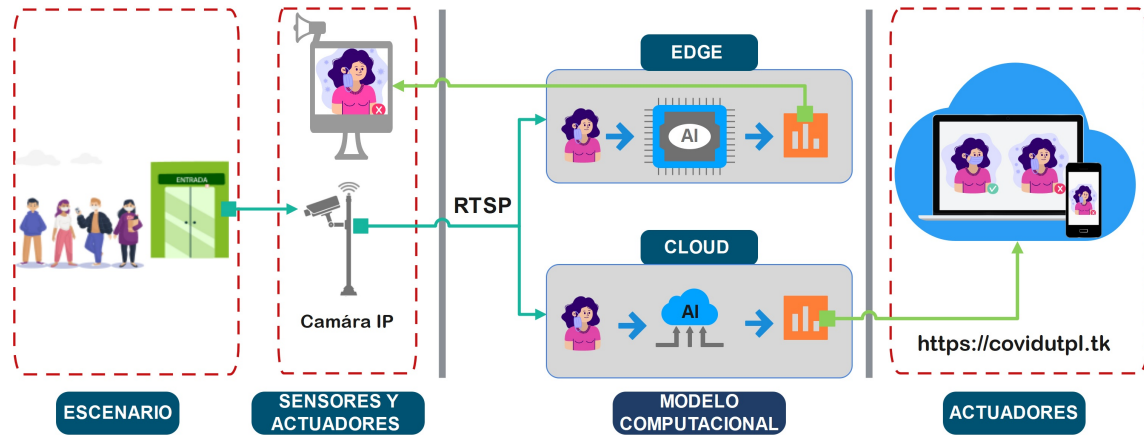


Figure 2. System architecture

### 2.1.1. Common structure for Cloud and Edge

According to [8], comparative analysis is emphasized in the broad explanation of similarities and differences of phenomena to provide valid reasons in a topic or area of interest. Consequently, this section describes the "similarities" of the comparison strategy between Cloud and Edge computing models. To evaluate the performance of the AIoT algorithm, it was discussed the use of the same transmission protocol, codec video, visual sensor (IP camera), training dataset, training algorithm, evaluation dataset, and execution algorithm for real-time mask detection in both models

### 2.1.2. Transmission protocol

Currently, there are several streaming protocols such as Real Time Streaming Protocol (RTSP), Real-Time Messaging Protocol (RTMP), Secure Reliable Transport (SRT), and WebRTC (RTC – Real Time Communication) [9]. In selecting the transmission protocol to be used in the comparative strategy of this research, the results of recent research and the compatibility of the transmission protocol with the surveillance video cameras available in the market were taken into account. According to [10], one of the most widely used streaming video protocols is RTSP, especially in environments with bandwidth restrictions, network congestion, energy efficiency, cost, reliability, and connectivity. Whereas, according to [11], the RTMP protocol offers better performance in live video streaming compared to the RTSP protocol.

When reviewing the compatibility of transmission protocols with the visual sensors (video surveillance cameras) offered in the market, cameras were found with two RTMP and RTSP protocols. To implement the RTMP protocol push mechanism, another component (a streaming server) must be added to the network, altering the flow of data across the network and the comparison architecture, and impacting the

traffic analysis result. On the other hand, the RTSP protocol pull mechanism is a convenient option to implement since both Cloud and Edge computing models can be connected to the same visual sensor (IP surveillance camera). Therefore, RTSP was selected as the transmission protocol for the comparative strategy, because it is better suited to the proposed comparison architecture.

### 2.1.3. Codec video

According to [11], the H.264 codec video is one of the most functional compression standards in Internet of Things (IoT) applications because it occupies less capacity when stored or transmitted. Also, the video compression standards of the H.264 codec are based on motion compensation. This codec is highly recommended for recording, compressing and distributing video files in real time [12]. Also, the H.264 codec video supports the RTSP protocol and is available in many of the visual sensors offered on the local market. Finally, based on the latter, it is determined that the H.264 codec is compatible with the proposed architecture.

### 2.1.4. Mask detection algorithm

AIoT combines two approaches, namely IoT and Artificial Intelligence (AI). [13]. IoT approach refers to the concept of interconnecting objects to the network, so that information can be collected through sensors automatically, without the exclusive intervention of people [14]. While AI refers to the approach of providing intelligence machines through algorithms, so that they can make decisions based on previously received training [15]. By uniting both approaches, an attempt is made to adhere a cognitive layer to the network, to achieve resource optimization through the autonomy that can be provided to machines to analyze situations and make decisions.

Media processing is a major challenge for AIoT

algorithms due to the large amount of data that this activity involves and due to the limited resources of IoT. In this case study "real-time mask use detection", the aim is to evaluate the performance of AIoT algorithms in Cloud and Edge computing models. For which, in the state-of-the-art it was identified that the technical solution for this type of object recognition problems is AIoT algorithms, based on Deep Learning with CNN (Convolutional Neural Network) architectures [16].

In terms of real-time object detection, the literature highlights the detector models of a stage for better performance compared to two stages. YOLO algorithm, a single-stage detector model, is characterized by a significant difference in speed compared to the two-stage R-CNN (Region Based Convolutional Neural Networks) and Fast-R-CNN models. YOLO is a thousand times faster than R-CNN and a hundred times faster than Fast-R-CNN [16]. In contrast to the approach adopted by YOLO's predecessor object detection algorithms, which reuse classifiers to perform detection, YOLO proposes the use of an end-to-end neural network that makes predictions of bounding boxes and class probabilities simultaneously in a single iteration [14].

For the present strategy of comparing the performance of AIoT algorithms between the Cloud and Edge computational models, it was decided to select the reduced version of YOLOv3, identified as YOLOv3-tiny for two reasons. The first is that this version is a small model ideal for deployments where computing resources are limited; i.e., it is compatible with the Edge deployment architecture, which is conducive to equitable comparison. While the second reason is because it is the latest version recognized as official, which means that it has access to the official support of the development community. YOLO model is widely implemented in solutions that require real-time object identification, due to its architecture and operation [16–19].

YOLOv3 was proposed as a solution that uses modern CNN, which uses residual networks and omits connections. According to [14], authors of YOLOv3, this version uses the much more complex Darknet-53 convolutional neural network as the model's spine, 106-layer with residual blocks and superior sampling networks. This architecture enables the YOLOv3 model to predict at 3 different scales, and extract feature maps at layers 82, 94, and 106 for these predictions.

### 2.1.5. Dataset

A training and validation image set is required for the detection algorithm preparation process. This work requires training the real-time object detector algorithm YOLOv3-tiny, so that it learns and detects three classes. In other words, for the implementation of the present case study "detection of mask use" the detec-

tion algorithm of people with 1) correct use of mask, 2) no mask and 3) incorrect use of mask will be trained. Figure 3 illustrates the dataset with the three required classes.



**Figure 3.** Dataset with three types: correct use of mask, no mask, incorrect use of mask

The dataset must contain information relevant to the context, i.e., images of people using masks of different colors and models for the first class; images of people of different ages and ethnicity for the second class; and images of people using the mask incorrectly, below the nose or mouth, for the third class.

For algorithm training, the dataset was customized by randomly selecting images from two public datasets Kaggle Medical Mask Dataset [20] and Masked Face (MAFA) dataset [21], because such datasets contain real images of people in different backgrounds, unlike other datasets that contain all three classes, but correspond only to the person's face. According to [17], in-context information is another approach used to improve detection accuracy or speed. Additionally, for the training of the detector algorithm, it is planned to divide the custom dataset according to the hold-out technique, which consists of dividing the dataset into two subsets of 80% for training and the remaining 20% of the data for testing [22]. In this way, the performance of the algorithm on unseen data can be evaluated after training [23]. While, in the execution phase of the training of the neuronal network specialized in the detection of masks, the technique «transfer learning» is used, which consists of transferring knowledge of a pre-trained model in a general context to a more specific one [24], i.e., for the detection of the 3 classes (with mask, without mask and incorrect mask) the base model of pre-trained YOLOv3-tiny will be used for detecting 80 classes of objects.

### 2.2. Execution algorithm in real time

Algorithm 1 describes by pseudo code the process for detecting all three classes (correct use of mask, no mask, and incorrect use of mask). This algorithm has

as input the flow of images (video stream) captured by the visual sensor of the network, while the output will be the detection(s) of people classified in the three options.

Before the detection process, it is necessary to prepare each frame of the video stream, by resizing the frame to multiple scales based on the YOLOv3-tiny architecture. Each frame is converted to RGB (red, green, blue) channels. Finally, the frame and its capture date are stored. All detections are then stored in the "Face" array using YOLOv3-tiny. Then, it is necessary to evaluate if there is any detection in the current frame; i.e., if the "Face" array contains any elements (higher than zero).

In case that there is no detection in the current frame, the process is completed, and the next frame of the video stream is worked on. Whereas, if there is at least one detection in the face array, it is required to evaluate for each detection the class to which it belongs to, to highlight its bounding box and assign the corresponding class label (ID - identification). In case that: 1) If the ID detection belongs to the "with mask" class, the green bounding box is highlighted; 2) if the ID detection belongs to the "without mask" class, the red bounding box is highlighted; and 3) if the ID detection corresponds to the "wrong mask" class, the orange bounding box is highlighted. In addition, for each detection, the detection bounding box must be cut and stored in JPG format with the date and time of detection.

**Algorithm 1** Mask detector from real-time video.

```

RTSP stream. Detection of mask foreach <Frame
in Stream> do
  Redimension Frame;
  Convert Frame to RGB;
  Store date and time;
  Identify Faces in the Frame using YOLOv3-tiny;
  if Faces > 0 then
    foreach Face in Faces do
      switch Face do
        case Correct use of mask do
          Highlight the Frame in green
        case No mask do
          Highlight the Frame with red
        case Incorrect use of mask do
          Highlight the Frame with OR-
          ANGE
          Cut Face and store Frame as a JPG file;
          Store Face, Dateandhour in the database;
  
```

**2.3. Edge architecture design**

Figure 4 illustrates the architecture design of the Edge computational model. The central processing unit is the Jetson Nano component, which has as input the

video stream captured by the network’s visual sensor (TPLINK tapo C310 V2 IP camera).

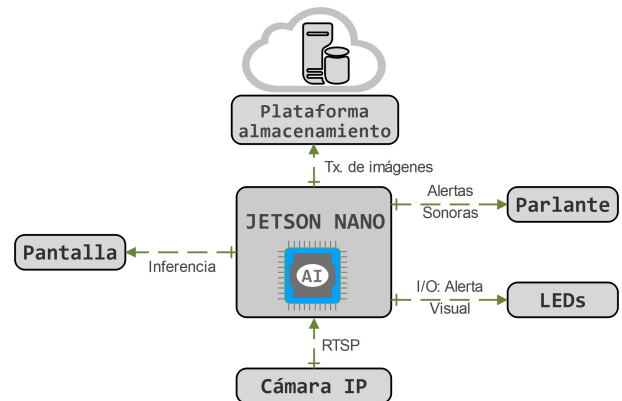


**Figure 4.** Architecture of the Edge computational model

The AIoT algorithm for real-time mask usage detection is executed on the central processing unit. Subsequently, four outputs occur on the system actuators in case of a detection: 1) the transmission of the images corresponding to the detections to a cloud repository, 2) an audible alert that highlights the detection class, 3) the activation of LEDs depending on the detected class, and 4) the display of the detection on a screen. Finally, Figure 5 shows the inference results in the Edge computational model.



**Figure 5.** Inference results in the Edge computational model

**2.4. Cloud architecture design**

Cloud platforms allow end users to deploy their AIoT solutions based on real-time video streaming, analysis, and storage, including Amazon Web Service (AWS) Kinesis Video Stream (KVS) and SafetyRadar [25]. The first platforms are characterized by offering different types of object detection, for example, houses, cars, animals, etc. The detection of different objects to be implemented requires technical knowledge to use these platforms, while the SafetyRadar platform specializes in the detection of masks and other biosafety implements, offering plug and play technology, hence

no technical expertise is required for deployment. However, all three platforms are paid.

For the present work, a custom architecture was designed for the cloud computing model, with control over the different network components. Generally, platforms do not allow the extraction of metrics required for comparison, which is the aim of this investigation.

Figure 6 illustrates the architecture design of the Cloud computational model. The video stream captured by the network's visual sensor is accessed via the RTSP transmission protocol from the local network. While two components are arranged in the cloud using a container architecture, specifically Docker [25], enabling the deployment and replication process of the deployment to be streamlined. The first container processes the video stream, while the second container publishes the results of the processing. In container 1, after the multimedia data, the input data is processed according to business logic, with the execution of the AIoT algorithm for the detection of mask use in real time. The results of such processing are then stored; in this case, the images with the detections performed. Finally, events made in a log are saved. Meanwhile container 2 presents the results so that end users can connect to the server and use the information they want through a Website.

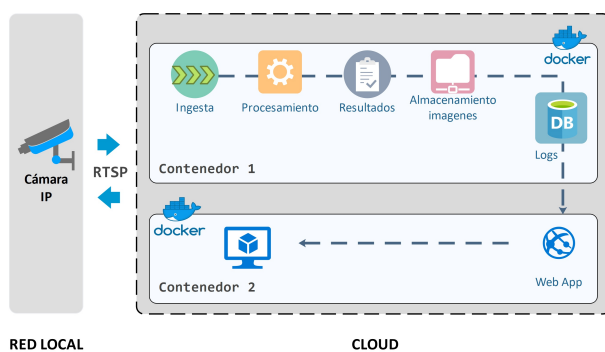


Figure 6. Architecture of Cloud computational model

Figure 7 shows the inference results of the Cloud computational model.

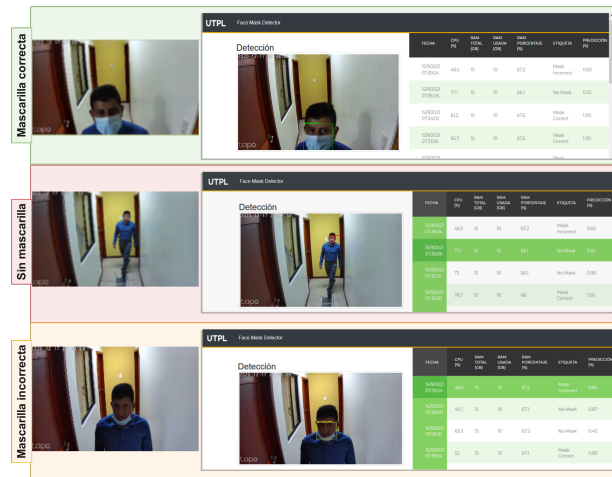


Figure 7. Inference results of the Cloud computational model

## 2.5. Technology used

Table 1 shows a summary of the technology used in this research. The first column identifies the technology used, the second column corresponds to the Cloud or Edge computational model where the technology is applied; the third column indicates which component to use. The last column provides justification for the use of each technology.

Table 1. Summary of technologies used

Tecnology	Model	Component	Justificación
JetPack SDK 4.5.1 [26]	Edge	Processing	Includes Jetson Linux Driver Pack (L4T) with Linux operating system and CUDA-accelerated libraries (TensorRT and cuDNN), for AI APIs.
Python3 [27]	Edge Cloud	Processing	Base language for video processing, results publication, and integration with vision and AI libraries.
Deepstream SDK 5.1 [28]	Edge	Processing	This Nvidia SDK provides a framework for building GPU-accelerated video analytics applications that run on the NVIDIA Jetson Nano platform.
Deepstream-services-library [29]	Edge	Processing	Python3 library required to make use of the deepstream SDK functionalities.
MySQLdb [30]	Edge	Results	Provides the Python API to access the MySQL database server.
reclone [31]	Edge	Results	Required to manage files in cloud storage.
Docker [32]	Cloud	Processing	It allows automating the deployment of the application in the containers located in the cloud.
Camgear [33]	Cloud	Processing	It is a high-performance, cross-platform video processing framework that enables real-time video processing.
OpenCV [34]	Cloud	Processing	Library that allows to process artificial vision in Python3. This facilitates in the first instance the reading of the trained model of YOLOv3-tiny, and later in the detection for each processed frame.
Firebase [35]	Cloud	Processing	It allows to store the Results of the detections in real time.
Flask [36]	Cloud	Results	Framework that is used for the creation of the web application.
Bootstrap [37]	Cloud	Results	Library for the design of the application that allows publishing the Results.

## 2.6. Experimental configuration

The image tagging and custom dataset splitting processes to be used in mask detection algorithm are

performed using the Python3 programming language. The dataset was divided with a distribution of 80% (716 images) for training and the remaining 20% (179 images) for testing (see Figure 8). The images in the custom training dataset contain the detection of one person or more people in the training, representing 3070 people with correct use of mask, 675 without mask and 113 with incorrect use of mask.

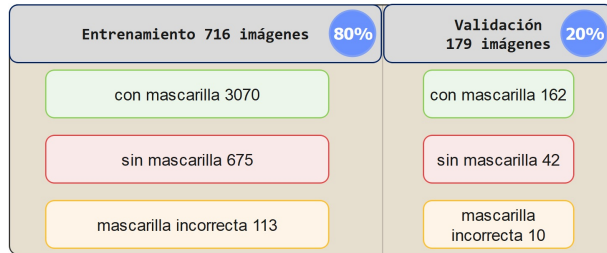


Figure 8. Dataset distribution for training and validation

The Google Colab [38] tool was used to run the AIoT algorithm training process, which has three inputs: 80% of the dataset images, YOLOv3-tiny configuration file (see Table 2 for configuration parameters), and YOLOv3-tiny pre-trained weight file with COCO dataset [39].

Table 2. Configuration training values for neuronal network

Detail	Calculus	Value
Number of classes	Correct use of mask, no mask and incorrect use of mask	classes=3
Maximum batch size	30000 (10000 per class)	max_batches = 30000
Dimensions of input image	width × height = 416 × 416	width=416 height=416
Number of filters in the convolutional later before YOLOv3-tin layer	(classes+5)*3 = 24	filters=24
Batch size and its subdivisions for training		batch=64 subdivisions=2

The training process lasted 16 hours, obtaining a mean accuracy (mAP) of 75.95%. Finally, the trained neuronal network was validated with the remaining 20% of the dataset (79 images), representing 162 people with correct use of mask, 42 without mask and 10 with incorrect use of mask. Table 3 shows the validation results.

Table 3. Validation results of the detection algorithm

Class	Precisión
Correct use of mask	85,97 %
No mask	68,72 %
Incorrect use of mask	73,15 %
<b>mAP</b>	<b>73,15 %</b>

### 3. Results and discussion

This section presents the results of the different experiments in two real scenarios to determine the performance of the two computational models. In this context, two environments were selected. The first indoor scenario corresponds to the entrance of people to a local church to participate in the Sunday Eucharist. For the second outdoor scenario, it was applied on a street with a high rate of pedestrian circulation, due to religious tourism to the Sanctuary of El Cisne between August and September, located in the province of Loja, southern Ecuador.

In both indoor and outdoor environments, it was monitored for a period of one hour, of which for a more detailed analysis the first 15 minutes are taken for the quantitative analysis of the results. In this context, 82 people entered indoors and 229 circulated outdoors. Figure 9 illustrates the total number of detections in indoor and outdoor environments.

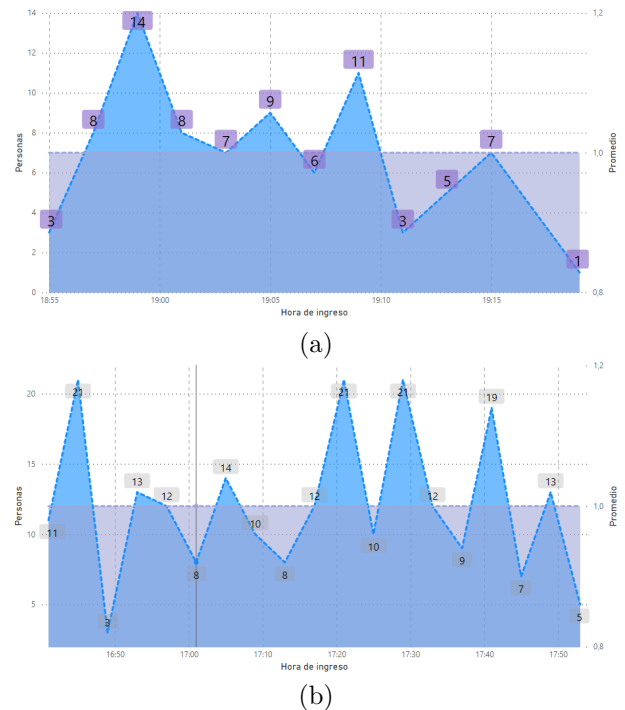


Figure 9. Flow of people: a) indoor, b) outdoor

The results of the experiment show that the flow of people in the outdoor environment doubled the indoor, having a mean income of 6 people in the internal environment and 12 people in the external environment. The count was carried out through the Camlytics tool. Figure 10 shows detection examples in the real indoor and outdoor scenarios.

### 3.1. Evaluation metrics

To evaluate the performance of the AIoT algorithm in Cloud and Edge computing models, the "Real-time Biosafety Mask Usage Detection" case study has been considered as evaluation metrics:

- Detection algorithm reliability: According to [16], [18], [40–42], determining the performance of the detection algorithm is based on four metrics: accuracy, precision, sensitivity, harmonic mean, mean of the average accuracy.
- Computational resources: it is recommended to analyze the resources occupied by the application based on [41]] and the ISO/IEC 25023 standard, analyzing network traffic, RAM memory, CPU and storage.
- Response time: This is another parameter that allows to measure the time it takes for the system to respond according to [41] and by ISO/IEC 25023 standard.



Figure 10. Indoor and outdoor live stage results

#### 3.1.1. Accuracy of detection algorithm

To evaluate the accuracy of ML-based classifiers (Machine Learning) a confusion matrix is used to know how effective the system is. According to [40], a confusion matrix, also known as an error matrix, is a method for 10 to summarize the performance of the result of a classification model, showing the number of correct

and incorrect predictions. Four metrics are calculated from the confusion matrix [16], [18], [40–42]: Accuracy (A: Accuracy, see Equation 1), precision (P: precision, see Equation 2), sensitivity or recall (R: Recall, see Equation 3), and the harmonic mean ( $f_\beta$ , see Equation 4). Additionally, three classes are identified due to the AIoT Edge and Cloud implementations of this experiment (MC: Correct use of mask, SM: No mask and MI: Incorrect use of mask), it is also necessary to calculate the average of the mean accuracy (mAP, see Equation 5) from the mean accuracy (AP) of each class.

$$A = \frac{TP+TN}{(TP+FP)+(TN+FN)} \quad (1)$$

$$P = \frac{TP}{TP+FP} \quad (2)$$

$$R = \frac{TP}{TP+FN} \quad (3)$$

$$f_\beta = \frac{(1+\beta^2)*(P*R)}{\beta^2*P+R} \quad (4)$$

$$mAP = \frac{AP_{MC}+AP_{SM}+AP_{MI}}{3} \quad (5)$$

Where: TP (True Positive) is when the observation is positive and is predicted to be positive; FN (False Negative) is when the observation is positive, but is predicted to be negative; TN (True Negative) is when the observation is negative and is predicted to be negative; and FP (False Positive) is when observation is negative, but is predicted to be positive, while  $\beta$  is used to assign different weights to the measures used in Equation 4 [42]. In the present work,  $\beta$  was assigned a value of 1. Table 4 shows the results obtained when deploying Edge and Cloud models in real-world scenarios. This is done by purging repeated detections in each environment.

Table 4. Confusion matrix

		True value		
		MI	SM	MC
Edge model indoors				
Prediction	MC	2	29	<b>191</b>
	SM	0	<b>36</b>	9
	MI	<b>3</b>	3	0
Edge model outdoors				
Prediction	MC	2	15	<b>170</b>
	SM	0	<b>52</b>	30
	MI	<b>1</b>	1	0
Cloud model indoors				
Prediction	MC	5	36	<b>165</b>
	SM	7	<b>29</b>	12
	MI	<b>1</b>	2	6
Cloud model outdoors				
Prediction	MC	3	45	<b>123</b>
	SM	2	<b>41</b>	40
	MI	<b>1</b>	2	2

Table 5 shows the results obtained after evaluating the Edge and Cloud implementations for detecting the use of masks by individuals in both indoor and outdoor environments, in time and real-world scenarios.

**Table 5.** Results obtained for A, P, R and  $f_\beta$

<b>Accuracy (A) %</b>				
Clase	Cloud		Edge	
	<i>indoor</i>	<i>outdoor</i>	<i>indoor</i>	<i>outdoor</i>
MC	76,7	64,7	85,2	82,6
SM	77,4	65	84,9	82,9
MI	90,7	94,8	97,9	98,7
Media	81,6	74,8	89,3	88,1
<b>Precision (P) %</b>				
MC	80	71,9	86	90
SM	60,4	49,4	80	63,4
MI	11,1	20	50	50
mAP	50,5	47,1	72	67,8
<b>Recall (R) %</b>				
MC	90,1	74,5	95,5	85
SM	43,3	46,6	52,9	76,5
MI	7,6	16,7	60	33,3
Media	47	45,9	69,5	64,8
<b>Harmonic mean (<math>f_\beta</math>) %</b>				
MC	84,8	73,2	90,5	87,4
SM	50,4	48	63,7	67,9
MI	9	18,2	54,5	40
Media	48,1	46,5	69,6	65,1

Table 4 shows the percentages obtained with respect to the accuracy, precision, recall, and harmonic mean metrics. Accuracy refers to the number of positive predictions that were correct; in this context, the results show that the Edge model is 10.5% more accurate than the Cloud model. On the other hand, precision refers to the percentage of positive cases detected; the results indicate that indoor accuracy is higher than outdoor in both models. The Edge is 39.9% more accurate than Cloud. Cloud accuracy is lower than Edge as some frames are lost or distorted during transmission in some cases. Regarding the recall metric, which refers to the proportion of positive cases that are correctly identified by the algorithm, the results indicate that the Edge model predicted 20.7% more correct than Cloud. Finally, the harmonic mean metric was used when the dataset is not balanced by providing inputs from different classes to the classifier. In this context, the results show that insufficient detections of the “incorrect use of mask” class have a dramatic impact on data distribution.

### 3.2. Use of resources

Among the resources analyzed for comparing the two Cloud and Edge computing models according to [41] and ISO/IEC 25023, are network traffic, RAM, CPU,

and disk storage usage. Since the results indicated a better development of the masks detector indoors, an analysis of the use of resources in this environment is performed in the following sections. In addition, Table 6 shows the characteristics of the hardware components on each of the two models, Cloud and Edge.

**Table 6.** Hardware characteristics of Cloud and Edge

Component	Cloud	Edge
GPU	—	NVIDIA Maxwell architecture with 128 NVIDIA CUDA® cores
CPU	Intel Xeon Processor (Skylake, IBRS) / 8 núcleos / 2100 MHz	Quad-core ARM Cortex-A57 MPCore processor
Memory RAM	31 GB virtual	4 GB 64-bit LPDDR4, 1600MHz 25.6 GB/s
Storage	246 GB	16 GB eMMC 5.1
Connectivity	Gigabit Ethernet	Gigabit Ethernet, Wi-Fi
Screen	—	HDMI 2.0 and eDP 1.4

#### 3.2.1. Network traffic

Network traffic measurements generated by streaming video from the IP camera on the Cloud model, and images from the Jetson Nano on the Edge model were taken using the Wireshark protocol analyzer on the inbound interface of the server hosting the Cloud model and the Web platform. Traffic measurements were obtained using video encoding parameters at 1008 Kbps, observing the behavior of the traffic in Mbps volume. It can be observed in Figure 11 the network traffic generated, where the blue upper curve represents the traffic from the IP camera to the Cloud computing model using the RSTP protocol; the lower green curve represents the traffic generated by the transmission of images processed with the detection algorithm on the Edge to the web platform (measured in Mbps). This information is represented as series over time, which corresponds to the first 15 minutes of indoors monitoring.

As a result, it can be seen that network traffic is significantly higher in the Cloud model compared to Edge model. The average network traffic in the cloud is 0.86 Mbps, with a maximum of 4.91 Mbps; while the average network traffic in the Edge is 0.07 Mbps, with a maximum of 0.26 Mbps. This is because all frames of the visual sensor in the Cloud model are transmitted without pre-filtering information; in the Edge model, images are only transmitted when there is a detection, which prevents network congestion.



**Figure 11.** Video transference rate to the Cloud and processed images from the Edge to the Web platform

### 3.2.2. Memoria RAM

Los modelos computacionales Cloud y Edge se caracterizan por la diferencia en la cantidad de recursos disponibles. Particularmente, en las implementaciones de este trabajo se dispuso de 4 GB de RAM en el modelo Edge y de 31 GB de RAM en el modelo Cloud. Los resultados indican (ver Figura 12) que el uso de RAM en el modelo Edge fluctuó entre 2,41 GB como mínimo, 2,43 GB como máximo, con una media de 2,42 GB. Mientras que en el modelo Cloud, el uso de RAM fluctuó entre 10,7 GB como mínimo, 12 GB como máximo, con una media de 11,55 GB. A partir de los datos obtenidos, se puede interpretar que, una vez designados los recursos al proceso YOLO, no existe mayor crecimiento durante la ejecución de las detecciones tanto en Cloud como Edge.

### 3.2.3. CPU

Regarding the processing capacity of the Cloud and Edge computing models, they differ significantly. From Figure 13, it is determined that the Edge model with the Jetson Nano integrates a 1.43 GHz processor, of which CPU use during the first 15 minutes of processing fluctuated between 22.95% minimum, 62.01% maximum, and an average of 29.59%. Whereas in the Cloud model, the server had a 4.8GHz processor, of which CPU utilization fluctuated between 1.75% minimum, 7.49% maximum, and an average of 3.31%. Therefore, it can be interpreted that because the Edge model has fewer resources, the effort is greater at processing detections. Conversely, because the Cloud model has better resources, the effort is minimal when running the mask usage detector.

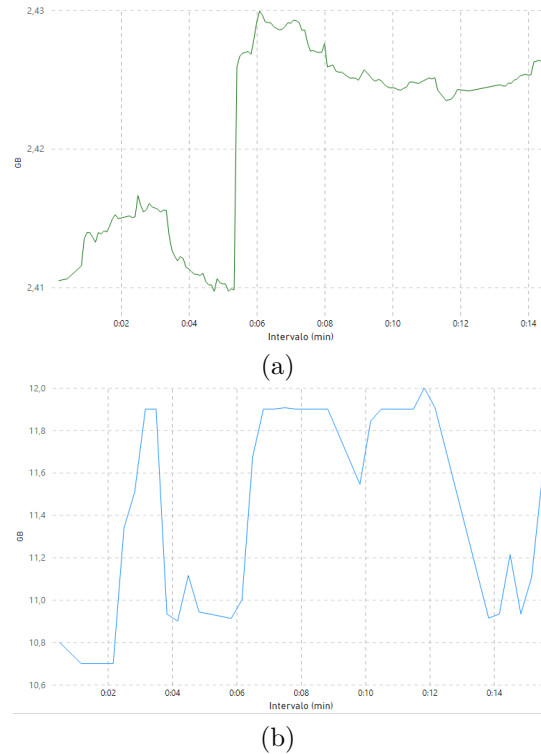


**Figure 12.** Use RAM memory during the first 15-monitoring minutes indoors. A) Edge model, b) Cloud model

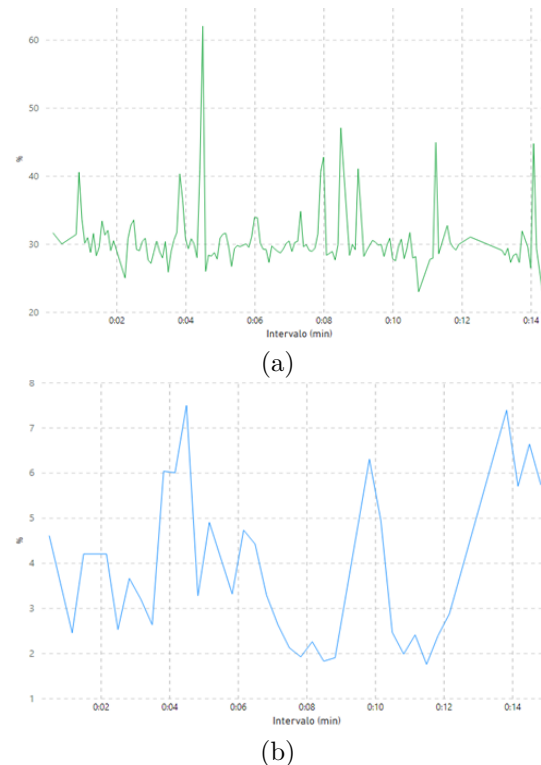


**Figure 13.** CPU use during the first 15-monitoring minutes indoors, a) Edge model, b) Cloud model

### 3.2.4. Storing

Disk space usage of detections grows significantly in both Cloud and Edge models. In the Cloud, this resource can increase in case of a larger demand by updating the cloud server lease. Conversely, Edge does not allow any increased storage capacity as it is limited in nature. The results show that disk space usage is similar in both Cloud and Edge models, approximately 90.7 MB indoors and 200.5 MB outdoors. It is important to note that the mask detector stores only the detection frame not the context or the entire image, so the storage capacity is optimized.

### 3.3. Response time

According to [41], and the ISO/IEC 25023 standard, the response time of a system is another metric that allows to evaluate the performance of a system. In this research, the response time value was used to obtain the events marked in the log files to identify the instant the image entered the model, and then to calculate the time elapsed until its publication. In this context, to calculate the response time in the Edge implementation, the time between the moment the detection occurs until the system finishes with the sound alert was considered. Figure 14a graphically shows the response times recorded on the Edge during the first 20 detections indoors, averaging 2.37 seconds of response.

On the other hand, measures from the time the capture occurs on the visual sensor to the publication of the results on the web page must be done to calculate the response time in the Cloud model. However, what it is possible to capture accurately is the time span from cloud discovery to portal publishing; so, in the Cloud time an average value of 2 seconds was added from the transfer rate for a 300 kB image with a  $1920 \times 1080$  resolution, which corresponds to the time it takes for the visual sensor to transmit the video to the cloud, which is indirectly proportional to the bandwidth provided by the network. The bandwidth that was available for the implementation of the Cloud model was 25Mbps. Figure 14b graphically shows the response times recorded in the Cloud model during the first 20 detections indoors, averaging 3.45 seconds of response.

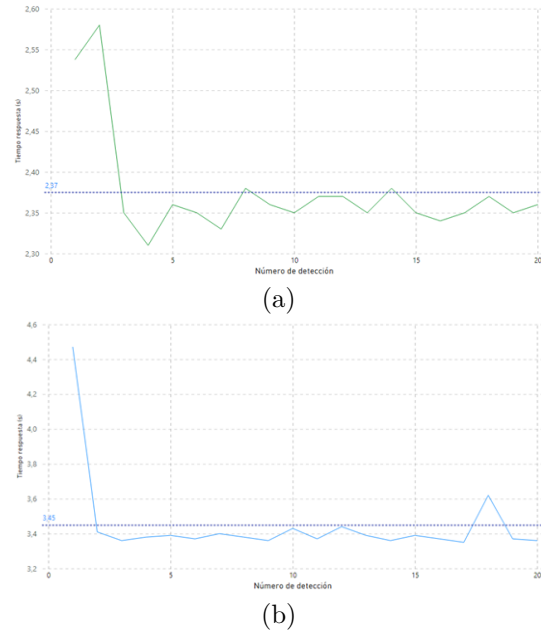


Figure 14. Response time, a) Edge model, b) Cloud model

### 3.4. Discussion of the results

After deploying the Cloud and Edge implementations in real-world scenarios, it is observed that the AIoT algorithm (specialized in identifying the use of biosafety masks) performed better in indoors on both models due to controlled flow (in one direction) and exclusive of people who constituted the entrance to the church. While the performance of the same AIoT algorithm was less efficient in outdoors in both implementations, due to the uncontrolled flow of people (in several directions) and not exclusive of people; other objects such as cars, bicycles, and even animals were part of the images captured by the visual sensor. AIoT algorithms for real-time object identification, using the Edge computational model, presented better performance compared to the Cloud model.

YOLO is a recommended tool for implementing solutions using AI in real-life scenarios that require immediate action. In particular, the results of this work yield 78.2% accuracy metrics on the Cloud model and 88.7% on the Edge model. Although there is a decrease in the classifier accuracy with 48.8% in the Cloud and 69.9% in the Edge, it was proven that the accuracy in both models reduces especially outdoors, due to the fact that the neural network was not sufficiently trained to identify small objects. Additionally it was noted that the detector also reduces when there are multiple people in the same frame to be detected in both models. To solve this problem a greater number of images containing multiple detections could be included in the training dataset.

The quality of the media flow and input for video processing in Cloud and Edge deployments impact

the performance of the AIoT algorithm. The real-time mask detector was tested with two visual sensor resolutions, high ( $1920 \times 1080$ ) and low ( $640 \times 360$ ), allowing to conclude that detection fails on small objects at a low resolution; however, large (nearby) objects are correctly identified in real time (see Figure 15), since frame processing does so smoothly.

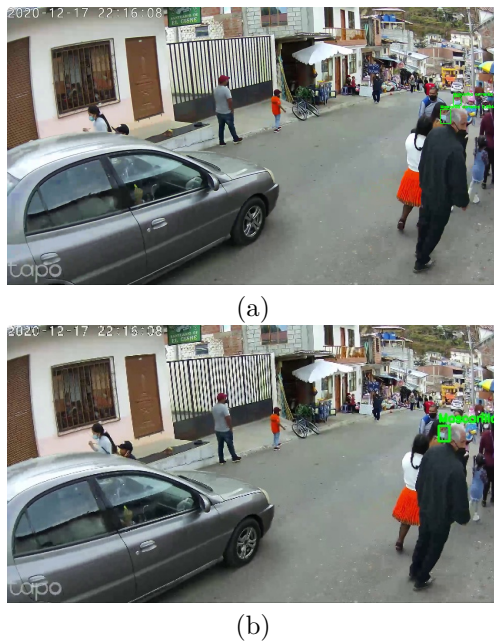


**Figure 15.** Mask detection at different resolutions: a)  $1920 \times 1080$  y b)  $640 \times 360$

The relationship between video streaming speed (frames per second) and its relevance in the business context of the AIoT solution needs to be evaluated. In this research, it was observed that it was not necessary to evaluate all the frames of the input. The AIoT algorithm first processed all received frames (15 frames per second), and too many detections belonging to the same person were obtained as output. Hence, it was concluded that it was necessary to filter the number of frames input to the detector (1 frame per second) and thus avoid processor saturation. In other words, the resources required to process each of the frames are unnecessary. To overcome this problem, frames per second are reduced, which consists of processing a certain frame for a certain interval. This resulted in optimization of processing resources when filtering input and storage output, as the number of detections for the same person dropped significantly, for example, from 1 GB to 100 MB.

Finally, having experimented with both Cloud and Edge models, several challenges are identified for future work. There is inconsistency between the detection speed of Machine Learning based sorting algorithms (ML) and the technology that allow the storage and management of actuators on the network. For example,

the biosafety mask usage detector works at a rate of 15 detections per second, but when wanting to store this information, the transaction takes one detection per second, thus causing congestion. Current database managers do not reach the speed required when working with AI-based classifiers. The same happens with visual or auditory actuators; it does not matter AIoT algorithm to detect multiple objects simultaneously if the time it takes for the speaker or display to show that information to the public requires one second per object.

### 3.5. System evaluation in a real environment

To assess the effectiveness and feasibility of the proposed method, a prototype system equipped with YOLOv3 Tiny is presented, which can be deployed at the entrances of public places. The prototype system based on the Edge computational model is illustrated in Figure 16, as well as the integration and implementation of the various hardware and software components, including an IP camera, a Jetson Nano computer, and a display with HDMI interface

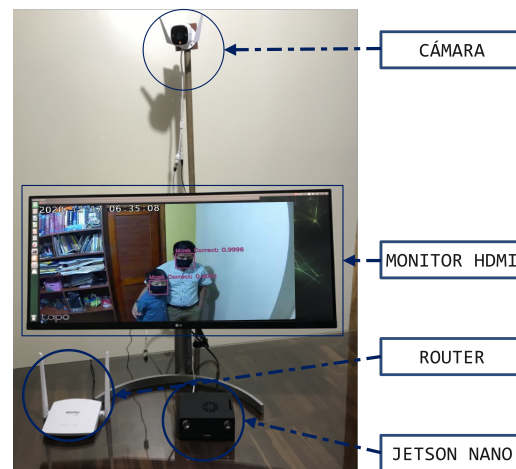


**Figure 16.** Implementation of the system

In Figure 5, the performance of the prototype can be proved for all three cases (correct use of mask, no mask, and incorrect use of mask). Also, visual alerts in the evaluation scenarios did not get people's attention when the AIoT algorithm provides detection feedback. Initially when people crossed the camera's viewing angle, the screen displayed the output of the labeled and painted bounding boxes with the class detected. It was evident that the purpose of the screen was not clear to the passerby, so some would greet or leave the camera's action area. This changed when adding the sound alerts that got people's attention. Users heard the following messages: "correct use of mask", "no mask detected", or "incorrect use of mask"; depending on the type of detection performed by the algorithm, pedestrians identified the purpose of the deployment

intuitively, and many of them corrected the incorrect use or absence of the mask.

#### 4. Conclusions

In this research, a system for detecting masks in real contexts has been designed, implemented and evaluated. The Edge computational model outperformed the Cloud model with 39.9% in the accuracy metric, related with the percentage of positive cases detected; and 10.5% on the accuracy metric, which refers to the percentage of positive predictions that were correct. In addition, there are advantages and disadvantages inherent to the intrinsic characteristics of each model. One of the advantages of cloud deployments is that they have high storage and processing capabilities, and if needing to increase RAM, disk, or processing resources, the model offers the scalability feature to the system. However, the disadvantage of the Cloud model is the high consumption of the network, since the sequence of frames is transmitted in video without prior data filtering. While in the Edge model, despite having limited resources, this disadvantage is offset by the fact that it is possible to perform a debugging of information, allowing applications to adjust to the amount of available RAM, processing, and bandwidth resources, where it could be observed that once the resources are allocated, the consumption of these resources does not fluctuate drastically.

In addition, on this side of the network, visual or auditory actuators can be used for human interactions in the context in which the model is being used. YOLOv3 application is an appropriate option for specialized real-time object detection in either the Cloud or Edge computational model. YOLOv3, as a single-stage object detector model, directly classifies and predicts the target at each location in the entire original image.

All of these features distinguish YOLOv3 from other detector models; however, accuracy and precision metrics are achieved when conducting a training process with a broad set of data that must contain multiple detections in the same image, which must be captured in different contexts and scales. In addition, the dataset can be diversified through the use of image augmentation techniques.

Finally, the analysis of the system in persuading people to wear masks is proposed for future work. The integration of additional sensors into the system to analyze air quality especially indoors is also considered.

#### Acknowledgments

The authors would like to thank the Private Technical University of Loja (UTPL) for funding this work

through the second call «FUNDING DEGREE AND MASTER RESEARCH - 2020».

#### References

- [1] R. Aragón Nogales, I. Vargas Almanza, and M. G. Miranda Novales, “COVID-19 por SARS-CoV-2: la nueva emergencia de salud,” *Revista Mexicana de Pediatría*, vol. 86, pp. 213–218, 2020. [Online]. Available: <https://dx.doi.org/10.35366/91871>
- [2] WHO, “Listings of WHO’s response to COVID-19,” World Health Organization. [Online]. Available: <https://bit.ly/3mAZ6LH>
- [3] —, “Vías de transmisión del virus de la COVID-19: Repercusiones para las recomendaciones relativas a las precauciones en materia de prevención y control de las infecciones.” [Online]. Available: <https://bit.ly/3epu4Sq>
- [4] OMS, “Who coronavirus (COVID-19) dashboard,” 2021. [Online]. Available: <https://bit.ly/3mDAO3r>
- [5] OPS, “Vacunas contra la COVID-19,” 2020. [Online]. Available: <https://bit.ly/3z0JGFs>
- [6] H. Ritchie, E. Mathieu, L. Rodés-Guirao, C. Appel, C. Giattino, E. Ortiz-Ospina, J. Hasell, B. Macdonald, D. Beltekian, M. Roser, and et al., “Coronavirus (COVID-19) vaccinations - statistics and research,” 2020. [Online]. Available: <https://bit.ly/3sEontro>
- [7] C. Costa and C. Tombesi, “COVID-19: Cuánto tiempo se demoró en encontrar la vacuna para algunas enfermedades (y por qué este coronavirus es un caso histórico),” 2020. [Online]. Available: <https://bbc.in/3pEV0Eh>
- [8] “Comparative research grant,” *Anthropology News*, vol. 36, no. 8, pp. 43–43, 1995. [Online]. Available: <https://anthrosource.onlinelibrary.wiley.com/doi/abs/10.1111/an.1995.36.8.43.1>
- [9] S. S. Bibak Sareshkeh, E. Magli, and P. Dal Zovo, “Combined ict technologies for supervision of complex operations in resilient communities,” Master’s thesis, 2020. [Online]. Available: <https://bit.ly/3HαιοPE>
- [10] I. Santos-González, A. Rivero-García, J. Molina-Gil, and P. Caballero-Gil, *Implementation and Analysis of Real-Time Streaming Protocols*, vol. 17, no. 4, 2017. [Online]. Available: <https://doi.org/10.3390/s17040846>

- [11] A. Nurrohman and M. Abdurrohman, “High performance streaming based on H264 and real time messaging protocol (RTMP),” in *2018 6th International Conference on Information and Communication Technology (ICoICT)*, 2018, pp. 174–177. [Online]. Available: <https://doi.org/10.1109/ICoICT.2018.8528770>
- [12] S. Basu, “What are video streaming codecs & container formats: Muvi live server,” 2020. [Online]. Available: <https://bit.ly/3ErJPCZ>
- [13] J. S. Katz, “Aiot: Thoughts on artificial intelligence and the internet of things,” *IEEE Internet of Things*, 2019. [Online]. Available: <https://bit.ly/3sBwGEZ>
- [14] J. Redmon and A. Farhadi, “Yolov3: An incremental improvement,” *ArXiv*, vol. abs/1804.02767, 2018. [Online]. Available: <https://bit.ly/3psJLYp>
- [15] A. M. Porcelli, “La inteligencia artificial y la robótica: sus dilemas sociales, éticos y jurídicos,” *Derecho global. Estudios sobre derecho y justicia*, vol. 6, pp. 49–105, 2020. [Online]. Available: <https://doi.org/10.32870/dgedj.v6i16.286>
- [16] X. Jiang, T. Gao, Z. Zhu, and Y. Zhao, “Real-time face mask detection method based on YOLOv3,” *Electronics*, vol. 10, no. 7, p. 837, 2021. [Online]. Available: <https://doi.org/10.3390/electronics10070837>
- [17] S. Sethi, M. Kathuria, and T. Kaushik, “Face mask detection using deep learning: An approach to reduce risk of coronavirus spread,” *Journal of Biomedical Informatics*, vol. 120, p. 103848, 2021. [Online]. Available: <https://doi.org/10.1016/j.jbi.2021.103848>
- [18] D. González Dondo, J. A. Redolfi, R. G. Araguás, and D. García, “Application of deep-learning methods to real time face mask detection,” *IEEE Latin America Transactions*, vol. 19, no. 6, pp. 994–1001, 2021. [Online]. Available: <https://bit.ly/3pw7DkM>
- [19] S. Sethi, M. Kathuria, and T. Kaushik, “A real-time integrated face mask detector to curtail spread of coronavirus,” *Computer Modeling in Engineering & Sciences*, vol. 127, no. 2, pp. 389–409, 2021. [Online]. Available: <https://doi.org/10.32604/cmescs.2021.014478>
- [20] I. Vich, “Medical masks dataset images tfrecords,” Kaggle, 2020. [Online]. Available: <https://bit.ly/3er0tb8>
- [21] S. Ge, J. Li, Q. Ye, and Z. Luo, “MAFA,” 2018. [Online]. Available: <https://bit.ly/3FBC52o>
- [22] S. Yadav and S. Shukla, “Analysis of k-Fold Cross-validation over hold-out validation on colossal datasets for quality classification,” in *2016 IEEE 6th International Conference on Advanced Computing (IACC)*, 2016, pp. 78–83. [Online]. Available: <https://doi.org/10.1109/IACC.2016.25>
- [23] E. Allibhai, “Holdout vs. Cross-validation in machine learning.” 2018. [Online]. Available: <https://bit.ly/3z2TbE0>
- [24] F. Zhuang, Z. Qi, K. Duan, D. Xi, Y. Zhu, H. Zhu, H. Xiong, and Q. He, “A comprehensive survey on transfer learning,” *Proceedings of the IEEE*, vol. 109, no. 1, pp. 43–76, 2021. [Online]. Available: <https://doi.org/10.1109/JPROC.2020.3004555>
- [25] L. Herrera-Izquierdo and M. Grob, “A performance evaluation between docker container and virtual machines in cloud computing architectures,” *Maskana*, vol. 8, pp. 127–133, 2017. [Online]. Available: <https://bit.ly/3z12oNf>
- [26] NVIDIA, “Jetpack sdk 4.5.1 archive,” 2021. [Online]. Available: <https://bit.ly/32BxzT1>
- [27] Python, “Welcome to python.org,” 2021. [Online]. Available: <https://bit.ly/3qqTd4Q>
- [28] NVIDIA, “Quickstart guide - deepstream 6.0 release documentation,” 2021. [Online]. Available: <https://bit.ly/3sDTa8s>
- [29] ProminenceAI, “Prominenceai/deepstream-services-library: A shared library of on-demand deepstream pipeline services for Python and C/C++,” GitHub. [Online]. Available: <https://bit.ly/3pyxM2y>
- [30] MongoDB, “The application data platform,” MongoDB. [Online]. Available: <https://bit.ly/3qrRsUL>
- [31] N. Craig-Wood, “Rclone syncs your files to cloud storage,” 2014. [Online]. Available: <https://bit.ly/3JIPNsu>
- [32] Docker, “Empowering app development for developers,” 2020. [Online]. Available: <https://www.docker.com/>
- [33] A. Thakur, C. Clauss, C. Hollinger, V. Boivin, B. Lowe, M. Schoentgen, and R. Bouckenoghe, “abhiTronix/vidgear: VidGear v0.2.3,” Oct. 2021. [Online]. Available: <https://doi.org/10.5281/zenodo.5602375>
- [34] OpenCV. (2021) Opencv courses holiday sale. [Online]. Available: <https://bit.ly/3ezvAS1>
- [35] Google Developers, “Firebase,” 2020. [Online]. Available: <https://bit.ly/3JinCeh>

- [36] Pallets, “Flask web development, one drop at a time,” Pallet, 2010. [Online]. Available: <https://bit.ly/3Hemy9h>
- [37] J. T. Mark Otto. (2021) Build fast, responsive sites with bootstrap. [Online]. Available: <https://bit.ly/32N15rK>
- [38] Google. (2021) Colaboratory. Google Research. [Online]. Available: <https://bit.ly/3EC3mk0>
- [39] T.-Y. Lin, M. Maire, S. Belongie, J. Hays, P. Perona, D. Ramanan, P. Dollár, and C. L. Zitnick, “Microsoft coco: Common objects in context,” in *Computer Vision – ECCV 2014*, D. Fleet, T. Pajdla, B. Schiele, and T. Tuytelaars, Eds. Springer International Publishing, 2014, pp. 740–755. [Online]. Available: <https://bit.ly/3sxpZUu>
- [40] M. S. Aslanpour, S. S. Gill, and A. N. Toosi, “Performance evaluation metrics for cloud, fog and edge computing: A review, taxonomy, benchmarks and standards for future research.” *Internet of Things*, vol. 12, p. 100273, 2020. [Online]. Available: <https://doi.org/10.1016/j.iot.2020.100273>
- [41] M. Ashouri, F. Lorig, P. Davidsson, and R. Spalazzese, “Edge computing simulators for iot system design: An analysis of qualities and metrics,” *Future Internet*, vol. 11, no. 11, p. 235, 2019. [Online]. Available: <https://doi.org/10.3390/fi11110235>
- [42] F. Oliveira-Teixeira, T. P. Donadon-Homem, and A. Pereira-Junior, “Aplicación de inteligencia artificial para monitorear el uso de mascarillas de protección,” *Revista Científica General José María Córdova*, vol. 19, no. 33, pp. 205–222, 2021. [Online]. Available: <https://doi.org/10.21830/19006586.725>





# PROTOTYPE OF A DEVICE FOR THE AUTOMATIC MEASUREMENT OF PHYSIOLOGICAL SIGNALS TO ASSIST THE DIAGNOSIS AND MONITORING OF PATIENTS WITH COVID-19

## PROTOTIPO DE UN DISPOSITIVO PARA LA MEDICIÓN AUTOMÁTICA DE SEÑALES FISIOLÓGICAS PARA ASISTIR AL DIAGNÓSTICO Y SEGUIMIENTO DE PACIENTES CON COVID-19

Karla Llanos<sup>1</sup> , Christian Landi<sup>1</sup> , Fernando Yupa<sup>1</sup> , Paola Vasquez<sup>1</sup> ,  
Ismael Criollo<sup>1</sup> , John Calle-Siguencia<sup>1</sup> , Fernando Urgilés-Ortiz<sup>1</sup> ,  
Ana Cecilia Villa-Parra<sup>1,\*</sup>

Received: 15-11-2021, Received after review: 20-12-2021, Accepted: 28-12-2021, Published: 01-01-2022

### Abstract

This article describes the design, construction and preliminary results of a device to automate the measurement of physiological signals to assist in the diagnosis and monitoring of COVID-19. The device uses a system to controlling linear actuators to turn on/off certified biomedical instruments, in addition to algorithms for image recognition of displays with measurements of temperature, oxygen saturation, pressure and heart rate. The system also includes a mobile application, which receives data in real time and creates a database for medical evaluation. Results obtained with the device have demonstrated to provide a high percentage of efficiency in the data acquisition. After several trials with users, SUS and PSSUQ tests were applied to allow verifying the users' feedback regarding the satisfaction and usability of the prototype, with high score, showing the good acceptance of the device from the users.

**Keywords:** Automation, Covid-19, eHealth, image processing, SUS, telemedicine

### Resumen

En el presente artículo se describe el diseño, construcción y resultados preliminares de un dispositivo para automatizar la medición de señales fisiológicas para asistir el diagnóstico y seguimiento de la COVID-19. El dispositivo utiliza un sistema para controlar actuadores lineales para encender/apagar instrumentos biomédicos certificados, además de algoritmos para el reconocimiento de imágenes de las pantallas de los instrumentos con mediciones de temperatura, saturación de oxígeno, presión arterial y frecuencia cardíaca. El sistema incluye también una aplicación móvil que recibe los datos de las mediciones a tiempo real y crea una base de datos para realizar una evaluación médica. Los resultados obtenidos demuestran un alto porcentaje de eficiencia en la adquisición de las mediciones. Después de hacer varias pruebas con usuarios, las evaluaciones SUS y PSSUQ permitieron verificar resultados satisfactorios respecto a la satisfacción y usabilidad del prototipo, demostrando la aceptación del dispositivo.

**Palabras clave:** automatización, COVID-19, e-Salud, procesamiento de imágenes, SUS, telemedicina

<sup>1,\*</sup>Grupo de Investigación en Ingeniería Biomédica GIIB, Universidad Politécnica Salesiana, Cuenca.  
Corresponding author ✉: [avilla@ups.edu.ec](mailto:avilla@ups.edu.ec).

## 1. Introduction

COVID-19 is a severe respiratory disease which originated in Wuhan (Hubei, China), starting an epidemic outbreak in December 2019. The World Health Organization (WHO) declared a worldwide health crisis in January 2020, due to the increasing global infection rates [1, 2]. In Ecuador, up to November 2021, the National Research Institute in Public Health (INSPI, Instituto Nacional de Investigación en Salud Pública) has recorded 526,615 cases with PCR tests and 33,219 confirmed deaths due to COVID-19 [3]. This disease attacks the respiratory system and among its most common symptoms it can be mentioned: fever, cough, headache, nasal congestion, fatigue, reduction of oxygen saturation, loss of taste and smell, syncope and deviation of gases in the blood [4–6]. Those who have acquired the disease show alterations in temperature, blood pressure (mainly hypertension), heart rate and oxygen saturation (due to the shortness of breath in severe COVID-19 cases).

In this scenario, the protocols recommended by health systems include measuring these physiological variables to make the diagnosis and prognosis of the disease [7, 8].

The technological advances are enabling to obtain data about the impact of the disease, and meet the requirements for taking care of the population during the pandemics [9]. For example, smartphones are tools that are being used to monitor physiological signals in various developments [10, 11], the use of wearable technology [12], the internet of things and big-data analytics [9], have a great potential for assisting in the diagnosis of diseases such as COVID-19, however, there are very few developments that integrate in a single system certified devices such as: digital oximeters, digital infrared thermometers and blood pressure monitors to acquire physiological signals of interest to create a medical history and databases relevant for decision making systems [13, 14].

Platforms for transmitting and storing data of a biomedical instrument (BI) [14] and developments that integrate networks for secure data communication [15, 16] demand robust digital telemedicine applications as fundamental resources for remote medical attention. Continuous monitoring with sensors and protocols for tracking through telemedicine platforms with internet of things, constitute valuable tools to reduce exposure and infection with COVID-19 of patients and medical staff [17–21].

With the objective of improving the protocols for diagnosis and treatment of COVID-19 with a technological tool, this work proposes the development of a portable device to carry out automatic measurement of heart rate, blood pressure, oxygen saturation level and body temperature. The device is based on the use of three certified BIs and an application to visualize

measured data and share them in a secure manner with health professionals for their evaluation. The development of this device and the tests conducted with the first prototype are described below.

## 2. Materials and Methods

Figure 1 shows the block diagram that describes the operation of the hardware and software stages of the device.

It includes a Raspberry Pi 3 B+ board (64 bits quad-core CPU, 1.4 GHz, 5 GHz wireless LAN, Bluetooth 4.2/BLE, Ethernet and PoE capability), three mini JS35A linear actuators of 12 V, 4 A (1.2 inches, 0.4 Nm, 0.6 inches/s, 0.07 kg).

The BIs are: a pulse oximeter (Jziki) which is adjusted to the index finger, an infrared thermometer (K&i), an automatic wrist blood pressure meter (URBEST) which shows systolic pressure/diastolic pressure/pulse rate.

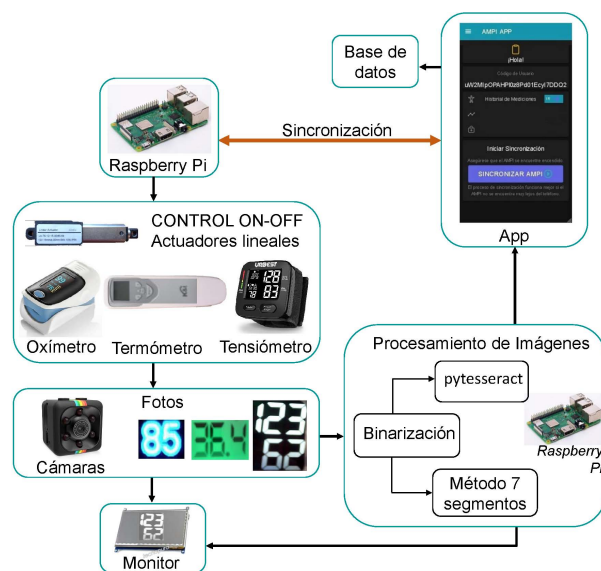


Figure 1. Block diagram of the device

It also includes three 12 megapixels  $4032 \times 3024$  Opticam SQ11 minicameras and a 3.5"  $320 \times 480$ P Raspberry touchscreen LCD monitor.

Measurements are made with the BIs placed on a metallic structure designed such that the actuators activate them to carry out the measurements automatically on the user's left arm. The BIs are not disassembled nor internally manipulated to guarantee the reliability of the measurements.

To start the measurements, it is necessary to synchronize the App with the Raspberry, and this enables to send the command to activate the BIs. After automatic start, measurements are made and the images from the screen of each BI are captured.

The images acquired are processed in the Raspberry PI for recognizing the value of the measurement carried out.

The monitor in the device enables visualizing the screen of the BIs during the measurements, for three periods of time. It starts with the thermometer, then the oximeter and finally it shows the screen of the blood pressure meter.

After measurements have been recorded, they are visualized in the monitor, and this information is sent to an application that also enables to visualize the measurements and to send the records to a database.

The standards IEC 60601-1-2 (electromagnetic compatibility), IEC 60601-1-6 (usability), IEC60601-1-8 (alarms and indicators) and IEC 60601-1-11 (use of medical devices at home) [22] were considered for the design of the mechanical structure, the electronic system and the digital platform. All this with the purpose of obtaining a reliable and safe prototype.

### 2.1. Mechanical Structure

Figure 2 shows the complete design of the device mechanical structure in Autodesk Inventor 2020, which consists of 15 pieces assembled by pressure self-catching.

The structure is made of polylactic acid (PLA), printed in 3D using an Ender 3 pro. This material was chosen due to its ease for printing and high mechanical resistance.

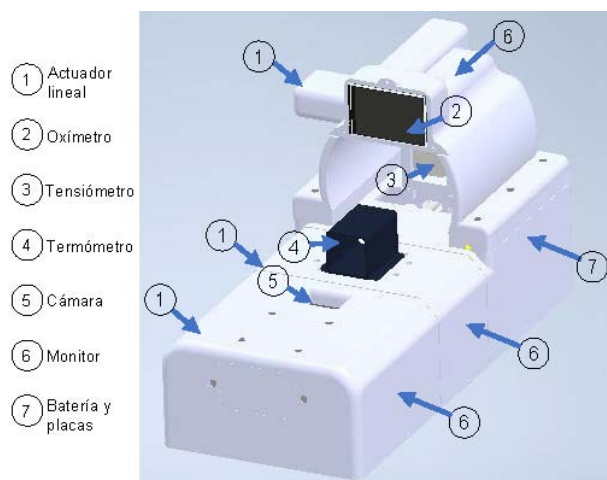


Figure 2. Design of the device and its components

The structure design was established based on the dimensions of the BIs and on the 50th percentile of anthropometric measures, with manual adjustment to the remaining percentiles. In this manner, the structure enables complying with the measurement protocols of each BI such that users place their left arm and the measurements are taken correctly.

The oximeter is located in the right side of the structure, to direct the index finger without requiring to apply pressure on the ends.

The thermometer is located in the proximal-palmar area of the hand for taking measurements.

The blood pressure meter is adjusted to the wrist according to the protocol of the BI.

The cameras are placed such that the image of the screen of each BI is acquired at a distance of 5 cm, without changes in the lightning.

The linear actuators have a stroke of 30 mm and have been placed horizontally on the structure in order to avoid overdimensioning it.

A sliding system was designed to transform a horizontal movement into a vertical one, to guarantee that the buttons of the medical instruments are operated safely.

Figure 3a shows the motor coupling, and Figure 3b shows the sliding system designed to generate a displacement of 4.5 mm to activate the medical devices.

Figure 3c shows the mechanism used to activate the on/off pushbutton of the blood pressure meter. The motor is coupled to element A which displaces horizontally to enable the sliding system (element B) to move in vertical direction, as shown in Figure 3d. This mechanism is replicated to activate the thermometer and the oximeter.

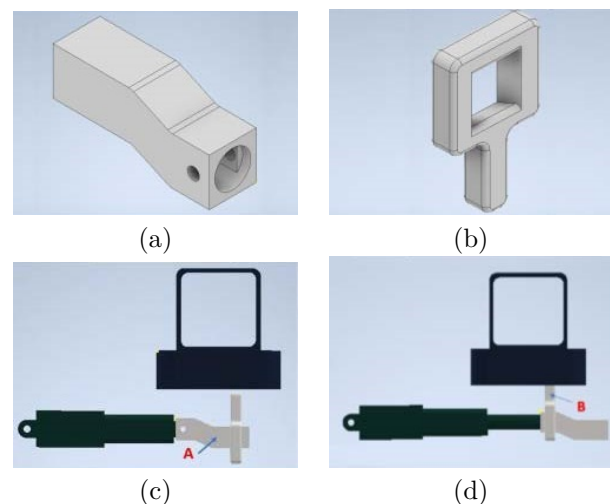


Figure 3. Mechanical elements to transform the horizontal movement of the motor into vertical movement of the sliding system (a) Motor coupling; (b) Sliding system; (c) Sliding system at the initial position; (d) Sliding system at the final position.

### 2.2. Electronic System

The electronic system consists of circuits to regulate the supply to the BIs and the boards (5V and 3.3V), establish the power stage for actuators (H-bridge), perform the control and guarantee battery charge (with

leads to indicate full charge and discharge). The device is powered by a 12V 4.4A Li-ion 3S2P Model 18650-3S2P rechargeable battery (0.3 Kg; 115 mm × 20 mm × 70 mm). It has fuses and diodes for protection of the supply stage, and also patient protection systems, such as isolation from the connectors to prevent electric discharges. The device considers the use of supply systems compatible with standards of electric safety to guarantee protection of users.

The Raspberry is used for control. It has been programmed in Python to: a) synchronize the hardware with the application (App) that enables sending the command to start the measurements from the smartphone.; b) control the three linear actuators for turning on the measurement instruments and c) use the monitor. The electronic boards and the battery are placed on the structure of the device (see Figure 2).

### 2.3. Image Recognition

For recognizing the information of the measurements taken by the medical equipment from the images of their displays, it was necessary to adopt a method based on the graphical representation of the numbers that show the measurement.

There are instruments that present the information using a digital typography, as shown in Figure 4, or with a seven-segment display configuration, as shown in Figure 5.

For this reason, a recognition method was developed for the oximeter (with digital typography) and for the thermometer and blood pressure meter (with displays).

It may be seen in Figure 4 that each of the digits has a light blue contour and a color similar to white in the inside (step 1). In this case it is necessary to binarize the image with a detection process in a color range that for the image acquired is white. The result is shown in step 2. After the image has been binarized and with the digits in black, the optical character recognition (OCR) tool known as pytesseract is employed. This is an open-source resource that enables identifying characters directly from images with extension jpeg, png, gif, bmp, tiff and others with Python that uses the Google Tesseract-OCR engine [23, 24].

After processing, a function is created that takes the image of the picture and returns the text detected in the image. The result of this process is observed in step 3.



**Figure 4.** Recognition of numbers with digital typography

For recognizing digits from the seven-segment display, as shown in Figure 5, the image is first converted

to grayscale (step 1), as indicated in step 2, and then the image is binarized to black and white (step 3).

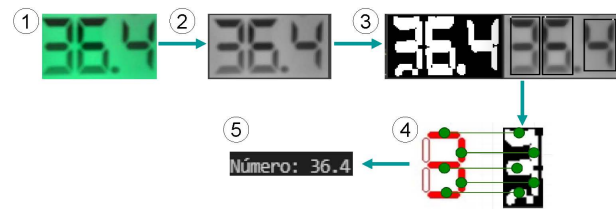
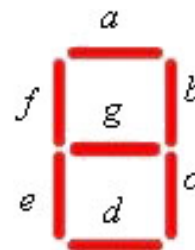


**Figure 5.** Recognition of numbers represented in a seven-segment display

Afterwards, it is used an algorithm designed to identify the region of each digit, as shown in step 4. For this purpose, the letters indicated in Figure 6a were assigned to each segment of the seven-segment matrix. Once the region of each digit has been identified, the critical points are compared with the table shown in Figure 6b, in which 0 represents a black pixel and 1 represents a white pixel. The comparison is carried out for each digit of the image and enables to obtain the result of step 5 (Figure 5) with the identification of the entire number.

Número	g	f	e	d	c	b	a
0	0	1	1	1	1	1	1
1	0	0	0	0	1	1	0
2	1	0	1	1	0	1	1
3	1	0	0	1	1	1	1
4	1	1	0	0	1	1	0
5	1	1	0	1	1	0	1
6	1	1	1	1	1	0	1
7	0	0	0	0	1	1	1
8	1	1	1	1	1	1	1
9	1	1	0	1	1	1	1



(a)

(b)

**Figure 6.** (a) Assignment of a name to the seven segments; (b) Table for comparing the segments identified for assigning the corresponding number

Once the numeric value of the measurement of each instrument has been obtained, the value is sent to the database of the App.

### 2.4. Digital Platform

Figure 7 shows the structure of the digital platform of the device, constituted by three subsystems.

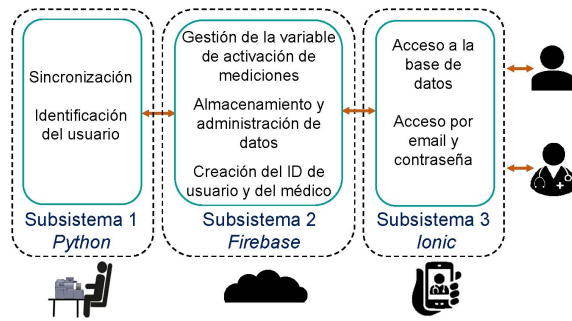


Figure 7. Subsystems of the digital platform

Subsystem 1, developed in Python, establishes the communication between the Raspberry Pi and the Firebase database (FDB) for synchronizing the device and verifying if there is a user in the database. When the Raspberry receives the signal to start the measurements, the device is activated (measurement instruments and image recognition) to send the measurement data and store them in the database. The data sent include the measurements of the three instruments, the measurement time and the user code. The code in the Raspberry Pi permanently listens and updates the changes of the variable that activates the process of taking measurements and sending them to the database.

Subsystem 2 was developed in the Firebase platform, which has a support for event listening and automatic update for Python. Two Firebase services were employed: a) Firebase Authentication, which enables saving and controlling recorded users' data, and linking this information to the database and b) Cloud Firestore which is a NoSQL database oriented to documents, that enables saving the measurement and the measurement initialization data.

Using these resources, the writing/reading of two FDB nodes (N1 and N2) is carried out with the Pyrebase library. N1 corresponds to "Device Status", which will give a signal to start the process for taking and recognizing the signals. N2, called "Unique user code", identifies the last user that synchronized the device with the App. The data writing has a function for storing the information in the FDB, which stores the data of the physiological signals measured.

Subsystem 3 consists of the App developed in Ionic (Open-source framework for developing mobile hybrid applications), to access the Firebase data in real-time and inform the user about the events for utilizing the device. The permanent listening of a Firebase Activation variable node is carried out at this stage, which permanently queries and updates the value of the "Device Status" variable of the FDB.

The App enables doing the registration, recovering user's password and starting the session to have access to the main menu. The menu gives access to the measurement history and to the synchronization of the App with the device. Each user should have a unique

code for activating the application, which is provided when the user creates an account. This unique code will identify the user and will be updated when he/she enters to the application.

A support menu has been programmed with information about device use, password change and personal data update. Data about the medical staff that will monitor the physiological signals is also required for managing user's data (identification and link with the device). In addition, each measurement record includes information about smell or taste loss consulted to the App, since these are relevant symptoms in the COVID-19 diagnosis [5].

### 2.5. Tests

Tests were carried out to verify the device functionality. These tests sought to determine: a) the time required by the device to record the physiological signals (body temperature, blood pressure and oxygen saturation); b) the error percentage of the tests to the image recognition system; c) evaluation of the App functionalities; d) evaluation of the device and the application by users according to the System Usability Scale (SUS) and the Post-Study System Usability Questionnaire (PSSUQ) and e) the error percentage in the measurements recorded in the app compared to the particular results of each instrument.

To estimate the time that the device will take to carry out a measurement, it is determined the time required by each process to complete correctly.

To verify the accuracy of image recognition, the values recorded in 20 photos obtained with the recognition algorithm were compared with the values recorded by a person while monitoring the measurement.

For App evaluation it was verified: correct registration and password recovery using a Google mail; database and storing service; information update in the database; service to share the measurement history; connectivity with the App in an operator data network, in a Wi-Fi network and with a weak connection signal; performance of the battery; if the device overheats and memory use.

Tests involved 16 healthy participants (7 men and 9 women, from 15 to 72 years of age), meeting biosecurity regulations and according to the following Test protocol: 1) The participants get an explanation about the operation of the device; 2) Each participant should sign a consent stating that he/she agrees with carrying out tests with the device; 3) Each participant is requested to access the App with his/her username and to synchronize the application with the device; 4) Each participant is requested to put his/her left arm in the device with the palm of the hand facing down and to close the band of the blood pressure meter as shown in Figures 8b and 8c; 5) Each participant is requested to make five measurements according to the

procedure for acquiring and visualizing the values of the physiological signals in the App; a rest of 180 s is taken between measurements; 6) Five measurements of the physiological variables are made using individually a blood pressure meter, a thermometer and an oximeter, according to the measurement protocol of each instrument; a rest of 180 s is taken between measurements; 7) After measurements are finalized, each participant is requested to answer the SUS and PSSUQ questionnaires to know the level of satisfaction with the algorithm corresponding to the method [25] and using the «PSSUQ Calculator» tool [26]; 8) The device is cleaned.

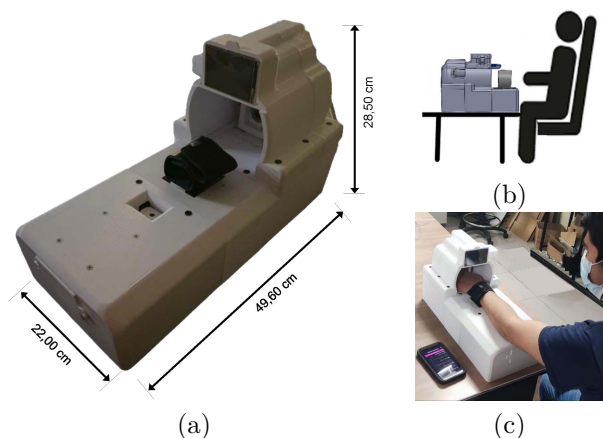


**Figure 8.** Prototype of the device (a) Integration of the elements and dimensions; (b) Correct position to take measurements; (c) User with his left arm in the device, with the blood pressure meter adjusted and the application synchronized for starting the measurements.

### 3. Results and discussion

Figure 8a shows the device with the integrated mechanical and electronic components. The dimensions of the device are 22cm × 49.60cm × 28.5cm with a weight of 1.125Kg. Considering that the BIs operate simultaneously, the total measurement time is estimated as the response time of the digital blood pressure meter, since this is the BI that takes the longer time to produce a response in its display. For this reason, it is considered that the device enables obtaining measurements of temperature, heart rate, blood pressure and level of oxygen saturation in 70 s. Since it is necessary to clean the device in case of various users, it is considered that the time required by a user to employ the device is 4 min. After cleaning the device with alcohol, it can be used again immediately. Based on this time, it is possible to make 12 consecutive measurements in an hour. Table 1 details the energy consumption of the device components, obtaining a total consumption of 3.20 Ah. Considering battery specifications and total consumption, the continuous operating time or autonomy is 1.37 h. For this reason, the device operates

without requiring power supply from the electric grid for a satisfactory time, thus fulfilling the portability and safety features according to standards such as IEC 60601.

**Table 1.** : Power consumption of the device during twelve measurements in an hour of use

Element	Time medición (h)	Current (A)	Consumption (Ah)
Raspberry	1,00	0,70	0,70
Actuator	0,02	0,04	0,48
Thermometer	0,005	0,36	0,36
Oxímetro	0,04	0,36	0,36
Blood pressure meter	0,075	0,6	0,60
Display	1,00	0,74	0,74
<b>Total consumption</b>			<b>3,20</b>

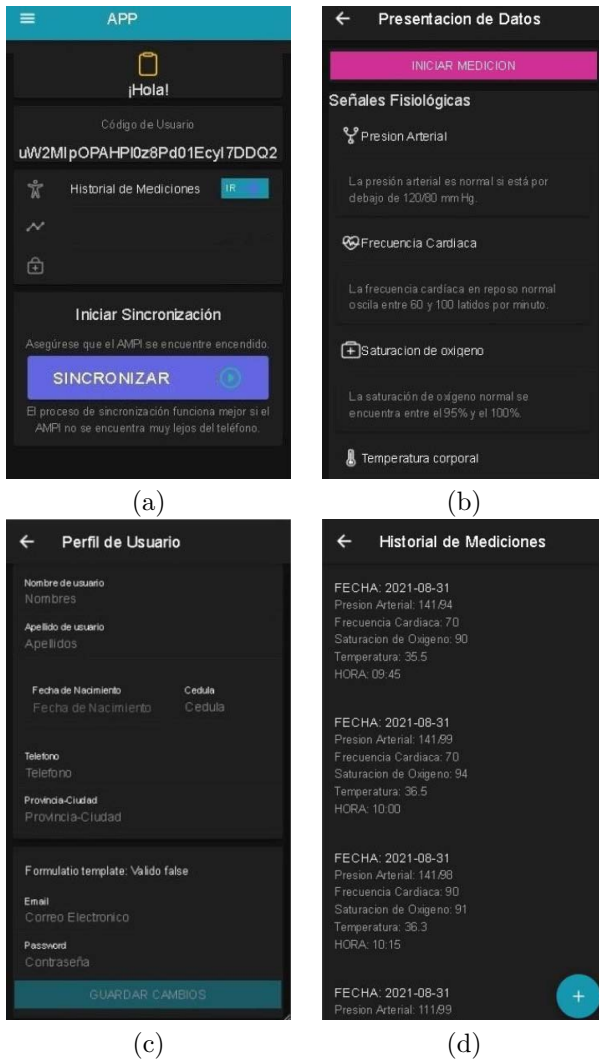
With respect to the recognition accuracy, when the response values of the recognition algorithm are compared with the values recorded during measurement monitoring, an accuracy of 100% was obtained. This success rate guarantees that the device records the values of commercial BIs integrated in a platform that stores the information for monitoring cases of COVID-19 and other respiratory diseases; it has been demonstrated that these data help in the diagnosis and that they are obtained securely. Regarding the operation of the App, it was verified that the access with authentication through e-mail and password is performed satisfactorily. Information about identification, service provider, date of account creation, last access data and unique user code are included during account creation.

Figure 9a shows the interface corresponding to the main page, which displays pages and main activities of the application, such as: greetings section, measurement history and synchronization with the device. Figure 9b shows the button for activating the device and starting taking physiological signals.

Figure 9c shows the information required to create the user's profile and Figure 9d shows an example of the measurements stored in the Firebase database obtained from the device.

During the tests, all measurements visualized in the display were sent to the database. This enabled verifying the correct operation of the digital platform for recording the measurements of all BIs. The App is simple and intuitive and constitutes an interface for the communication between user and device.

It was verified that the application works perfectly with different operating systems (Android and IOS) and from a web page.



**Figure 9.** App Interface (a) Main page; (b) Interface to start the measurement; (c) User profile;(d) Measurement history

It was verified that the application works perfectly with different operating systems (Android and IOS) and from a web page. Similarly, the application works correctly with seven different smartphone brands. The average time to open the application and show the main interface is  $3.25s \pm 1.75s$ .

It was verified that no mobile device overheated and that the average battery consumption of the application is 5.10%. In case of using the total memory, it was verified an average use of 13 MB of RAM and 25.9 of storage. These results confirm that the application has a functionality of 100% and may be employed without problems in different mobile devices.

Regarding the device measurement accuracy compared with the measurements obtained using the instruments individually and manually activated, for oxygen saturation, heart rate and body temperature, the percentage of accuracy exceeds 98%. For blood pressure, the percentage of accuracy exceeds 96%. The

results also demonstrate that the device mechanical structure, which integrates the BIs and enables their automatic activation, does not alter measurement protocols. The BIs employed are described in different proposals as part of telemedicine and internet of things platforms. Although in the case of blood pressure it is recommended manual measurement [27], records obtained with digital systems are considered valid and useful in protocols for diagnosing and monitoring respiratory system diseases [19], [21], [28]. Therefore, the device developed is considered a contribution as a tool for assisting in such diagnosis and monitoring.

Table 2 shows the results of the SUS evaluation in which every participant answered ten questions using a scale from 1 to 5 (E1: totally disagree; E2: disagree; E3: neutral; E4: agree; E5: totally agree). The questions answered were: 1) “I believe that I would use this device frequently”; 2) “I find this device unnecessarily complex”; 3) “I believe that this device was easy to use”; 4) “I believe that I would need help from a person with technical knowledge to use this device”; 5) “The functionalities of this device are well integrated”; 6) “I believe that the device is inconsistent”; 7) “I Imagine that most of the people would learn to use this device quickly”; 8) “I find that this device is confusing”; 9) “I feel confident when using this device”; 10) “I needed to learn many things before being able to use this device”.

The SUS score calculated with the algorithm corresponding to method [25] was  $82.50 \pm 17.17$ .

Over 60% of the participants think that they would use this device frequently, that it was easy to use and that its functionalities are well integrated.

**Table 2.** Results of the SUS questionnaire

Question	% E1	% E2	% E3	% E4	% E5
1	10	15	13	12	50
2	56	25	0	19	0
3	0	19	6	12	63
4	19	19	6	6	50
5	0	31	6	0	63
6	57	6	6	31	0
7	6	38	12	0	44
8	61	19	20	0	0
9	0	44	6	6	44
10	63	6	6	25	0

Regarding the PSSUQ questionnaire score, the result about App performance and satisfaction is 1.47. The usefulness of the system had a mean score of 1.25; the information quality obtained a score of 1.5 and the interface quality a score of 1.67. These results indicate that the application is at a high level of satisfaction and usability, since a smaller score between 1 and 7 indicates a better performance.

The participants initially thought that the device may be considered complex, however, the instructions provided, the availability of an operation manual and

the practice help users to easily use the device. However, half of the participants expressed that they would feel more secure with a professional guiding them. The group of higher age stated the need of having a person to assist them with the use of the App. This fact shows that new technologies must include a training aimed at the population who do not know about digital platforms. Considering the potential of applications in the middle of the pandemics and the new generation of health services [29], it is transcendental to boost the inclusion of digital alphabetization so that telemedicine proposals have a greater impact.

Another group expressed that manipulating a cell phone with only one hand may be difficult, however, the display facilitates starting the measurements and tracking the data obtained. This gives security to users, since some participants expressed that there were errors in data transmission, which demanded repeating the measurements. It is important to incorporate alarms and audio messages in the App as optional resources to guide those users that require additional help.

Overall, participants thought that the device is a good equipment; however, it is necessary to get used to have a device of this kind at home. A participant expressed being uncomfortable of not being able to see the hand during measurements, which states the possibility of considering new materials for the structure that enable visualizing the measurement process to guarantee confidence of users on the device.

It is necessary to conduct a study with population that already got infected with COVID-19, with the objective of analyzing the impact of the device as a tool to take care of this population.

It is considered that the proposed device constitutes a solid foundation to develop new platforms based on artificial intelligence and data analysis algorithms to diagnose asymptomatic cases of COVID-19, and to establish prediction models with data acquired in real-time [9], [20].

The availability of innovative resources in an accessible manner will enable strengthening health services in the future.

#### 4. Conclusions

The proposed prototype of a device for automatic measurement of physiological signals of interest for diagnosing COVID-19 is easy to use, portable, non-invasive, guarantees measurement validity and patient safety.

The App enables the user to handle a medical history with key information for monitoring COVID-19 and other respiratory diseases. The usability tests were very important to know aspects to be improved in the mechanical structure and in the digital platform.

#### References

- [1] WHO. (2020) Archived: WHO Timeline - COVID-19. World Health Organization. [Online]. Available: <https://bit.ly/32GwzNj>
- [2] A. Trilla, “Un mundo, una salud: la epidemia por el nuevo coronavirus COVID-19,” *Medicina Clínica*, vol. 154, no. 5, pp. 175–177, 2020. [Online]. Available: <https://doi.org/10.1016/j.medcli.2020.02.002>
- [3] Ministerio de Salud. (2021) Actualización de casos de coronavirus en Ecuador. Instituto Nacional de Investigación en Salud Pública, Ecuador. [Online]. Available: <https://bit.ly/3Fyqtgx>
- [4] M. Villegas-Chiroque, “COVID-19 pandemic: fight or flight,” *Revista Experiencia en Medicina del Hospital Regional Lambayeque*, vol. 6, no. 1, 2020. [Online]. Available: <https://doi.org/10.37065/rem.v6i1.424>
- [5] C. Menni, C. H. Sudre, C. J. Steves, S. Ourselin, and T. D. Spector, “Quantifying additional COVID-19 symptoms will save lives,” *The Lancet*, vol. 395, no. 10241, pp. e107–e108, Jun 2020. [Online]. Available: [https://doi.org/10.1016/S0140-6736\(20\)31281-2](https://doi.org/10.1016/S0140-6736(20)31281-2)
- [6] B. Mizrahi, S. Shilo, H. Rossman, N. Kalkstein, K. Marcus, Y. Barer, A. Keshet, N. Shamir-Stein, V. Shalev, A. E. Zohar, G. Chodick, and E. Segal, “Longitudinal symptom dynamics of COVID-19 infection,” *Nat Commun*, vol. 11, no. 1, p. 6208, Dec. 2020. [Online]. Available: <https://doi.org/10.1038/s41467-020-20053-y>
- [7] A. Bella, R. Latif, A. Saddik, and F. Z. Guerrouj, “Monitoring of physiological signs and their impact on the COVID-19 pandemic: Review,” *E3S Web of Conferences*, vol. 229, p. 01030, 2021. [Online]. Available: <https://doi.org/10.1051/e3sconf/202122901030>
- [8] A. Espinosa Brito, “A propósito de la COVID-19: Mide tu presión arterial, contrólala y vive más,” *Revista Finlay*, vol. 11, no. 3, 2021. [Online]. Available: <https://bit.ly/32I53is>
- [9] D. S. W. Ting, L. Carin, V. Dzau, and T. Y. Wong, “Digital technology and COVID-19,” *Nature Medicine*, vol. 26, no. 4, pp. 459–461, Apr 2020. [Online]. Available: <https://doi.org/10.1038/s41591-020-0824-5>
- [10] R. Rethnakumar, M. G. Md Johar, M. H. Alkawaz, R. A. A. Helmi, and N. M. Tahir, “Smartphone based application for

- body temperature and heart rate measurements,” in *2021 IEEE 12th Control and System Graduate Research Colloquium (ICSGRC)*, 2021, pp. 189–194. [Online]. Available: <https://doi.org/10.1109/ICSGRC53186.2021.9515284>
- [11] A. Depari, A. Flammini, S. Rinaldi, and A. Vezzoli, “A portable multi-sensor system for non-invasive measurement of biometrical data,” *Procedia Engineering*, vol. 47, pp. 1323–1326, 2012. [Online]. Available: <https://doi.org/10.1016/j.proeng.2012.09.399>
- [12] S. Mirjalali, S. Peng, Z. Fang, C.-H. Wang, and S. Wu, “Wearable sensors for remote health monitoring: Potential applications for early diagnosis of COVID-19,” *Advanced Materials Technologies*, vol. n/a, no. n/a, p. 2100545, 2021. [Online]. Available: <https://doi.org/10.1002/admt.202100545>
- [13] L. G. Meza Contreras, M. Botero, and W. Ardila, “Diseño de procedimientos para la calibración de tensiómetros según la norma técnica NTC-ISO/IEC 17025,” *Revista Colombiana de Física*, vol. 43, no. 2, p. 323, 2011. [Online]. Available: <https://bit.ly/3124ijU>
- [14] L. P. Motta, P. P. F. d. Silva, B. M. Borguezan, J. L. M. d. Amaral, L. G. Milagres, M. N. Bóia, M. R. Ferraz, R. Mogami, R. A. Nunes, and P. L. d. Melo, “An emergency system for monitoring pulse oximetry, peak expiratory flow, and body temperature of patients with COVID-19 at home: Development and preliminary application,” *PLoS One*, vol. 16, no. 3, p. e0247635, Mar. 2021. [Online]. Available: <https://doi.org/10.1371/journal.pone.0247635>
- [15] J. Martinho, L. Prates, and J. Costa, “Design and implementation of a wireless multiparameter patient monitoring system,” *Procedia Technology*, vol. 17, pp. 542–549, 2014. [Online]. Available: <https://doi.org/10.1016/j.protcy.2014.10.261>
- [16] D. M. D’Addona, R. Rongo, R. Teti, and R. Martina, “Bio-compatible cyber-physical system for cloud-based customizable sensor monitoring of pressure conditions,” *Procedia CIRP*, vol. 67, pp. 150–155, 2018. [Online]. Available: <https://doi.org/10.1016/j.procir.2017.12.245>
- [17] M. M. Yassin, A. M. Saber, M. N. Saad, A. M. Said, and A. M. Khalifa, “Developing a low-cost, smart, handheld electromyography biofeedback system for telerehabilitation with clinical evaluation,” *Medicine in Novel Technology and Devices*, vol. 10, p. 100056, 2021. [Online]. Available: <https://doi.org/10.1016/j.medntd.2020.100056>
- [18] M. Martínez-García, M. Bal-Alvarado, F. Santos Guerra, R. Ares-Rico, R. Suárez-Gil, A. Rodríguez-Álvarez, A. Pérez-López, E. Casariego-Vales, e. N. d. E. de Seguimiento Compartido TELEA-COVID Lugo, and E. T. C.-. (Lugo), “[monitoring of COVID-19 patients by telemedicine with telemonitoring],” *Elsevier Public Health Emergency Collection*, vol. 220, no. 8, pp. 472–479, Jun. 2020. [Online]. Available: <https://dx.doi.org/10.1016/j.rce.2020.05.013>
- [19] B. Clipper, “The influence of the COVID-19 pandemic on technology: Adoption in health care,” *Nurse Lead*, vol. 18, no. 5, pp. 500–503, Jun. 2020. [Online]. Available: <https://doi.org/10.1016/j.mnl.2020.06.008>
- [20] Y. Coelho, L. Lampier, C. Valadão, E. Caldeira, D. Delisle-Rodríguez, A. C. Villa-Parra, C. Cobos-Maldonado, J. Calle-Siguencia, F. Urgilés-Ortiz, and T. Bastos-Filho, “Towards the use of artificial intelligence techniques in biomedical data from an integrated portable medical assistant to infer asymptomatic cases of covid-19,” in *Information Technology and Systems*, Á. Rocha, C. Ferrás, P. C. López-López, and T. Guarda, Eds. Springer International Publishing, 2021, pp. 24–34. [Online]. Available: [https://doi.org/10.1007/978-3-030-68418-1\\_3](https://doi.org/10.1007/978-3-030-68418-1_3)
- [21] F. Z. Fagroud, H. Toumi, E. H. Ben Lahmar, M. A. Talhaoui, K. Achtaich, and S. E. Filali, “Impact of IoT devices in E-Health: A review on IoT in the context of COVID-19 and its variants,” *Procedia Comput Sci*, vol. 191, pp. 343–348, Sep. 2021. [Online]. Available: <https://doi.org/10.1016/j.procs.2021.07.046>
- [22] A. Ravizza, C. De Maria, L. Di Pietro, F. Sternini, A. L. Audenino, and C. Bignardi, “Comprehensive review on current and future regulatory requirements on wearable sensors in preclinical and clinical testing,” *Frontiers in Bioengineering and Biotechnology*, vol. 7, p. 313, 2019. [Online]. Available: <https://doi.org/10.3389/fbioe.2019.00313>
- [23] S. Hoffstaetter, J. Bochi, M. Lee, L. Kistner, R. Mitchell, E. Cecchini, J. Hagen, D. Morawiec, E. Bedada, and U. Akyüz. (2021) Pytesseract 0.3.8. Python Software Foundation. [Online]. Available: <https://bit.ly/3mCXRvn>
- [24] R. de la Vega. (2021) Pytesseract: Reconocimiento óptico de caracteres en Python. PHAROS. [Online]. Available: <https://bit.ly/3qypbfc>
- [25] M. Almenara Masbernat, “Modelo teórico-práctico para la implementación del diseño centrado en el usuario en el desarrollo, la

- validación y la aceptación de los productos de apoyo para personas con enfermedades de origen neurológico,” Ph.D. dissertation, 2018. [Online]. Available: <https://bit.ly/3pxFqtL>
- [26] UIUX Trend. (2021) Pssuq calculator. UIUX Trend. [Online]. Available: <https://bit.ly/3z1Xgsa>
- [27] I. Guerra Llamas, D. H. Gascueña, C. Ledemas Torres, and I. García Pérez, “Diferencias en las tomas de tensión arterial manual y automática,” *Fundación Renal Íñigo Álvarez de Toledo. Madrid*, 2014. [Online]. Available: <https://bit.ly/3z5F2FW>
- [28] V. Santos, M. Trujillo, K. Portilla, and A. Rosales, “Accessible eHealth system for heart rate estimation,” in *Advances in Emerging Trends and Technologies*, M. Botto-Tobar, J. León-Acurio, A. Díaz Cadena, and P. Montiel Díaz, Eds. Springer International Publishing, 2020, pp. 260–269. [Online]. Available: [https://doi.org/10.1007/978-3-030-32022-5\\_25](https://doi.org/10.1007/978-3-030-32022-5_25)
- [29] P. Eslami, S. R. Niakan Kalhori, and M. Taheriyani, “eHealth solutions to fight against COVID-19: A scoping review of applications,” *Medical Journal of the Islamic Republic of Iran*, vol. 35, p. 43, Apr. 2021. [Online]. Available: <https://doi.org/10.47176/mjiri.35.43>



# A REVIEW OF THE STATE-OF-THE-ART OF SOLAR THERMAL COLLECTORS APPLIED IN THE INDUSTRY

## UNA REVISIÓN DE LOS ÚLTIMOS AVANCES DE LOS COLECTORES SOLARES TÉRMICOS APLICADOS EN LA INDUSTRIA

Willian Carrión-Chamba<sup>1</sup> , Wilson Murillo-Torres<sup>1</sup> ,  
Andrés Montero-Izquierdo<sup>2,\*</sup>

Received: 16-05-2021, Received after review: 28-06-2021, Accepted: 03-08-2021, Published: 01-01-2022

### Abstract

The energy consumption associated with the industry sector represents 38% of the global energy demand, being an important aspect that marks the development of a country. In this sense, it is extremely important to diversify the different energy sources and incorporate the use of renewable energy sources, such as solar energy, not only with the idea of ensuring energy supply, but also as elements that enable the reduction of energy emissions generated by the use of fossil fuels. This work addresses the main solar collector technologies that may be incorporated into different types of industries, based on experiences and research in other countries. Based on this review, it has been seen that an important part of the industries worldwide requires temperatures up to 250 °C in their processes, which makes suitable the use of solar energy technology. Depending on each industry, flat plate, vacuum tube, Fresnel type or parabolic trough solar collectors may be used. Finally, the savings associated with some facilities are detailed and the challenges related to this sector are addressed.

**Keywords:** Solar energy, solar thermal collectors, industrial applications.

### Resumen

El consumo energético asociado al sector de la industria representa el 38 % de la demanda de energía a nivel global, siendo un aspecto importante que marca el desarrollo de un país. En este sentido, es sumamente importante diversificar las distintas fuentes de energía e incorporar el uso de fuentes renovables de energía, como la solar, no solamente con la idea de asegurar el suministro energético, sino también considerando como elementos que permitan la reducción de las emisiones generadas por el uso de combustibles fósiles. El presente trabajo aborda las principales tecnologías de colectores solares que pueden ser incorporadas a distintos tipos de industrias, basado en experiencias e investigaciones en otros países. Sobre la base de esta revisión, se ha visto que una buena parte de las industrias a nivel mundial requieren temperaturas en sus procesos hasta los 250 °C, lo que hace idóneo el uso de esta tecnología. En función de cada industria, se podrán usar colectores solares de placa plana, de tubos de vacío, del tipo Fresnel o cilindro parabólicos. Por último, se detallan los ahorros asociados a algunas instalaciones y se abordan los desafíos relacionados con este sector.

**Palabras clave:** energía solar, colectores solares térmicos, aplicaciones industriales

<sup>1</sup>Facultad de Ciencias Químicas, Universidad de Cuenca, Ecuador.

<sup>2,\*</sup>Grupo de Ingeniería de Reactores, Catálisis y Tecnologías del Medio Ambiente - IRCMA, Facultad de Ciencias Químicas, Universidad de Cuenca, Ecuador. Corresponding author ✉: andres.montero@ucuenca.edu.ec.

Suggested citation: Carrión-Chamba, W.; Murillo-Torres, W. and Montero-Izquierdo, A. "A review of the state-of-the-art of solar thermal collectors applied in the industry," *Ingenius, Revista de Ciencia y Tecnología*, N.º 27, pp. 59-73, 2022, DOI: <https://doi.org/10.17163/ings.n27.2022.06>.

## 1. Introduction

Energy is a key component for the well-being and economic development of a nation, and thus an economy based on industrialization is one of the reasons of the increasing trend in energy consumption [1]. The industry sector employs 38 % of the global energy demand, representing the economic activity with the highest consumption of this resource [2]. For manufacturing industries, the energy sources generally come from fossil fuels and natural gas. However, greenhouse gas emissions produced by combustion of hydrocarbons, have become an environmental problem that accelerates the effects of climate change [3]. The current challenge faced by the industry sector is incorporating efficient alternatives of sustainable energy to reduce the air pollution levels [4]. In this situation, a solution is the implementation of systems based on renewable energies and energy efficiency measures, considering that in the future fossil fuels will reach their extraction limit. Due to its abundance and free availability, solar energy is one of the renewable resources with the greatest potential to reduce the levels of CO<sub>2</sub> emissions to the atmosphere [5]. It is possible to take advantage of solar radiation in two ways: direct conversion in electricity through photovoltaic cells and thermal conversion using solar collectors [6].

The use of solar thermal energy in industry has been the subject of research activity from the 70s through programs of the International Energy Agency (IEA) such as the Solar Heating & Cooling Programme [7]. At the end of 2019 the installed solar thermal power was 700 MWt, considering at least eight hundred projects with a total capturing area of approximately one-million square meters installed worldwide [8]. Food, textile, paper, metal, plastic and chemical industries highlight among the main industries that use solar thermal energy in their manufacturing processes [9]. According to the type of industrial process, solar collectors may be classified in three categories based on their temperature range: low temperature (< 150 °C), medium temperature (150 - 400 °C) and high temperature (> 400 °C) [10]. However, in commercial and industrial companies there is a greater demand at temperatures below 250 °C [11]. This paper comprises a review of the latest advances on solar thermal collectors applied to industry through the presentation of technical, economic and environmental aspects, considering real facilities and dynamic simulations of the systems analyzed.

## 2. The use of solar thermal energy

The solar thermal energy consists of using energy from the sun to heat a heat carrying fluid and transfer this heat to another medium within a process or system. This type of renewable energy can substitute or re-

duce the use of fossil fuels and due to the existence of a competitive market it is considered as one of the most economic commercial alternatives for producing heat [12]. However, the intermittency of solar energy makes necessary to have available auxiliary thermal storage systems, which results in larger investment costs and, in turn, lower economic viability for the execution of new projects [13]. Thermal energy may be stored in the form of latent heat or sensible heat; however, in the latent heat mechanism with phase change materials (PCM) it is required a smaller storage volume since the energy density is larger than in heat sensible materials [7].

Solar thermal collectors are devices in charge of transforming solar energy into thermal energy through different operating principles that vary according to the type of collector used [14]. The main aspects to be taken into account in industrial applications for installing a solar thermal system are the target temperature, energy requirement, economic criteria, space availability and degree of maturity of the technology analyzed [15]. Based on temperature ranges and the use in industry, this work covers low and medium temperature collectors.

### 2.1. Low temperature collectors

#### 2.1.1. Flat plate collector

The flat plate collector (FPC) transforms solar energy into thermal energy using a panel constituted by a glazed cover, which enables solar light to pass, hit and be absorbed by the selective surface of an absorbing plate. Figure 1 shows the cross section of an FPC where its components may be seen.

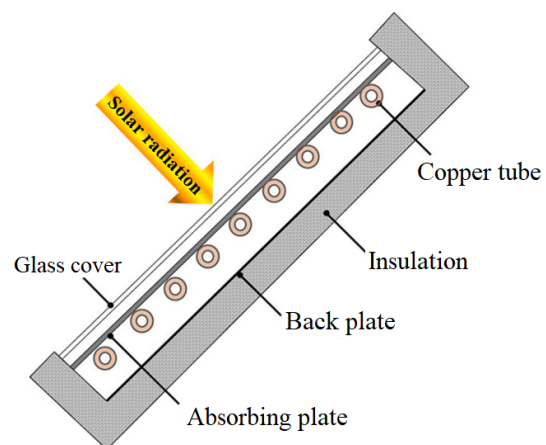


Figure 1. Parts of a flat plate collector [16]

After being intercepted by the plate, the thermal energy is transferred to the inside of the tubes through which the heat carrying fluid circulates, to finally go to a storage system, or be used directly [17]. The system heat loss is reduced using thermal insulation in the

lower and lateral parts of the carcass; similarly, the glass cover minimizes the convection and radiation heat losses emitted from the absorbing plate [18]. A particular feature of the FPCs is that they take advantage of direct and diffuse solar radiation; however, since they are stationary, they receive less energy per unit area of the collector [17]. These devices operate in a low temperature interval ( $< 100\text{ }^{\circ}\text{C}$ ) and since they have a simple structure compared with other collectors, they have a low cost in the market [19].

### 2.1.2. Vacuum tube collector

The vacuum tube collector or evacuated tube collector (ETC) consists of a specific number of crystal tubes each of which is constituted by two concentric tubes. The inner tube is covered by a selective absorbing layer, while each concentric unit is separated by the vacuum sealing principle [18]. The objective of generating vacuum is to reduce the convection and conduction heat losses; in addition, it is a technical advantage that enables operating the device at temperatures higher than FPCs.

The operation temperature of an ETC may reach values up to  $120\text{ }^{\circ}\text{C}$  [20]. In addition, the high thermal efficiency and the relatively low cost of this collector are the main reasons of its high competitiveness in the market [21]. There are two main types of ETCs:

1. Heat-pipe ETC: This collector is based on the operating principle known as evaporation-condensation cycle. The process starts when the heat tube receives solar radiation which makes that the highly volatile fluid (for example, methanol or ethanol) contained in it changes from liquid to gaseous state, causing that the vapor goes to the upper part of the tube where the condenser is located [18]. After condensing the vapor releases latent heat to the main circuit and then the condensed liquid returns to the lower part of the tube to complete the circulation cycle [22]. Figure 2 shows the cross section of a heat-pipe vacuum tube collector.

2. Direct flow ETC. In this collector, the inside of the absorbing tube is vacuum insulated and has a U-shaped tube built-in which enables the inlet and outlet of the fluid (Figure 3). The inner tube is made up of metal and is covered with a coating of selective material to accelerate heat transfer to the fluid and reduce radiation losses. During the process, the cold fluid enters and absorbs heat from the U-shaped tubes heated by solar radiation to finally be discharged through the outlet of the pipes [17].

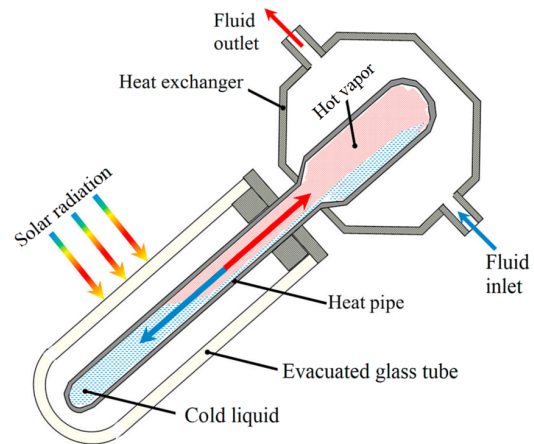


Figure 2. Cross-section of a heat-pipe tube collector [16]

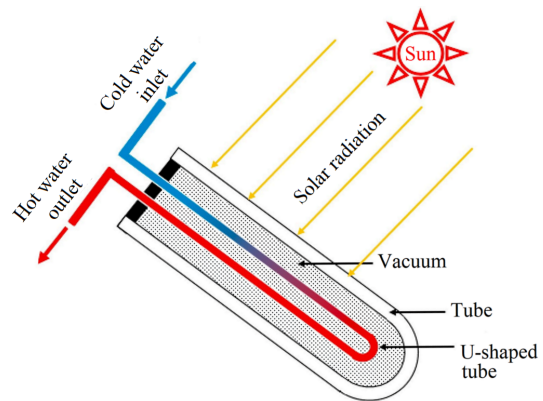


Figure 3. Cross-section of a direct flow vacuum tube collector [9]

### 2.1.3. Compound parabolic collector

The compound parabolic collector (CPC) consists of two parabolic surfaces covered by reflective material that share the same center. The absorbing tube is located in the center of these parabolas, which enables capturing the incident solar radiation that enters the opening area of the collector within the acceptance angle [19].

The construction design of these devices enables a better use of the diffuse solar radiation and reduces the action of performing continuous tracking adjustments [23]. There are various models which adapt to achieve a higher efficiency; a very practical example is to couple the CPC with vacuum tubes. In industrial applications, the CPCs reach temperatures  $< 150\text{ }^{\circ}\text{C}$  [24]. Figure 4 shows a schematic representation of this collector where it is seen the two parabolic surfaces that concentrate solar radiation in the absorbing tube.

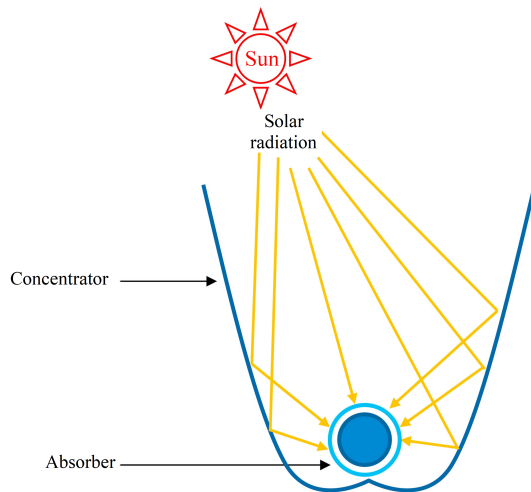


Figure 4. Compound parabolic collector [9]

## 2.2. Medium temperature collectors

### 2.2.1. Evacuated flat plate collector

The evacuated flat plate collector (EFPC) combines the design of the FPC and the vacuum principle of the ETC. Figure 5 shows that a collector of this type consists of: a structure constituted by an aluminum carcass and various elements such as a glass cover, an absorbing plate, a copper coil for heat exchange and a lower plate. The inner vacuum enables achieving a higher thermal efficiency since the conduction and convection losses are eliminated; in addition, this effect causes that the collector occupies less surface than the ETC. Medium temperatures between 120 and 180 °C may be reached with this technology, to fulfill requirements of industrial heat [25].

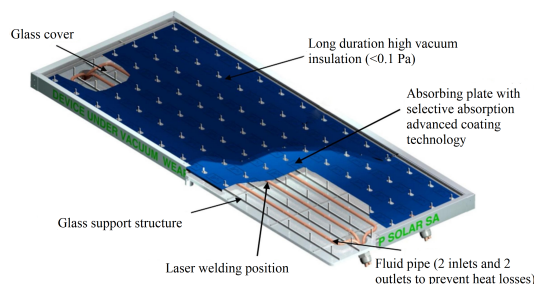


Figure 5. Structure of the evacuated flat plate collector [25]

### 2.2.2. Parabolic Cylinder collector

The parabolic cylinder collector or parabolic trough collector (PTC) has a parabolic-shaped sheet that reflects direct solar radiation and concentrates it in the receiving tube located along the focal line. In general, the metal absorbing tube is covered with a selective material (copper) which improves heat transfer to the

inside of the tube through which the heat carrying fluid circulates. This absorbing pipeline is vacuum insulated with a glass tube to reduce the convection thermal losses, although optical losses are produced by the effect of reflection [19]. These collectors should be coupled to a tracking system to get aligned to the sun trajectory during the day (Figure 6).

The orientation of the collector may be configured in north-south direction with east-west tracking to capture more energy during summer; whereas, if the objective is maximizing the energy during winter the appropriate direction of the collector should be east-west with north-south tracking [26]. Solar concentration modules with a capturing area smaller than 250 m<sup>2</sup> and operating at a medium temperature below 300 °C are normally used in industrial processes with this type of collectors [27].

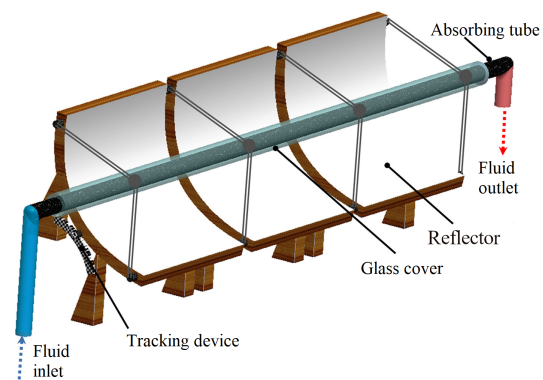


Figure 6. Scheme of a parabolic cylinder collector [16]

### 2.2.3. Linear Fresnel collector

The linear Fresnel collector (LFC) consists of two main parts: a stationary absorbing tube through which the heat carrying fluid circulates and a series of reflecting mirrors aligned horizontally that are coupled to a uniaxial tracking system [19]. The operating principle of the collector occurs when the solar radiation impacts on the reflecting mirrors (either curved or flat) and is directed to concentrate in the absorbing tube (Figure 7).

To maximize the concentration of solar energy, particular designs decide to install a CPC collector on the upper part of the receiver or focal point with the objective of redirecting solar radiation to the absorbing tube [28]. One of the advantages that make an LFC competitive with respect to a PTC is its simple construction, which implies a lower investment cost; however, optical and geometrical limitations such as shading and blocking between mirrors reduce the degree of efficiency of the collector [27]. In industrial processes, this type of collector may reach medium temperature intervals (60 °C < T < 250 °C) [29].

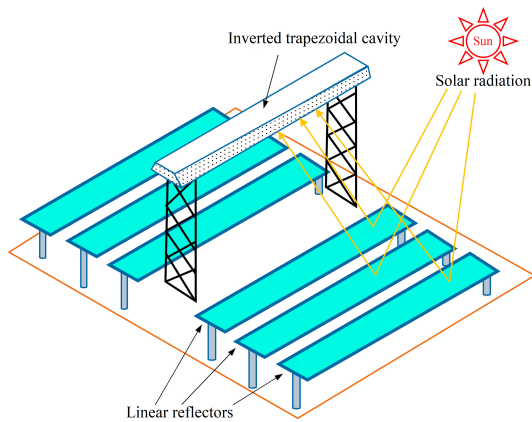


Figure 7. Scheme of a linear Fresnel collector [9]

The efficiency ( $\eta$ ) equation may be employed to compare the performance between collectors.

$$\eta = a_0 - a_1 \frac{(T_m - T_{amb})}{G} - a_2 \frac{(T_m - T_{amb})^2}{G} \quad (1)$$

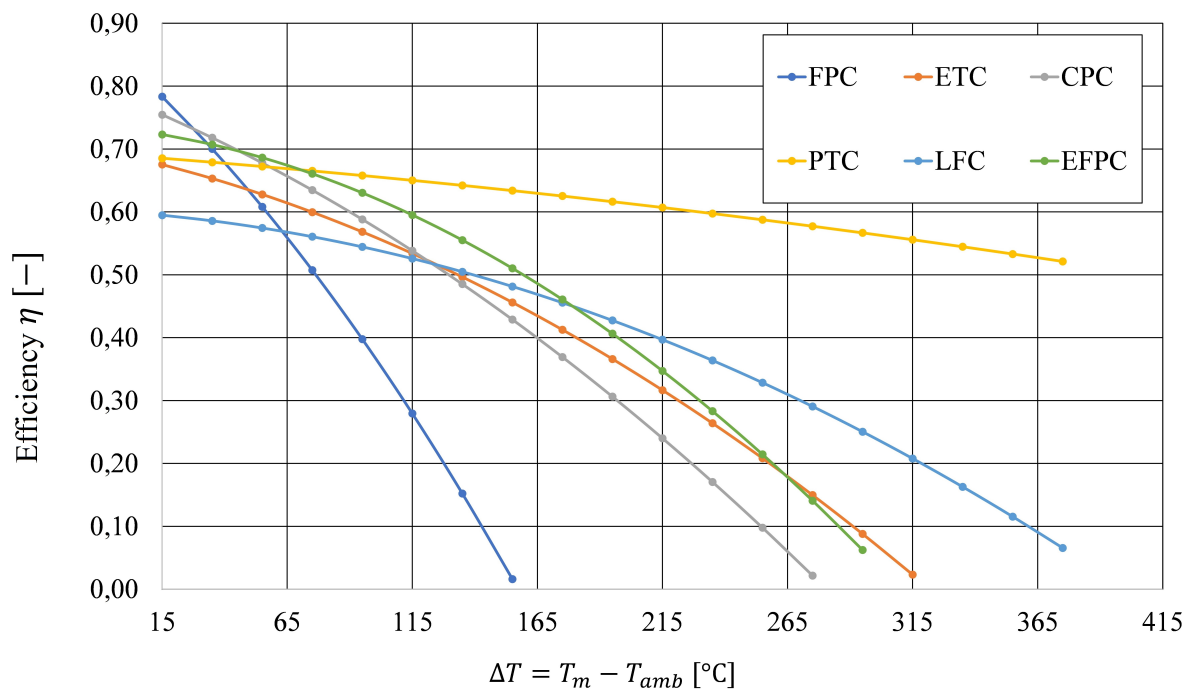


Figure 8. Comparison between solar collectors (Prepared by the authors)

### 3. Application of solar thermal energy in industry

Solar thermal energy has become a key component that will contribute to the decarbonization of the industry sector. The worldwide heat consumption in the industry sector is approximately 85 EJ, of which 30 % corresponds to the demand of low temperature heat [30]. A review of case studies is presented here-

after, based on computer simulation, for industrial applications.

A research study to evaluate the viability of integrating an FPC as a heat generation system for preheating raw material in two fish flour producing companies was conducted in South Africa. The study demonstrated that the installation profitability is justified in factory A, because it is required a relatively constant heat monthly demand and due to the high

Figure 8 shows a comparison between efficiencies for various solar thermal collectors according to Equation (1), where:  $T_m$  corresponds to the mean temperature of the heat carrying fluid,  $T_{amb}$  is the ambient temperature,  $a_0$  is the optical performance,  $a_1$  is the first-order coefficient of losses,  $a_2$  is the second-order coefficient of losses and  $G$  is the global irradiance. For this comparison, it is assumed a global irradiance of  $1000 \text{ W/m}^2$  and an ambient temperature of  $20 \text{ }^\circ\text{C}$ ; it is observed through equation (1) that FPC collectors achieve a high efficiency for a low  $\Delta T$ , whereas as this variable increases its efficiency is drastically reduced. The opposite occurs with the remaining collectors, for which the efficiency reduces as the value of  $\Delta T$  increases not so drastically. It is even observed that the PTC collector maintains its efficiency almost constant as the temperature differential  $\Delta T$  increases.

cost of fuel oil which make this system a competitive solar technology. However, installing an FPC system in factory B is not feasible due to the low cost of carbon and because the seasonal demand profile is variable [31]. A study to evaluate the performance of incorporating a heat storage system with phase change materials together with FPC collectors in the tropical zone of Merida-Mexico revealed that lauric acid, due to its thermophysical characteristics, is the most appropriate PCM to obtain a higher thermal gain throughout the year. In addition, the financial analysis indicated that the maximum value of 17.2 % in the internal rate of return is achieved if the heat storage system is coupled with an arrangement of five FPC collectors for the water heating process in a clothing factory [32].

On the other hand, Anastasovski [33] analyzed the performance of eighteen solutions for integrating solar heat in an ethanol producing industry considering

ETC and PTC technologies, considering solar radiation in typical days during the seasons of the year. The findings show that the most attractive solution is the design with ETCs coupled to a heat storage system with high pressure water during the winter solstice, since it enables replacing 35 % of the heat required and recover the investment in approximately 4.5 years.

In other study, Maillot, Castaing-Lasvignottes and Marc [34] simulated four different cases to assess the direct and indirect integration of coupling ETC collectors in the vapor generation system of a yogurt producing industry. According to the technical evaluation, the highest saving of fuel is 24 %, which is achieved when the collectors with a capturing area of 555 m<sup>2</sup> are directly integrated in the tank of the boiler.

Table 1 shows technical aspects for industrial applications, existing and at a simulation level, based on thermal systems with FPC and ETC technologies.

**Table 1.** Technical, economic and environmental aspects of the application and simulation of solar collectors with FPC and ETC technologies for industrial processes in different countries of the world

Location	Industry	Temperature industrial process (°C)	Capturing area collector (m <sup>2</sup> )	Solar fraction (%)	Savings	Source
South Africa	Production of fish flour preheating	70	384-FPC	81	32 061 liters of fuel oil	[31]
Macedonia	Production of ethanol water heating preparation of saline solutions and molasses	95	n/a-ETC	n/a	approx. 57 % of fuel oil	[33]
Reunion Island	Yogurt-vapor generation from the direct integration of the solar collector in the tank of the boiler	160-170	555-ETC	n/a	24 % of fuel	[34]
Marocco	Milk-water heating drying and cleaning of fruits, colling and pasteurization	60-90	400-ETC	41	77,23 tCO <sub>2</sub> e/year	[35]
Ethiopia	Clothes-water heating dyeing	50-90	472-ETC	56,3	252,2 tCO <sub>2</sub> e/year	[36]

In the case of CPC collectors, Milczarek *et al.* [37] experimented with the drying of tomato and plum marcs with a solar drum dryer, for which they used 26 external CPC with a capturing area of 98.3 m<sup>2</sup> that enabled heating the drum surface to a minimum temperature of 92°C. The final result demonstrated the effectiveness of solar thermal energy to achieve

stability in the storage of these fruits and vegetables. In Argentina, the CPCs have shown to be an economic and environmentally viable alternative at temperatures that oscillate between 100 y 150 °C since the leveled energy cost is between 2.5 and 16.9 euros per kWh/m<sup>2</sup>. Similarly, the ranges associated to the reduction of greenhouse gas emissions by substituting electricity

and natural gas by this solar system are between 179 and 348 kgCO<sub>2</sub>/m<sup>2</sup>·year and between 113 and 220 kgCO<sub>2</sub>/m<sup>2</sup>·year, respectively.

Table 2 shows cases about applications and simulations with PTC and LFC capturing technologies.

**Table 2.** Technical, economic and environmental aspects of the application and simulation of solar collectors with PTC and LFC technologies for industrial processes in different countries of the world

Location	Industry	Temperature industrial process (°C)	Capturing area collector (m <sup>2</sup> )	Solar fraction (%)	Savings	Source
Italy (Molina di Fiemme)	Pasta-water heating-drying of pasta	135	840-PTC	23	4,7 tCO <sub>2</sub> /week	[11]
Cyprus (Limasol)	Drinks-vapor generation-cleaning, pasteurization and sterilization	188	288-PTC	n/a	40 €/t of vapor	[38]
Switzerland (Saignelégier)	LMilk-water heating-cleaning	117	627-PTC	12	69 tCO <sub>2</sub> /year	[39]
Portugal (Santarém)	Production of agglomerated of expanded cork preheating of boiler feeding water	170	1328-PTC	36,9	76,5 tep and 201,8 tCO <sub>2</sub> e/GJ	[40]
Morocco (Rabat)	Asphalt-bitumen heating	160	n/a-PTC	40	0,75-1,5 tCO <sub>2</sub> /year/kW	[41]
Indonesia	Niquel mining vapor generation for sulfur heating	135-145	n/a-LFC	n/a	45 000 USD/year	[42]
Italy (Sicily)	Wheat pasta overhead water pasta drying	120-140	6602-LFC	40	n/a	[43]

The study by means of dynamic modeling of a solar field with PTCs, for water heating in the process of drying Italian pasta in an Italian factory, evidenced that the design of this system has the capability of guaranteeing 23 % of the weekly thermal energy demand used in this process [11]. In the work by Ghazouani, Bouya and Benaissa [15], the design and operating parameters of a small PTC were analyzed with the purpose of maximizing the thermal and economic efficiency and the energy performance under the meteorologic conditions of the city of Rabat; with the improvement of the technical features of the collector they were able to supply more than 12.84 MWh/year at a competitive smaller cost of 0.022 USD/kWh with each device.

In the case of milk industry, Biencinto *et al.* [44] proposed an innovative thermal storage system supplied by a field of PTCs to contribute to the heat demand at three different temperature levels in the pasteurization process. According to the simulation results, the use of thermal storage based on pentaglycerine (PCM) covering a range of three hours may fulfill 20-27 % and 40-52 % of the annual energy demand in the cities of Graz-Austria and Almería-Spain, respectively.

In their study conducted for the implementation of solar thermal energy in the milk industry in India, Sharma *et al.* [45] determined that through the installation of PTCs it is possible to reach a solar fraction between 16 and 33 % according to the location of each factory. However, the low cost of fossil fuels and the inability of solar systems to fulfill the total heat demand in manufacturing processes, make these investments unsecure.

May Tzuc *et al.* [46] performed an optimization model with PTCs to be integrated in the milk industry considering four different types of climates in Mexico. The research states that these collectors may fulfill a demand ranging between 40 and 80 % of the heat used in pasteurization. Similarly, the annual saving in emissions for the four climatic regions with the application of this technology oscillates between 39.5 and 95.3 tCO<sub>2</sub>.

Cortés *et al.* [47] indicated that the integration of PTCs in the food industry in Chile results technically and economically feasible, because this technology would be competitive with fossil fuels if in most of the regions of the country the installation cost of the solar

field is under 250 USD/m<sup>2</sup>.

Ktistis, Agathokleous and Kalogirou [38] demonstrated that PTCs coupled with a concrete storage system is a viable alternative to be used in the drinks industry in Cyprus, since the vapor production cost for cleaning, pasteurization and sterilization processes of the factory with this solar system is 10 €/t, as opposed to 50 €/t which is the cost of vapor generation when a conventional boiler is employed with fuel price of 700 euros per ton.

Regarding LFCs, Laadel *et al.* [48] argued that this solar collector coupled to a heat system is technically suitable for integration in Moroccan industries, since they may reach solar fraction values up to 40 % without including thermal storage. Buscemi *et al.* [43] examined the possibility of generating heat from a solar field with LFCs for pasta drying in an Italian factory. The simulation result of this solar system with concrete storage generates a solar fraction of 40 % and an investment recovery time of eight years.

There are research works about the application of solar heat which are exploring other sectors and operations, such as for example the asphalt industry for heating bitumen [41]; in management processes of industrial and residual waters [49] and in vapor generation for the pharmaceutical industry using LFCs [50].

In this context, the contribution of new research works about adjusting the design of solar collectors has enabled searching for alternatives to improve performance and reduce the leveled cost of heat for these thermal systems. For example, the innovative design of

an FPC with only one collector tube with spiral shape compared with a conventional FPC with the same area and tubes of the same diameter and length, achieves an improvement of 21.45 % in thermal efficiency when operating with a mass flow of 0.026 kg/s and 1011 W/m<sup>2</sup>; in addition, the pressure drop of the fluid is reduced with the spiral design of the tube and it is possible to save 30 % of the total of manufacturing materials [51].

An experiment conducted in Las Vegas-USA about the design of a support structure for a PTC using wood, demonstrated that the collector may have an appropriate performance for thirty years with a continuous monitoring and maintenance of the wood. The economic analysis determined that the estimated installation cost of this design was 56.14 USD/m<sup>2</sup>, which significantly reduces the leveled cost of heat for generation of vapor in the industrial process [52].

#### 4. Suppliers of solar thermal collectors

According to the Solar Payback program, 251 MW<sub>t</sub> related to solar thermal systems were installed during 2019, intended to industry worldwide, a value significantly larger than the 39 MW<sub>t</sub> installed in 2018 [53]. This program counts around 76 worldwide suppliers of solar capturing technologies, most of which produce their own systems. Table 3 presents the suppliers that had installed more than ten projects by the end of 2019, under the modality of «turnkey»

**Table 3.** Suppliers of «turnkey» solar collectors [53]

Collector	Supplier/Country	Projects	Area (m <sup>2</sup> )
FPC	Modulo Solar/Mexico	89	15 616
	Inter Solar Systems/India	22	10 400
ETC	Sunrain Solar Energy /China	72	52 970
	Linuo Paradigma/China	47	90 470
	Ritter Energie-und Umwelttechnik/Germany	29	5165
	Sunda Solar Energy/ China	16	9432
	Himin/China	15	29 627
PTC	Inventive Power/Mexico	66	10 570
	Vicot Solar Technology/China	24	22 560
	Soliterm/Germany	20	37 069
Paraboloid dish	Megawatt Solutions/India	32	16 545
Heat supply contract	Millennium Energy Industries (MEI)/Jordan	22	3611
	Solid Energy Systems/Austria	15	11 779
n/a	Casolar/Mexico	14	n/a

## 5. Costs of the technologies

In order to integrate a solar heat system in an industry, it is necessary to consider the operating temperature of the solar collector, its cost, the operating and maintenance requirements, as well as other factors related with the use of soil, the time variability of production and the price of fuels [54]. It is also necessary to know that the cost of collectors generally represents between 50 and 70 % of the solar thermal system investment [55]. Table 4 details the areal cost of the different solar capturing technologies, however, it should be taken into account that the information provided about the economic values of the devices is based on referential amounts from simulations and scientific studies.

## 6. Saving in greenhouse gases emissions

In 2018, direct emissions of CO<sub>2</sub> coming from the industry sector reached a value of 8.5 GtCO<sub>2</sub>, which represents 24 % of global emissions. The Sustainable Development Scenario proposed by IEA mentions that to reach zero net emissions in 2070, industry emissions must be reduced 1.2 % annually to reach 7.4 GtCO<sub>2</sub> in 2030 [56]. The different solar capturing technologies are an alternative to contribute to achieve this environmental goal. A study conducted in China determined that the ten industrial sectors that integrate solar capturing technologies in their productive processes may reduce approximately 98.22 million tCO<sub>2</sub> in 2020 [55].

**Table 4.** Costs of the different solar capturing technologies

Collector	Country	Cost (USD/m <sup>2</sup> )	Source
FPC	Mexico	287 *	[57]
	Chile	330-687	[54]
	Zimbabwe	220-347	[58]
ETC	Mexico	472 *	[57]
	Chile	460-817	[54]
	Zimbabwe	157-433	[58]
CPC	Spain	268-387 *	[59]
	Italy	131 *	[11]
PTC	Mexico	402 *	[57]
	Spain	393-666 *	[59]
	Chile	379-1263	[54]
	Italy	262 *	[11]
LFC	Spain	309-506 *	[59]
	Italy	199 *	[11]

\*Monetary units adjusted from euros to USD, considering an exchange rate of 1.19 USD per euro, according to the average price of the currency in the period July 2020-July 2021 [60].

On the other hand, McMillan *et al.* [61] demonstrated that in USA the PTCs combined with a sensible heat storage system using water or synthetic oil, are the technology that may be employed to fulfill the heat demand in industrial processes in most of the country; and its installation might represent an annual saving of 137 million of metric tons of CO<sub>2</sub>.

Another research evidenced that the installation of solar thermal systems in various processes of the cotton textile industry in India might reduce between 2.46 and 7.67 million tCO<sub>2</sub> annually [62]. In Europe, Kylili *et al.* [63] analyzed the emissions reducing potential associated with the installation of low temperature solar thermal systems for heating water in industries. In their study, they evaluated the pollution degree based on the phases of the life cycle of the system, and concluded that it is possible to save between 35 and 75 GJ of energy, and between 2 and 5 tCO<sub>2</sub>/kWt depending on the geographic zone.

## 7. Research challenges and opportunities

According to the literature reviewed, there is a progressive trend in the use of solar thermal energy in various industrial processes, but the real installed capacity is still small. Hereafter, some topics that may be addressed are presented, in order to promote the extensive use of solar thermal energy in industry.

- Development of new thermal collectors and storage technologies: research on new materials that improve the thermal generation efficiency and reduce the weight of collectors. In storage systems it is essential to search for alternatives with higher thermodynamic efficiency to reduce the impact of solar intermittency [64].
- Adaptability to industrial processes: the industry sector requires an innovative integration between solar collectors and process technologies that are adapted to different sectors and location of industries [64].
- Investment in R+D: The current crisis related to COVID-19 will reduce the R+D investment in the private sector, and thus the Governments of the most important economies will be in charge of promoting policies and economic support that motivate the R+D in this area [65].

## 8. Conclusions

Until 2019, the solar thermal energy incorporated in industrial processes represented an installed power of 700 MW<sub>t</sub>, being a continuously growing alternative within this economic sector.

In the industrial sector, solar thermal collectors are mainly used for water heating and vapor generation. Food industries are the ones that have mostly integrated these technologies, since most of their processes require low temperature heat. However, various studies have evaluated that solar thermal energy may be implemented in mining, textile and pharmaceutical industries, among others.

In order to integrate solar thermal technologies in industry, it should be mainly considered the thermal energy demand of the process, the production profile, the available space, the geographic location, and the type and cost of the collector.

It has been seen that the main obstacles that prevent the expansion of solar thermal technologies in the industrial market are the low cost of fossil fuels, economic thermal storage systems still being researched and nonexistent or inefficient energy policy.

## References

- [1] B. Koçak, A. I. Fernandez, and H. Paksoy, "Review on sensible thermal energy storage for industrial solar applications and sustainability aspects," *Solar Energy*, vol. 209, pp. 135–169, 2020. [Online]. Available: <https://doi.org/10.1016/j.solener.2020.08.081>
- [2] IEA. (2020) World energy balances: Overview. [Online]. Available: <https://bit.ly/3jEw90a>
- [3] S. H. Farjana, N. Huda, M. A. P. Mahmud, and R. Saidur, "Solar industrial process heating systems in operation - current ship plants and future prospects in Australia," *Renewable and Sustainable Energy Reviews*, vol. 91, pp. 409–419, 2018. [Online]. Available: <https://doi.org/10.1016/j.rser.2018.03.105>
- [4] V. Pranesh, R. Velraj, S. Christopher, and V. Kumaresan, "A 50 year review of basic and applied research in compound parabolic concentrating solar thermal collector for domestic and industrial applications," *Solar Energy*, vol. 187, pp. 293–340, 2019. [Online]. Available: <https://doi.org/10.1016/j.solener.2019.04.056>
- [5] S. H. Farjana, N. Huda, M. P. Mahmud, and R. Saidur, "Solar process heat in industrial systems - a global review," *Renewable and Sustainable Energy Reviews*, vol. 82, pp. 2270–2286, 2018. [Online]. Available: <https://doi.org/10.1016/j.rser.2017.08.065>
- [6] S. K. Verma, N. K. Gupta, and D. Rakshit, "A comprehensive analysis on advances in application of solar collectors considering design, process and working fluid parameters for solar to thermal conversion," *Solar Energy*, vol. 208, pp. 1114–1150, 2020. [Online]. Available: <https://doi.org/10.1016/j.solener.2020.08.042>
- [7] C. A. Schoeneberger, C. A. McMillan, P. Kurup, S. Akar, R. Margolis, and E. Masanet, "Solar for industrial process heat: A review of technologies, analysis approaches, and potential applications in the united states," *Energy*, vol. 206, p. 118083, 2020. [Online]. Available: <https://doi.org/10.1016/j.energy.2020.118083>
- [8] W. Weiss and M. Spörk-Dür, *Solar Heat Worldwide*. IEA Solar Heating & Cooling Programme, Austria, 2020. [Online]. Available: <https://bit.ly/2WT0yPM>
- [9] K. Ravi Kumar, N. V. V. Krishna Chaitanya, and N. Sendhil Kumar, "Solar thermal energy technologies and its applications for process heating and power generation - a review," *Journal of Cleaner Production*, vol. 282, p. 125296, 2021. [Online]. Available: <https://doi.org/10.1016/j.jclepro.2020.125296>
- [10] IEA. (2017) Renewable energy for industry. [Online]. Available: <https://bit.ly/3BGLYty>
- [11] M. Bolognese, D. Viesi, R. Bartali, and L. Crema, "Modeling study for low-carbon industrial processes integrating solar thermal technologies. a case study in the italian alps: The felicetti pasta factory," *Solar Energy*, vol. 208, pp. 548–558, 2020. [Online]. Available: <https://doi.org/10.1016/j.solener.2020.07.091>
- [12] A. Shahsavari and M. Akbari, "Potential of solar energy in developing countries for reducing energy-related emissions," *Renewable and Sustainable Energy Reviews*, vol. 90, pp. 275–291, 2018. [Online]. Available: <https://doi.org/10.1016/j.rser.2018.03.065>
- [13] A. Gautam and R. Saini, "A review on sensible heat based packed bed solar thermal energy storage system for low temperature applications," *Solar Energy*, vol. 207, pp. 937–956, 2020. [Online]. Available: <https://doi.org/10.1016/j.solener.2020.07.027>
- [14] L. Evangelisti, R. De Lieto Vollaro, and F. Asdrubali, "Latest advances on solar thermal collectors: A comprehensive review," *Renewable and Sustainable Energy Reviews*, vol. 114, p. 109318, 2019. [Online]. Available: <https://doi.org/10.1016/j.rser.2019.109318>
- [15] M. Ghazouani, M. Bouya, and M. Benaissa, "Thermo-economic and exergy analysis and optimization of small ptc col-

- lectors for solar heat integration in industrial processes,” *Renewable Energy*, vol. 152, pp. 984–998, 2020. [Online]. Available: <https://doi.org/10.1016/j.renene.2020.01.109>
- [16] S. Suman, M. K. Khan, and M. Pathak, “Performance enhancement of solar collectors - a review,” *Renewable and Sustainable Energy Reviews*, vol. 49, pp. 192–210, 2015. [Online]. Available: <https://doi.org/10.1016/j.rser.2015.04.087>
- [17] M. Imtiaz Hussain, C. Ménézo, and J.-T. Kim, “Advances in solar thermal harvesting technology based on surface solar absorption collectors: A review,” *Solar Energy Materials and Solar Cells*, vol. 187, pp. 123–139, 2018. [Online]. Available: <https://doi.org/10.1016/j.solmat.2018.07.027>
- [18] M. P. Islam and T. Morimoto, “Advances in low to medium temperature non-concentrating solar thermal technology,” *Renewable and Sustainable Energy Reviews*, vol. 82, pp. 2066–2093, 2018. [Online]. Available: <https://doi.org/10.1016/j.rser.2017.08.030>
- [19] G. Barone, A. Buonomano, C. Forzano, and A. Palombo, “Chapter 6 - solar thermal collectors,” in *Solar Hydrogen Production*, F. Calise, M. D. D’Accadia, M. Santarelli, A. Lanzini, and D. Ferrero, Eds. Academic Press, 2019, pp. 151–178. [Online]. Available: <https://doi.org/10.1016/B978-0-12-814853-2.00006-0>
- [20] A. Veera Kumar, T. Arjunan, D. Seenivasan, R. Venkatramanan, and S. Vijayan, “Thermal performance of an evacuated tube solar collector with inserted baffles for air heating applications,” *Solar Energy*, vol. 215, pp. 131–143, 2021. [Online]. Available: <https://doi.org/10.1016/j.solener.2020.12.037>
- [21] M. Aramesh and B. Shabani, “On the integration of phase change materials with evacuated tube solar thermal collectors,” *Renewable and Sustainable Energy Reviews*, vol. 132, p. 110135, 2020. [Online]. Available: <https://doi.org/10.1016/j.rser.2020.110135>
- [22] A. Shafieian, M. Khiadani, and A. Nosrati, “A review of latest developments, progress, and applications of heat pipe solar collectors,” *Renewable and Sustainable Energy Reviews*, vol. 95, pp. 273–304, 2018. [Online]. Available: <https://doi.org/10.1016/j.rser.2018.07.014>
- [23] S. A. Waghmare and N. P. Gulhane, “Design configurations and possibilities of reflector shape for solar compound parabolic collector by ray tracing simulation,” *Optik*, vol. 176, pp. 315–323, 2019. [Online]. Available: <https://doi.org/10.1016/j.ijleo.2018.09.082>
- [24] C. Jiang, L. Yu, S. Yang, K. Li, J. Wang, P. D. Lund, and Y. Zhang, “A review of the compound parabolic concentrator (cpc) with a tubular absorber,” *Energies*, vol. 13, no. 3, p. 695, 2020. [Online]. Available: <https://doi.org/10.3390/en13030695>
- [25] D. Gao, G. Gao, J. Cao, S. Zhong, X. Ren, Y. N. Dabwan, M. Hu, D. Jiao, T. H. Kwan, and G. Pei, “Experimental and numerical analysis of an efficiently optimized evacuated flat plate solar collector under medium temperature,” *Applied Energy*, vol. 269, p. 115129, 2020. [Online]. Available: <https://doi.org/10.1016/j.apenergy.2020.115129>
- [26] L. Kumar, M. Hasanuzzaman, and N. Rahim, “Global advancement of solar thermal energy technologies for industrial process heat and its future prospects: A review,” *Energy Conversion and Management*, vol. 195, pp. 885–908, 2019. [Online]. Available: <https://doi.org/10.1016/j.enconman.2019.05.081>
- [27] E. Zarza-Moya, “7 - concentrating solar thermal power,” in *A Comprehensive Guide to Solar Energy Systems*, T. M. Letcher and V. M. Fthenakis, Eds. Academic Press, 2018, pp. 127–148. [Online]. Available: <https://doi.org/10.1016/B978-0-12-811479-7.00007-5>
- [28] O. A. López-Núñez, J. A. Alfaro-Ayala, O. Jaramillo, J. Ramírez-Minguela, J. C. Castro, C. E. Damian-Ascencio, and S. Cano-Andrade, “A numerical analysis of the energy and entropy generation rate in a linear fresnel reflector using computational fluid dynamics,” *Renewable Energy*, vol. 146, pp. 1083–1100, 2020. [Online]. Available: <https://doi.org/10.1016/j.renene.2019.06.144>
- [29] D. Sakthivadivel, K. Balaji, D. Dsilva Winfred Rufuss, S. Iniyan, and L. Suganthi, “Chapter 1 - solar energy technologies: principles and applications,” in *Renewable-Energy-Driven Future*, J. Ren, Ed. Academic Press, 2021, pp. 3–42. [Online]. Available: <https://doi.org/10.1016/B978-0-12-820539-6.00001-7>
- [30] Solar Payback, *Calor Solar para la Industria*. Solar Payback. [Online]. Available: <https://bit.ly/3jJE10l>
- [31] D. Oosthuizen, N. J. Goosen, and S. Hess, “Solar thermal process heat in fishmeal production: Prospects for two south african fishmeal factories,” *Journal of Cleaner Production*, vol. 253, p. 119818, 2020. [Online]. Available: <https://doi.org/10.1016/j.jclepro.2019.119818>

- [32] A. Cetina-Quiñones, J. Xamán, A. Bassam, M. Escalante Soberanis, and I. Perez-Quintana, “Thermo-economic analysis of a flat solar collector with a phase changing material under tropical climate conditions: Residential and industrial case,” *Applied Thermal Engineering*, vol. 182, p. 116082, 2021. [Online]. Available: <https://doi.org/10.1016/j.applthermaleng.2020.116082>
- [33] A. Anastasovski, “Improvement of energy efficiency in ethanol production supported with solar thermal energy – a case study,” *Journal of Cleaner Production*, vol. 278, p. 123476, 2021. [Online]. Available: <https://doi.org/10.1016/j.jclepro.2020.123476>
- [34] C. Maillot, J. Castaing-Lasvignottes, and O. Marc, “Modelling and dynamic simulation of solar heat integration into a manufacturing process in reunion island,” *Procedia Manufacturing*, vol. 35, pp. 118–123, 2019, the 2nd International Conference on Sustainable Materials Processing and Manufacturing, SMPM 2019, 8-10 March 2019, Sun City, South Africa. [Online]. Available: <https://doi.org/10.1016/j.promfg.2019.05.013>
- [35] A. Allouhi, Y. Agrouaz, M. Benzakour Amine, S. Rehman, M. Buker, T. Kousksou, A. Jamil, and A. Benbassou, “Design optimization of a multi-temperature solar thermal heating system for an industrial process,” *Applied Energy*, vol. 206, pp. 382–392, 2017. [Online]. Available: <https://doi.org/10.1016/j.apenergy.2017.08.196>
- [36] F. B. Tilahun, R. Bhandari, and M. Mamo, “Design optimization and control approach for a solar-augmented industrial heating,” *Energy*, vol. 179, pp. 186–198, 2019. [Online]. Available: <https://doi.org/10.1016/j.energy.2019.04.142>
- [37] R. R. Milczarek, J. J. Ferry, F. S. Alleyne, C. W. Olsen, D. A. Olson, and R. Winston, “Solar thermal drum drying performance of prune and tomato pomaces,” *Food and Bioprocess Processing*, vol. 106, pp. 53–64, 2017. [Online]. Available: <https://doi.org/10.1016/j.fbp.2017.08.009>
- [38] P. K. Ktistis, R. A. Agathokleous, and S. A. Kalogirou, “Experimental performance of a parabolic trough collector system for an industrial process heat application,” *Energy*, vol. 215, p. 119288, 2021. [Online]. Available: <https://doi.org/10.1016/j.energy.2020.119288>
- [39] M. H. Rittmann-Frank, J. Möllenkamp, M. Caflisch, and A. Häberle, “Evaluation of solar process heat systems in switzerland,” *AIP Conference Proceedings*, vol. 2033, no. 1, p. 150005, 2018. [Online]. Available: <https://doi.org/10.1063/1.5067158>
- [40] A. Castro, J. a. P. Cardoso, L. F. Mendes, P. Azevedo, and J. a. F. Mendes, “Pre-heating boiler feedwater for expanded cork agglomerate production using a parabolic trough system,” *AIP Conference Proceedings*, vol. 2033, no. 1, p. 150002, 2018. [Online]. Available: <https://doi.org/10.1063/1.5067155>
- [41] M. Ghazouani, M. Bouya, M. Benaissa, K. Anoune, and M. Ghazi, “Thermal energy management optimization of solar thermal energy system based on small parabolic trough collectors for bitumen maintaining on heat process,” *Solar Energy*, vol. 211, pp. 1403–1421, 2020. [Online]. Available: <https://doi.org/10.1016/j.solener.2020.10.074>
- [42] Suyanto, R. Hantoro, A. Suharto, R. Saleh, and T. D. Reynaldi, “A review of linear fresnel reflector technology for heating sulphur liquid in nickel processing industry,” *AIP Conference Proceedings*, vol. 2088, no. 1, p. 020034, 2019. [Online]. Available: <https://doi.org/10.1063/1.509528>
- [43] A. Buscemi, D. Panno, G. Ciulla, M. Beccali, and V. Lo Brano, “Concrete thermal energy storage for linear fresnel collectors: Exploiting the south mediterranean’s solar potential for agri-food processes,” *Energy Conversion and Management*, vol. 166, pp. 719–734, 2018. [Online]. Available: <https://doi.org/10.1016/j.enconman.2018.04.075>
- [44] M. Biencinto, R. Bayón, L. González, R. Christodoulaki, and E. Rojas, “Integration of a parabolic-trough solar field with solid-solid latent storage in an industrial process with different temperature levels,” *Applied Thermal Engineering*, vol. 184, p. 116263, 2021. [Online]. Available: <https://doi.org/10.1016/j.applthermaleng.2020.116263>
- [45] A. K. Sharma, C. Sharma, S. C. Mullick, and T. C. Kandpal, “Financial viability of solar industrial process heating and cost of carbon mitigation: A case of dairy industry in india,” *Sustainable Energy Technologies and Assessments*, vol. 27, pp. 1–8, 2018. [Online]. Available: <https://doi.org/10.1016/j.seta.2018.03.007>
- [46] O. May Tzuc, A. Bassam, L. J. Ricalde, O. Jaramillo, M. F.-B. nuelos, and M. Escalante Soberanis, “Environmental-economic optimization for implementation of parabolic collectors in the industrial process heat generation: Case study of mexico,” *Journal of Cleaner Production*, vol. 242, p. 118538, 2020. [Online]. Available: <https://doi.org/10.1016/j.jclepro.2019.118538>
- [47] F. Cortés, M. Ibarra, F. Moser, I. Muñoz, A. Crespo, and C. Murray, “Techno-economical evaluation of parabolic trough collectors systems

- for steam processes in the chilean industry,” *AIP Conference Proceedings*, vol. 2033, no. 1, p. 150003, 2018. [Online]. Available: <https://doi.org/10.1063/1.5067156>
- [48] N. E. Laadel, H. Agalit, A. Mouaky, and E. G. Bennouna, “Potential of solar heat integration in medium temperature industrial processes in morocco,” *AIP Conference Proceedings*, vol. 2126, no. 1, p. 150005, 2019. [Online]. Available: <https://doi.org/10.1063/1.5117661>
- [49] C. Brunner, B. Muster-Slawitsch, A. Grubbauer, J. Koschikowski, I. Oller, C. Sattler, K. Hennecke, D. Krüger, M. Duke, and C. Ozansoy, *Solar Energy in Industrial Water and Wastewater management*. IEA Solar Heating & Cooling Programme, 2018. [Online]. Available: <https://bit.ly/3BNw9kH>
- [50] A. Frein, M. Motta, M. Berger, and C. Zahler, “Solar dsq plant for pharmaceutical industry in jordan: Modelling, monitoring and optimization,” *Solar Energy*, vol. 173, pp. 362–376, 2018. [Online]. Available: <https://doi.org/10.1016/j.solener.2018.07.072>
- [51] S. K. Verma, K. Sharma, N. K. Gupta, P. Soni, and N. Upadhyay, “Performance comparison of innovative spiral shaped solar collector design with conventional flat plate solar collector,” *Energy*, vol. 194, p. 116853, 2020. [Online]. Available: <https://doi.org/10.1016/j.energy.2019.116853>
- [52] N. R. Peralta and P. Gleckman, “The engineering design of a high-performance parabolic trough collector using lumber for the support structure,” *Solar Energy*, vol. 191, pp. 382–399, 2019. [Online]. Available: <https://doi.org/10.1016/j.solener.2019.08.038>
- [53] Solar Payback. (2019) Mapa mundial de proveedores ship. [Online]. Available: <https://bit.ly/3zRXZvJ>
- [54] G. Quiñones, C. Felbol, C. Valenzuela, J. M. Cardemil, and R. A. Escobar, “Analyzing the potential for solar thermal energy utilization in the chilean copper mining industry,” *Solar Energy*, vol. 197, pp. 292–310, 2020. [Online]. Available: <https://doi.org/10.1016/j.solener.2020.01.009>
- [55] T. jia, J. Huang, R. Li, P. He, and Y. Dai, “Status and prospect of solar heat for industrial processes in china,” *Renewable and Sustainable Energy Reviews*, vol. 90, pp. 475–489, 2018. [Online]. Available: <https://doi.org/10.1016/j.rser.2018.03.077>
- [56] IEA. (2020) Tracking industry 2020. International Energy Agency, Paris. [Online]. Available: <https://bit.ly/3neCjpU>
- [57] H. Ortega, *Energía solar térmica para procesos industriales en México. Estudio base de mercado*. Comisión Nacional para el Uso Eficiente de la Energía (CONUEE), Asociación Nacional de Energía Solar (ANES), Deutsche Gesellschaft für Internationale Zusammenarbeit (GIZ) GmbH, 2018. [Online]. Available: <https://bit.ly/3l0qa5o>
- [58] T. Hove, “A thermo-economic model for aiding solar collector choice and optimal sizing for a solar water heating system,” in *Africa-EU Renewable Energy Research and Innovation Symposium 2018 (RERIS 2018)*, M. Mpholo, D. Steuerwald, and T. Kukeera, Eds. Cham: Springer International Publishing, 2018, pp. 1–19. [Online]. Available: [https://doi.org/10.1007/978-3-319-93438-9\\_1](https://doi.org/10.1007/978-3-319-93438-9_1)
- [59] I. Lillo-Bravo, E. Pérez-Aparicio, N. Sancho-Caparrini, and M. A. Silva-Pérez, “Benefits of medium temperature solar concentration technologies as thermal energy source of industrial processes in spain,” *Energies*, vol. 11, no. 11, p. 2950, 2018. [Online]. Available: <https://doi.org/10.3390/en1112950>
- [60] BCE. (2021) Consulta por monedas extranjeras. Banco Central del Ecuador. [Online]. Available: <https://bit.ly/3h9OS2a>
- [61] C. McMillan, C. Schoeneberger, J. Zhang, P. Kurup, E. Masanet, R. Margolis, S. Meyers, M. Bannister, E. Rosenlieb, and W. Xi, *Opportunities for Solar Industrial Process Heat in the United States*. National Renewable Energy Laboratory. NREL/TP-6A20-77760, 2021. [Online]. Available: <https://bit.ly/3zYSsDG>
- [62] A. K. Sharma, C. Sharma, S. C. Mullick, and T. C. Kandpal, “Ghg mitigation potential of solar industrial process heating in producing cotton based textiles in india,” *Journal of Cleaner Production*, vol. 145, pp. 74–84, 2017. [Online]. Available: <https://doi.org/10.1016/j.jclepro.2016.12.161>
- [63] A. Kylili, P. A. Fokaides, A. Ioannides, and S. Kalogirou, “Environmental assessment of solar thermal systems for the industrial sector,” *Journal of Cleaner Production*, vol. 176, pp. 99–109, 2018. [Online]. Available: <https://doi.org/10.1016/j.jclepro.2017.12.150>
- [64] C. Brunner, B. Muster-Slawitsch, S. Meitz, and E. Frank, *Solar Heat Integrations in Industrial Processes*. IEA Solar Heating and Cooling Technology Collaboration Programme, 2020. [Online]. Available: <https://bit.ly/3BNG8qb>
- [65] IEA, *Energy Technology Perspectives 2020*. International Energy Agency, 2020. [Online]. Available: <https://bit.ly/3tqcpe8>







# DESIGN AND CONSTRUCTION OF A FRICTION WELDING EQUIPMENT WITH LASER ASSISTANCE FOR THE JOINT OF AISI 1045 STEEL AND ALUMINUM 2017-T4 SHAFTS

## DISEÑO Y CONSTRUCCIÓN DE UN EQUIPO DE SOLDADURA POR FRICCIÓN CON ASISTENCIA LÁSER PARA LA UNIÓN DE EJES DE ACERO AISI 1045 Y ALUMINIO 2017-T4

José Luis Mullo<sup>1,2</sup> , Jorge Andrés Ramos-Grez<sup>1,3</sup> ,  
 Germán Omar Barrionuevo<sup>1,\*</sup>

Received: 17-04-2021, Received after review: 12-08-2021, Accepted: 02-09-2021, Published: 01-01-2022

### Abstract

Welding metal alloys with dissimilar melting points make conventional welding processes unfeasible to be used. On the other hand, friction welding has proven to be a promising technology capable of joining materials, while preventing the temperature from exceeding the melting point. However, obtaining a welded joint with mechanical properties that are similar to the base materials remains a challenge. In the development of this work, a laser-assisted rotary friction welding equipment was designed and manufactured. A 3 HP conventional lathe was used to provide rotary movement, and a hydraulic pressure system that applies axial force through a simple effect cylinder was designed to generate friction to obtain the union between the base materials.

### Resumen

La soldadura de materiales disímiles hace que los procesos de soldadura convencional no sean factibles de ser utilizados. La soldadura por fricción, por otro lado, ha demostrado ser una tecnología prometedora capaz de unir materiales sin que la temperatura supere su punto de fusión. Sin embargo, la obtención de las propiedades mecánicas de la junta soldada con características similares a los materiales base sigue siendo un desafío. En el desarrollo de este trabajo se diseñó y fabricó un equipo de soldadura por fricción rotatoria con asistencia láser. Para proporcionar el movimiento rotatorio se empleó un torno convencional de 3 HP de potencia y para generar fricción se diseñó un sistema hidráulico de presión el cual aplica fuerza axial mediante un cilindro de simple efecto para obtener la unión entre los materiales base.

<sup>1,\*</sup>Departamento de Ingeniería Mecánica y Metalúrgica, Escuela de Ingeniería, Pontificia Universidad Católica de Chile, Av. Vicuña Mackenna 4860, Macul, Santiago, Chile. Corresponding author ✉: gobarrionuevo@uc.cl

<sup>2</sup>Carrera de Tecnología Superior en Mecánica Automotriz, Instituto Superior Tecnológico Ciudad de Valencia (ISTCV), Quevedo, Ecuador

<sup>3</sup>Centro de Investigación en Nanotecnología y Materiales Avanzados (CIEN-UC), Av. Vicuña Mackenna, 4860, Macul, Santiago, Chile.

Suggested citation: Mullo, J. L.; Ramos-Grez, J. A. and Barrionuevo, G. O. "Design and construction of a friction welding equipment with laser assistance for the joint of AISI 1045 steel and aluminum 2017-T4 shafts," *Ingenius, Revista de Ciencia y Tecnología*, N.º 27, pp. 74-84, 2022, DOI: <https://doi.org/10.17163/ings.n27.2022.07>.

In the implemented equipment, joints of AISI 1045 steel and 2017-T6 aluminum shafts were made. The welded joints were metallurgically evaluated, emphasizing on the chemical composition at the weld interface. For microstructure characterization, scanning electron microscopy (SEM), energy dispersion spectroscopy (EDS), and glow discharge optical emission spectrometry (GDOES) were used to measure the initial composition of the welded materials. The results obtained show an adequate joint between the base materials, denoting the usefulness of the equipment manufactured for the union of dissimilar materials.

**Keywords:** Steel, Aluminum, Laser, Dissimilar materials, Microstructure, Friction welding

En el equipo implementado se realizaron uniones de ejes de acero AISI 1045 con aluminio 2017-T6; las uniones soldadas se evaluaron metalúrgicamente, haciendo hincapié en la composición química en la interfaz de la soldadura. Para la caracterización de la microestructura se empleó microscopía electrónica de barrido (SEM), espectroscopía de dispersión de energía (EDS) y espectrometría de emisión óptica de descarga luminiscente (GDOES) para medir la composición inicial de los materiales que se soldaron. Los resultados obtenidos muestran una adecuada unión entre los materiales base, denotando la utilidad del equipo fabricado para la unión de materiales disímiles.

**Palabras clave:** acero, aluminio, láser, materiales disímiles, microestructura, soldadura por fricción

## 1. Introduction

The processes for joining metals have become an essential need for different industries related to metallurgy and welding. Depending on the sector, the appropriate selection of materials and procedures, together with security and quality standards, are essential aspects in the engineering industry [1]. When it is required to join materials with different characteristics, conventional fusion welding is unfeasible due to its metallurgic limitations. At present, conventional processes are not enough due to the difference between their melting points that generate intermetallic compounds of fragile features which are not beneficial at all for the welded joint [2]. Based on this issue, solid-state welding has been a promising joining process, in which two working pieces are joined under pressure, generating heat due to friction at temperatures below the melting point of the base materials [3]. Such friction welding (FW) has been an alternative solid-state joining method, since it produces a coalescence of materials under a compression force between two working pieces that rotate or move in contact producing heat and plastically displacing the material until creating a contact interface [4]. The weld metal, the flux and the protection gas are not necessary in this process, due to its simplicity. The process stated under the base of academic studies, has placed it among one of the best for the series production of joints in dissimilar materials [5]. For this reason, the FW process is used in the automotive, aeronautic, oil and electric industries, among others.

Joining steels with other materials in friction welding processes may have unexpected phase propagations, grain boundary corrosion or generation of delta and sigma ferrite phases in the welding interface. Therefore, some precautions have been considered, such as determining the variables with respect to thermal treatments, increasing welding velocity, because in this manner it will be achieved a certain homogeneity in the temperature distribution in the two components [6]. Under this context, obtaining welded joints with appropriate mechanical and metallurgic properties would contribute to the increasing interest in a broad range of industrial applications. Manufacturing components in the transportation and aeronautic industry, require welded cylindrical elements with good mechanical properties, low specific weight and good resistance to corrosion. Concretely, introducing steel and aluminum pieces in rotating systems and in steel structures require the development of reliable, efficient and economic joining processes. Through the application of a laser beam it might be possible to optimize the welding quality in a conventional FW process. Li, Yu, Li, Zhang and Wang [7] state that, during the conventional FW process, heat generation is mainly determined by the rotation speed, the friction pressure and the friction time. Thus, heating energy is very

limited, especially for welding slim axes.

The weld joint of the rotary friction welding process is the most important part and must be analyzed, characterized by a narrow heat affected zone (HAZ), presence of plastically deformed material around the welding (flash) and absence of a melted zone. Taban, Gould and Lippold [8] made joints between shafts of a 6061-T6 aluminum and AISI 1018 steel alloy, using rotational speeds up to 4200 rpm, friction pressure of 23 MPa, friction time of 1 s, forging times of 5 s and forging pressure of 60 MPa. Results showed a tensile strength of 250 MPa with failures in the plastic zone due to the existence of an interface with Al-Fe intermetallic compound, with a thickness of 250 nm related to the  $Fe_2Al_5$  phases that are formed at temperatures above 1200 °C [9]. Handa and Chawla [10] adapted a conventional lathe with a pressure and brake system to create a RFW machine. The authors found that the maximum tensile strength and the impact resistance are acceptable at a rotational speed of 1250 rpm with an axial pressure of 120 MPa, for AISI 1021 steel welded joints with a diameter of 20 mm. On the other hand, Luo *et al.* [11] developed a method for joining a shock absorber and its rod, with the purpose of reducing the welding burrs. In this way they determined that, with an appropriate selection of parameters, the friction welding process is very effective for this type of applications, as opposed to conventional methods, because the obtained microstructure shows more uniform grains in the absence of phase change, which does not happen under fusion welding processes.

The main advantages of the CDFW process are the material saving, the short production time and the possibility of welding dissimilar materials. At present it is used for manufacturing elements in the automotive industry such as valves, gears, half shafts, turbo fan shafts, connections, pistons, etc. Ferrous and non-ferrous alloys are used to manufacture such elements [12]. Due to its versatility, friction welding has a generalized industrial use as a mass production process for joining materials [5]. However, to make dissimilar joints, the FW process requires alternative preheating methods with the purpose of providing better properties to the welded materials. For this reason, a rotary friction welding equipment was built during the development of this work, in which a preheating through laser is also applied to accelerate the process and improve coupling between base materials.

The operating principle for this experiment is illustrated in Figure 1, which describes the stages of the laser-assisted experiment in its design stage. In the development carried out,  $\omega$  represents the rotational velocity in the left end,  $F_1$  the friction force and  $F_2$  the forging force. For this configuration, a laser beam acts on one of the materials, increasing its temperature before the rotary friction welding (RFW) process starts.

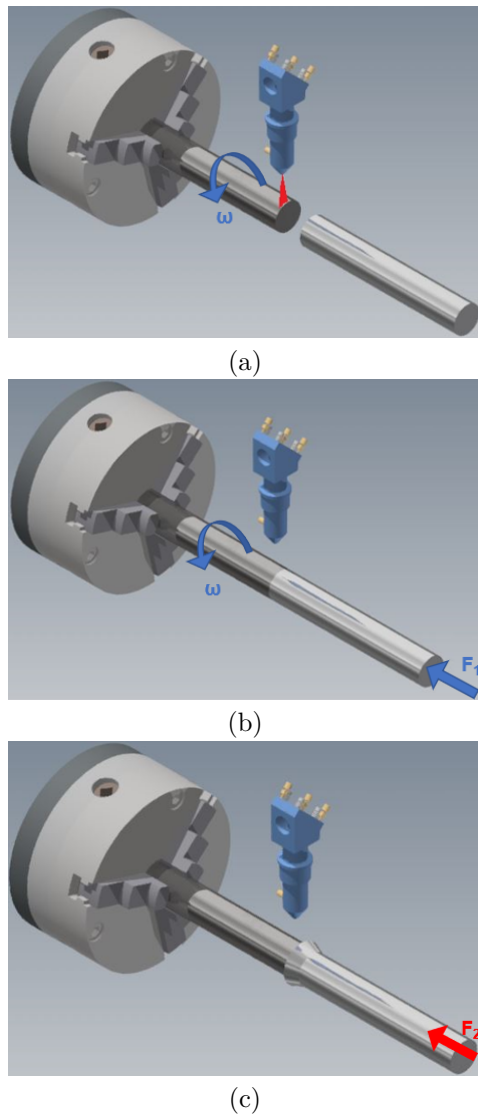


**Figure 1.** Stages of the laser-assisted friction welding process. a) Rotation of the steel shaft and laser activation. b) End of the laser application and start of the friction process through the application of the  $F_1$  force. c) Suspension of the rotation and application of the forging axial force [13]

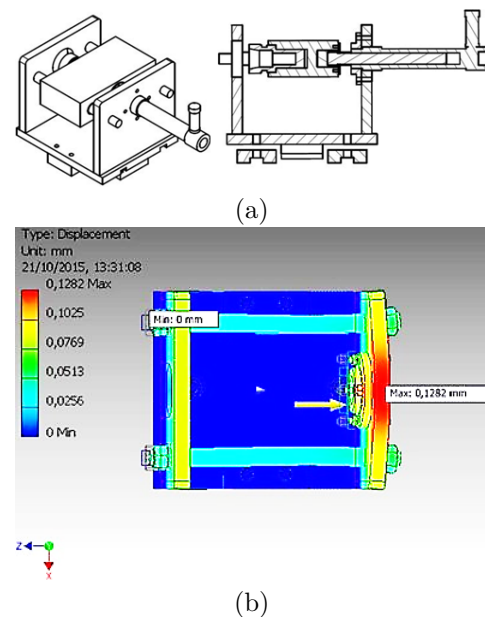
## 2. Materials and methods

An extensive literature review was conducted for the design process, identifying publications that present rotary friction welding known as Continuous drive friction welding [14–19]. Two essential mechanisms are identified in this process: one of rotation and another one of pressure. To move the shaft, it has been chosen a 3 HP conventional lathe, with a rotational velocity of 2000 rpm and a distance of 1000 mm between centers. Whereas for the friction and forging system, it was designed a hydraulically operated pressure system which enables making the friction joints at various pressure levels. The pressure mechanism consists of a hydraulic

system with a capacity of 5 tons, driven by a 300 c.c. hydraulic pump. The pressure mechanism also has a manometer that enables visualizing the friction and forging pressures.

For designing the pressure mechanism (Figure 2), a pressure counterpoint was coupled to the lathe, the design was carried out in the 3D Autodesk Inventor design software. Materials were used according to the stress degree to be withstood in the welding process. The structure of the device is built in AISI 1020 steel, while AISI 1045 and AISI 4120 steels were used for the parts that will receive a higher stress such as the nozzle fitting, the vibration damping block and the mounting flange, respectively. Figure 2a shows the designed engineering (CAE), the parts of the system were subject to a 1000 kg force to verify the maximum stress and its deformation in the shafts. The maximum deformation on the X axis, with a value of 0.1282 mm, may be observed in Figure 2b; this value is acceptable for the weld joints to be concentric and of quality.

For hydraulic design it was considered that the maximum force between test tubes is 1000 kg, according to the research conducted in [20]. The force established will enable making welding in steel or aluminum shafts with diameters up to 20 mm. An experimental test was conducted using a universal compression test machine to determine the hydraulic pressure. Applying pressure with the hydraulic piston and measuring the maximum force attained, it is obtained a pressure value that enables establishing the capacities of the system. Table 1 presents a pressure analysis for each pressure value in the cylinder.

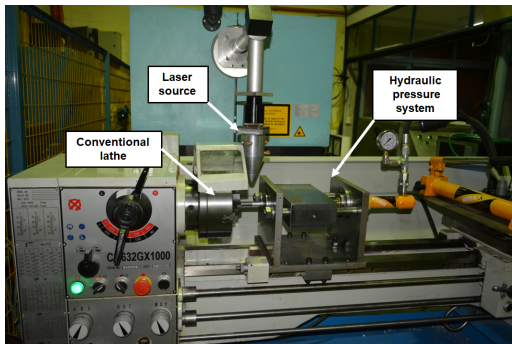


**Figure 2.** Design of the hydraulic pressure system, a) Computer assisted design, b) simulation of the maximum displacement

**Table 1.** Test pressures

Cylinder pressure (MPa)	Forced applied (kg)	Displacement (mm)
25,4	254	0,93
52	520	1,27
100	1000	1,79
149,9	1499	2,21
200,4	2004	2,62
624,4	6244	5.17

A CO<sub>2</sub> laser equipment (Oerlikon OPL3500) with a power of 3.5 kW, a wavelength of 10.6 μm and TEM00 (Figure 3) was used as heat source. Preheating is applied using this equipment so that the joint between the base materials is more efficient according to the results reported in the literature [21–27].

**Figure 3.** Laser-assisted friction welding (LAFW) equipment

The friction welding process was made on AISI 1045 shafts and 2017-T4 aluminum shafts, each with a diameter of 15 mm and a length of 180 mm. The nominal chemical compositions of the base materials are shown in Table 2. The mechanical properties of the base materials are presented in Table 3.

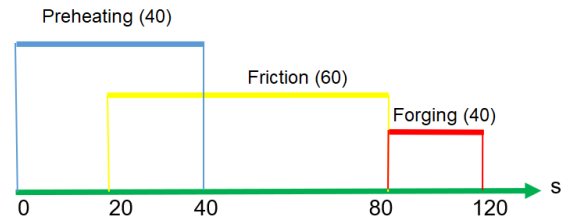
**Table 2.** Chemical composition of the base materials

Material	Elements (wt %)			
	Fe	C	Mn	Si
AISI 1045	98.41	0.40	0.72	0.22
	Cu	Al	P	S
	0.13	0.02	0.01	0.01
AA 2017	Al	Cu	Mg	Mn
	92.92	4.25	1.58	0.84
	Fe	Zn	Cr	Si
	0.34	0.04	0.01	0.002

**Table 3.** Mechanical properties of the base materials

Material	Shear stress (MPa)	Creep stress (MPa)	Hardness (HV)
AISI 1045	617-680	330-392	260-330
AA 2017	370-420	215-260	105-120

The joining process consists of preheating the steel shaft for 40 seconds; the friction process starts when a rotational velocity between 1600 and 1800 rpm is reached, then the axial friction pressure is applied (14/21 MPa) through the hydraulic mechanism for 60 seconds, until achieving the forging. At last, a forging pressure (42.1 MPa) was applied for 40 seconds. These constant parameter values were chosen after various preliminary tests, in which it was found that these were the optimal values with respect to the capacity of the hardware used (Figure 4).

**Figure 4.** Parameters of the welding process

Where, for the time of laser preheating the pressure,  $P = 0$  MPa. Afterwards for the friction time, the friction pressure  $P_f = 14$  and 21 MPa. At last, at forging time the forging pressure increases to  $P_u = 42.1$  MPa.

For macro and microstructural evaluation, 12 specimens obtained with the laser-assisted welding process were analyzed. The cross sections of the welded joints were subject to a metallographic preparation of coarse polishing with 200, 400, 600, 800 sandpapers, up to a grain sandpaper 1000 according to the ASTM E407 standard. It was applied a fine polishing using alumina with an average grain diameter of 0.04 μm and a diamond paste abrasive with a diameter of 0.01 μm to prevent irregularities on the sample surface. The equipment used to observe the microstructure is a MEIJI microscope model IM 7200 with an amplification up to 100x, 500x y 1000x.

With the purpose of visualizing the phases present and the grain size, a chemical attack was carried out on the steel through immersion for 10 seconds in a Nital solution (alcohol at 95 % and HNO<sub>3</sub> nitric acid in 5 ml). For the aluminum component, a swab was impregnated for 15 seconds with a hydrofluoric acid solution (1 ml of hydrogen fluoride HF and 200 ml of H<sub>2</sub>O). The measurement of the grain size was carried out according to the ASTM E112 standard using the

intercept method for all cases. At last, a comparison was made between the conventional FW process and the LAFW process developed by the authors.

### 3. Results and discussion

During the welding process it is observed the application of the laser to the steel, and after the application of friction and forging a flash is formed around the aluminum shaft (Figure 5). The formation of the flash is mainly influenced by the characteristics of the material added to the friction pressure, which produces a more significant deformation, causing a larger effect of the flash due to the higher mechanical pressure [20].

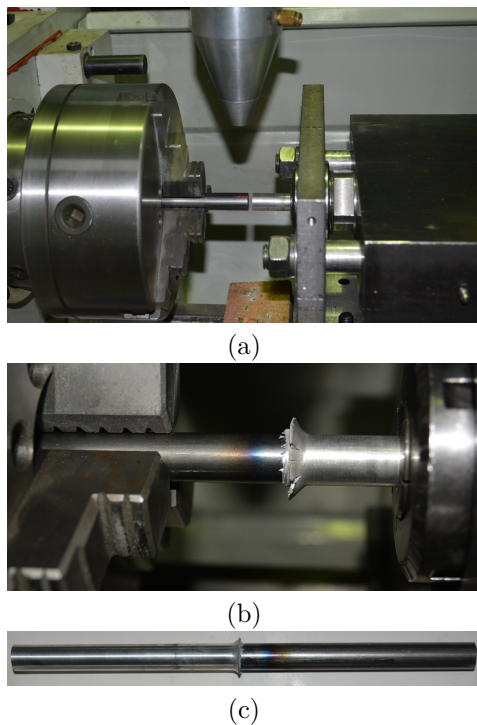


**Figure 5.** Welding process. a) Application of the laser on the steel shaft. b) Formation of the flash in the aluminum shaft. c) Welded test tube

In general, the aspect of the welded joint for the conditions established is symmetrical, the friction pressure mainly has influence on a flash effect that generally occurs in the aluminum side [8]. A larger mechanical pressure leads to a greater deformation of the material which in turn produces a larger flash effect (Figure 6).



**Figure 6.** Welded test tubes, where it may be observed different configurations of the flash on the aluminum shaft

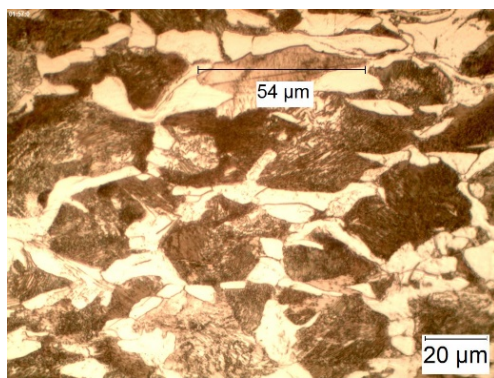
The joint between aluminum and steel starts from the outer region and moves towards the center. The joint shown in Figure 7a presents a homogeneous joint, due to the additional heat supplied by the laser which promotes the homogenization of the material enabling the fusion of both materials [14]. To determine the quality of the joint it is necessary to analyze the microstructure through the chemical attack, to verify the deformation of the aluminum in the steel (Figure 7b).



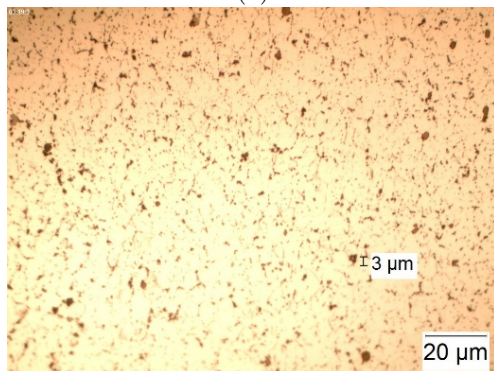
**Figure 7.** Cross section – Micrograph of the steel-aluminum joint 500x

For steel-aluminum joints produced through friction welding, it is known that there are four zones defined from the ends towards the center: non-deformed zone (NDZ), heat affected zone (HAZ), thermo-mechanically affected zone (TMAZ) and Fe-Al reaction

or interface layer. In the case of the steel, the NDZ presents a matrix constituted by approximately 39.36 % of ferrite and 60.64 % of perlite. The matrix has a 0.45 % of carbon and an ASTM 6 grain size, which corresponds to an AISI 1045 steel (Figure 8a). The HAZ shows a light grain refinement, similar to the ones obtained in [28]. The most critical microstructure zone is the TMAZ, which is characterized by a greater grain refinement, because there is a temperature increase and fast cooling. With respect to the aluminum, the NDZ presents a matrix constituted by approximately 93.85 % of aluminum and 6.15 % of copper. The matrix has an ASTM 10 grain size which corresponds to an AA 2017 aluminum (Figure 8b).



(a)



(b)

**Figure 8.** Optical microscopy at 10000x of the thermo mechanically affected zone a) Steel. b) Aluminum

The HAZ presents a grain refinement similar to the ones obtained in [29]. There is a greater thermo-mechanical deformation due to the fusion by friction since it is a material with a lower melting point than steel.

With respect to the laser-assisted TMAZ, it was analyzed at an amplification of 1000x as described in Figure 8a, and in Table 4 it may be observed the 53.31 % of the perlite matrix, and it also appears 46.49 % of non-circular ferrite due to the heating and fast cooling produced by friction pressure and laser assistance. The grain size is ASTM 6, with an average dimension of approximately 54 microns calculated through the intercept method. In Figure 8b there is a 94.56 % of

aluminum and 5.44 % of copper. There is grain size of ASTM 9 and a maximum diameter of three microns.

**Table 4.** Phases and elements present in the base materials

AISI 1045		
Perlite area	1 020 967,40	$\mu\text{m}^2$
Ferrite area	887 088,60	$\mu\text{m}^2$
Perlite %	53,51%	
Ferrite %	46,49%	
Total area	1 908 056	$\mu\text{m}^2$
AA 2017-T4		
Copper area	103 810,60	$\mu\text{m}^2$
Aluminum area	1 804 245,40	$\mu\text{m}^2$
Copper %	5,44%	
Aluminum %	94,56%	
Total area	1 908 056	$\mu\text{m}^2$

Figure 9 shows the analysis points for determining the chemical composition of each material by means of glow discharge optical emission spectrometry (GDOES), aluminum to the left and steel to the right, In the center there is the weld interface (point 3). The results obtained are presented in Table 5. It is clearly distinguished the larger concentration of aluminum (Al) around 82 %, copper (Cu) about 9 % and manganese (Mn) above 5 % for the 2017-T4 alloy. For the 1045 steel there is an iron (Fe) concentration greater than 97 %. Whereas in the interface the chemical composition is redistributed in 62 % Fe and 33 % Al, with smaller content of Cu and Mn.

To complement the microstructure analysis, Figure 10 shows an elementary mapping by means of energy dispersive spectroscopy (EDS). It may be observed the variation in the content of elements along the weld interface. In the upper part there is Fe at a greater concentration, identified by the red color corresponding to the 1045 steel alloy. In the lower part it is distinguished the Al in yellow color corresponding to the 2017-T4 alloy. It is also possible to distinguish a high concentration of Cu in the lower part and silicon (Si) to a lesser extent, in both the steel alloy and in the aluminum.

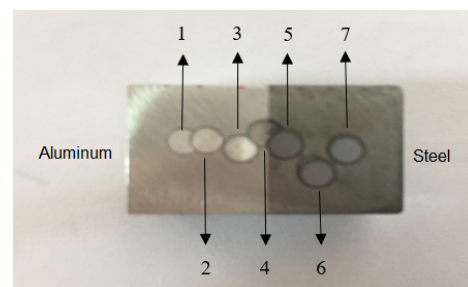


**Figure 9.** Glow discharge optical emission spectrometry, analysis points to determine elementary chemical composition

**Table 5.** Measurement of the chemical composition by means of GDOES at the points indicated

Point	Fe [%]	C [%]	Mn [%]	Si [%]	P [%]	S [%]	Ni [%]	Cu [%]	Al [%]	Zn [%]
1	0,78	0,131	5,671	0,184	0,321	0,6831	0,153	8,973	<b>81,891</b>	0,298
2	0,78	0,133	5,588	0,188	0,3017	0,7894	0,153	8,895	<b>81,971</b>	0,294
3	0,73	0,124	5,513	0,173	0,3363	0,8181	0,183	9,08	<b>81,851</b>	0,277
4	61,93	0,063	1,079	0,222	0,0465	0,0148	0,128	3,228	32,786	0,094
5	<b>97,84</b>	0,131	0,849	0,185	0,0138	0,0102	0,185	0,504	0,019	0,007
6	<b>97,88</b>	0,134	0,828	0,18	0,0134	0,0097	0,181	0,494	0,018	0,009
7	<b>97,87</b>	0,133	0,833	0,182	0,0128	0,0097	0,181	0,505	0,013	0,006

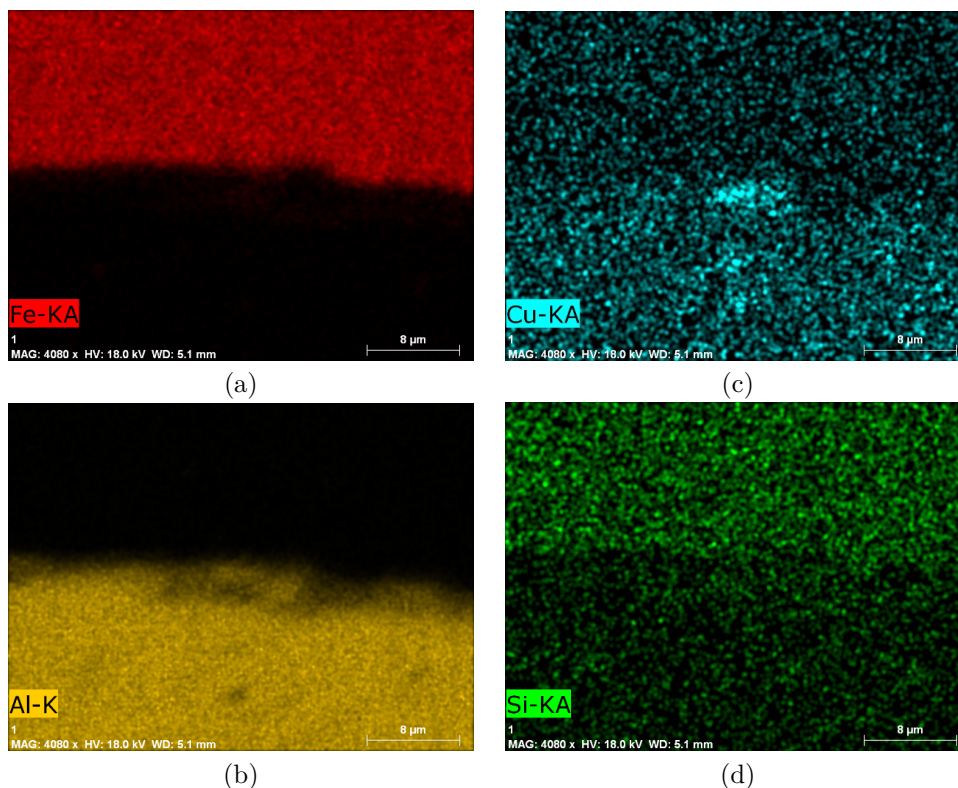


**Figure 10.** Energy dispersive spectroscopy (EDS) – Elementary mapping

#### 4. Conclusions

A laser-assisted friction welding system was developed, where it may be controlled the rotational speed of the system through a frequency drive. The optimum speed chosen through experimental tests corresponds to a range between 1600 and 1800 rpm.

The developed hydraulic pressure system is capable of providing an axial force above 9800 N, enabling to make welding in steel-aluminum shafts with diameters up to 20 mm. The pressure range to generate friction and accelerate the welding process is in the range from 14 to 21 MPa.

The application of the laser beam on the steel shaft enables homogenizing the microstructure, which in

turn accelerates the welding process so that there is a larger weld interface between the steel and aluminum shafts, which have been verified in the microstructure analyses.

It was determined the grain size for each element, for the steel an average grain of ASTM 8 with a maximum diameter of 6 microns. For the aluminum, there is a grain size of ASTM 9 and a maximum diameter of 3 microns.

In the weld interface it was determined a decrease in iron (Fe) and aluminum (Al). The Fe decreases from 97.8 % to 61.9 %, whereas the aluminum goes from 81.9 % to 32,8 %. It could be also determined the existence of manganese, copper and silicon in smaller proportion than the base materials.

## References

- [1] A. Handa and V. Chawla, “Experimental evaluation of mechanical properties of friction welded dissimilar steels under varying axial pressures,” *Strojnícky časopis - Journal of Mechanical Engineering*, vol. 66, no. 1, pp. 27–36, 2016. [Online]. Available: <https://doi.org/10.1515/scjme-2016-0008>
- [2] S. D. Meshram, T. Mohandas, and G. M. Reddy, “Friction welding of dissimilar pure metals,” *Journal of Materials Processing Technology*, vol. 184, no. 1, pp. 330–337, 2007. [Online]. Available: <https://doi.org/10.1016/j.jmatprotec.2006.11.123>
- [3] W. Cai, G. Daehn, A. Vivek, J. Li, H. Khan, R. S. Mishra, and M. Komarasamy, “A State-of-the-Art Review on Solid-State Metal Joining,” *Journal of Manufacturing Science and Engineering*, vol. 141, no. 3, p. 031012, 01 2019, 031012. [Online]. Available: <https://doi.org/10.1115/1.4041182>
- [4] P. Sathiya, S. Aravindan, and A. Noorul Haq, “Effect of friction welding parameters on mechanical and metallurgical properties of ferritic stainless steel,” *The International Journal of Advanced Manufacturing Technology*, vol. 31, no. 11, pp. 1076–1082, Feb. 2007. [Online]. Available: <https://doi.org/10.1007/s00170-005-0285-5>
- [5] A. Hascalik and N. Orhan, “Effect of particle size on the friction welding of Al<sub>2</sub>O<sub>3</sub> reinforced 6160 Al alloy composite and SAE 1020 steel,” *Materials and Design*, vol. 28, no. 1, pp. 313–317, 2007. [Online]. Available: <https://doi.org/10.1016/j.matdes.2005.06.001>
- [6] N. Ozdemir, F. Sarsilmaz, and A. Hascalik, “Effect of rotational speed on the interface properties of friction-welded AISI 304L to 4340 steel,” *Materials and Design*, vol. 28, no. 1, pp. 301–307, 2007. [Online]. Available: <http://dx.doi.org/10.1016/j.matdes.2005.06.011>
- [7] W.-Y. Li, M. Yu, J. Li, G. Zhang, and S. Wang, “Characterizations of 21-4N to 4Cr<sub>9</sub>Si<sub>2</sub> stainless steel dissimilar joint bonded by electric-resistance-heat-aided friction welding,” *Materials and Design*, vol. 30, no. 10, pp. 4230–4235, 2009. [Online]. Available: <https://doi.org/10.1016/j.matdes.2009.04.032>
- [8] E. Taban, J. E. Gould, and J. C. Lippold, “Dissimilar friction welding of 6061-t6 aluminum and aisi 1018 steel: Properties and microstructural characterization,” *Materials and Design (1980-2015)*, vol. 31, no. 5, pp. 2305–2311, 2010. [Online]. Available: <https://doi.org/10.1016/j.matdes.2009.12.010>
- [9] S. Fukumoto, H. Tsubakino, K. Okita, M. Aritoshi, and T. Tomita, “Amorphization by friction welding between 5052 aluminum alloy and 304 stainless steel,” *Scripta Materialia*, vol. 42, no. 8, pp. 807–812, 2000. [Online]. Available: [https://doi.org/10.1016/S1359-6462\(00\)00299-2](https://doi.org/10.1016/S1359-6462(00)00299-2)
- [10] A. M. I. T. HANDA and V. I. K. A. S. CHAWLA, “Experimental study of mechanical properties of friction welded aisi 1021 steels,” *Sadhana*, vol. 38, no. 6, pp. 1407–1419, Dec. 2013. [Online]. Available: <https://doi.org/10.1007/s12046-013-0181-x>
- [11] J. Luo, Y. H. Ye, J. J. Xu, J. Y. Luo, S. M. Chen, X. C. Wang, and K. W. Liu, “A new mixed-integrated approach to control welded flashes forming process of damping-tube-gland in continuous drive friction welding,” *Materials and Design*, vol. 30, no. 2, pp. 353–358, 2009. [Online]. Available: <https://doi.org/10.1016/j.matdes.2008.04.075>
- [12] S. Celik and I. Ersozlu, “Investigation of the mechanical properties and microstructure of friction welded joints between AISI 4140 and AISI 1050 steels,” *Materials & Design*, vol. 30, no. 4, pp. 970–976, 2009. [Online]. Available: <https://doi.org/10.1016/j.matdes.2008.06.070>
- [13] J. L. Mullo, J. A. Ramos-Grez, and G. O. Barrionuevo, “Effect of laser heat treatment on the mechanical performance and microstructural evolution of AISI 1045 steel-2017-T4 aluminum alloy joints during rotary friction welding,” *Journal of Materials Engineering and Performance*, vol. 30, no. 4, pp. 2617–2631, Apr. 2021. [Online]. Available: <https://doi.org/10.1007/s11665-021-05614-6>
- [14] G. L. Wang, J. L. Li, W. L. Wang, J. T. Xiong, and F. S. Zhang, “Rotary friction welding on dissimilar metals of aluminum and brass by using pre-heating method,” *The International Journal of Advanced Manufacturing Technology*, vol. 99, no. 5, pp. 1293–1300, Nov. 2018. [Online]. Available: <https://doi.org/10.1007/s00170-018-2572-y>
- [15] S. Celik and I. Ersozlu, “Investigation of the mechanical properties and microstructure of friction welded joints between AISI 4140 and AISI 1050 steels,” *Materials and Design*, vol. 30, no. 4, pp. 970–976, 2009. [Online]. Available: <https://doi.org/10.1016/j.matdes.2008.06.070>
- [16] W. Li, A. Vairis, M. Preuss, and T. Ma, “Linear and rotary friction welding review,” *International Materials Reviews*, vol. 61, no. 2, pp. 71–100, 2016. [Online]. Available: <https://doi.org/10.1080/09506608.2015.1109214>

- [17] P. Ferro, Y. Wei, and F. Sun, "Microstructures and mechanical properties of Al/Fe and Cu/Fe joints by continuous drive friction welding," *Advances in Materials Science and Engineering*, vol. 2018, p. 2809356, Jun. 2018. [Online]. Available: <https://doi.org/10.1155/2018/2809356>
- [18] O. D. Hincapié, J. A. Salazar, J. J. Restrepo, J. A. Graciano-Uribe, and E. A. Torres, "Weldability of aluminum-steel joints using continuous drive friction welding process, without the presence of intermetallic compounds," *Engineering Journal*, vol. 24, no. 1, pp. 129–144, 2020. [Online]. Available: <https://doi.org/10.4186/ej.2020.24.1.129>
- [19] X. Li, J. Li, F. Jin, J. Xiong, and F. Zhang, "Effect of rotation speed on friction behavior of rotary friction welding of aa6061-t6 aluminum alloy," *Welding in the World*, vol. 62, no. 5, pp. 923–930, Sep. 2018. [Online]. Available: <https://doi.org/10.1007/s40194-018-0601-y>
- [20] E. Taban, J. E. Gould, and J. C. Lipold, "Dissimilar friction welding of 6061-t6 aluminum and aisi 1018 steel: Properties and microstructural characterization," *Materials and Design (1980-2015)*, vol. 31, no. 5, pp. 2305–2311, 2010. [Online]. Available: <https://doi.org/10.1016/j.matdes.2009.12.010>
- [21] X. Fei, X. Jin, N. Peng, Y. Ye, S. Wu, and H. Dai, "Effects of filling material and laser power on the formation of intermetallic compounds during laser-assisted friction stir butt welding of steel and aluminum alloys," *Applied Physics A*, vol. 122, no. 11, p. 936, Oct. 2016. [Online]. Available: <https://doi.org/10.1007/s00339-016-0462-4>
- [22] T. Wada, Y. Morisada, Y. Sun, H. Fujii, Y. Kawahito, M. Matsushita, and R. Ikeda, "Friction stir welding of medium carbon steel with laser-preheating," *ISIJ International*, vol. 60, no. 1, pp. 153–159, 2020. [Online]. Available: <https://doi.org/10.2355/isijinternational.ISIJINT-2019-394>
- [23] X. Fei, J. Li, W. Yao, and L. Jin, "Study of temperature on microstructure and mechanical properties on fe/al joint in laser-assisted friction stir welding," *AIP Advances*, vol. 8, no. 7, p. 075214, 2018. [Online]. Available: <https://doi.org/10.1063/1.5039417>
- [24] M. Kutsuna, N. Yamagami, M. J. Rathod, and H. Y. A. Ammar, "Laser roll welding for joining of low-carbon steels to aluminium alloys," *Welding International*, vol. 20, no. 6, pp. 446–456, 2006. [Online]. Available: <https://doi.org/10.1533/wint.2006.3599>
- [25] Q. Guan, J. Long, P. Yu, S. Jiang, W. Huang, and J. Zhou, "Effect of steel to aluminum laser welding parameters on mechanical properties of weld beads," *Optics and Laser Technology*, vol. 111, pp. 387–394, 2019. [Online]. Available: <https://doi.org/10.1016/j.optlastec.2018.09.060>
- [26] S. L. Campanelli, G. Casalino, C. Casavola, and V. Moramarco, "Analysis and comparison of friction stir welding and laser assisted friction stir welding of aluminum alloy," *Materials (Basel, Switzerland)*, vol. 6, pp. 5923–5941, Dec 2013. [Online]. Available: <https://doi.org/10.3390/ma6125923>
- [27] M. Merklein and A. Giera, "Laser assisted friction stir welding of drawable steel-aluminium tailored hybrids," *International Journal of Material Forming*, vol. 1, no. 1, pp. 1299–1302, Apr. 2008. [Online]. Available: <https://doi.org/10.1007/s12289-008-0141-x>
- [28] M. Yilmaz, M. Çöl, and M. Acet, "Interface properties of aluminum/steel friction-welded components," *Materials Characterization*, vol. 49, no. 5, pp. 421–429, 2002. [Online]. Available: [https://doi.org/10.1016/S1044-5803\(03\)00051-2](https://doi.org/10.1016/S1044-5803(03)00051-2)
- [29] N. R. J. Hynes, P. Nagaraj, and J. A. J. Sujana, "Investigation on joining of aluminum and mild steel by friction stud welding," *Materials and Manufacturing Processes*, vol. 27, no. 12, pp. 1409–1413, 2012. [Online]. Available: <https://doi.org/10.1080/10426914.2012.667894>





# PEDESTRIAN DETECTION AT DAYTIME AND NIGHTTIME CONDITIONS BASED ON YOLO-v5

## DETECCIÓN DE PEATONES EN EL DÍA Y EN LA NOCHE USANDO YOLO-v5

Bryan Montenegro<sup>1,3</sup> , Marco Flores-Calero<sup>2,3,\*</sup> 

Received: 13-05-2021, Received after review: 12-08-2021, Accepted: 13-09-2021, Published: 01-01-2022

### Abstract

This paper presents new algorithm based on deep learning for daytime and nighttime pedestrian detection, named multispectral, focused on vehicular safety applications. The proposal is based on YOLO-v5, and consists of the construction of two subnetworks that focus on working with color (RGB) and thermal (IR) images, respectively. Then the information is merged, through a merging subnetwork that integrates RGB and IR networks to obtain a pedestrian detector. Experiments aimed at verifying the quality of the proposal were conducted using several public pedestrian databases for detecting pedestrians at daytime and nighttime. The main results according to the mAP metric, setting an IoU of 0.5 were: 96.6 % on the INRIA database, 89.2 % on CVC09, 90.5 % on LSIFIR, 56 % on FLIR-ADAS, 79.8 % on CVC14, 72.3 % on Nightowls and 53.3 % on KAIST.

**Keywords:** Infrared, color, multispectral, pedestrian, deep learning, YOLO-v5

### Resumen

En este artículo se presenta un nuevo algoritmo basado en aprendizaje profundo para la detección de peatones en el día y en la noche, denominada multispectral, enfocado en aplicaciones de seguridad vehicular. La propuesta se basa en YOLO-v5, y consiste en la construcción de dos subredes que se enfocan en trabajar sobre las imágenes en color (RGB) y térmicas (IR), respectivamente. Luego se fusiona la información, a través, de una subred de fusión que integra las redes RGB e IR, para llegar a un detector de peatones. Los experimentos, destinados a verificar la calidad de la propuesta, fueron desarrollados usando distintas bases de datos públicas de peatones destinadas a su detección en el día y en la noche. Los principales resultados en función de la métrica mAP, estableciendo un IoU en 0.5 son 96.6 % sobre la base de datos INRIA, 89.2 % sobre CVC09, 90.5 % en LSIFIR, 56 % sobre FLIR-ADAS, 79.8 % para CVC14, 72.3 % sobre Nightowls y KAIST un 53.3 %.

**Palabras clave:** infrarrojo, color, multispectral, peatones, aprendizaje profundo, YOLO-v5

<sup>1</sup>Ingeniería en Electrónica, Automatización y Control, Universidad de las Fuerzas Armadas ESPE, Av. Gral. Rumiñahui s/n, PBX 171-5-231B, Sangolquí (Pichincha), Ecuador.

<sup>2</sup>Departamento de Eléctrica, Electrónica y Telecomunicaciones, Universidad de las Fuerzas Armadas ESPE, Av. Gral. Rumiñahui s/n, PBX 171-5-231B, Sangolquí (Pichincha), Ecuador.

<sup>3,\*</sup>Departamento de Sistemas Inteligentes I&H Tech. Corresponding author ✉: mjflores@espe.edu.ec.

Suggested citation: Montenegro, B. and Flores-Calero, M. "Pedestrian detection at daytime and nighttime conditions based on YOLO-v5," *Ingenius, Revista de Ciencia y Tecnología*, N.º 27, pp. 85-95, 2022, DOI: <https://doi.org/10.17163/ings.n27.2022.08>.

## 1. Introduction

At present, car accidents are a public health problem worldwide, since they cause a high number of victims and injured, medical treatment costs, rehabilitation, psychological disorders, personal and property insurance, they consume resources that might be aimed at other health areas [1], where pedestrians are exposed to a high accident rate, reaching up to 22 % of the cases [2]. Many of these misfortunes may be prevented, because they are generated by the risky, negligent and irresponsible action of drivers and/or the pedestrians themselves [3]. In the case of Ecuador, run overs represent more than 10 % of the deaths due to car accidents.

In this scenario, pedestrian detection systems (PDS) are one of the most important technological components to prevent possible dangerous situations and reduce run overs. Therefore, pedestrian detection is an active and interesting research topic, due to the challenges that must be overcome when working in uncontrolled environments and with limited sensors in the perception of the road scene.

In the case of atmospheric conditions, excessive sun, rains, or mist change lighting conditions, and to make matters worse, the night magnifies these risk factors due to the absence of natural light [4–6]. With respect to pedestrians, they use different types of clothes, in different colors, change the body posture and may be at any position of the road scene. Regarding the information captured by the camera, it is generally incomplete due to the reduced field of vision of the sensor, the distance that separates the pedestrian from the camera reduces the resolution of the captured image. The movement and vibration of the vehicle generate distortion of the image. In addition, the geometry of the road has direct influence on the quality of the information captured by the camera [5], [7].

Fortunately, at present there are public databases specialized in pedestrian detection, at daytime or nighttime, together or separate, in the context of intelligent and autonomous vehicles, which may be used for the experimental part [8–10].

Thus, the main objective of this work is the implementation of a new deep learning (DL) architecture based on YOLO-v5 [4], [11–15], to obtain a cutting-edge system specialized in pedestrian detection at nighttime and/or daytime, using visual information in the range of visible and infrared light, that generates results comparable to the existing ones in the state of the art.

The content of this document is organized as follows: section 2 presents the state of the art in the field of the PDS using DL techniques. Afterwards, section 3 describes the architecture of the detection system based on YOLO-v5 for classification/detection of pedestrians at nighttime and/or daytime. The

following section shows the results of the experimental evaluation, conducted on various public databases aimed at the implementation of PDS, at daytime or nighttime. Finally, the last part is devoted to the conclusions and future works.

### 1.1. State of the art

At present, DL architectures are being widely used in the construction of PDS, whose objective is the detection of pedestrians in real driving scenarios [4], [6], [12], [15], [16]. For this purpose, cameras in the range of visible light (RGB images) and infrared (IR images) have been used, to capture visual information at daytime or nighttime, far or close, together or separate.

Thus, Kim *et al.* [17] used CNNs on night images captured with a visible spectrum camera. The experiments were conducted on the KAIST [18] and CVC-14 [10] databases.

Ding *et al.* [19] put into operation a CNN architecture based on two R-FCN subnetworks, one for color images and another for thermal images. Large subnetworks, thermal and color, were merged in the middle of the architecture; it was done similarly for small subnetworks. To obtain separate detections for pedestrians of large and small scale, the NMS (non-maximum suppression) algorithm is used at the end of the network to merge the results of the two subnetworks and obtain a robust detection. By merging the two channels, the error rate versus FPPI is reduced from 40 %, obtained with separate channels, to 34 %. In addition, the percentage of losses with R-FCN is 69 %, whereas with Faster-RCNN is 51 %.

Köing *et al.* [5] have installed an RPN network for detecting persons in the visible and infrared spectra; then, they have used the Boosted Decision Tree technique to merge the information, obtaining an error rate of 29.83 % on the KAIST database [18].

Zhang *et al.* [16] combined RPN and Boosted Forest for detecting pedestrians on the Caltech [20], INRIA [21], ETHZ and KITTI [22] databases; they used bootstrap techniques to improve the training, reaching an error rate of 9.6 %; the algorithm has a processing time of 0.6 seconds per frame. In addition, they proved that Faster R-CNN does not work properly, because the feature maps do not have enough information to detect pedestrians at a great distance, which results in a drawback to be overcome.

Zhang *et al.* [15] developed a Faster R-CNN architecture in the visible and infrared spectra. The experimental results were obtained on the Caltech database 20, and in nighttime situations on an own database, obtaining an error rate of 19 % and 24 %, respectively, with a processing time of 103 milliseconds (9.7 fps) on  $640 \times 480$  pixels images.

Liu *et al.* [4] used a Faster-RCNN architecture for detecting pedestrians in the visible and infrared

spectra, with an error rate of 37 % on the KAIST database [18].

Song *et al.* [11] proposed a hybrid network based on Yolo-v3 called MSFFN (multispectral feature fusion network), which consists of a DarkNet-53 structure and two subnetworks, MFEV and MFEI for color and infrared images, respectively. The feature maps of MFEV are divided in three scales of  $(13 \times 13)$ ,  $(26 \times 26)$  and  $(52 \times 52)$ , and analogously for MFEI, and then merged in the final part of the architecture. MSFFN achieves a mAP of 85.4 % compared to the 84.9 % of Faster-RCNN on KAIST [18], another remarkable aspect is the 56 fps of MSFFN, compared to the 28 fps of Faster-RCNN.

Cao *et al.* [8] presented improvements in the parameters for the detection in YOLO-v3, modifying the size of the grid to  $(10 \times 10)$ , applying Soft-NMS instead of NMS, with a superposition threshold of 0.2 and, finally, adding a new feature map of  $(104 \times 104)$ . The experiments were conducted on INRIA [21], obtaining a precision of 93.74 % and a recall of 88.14 %, with a processing speed of 9.6 milliseconds per frame.

Yu *et al.* [23] modified the Faster R-CNN, concatenating three different levels of VGG16 with the ROIs, which is then normalized, scaled and dimensioned. A miss-rate (MR) of 10.31 % was obtained on the INRIA database [21] with these changes.

Zhou *et al.* [24] proposed a system to improve the performance in the detection with occlusion with their MSFMN (Mutual-Supervised Feature Modulation Network), constituted by two branches supervised by annotations of entire body and visible parts, that generates training examples which are better focused. In addition, it is calculated the similarity in the losses between the boxes corresponding to entire body and visible parts, enabling learning more robust features, mainly for occluded pedestrians. The merge is performed at the end, multiplying the two classification scores. The experiments were conducted on the CityPersons database [24], obtaining a 38.45 % for a strong occlusion.

On the other hand, Tesema *et al.* [25] put into operation a hybrid architecture that receives the name of HCD (SDS-RPN), with a Log-average Miss Rate of 8.62 % on Caltech [20]. On the other hand, Kyrkou [26] presented the YOLOPED system which is based on the DenseNet architecture. Instead of FPN, each resolution is resized to the size of the deepest feature map in the column, enabling to combine them through a concatenation which is used in header detection. At last, a new loss function is implemented, combining the features of YoloV2 [27], SSD [28] and lapNet [29].

An evaluation in PETS2009 yielded a precision of 85.7 %, a miss rate of 12 %, with a processing of 33.3 fps. Wolpert *et al.* [12] have proposed to combine RGB and thermal images, using Faster R-CNN without anchor boxes, adapting the CSPNet [12] architecture to

merge the IR images at the end of the architecture, reaching an MS average of 7.40 % on KAIST [18]. Zhou *et al.* [30] have presented the MBNet (Modality Balance Network), based on SSD with a DMAF (Differential Modality Aware Fusion) module, which merges and complements the information between the RGB and thermal features. The IAFA (Illumination Aware Feature Alignment) detection handles the equilibrium between the two detection modalities, and the performance achieves miss rates of 21.1 % and 8.13 % on CVC-14 [10] and KAIST [18], respectively.

Wang [31] uses an architecture called CSP, constituted by a feature extraction part based on Resnet-101 and a detection stage, which in turn is used to predict the center, scalar and offset. They use Batch Normalization (BN) to accelerate the training process and improve the performance of the CNNs. A most recent technique is Switch Normalization (SN), which uses a weighted average of the statistical mean and variance of the normalization by blocks. It was proved that using BN for the CSP model an MR (miss rate) of 11.29 % was obtained, whereas SN yields a MR of 10.91 % on the CityPersons database.

Appropriate scaling of images helps to reduce the computational load and to eliminate noise, using CSP with SN and an input of  $(1024 \times 2048)$  yields an MR of 11.41 %, whereas an MR of 10.80 % is achieved with an input of  $(640 \times 1280)$ . Shopovska *et al.* [32] presented an architecture similar to the generative adversarial networks (GAN). This network has two inputs, an RGB and a thermal, giving as output an image that maintains the pedestrians with good visibility, whereas the information obtained from the thermal images enhances the color of pedestrians with bad visibility. This image is used as the input to a Faster RCNN VGG16 network, yielding MRs of 52.07 % and 43.25 %, for daytime and nighttime images, respectively, in the KAIST database [18], and MRs of 69.14 % and 63.52 % for daytime and nighttime images, respectively, in the CVC-14 database [10].

## 2. Materials and methods

Figure 1 shows the general scheme of the proposed multispectral system for pedestrian detection. The system takes visual information coming from color or thermal images, to feed two subnetworks, named RGB and IR, respectively. Then, the merging network concatenates the outputs to locate pedestrians at daytime or nighttime, jointly or separately. The subnetworks are constituted by an architecture based on YOLO-v5 (You Only Look Once) [11], [26], [33–35].

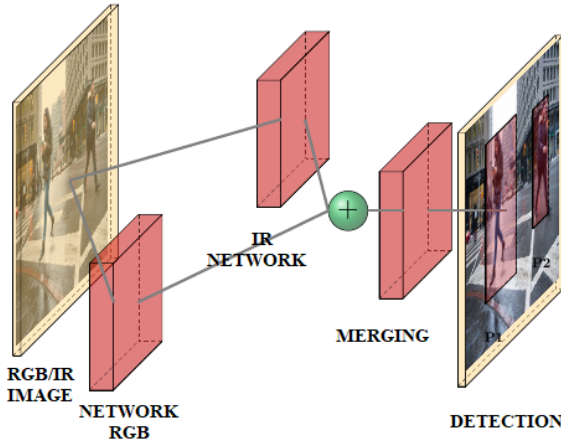


**Figure 1.** General scheme of the multispectral system based on YOLO-v5, for pedestrian detection on color and thermal images

## 2.1. Description of the YOLO-v5 architecture

YOLO is an acronym for «You Only Look Once» [11], [27], [33–35]. It is a very popular model with high-performance in the field of object detection, being considered a cutting-edge technology in real-time detection (FPS). YOLO-v5 is the fifth generation of one-stage detectors [36]. Yolo-v5 is implemented in Pytorch. Table 1 shows the composition of the customized layers that describe the architecture, according to the base layers of Pytorch.

In Table 1, SF is an acronym for Scale Factor; on the other hand, the symbol #s represents variable parameters which are handled according to the values established in the column of parameters in Table 2, which mainly define the size of the Kernel Stride, Padding and Channels.

Finally, the symbol – represents that it receives no parameter.

Figure 2 shows the YOLO-v5 architecture, constituted by subnetworks IR and RGB, with the layers mentioned in Table 1.

**Table 1.** Composition of the customized layers implemented in YOLO-v5 [36]

Name	Composition	Parameters		
		Kernel	Stride	Channels
Conv	conv2d	#	#	#
	BatchNom2d	-	-	-
	Hardwish	-	-	-
Focus	Conv	3 x 3	1	32
	concat	-	-	-
BottleNeckCSP	Conv	3 x 3	1	#
	Conv	3 x 3	1	#
	Conv	3 x 3	1	#
	conv2d	3 x 3	1	#
	conv2d	3 x 3	1	#
	concat	-	-	-
	BatchNom2d	-	-	-
	LeakyRelu	-	-	-
SPP	Conv	3 x 3	1	512
	-	<b>Kernel</b>	<b>Stride</b>	<b>Padding</b>
	Maxpool2d	5 x 5	1	2
	Maxpool2d	9 x 9	1	4
	Maxpool2d	13 x 13	1	6
	concat	-	-	-
Upsample	concat	-	-	-
	Conv	3 x 3	1	512
Upsample	nn.Upsample	<b>Size</b>	<b>SF</b>	<b>Mode</b>
		none	2	nearest

## 2.2. Proposed architecture

The proposed architecture is focused on creating a system capable of merging two subnetworks that work with RGB and IR images, respectively. The merging network concatenates layers 17 and 40 (small pedestrians), and layers 20 and 43 (large pedestrians), described in Table 2, to locate pedestrians at daytime or nighttime, jointly or separately.

Table 2 shows the specific layers that constitute each of the subnetworks; each layer has an identifier (id), which is used in origin to identify the layers to which they are connected. The origin –1 indicates that it is a connection to the previous layer; the number indicates the number of times that the layer is repeated, and finally, the arguments received by each layer are indicated in parameters.

The layers that contain the feature maps of the RGB and IR networks are concatenated, to merge the information through a BottleneckCSP layer. This combined information is sent to the detection layer to generate bounding boxes and the class prediction.

**Table 2.** Distribution and connections of the subnetworks that constitute the architecture of the system based on YOLO-v5 [36], for detecting pedestrians at daytime and nighttime

Network	Id	Origin	Number	Module	Parameters
RGB	0	-1	1	Focus	[32,3]
	1	-1	1	Conv	[64,3,2]
	2	-1	3	BottleneckCSP	[64]
	3	-1	1	Conv	[128,3,2]
	4	-1	9	BottleneckCSP	[128]
	5	-1	1	Conv	[256,3,2]
	6	-1	9	BottleneckCSP	[256]
	7	-1	1	Conv	[512,3,2]
	8	-1	1	SPP	[512,[5,9,13]]
	9	-1	3	BottleneckCSP	[512,False]
	10	-1	1	Conv	[1]
	11	-1	1	Upsample	[256,False]
	12	[-1,6]	1	concat	[1]
	13	-1	3	BottleneckCSP	[256,False]
	14	-1	1	Conv	[128,1,1]
	15	-1	1	Upsample	[None,2,Nearest]
	16	[-1,4]	1	concat	[1]
	17	-1	3	BottleneckCSP	[128,False]
	18	-1	1	Conv	[128,3,2]
	19	[-1,14]	1	concat	[1]
	20	-1	3	BottleneckCSP	[256,False]
	21	-1	1	Conv	[256,3,2]
	22	[-1,10]	1	concat	[1]
23	-1	3	BottleneckCSP	[512,False]	
IR	24	0	1	Conv	[64,3,2]
	25	-1	3	BottleneckCSP	[64]
	26	-1	1	Conv	[128,3,2]
	27	-1	9	BottleneckCSP	[128]
	28	-1	1	Conv	[256,3,2]
	29	-1	9	BottleneckCSP	[256]
	30	-1	1	Conv	[512,3,2]
	31	-1	1	SPP	[512,[5,9,13]]
	32	-1	3	BottleneckCSP	[512,False]
	33	-1	1	Conv	[1]
	34	-1	1	Upsample	[256,False]
	35	[-1,29]	1	concat	[1]
	36	-1	3	BottleneckCSP	[256,False]
	37	-1	1	Conv	[128,1,1]
	38	-1	1	Upsample	[None,2,Nearest]
	39	[-1,27]	1	concat	[1]
	40	-1	3	BottleneckCSP	[128,False]
	41	-1	1	Conv	[128,3,2]
	42	[-1,37]	1	concat	[1]
	43	-1	3	BottleneckCSP	[256,False]
	44	-1	1	Conv	[256,3,2]
	45	[-1,33]	1	concat	[1]
	46	-1	3	BottleneckCSP	[512,False]
	Fusión	47	[17,40]	1	concat
48		-1	3	BottleneckCSP	[128,False]
49		[20,43]	1	concat	[1]
50		-1	3	BottleneckCSP	[256,False]
51		[23,46]	1	concat	[1]
52		-1	3	BottleneckCSP	[512,False]
Detect	53	[48,50,52]	3	Detect	[1, anchors]

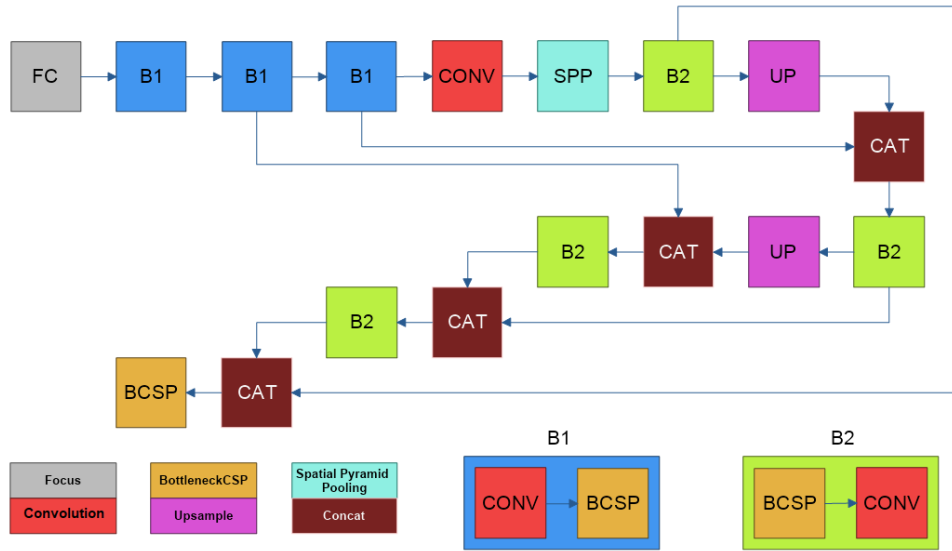


Figure 2. Graphical representation of the YOLO-v5 architecture

### 3. Results and discussion

Multiple experiments have been conducted to get the proposed model, using reference databases in the state of the art, and standard evaluation metrics used in object detection.

#### 3.1. Description of the databases

The public pedestrian databases in the visible and infrared spectra are INRIA [21], CVC 09 [9], CVC-14 [10], LSI Far Infrared Pedestrian Dataset (LSIFIR) [37], FLIR-ADAS [38], Nightowls [39] and KAIST [18].

These databases were selected because they are specialized in daytime and nighttime vehicle applications, and include labeling of the true region,  $B_{gt}$ , where pedestrians are effectively located.

- **INRIA** [21]. The INRIA public database is one of the most widely used in pedestrian detection. It has a set of images divided in «train» and «test»; the «train» folder contains 614 images for training, whereas the «test» folder includes 288 images for testing. Table 3 shows the content.

Table 3. Content of the INRIA database

	Detection
Train	614(614) <sup>a</sup>
Test	288(288)

<sup>a</sup> The value in parenthesis represents the number of frames that contain pedestrians.

- **CVC-09** [9]. These are the databases most widely used for detecting pedestrians at nighttime and daytime, respectively. In this case it was used for training, and afterwards for validation. Table 4 describes the train and test sets. This database is labeled with the pedestrians present in the scene,  $B_{gt}$ .

Table 4. Content of the CVC-09 database at nighttime

	Positive	Negative
Train	2200	1002
Test	2284	-

- **LSIFIR** [37]. It is another important database for developing algorithms for pedestrian detection at nighttime. Table 5 describes the train and test sets, with their corresponding sizes. As it was the case for the CVC-09, this database was used for the training, validation and testing of the proposal.

Table 5. Content of the LSI FIR database

	Classification	Detection
Train	43 391(10 209) <sup>a</sup>	2936(3225)
Test	22 051(5945)	5788(3279)

<sup>a</sup> The value in parenthesis represents the number of frames that contain pedestrians.

- **FLIR-ADAS** [38]. This database includes thermal images for developing autonomous driving systems. The objective of these images is to help in the development of safer systems, which combined with color images and information from LIDAR sensors, may enable creating a robust system for pedestrian detection. It has 8862 images for training and 5838 for testing, see Table 6.

**Table 6.** Content of the FLIR-ADAS database

Detection	
Train	8862(5838) <sup>a</sup>
Test	1366(1206)

<sup>a</sup> The value in parenthesis represents the number of frames that contain pedestrians.

- **CVC-14** [10]. It is constituted by two sequences of thermal images taken at daytime and nighttime. It includes more than 6000 images for training and 700 for validation.
- **Nightowls** [39]. It is focused on the detection of pedestrians at nighttime. The images were captured using a standard camera, with a  $1024 \times 640$  resolution. The sequences were captured in three countries, under all weather conditions and at all seasons, to obtain a greater variability in the scenes.
- **KAIST** [18]. Multispectral database that contains a set of  $640 \times 480$  images, taken by two cameras, one thermal and one color with a frequency of 20 Hz. They were taken at daytime and nighttime to consider different lighting conditions. The number of thermal and color images is the same, for a total of 100,368 images for training and 90,280 for testing, see Table 7.

**Table 7.** Content of the KAIST database

	Detection	
	Color	Thermal
Trains	50 184(#) <sup>a</sup>	50 184(#)
Test	45 140(#)	45 184(#)

<sup>a</sup> The value in parenthesis represents the number of frames that contain pedestrians.

### 3.2. Evaluation metrics

The following protocols will be followed for the evaluation:

- **P-R Curve (Precision-Recall)**. Precision (Prec) is the ratio between relevant cases and cases recovered. Recall (Rec) is the ratio between relevant cases that have been recovered and total of relevant cases. The equations for these cases are the following:

$$Pres = \frac{TP}{TP + FP} \quad (1)$$

$$Rec = \frac{TP}{TP + FN} \quad (2)$$

- **AP (Average Precision)**. This index was proposed for the VOC2007 challenge [40] to evaluate the performance of detectors, and is related to the area under the P-R curve of one class. The mAP is an average of the APs for all classes.

To estimate the metrics, it is required an index that enables identifying a correct prediction, which in this case is the IoU (Intersection-over-Union). IoU determines the ratio between the regions that correspond to true positives (TP) and false positives (FP), by means of (3).

$$IoU = \frac{Area(B_{det} \cap B_{gt})}{Area(B_{det} \cup B_{gt})} \quad (3)$$

Where  $B_{gt}$  is the true ROI and  $B_{det}$  is the detected ROI. In this case, a TP occurs for an IoU greater than 0.5; otherwise, it is an FP. Equations (1) and (2) may be evaluated with these values.

### 3.3. Implementation details

The proposed architecture is constituted by four main parts, which are the IR and RGB subnetworks, the feature merging block and the detection block. The training of the architecture will consist of a training stage of strong adjustment, and a training stage of fine adjustment. The SGD (stochastic gradient descent) optimization algorithm with a learning rate (LR) of 0.01 is used for the training of strong adjustment, fixing 100 epochs for training the whole architecture with the RGB images; the SGD technique prevents being stuck in a relative minimum of the objective function. Then, the weights corresponding to the RGB subnetwork are frozen, and 100 epochs are fixed for training the architecture with the IR images.

At last, to conclude the strong adjustment stage, the weights corresponding to the IR and RGB subnetworks will be frozen, and the merge layers will be trained for 50 epochs with the IR and RGB images

combined in equal parts, to prevent the merge layers from being biased by the features of the IR or RGB images.

In the fine adjustment stage the LR is modified to 0.0001, all weights of the architecture are frozen except the ones corresponding to the RGB subnetwork and the training is performed for 50 epochs with the RGB images; then, all the weights are frozen except the ones of the IR subnetwork, and the training is carried out for 50 epochs with the IR images. In the last step all the weights are frozen except the ones of the merge layer, and a training is performed for 25 epochs with the IR and RGB images in equal parts.

At this time, this procedure was applied to each of

the databases listed in this work

### 3.4. Results

Table 8 presents the performance of the detection method, when it is evaluated with various metrics on the selected databases.

In all cases, the processing time was 29.8 milliseconds.

Figure 3 displays plots of the P-R curves for the proposed architecture on each of the selected databases. It may be concluded from Table 8 and Figure 3 that the best performance was obtained on INRIA [21], followed by CVC09 [9] and LSIFIR [37].

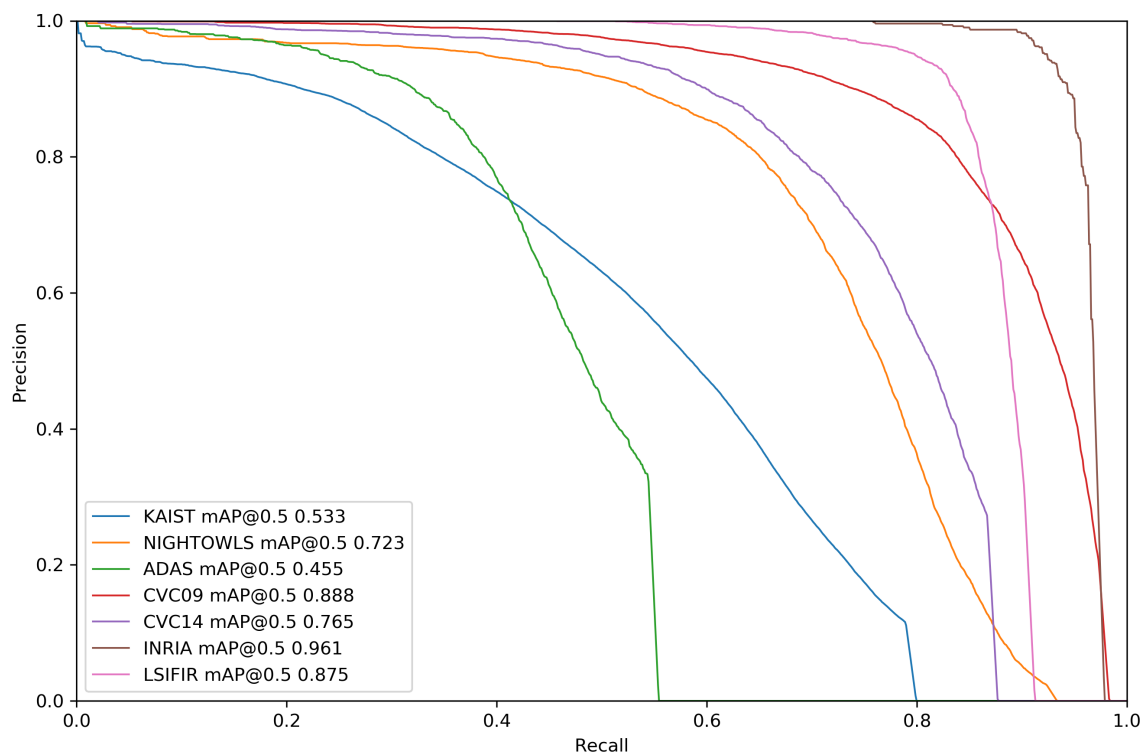


**Figure 3.** Plots of the P-R curves for the different pedestrian databases

**Table 8.** Evaluation of the Yolo-v5 [36] architecture on various public databases on the visible and infrared spectra. LAMS is an acronym for Log Average Miss Rate

	INRIA	CVC09	LSIFIR	FLIR-ADAS	CVC14	Nightowls	KAIST
<b>mAP@50</b>	96.6	89.2	90.5	56	79.8	72.3	53.3
<b>Precisión</b>	69.8	67.4	89.2	72.1	86.4	80.7	52.5
<b>Recall</b>	90	89	83.4	40.1	61.6	64.6	53.7
<b>LAMS</b>	6	20	17	69	36	36	67

## 4. Conclusions

This work has presented a system for detecting pedestrians at daytime and nighttime using modern image

processing techniques and deep learning, where a new DL architecture based on YOLO-v5 was developed with DenseNet, for detecting pedestrians at daytime and nighttime using images in the visible and far infrared spectra, whose mAP is 96.6 % for the case of INRIA, 89.2 % on CVC09, 90.5 % on LSIFIR, 56 % on FLIR-ADAS, 79.8 % for CVC14, 72.3 % on Nightowls and 53.3 % for KAIST.

Future work will be aimed at improving the proposed architecture and testing it on the most relevant databases in this field of knowledge.

## Acknowledgements

The computing equipment, GPU, has been funded by the I&H Tech company.

In addition, we wish to thank the researchers that have published their databases and deep learning architectures, for the use of the scientific community; this work would not have been possible without them.

Finally, we wish to express our acknowledgements to the anonymous reviewers for their collaboration.

## References

- [1] WHO. (2018) Road traffic injuries. World Health Organization. [Online]. Available: <https://bit.ly/3pnr9Rc>
- [2] ANT. (2015) Estadísticas de siniestros de tránsito octubre 2015. Agencia Nacional de Tránsito del Ecuador. [Online]. Available: <https://bit.ly/3aUIWGv>
- [3] —. (2017) Estadísticas de siniestros de tránsito agosto 2017. Agencia Nacional de Tránsito del Ecuador. [Online]. Available: <https://bit.ly/3aUIWGv>
- [4] J. Liu, S. Zhang, S. Wang, and D. N. Metaxas, “Multispectral deep neural networks for pedestrian detection,” 2016. [Online]. Available: <https://bit.ly/2Z3BLJu>
- [5] D. König, M. Adam, C. Jarvers, G. Layher, H. Neumann, and M. Teutsch, “Fully convolutional region proposal networks for multispectral person detection,” in *2017 IEEE Conference on Computer Vision and Pattern Recognition Workshops (CVPRW)*, 2017, pp. 243–250. [Online]. Available: <https://doi.org/10.1109/CVPRW.2017.36>
- [6] D. Guan, Y. Cao, J. Yang, Y. Cao, and M. Y. Yang, “Fusion of multispectral data through illumination-aware deep neural networks for pedestrian detection,” *Information Fusion*, vol. 50, pp. 148–157, 2019. [Online]. Available: <https://doi.org/10.1016/j.inffus.2018.11.017>
- [7] J. Li, X. Liang, S. Shen, T. Xu, J. Feng, and S. Yan, “Scale-aware fast R-CNN for pedestrian detection,” *IEEE Transactions on Multimedia*, vol. 20, no. 4, pp. 985–996, 2018. [Online]. Available: <https://doi.org/10.1109/TMM.2017.2759508>
- [8] J. Cao, C. Song, S. Peng, S. Song, X. Zhang, Y. Shao, and F. Xiao, “Pedestrian detection algorithm for intelligent vehicles in complex scenarios,” *Sensors*, vol. 20, no. 13, p. 3646, 2020. [Online]. Available: <https://doi.org/10.3390/s20133646>
- [9] Caltech. (2016) Caltech pedestrian detection benchmark. [Online]. Available: <https://bit.ly/3aXuZb4>
- [10] Pascal. (2016) Inria person dataset. [Online]. Available: <https://bit.ly/30APbxi>
- [11] X. Song, S. Gao, and C. Chen, “A multispectral feature fusion network for robust pedestrian detection,” *Alexandria Engineering Journal*, vol. 60, no. 1, pp. 73–85, 2021. [Online]. Available: <https://doi.org/10.1016/j.aej.2020.05.035>
- [12] A. Wolpert, M. Teutsch, M. S. Sarfraz, and R. Stiefelhagen, “Anchor-free small-scale multispectral pedestrian detection,” 2020. [Online]. Available: <https://bit.ly/3G8k5gL>
- [13] S. Ren, K. He, R. Girshick, and J. Sun, “Faster R-CNN: Towards real-time object detection with region proposal networks,” 2016. [Online]. Available: <https://bit.ly/3B167d1>
- [14] C. Ertler, H. Possegger, M. Opitz, and H. Bischof, “Pedestrian detection in RGB-D images from an elevated viewpoint,” in *Proceedings of the 22nd Computer Vision Winter Workshop*, W. Kropatsch, I. Janusch, and N. Artner, Eds. Austria: TU Wien, Pattern Recognition and Image Processing Group, 2017. [Online]. Available: <https://bit.ly/3AYTI9w>
- [15] X. Zhang, G. Chen, K. Saruta, and Y. Terata, “Deep convolutional neural networks for all-day pedestrian detection,” in *Information Science and Applications 2017*, K. Kim and N. Joukov, Eds. Singapore: Springer Singapore, 2017, pp. 171–178. [Online]. Available: [https://doi.org/10.1007/978-981-10-4154-9\\_21](https://doi.org/10.1007/978-981-10-4154-9_21)
- [16] L. Zhang, L. Lin, X. Liang, and K. He, “Is faster r-cnn doing well for pedestrian detection?” in *Computer Vision – ECCV 2016*, B. Leibe, J. Matas, N. Sebe, and M. Welling, Eds. Cham: Springer International Publishing, 2016, pp. 443–457. [Online]. Available: [https://doi.org/10.1007/978-3-319-46475-6\\_28](https://doi.org/10.1007/978-3-319-46475-6_28)

- [17] J. H. Kim, H. G. Hong, and K. R. Park, "Convolutional neural network-based human detection in nighttime images using visible light camera sensors," *Sensors*, vol. 17, no. 5, 2017. [Online]. Available: <https://doi.org/10.3390/s17051065>
- [18] S. Hwang, J. Park, N. Kim, Y. Choi, and I. S. Kweon, "Multispectral pedestrian detection: Benchmark dataset and baseline," in *2015 IEEE Conference on Computer Vision and Pattern Recognition (CVPR)*, 2015, pp. 1037–1045. [Online]. Available: <https://doi.org/10.1109/CVPR.2015.7298706>
- [19] L. Ding, Y. Wang, R. Laganieri, D. Huang, and S. Fu, "Convolutional neural networks for multispectral pedestrian detection," *Signal Processing: Image Communication*, vol. 82, p. 115764, 2020. [Online]. Available: <https://doi.org/10.1016/j.image.2019.115764>
- [20] Caltech. (2012) Caltech pedestrian detection benchmark. [Online]. Available: <https://bit.ly/3pkn93o>
- [21] Pascal. (2012) INRIA person dataset. [Online]. Available: <https://bit.ly/3IAO6Hw>
- [22] A. Geiger, P. Lenz, and R. Urtasun, "Are we ready for autonomous driving? The KITTI vision benchmark suite," in *Conference on Computer Vision and Pattern Recognition (CVPR)*, 2012. [Online]. Available: <https://bit.ly/3n6oBnq>
- [23] X. Yu, Y. Si, and L. Li, "Pedestrian detection based on improved faster rcnn algorithm," in *2019 IEEE/CIC International Conference on Communications in China (ICCC)*, 2019, pp. 346–351. [Online]. Available: <https://doi.org/10.1109/ICCCChina.2019.8855960>
- [24] Y. He, C. Zhu, and X.-C. Yin, "Mutual-supervised feature modulation network for occluded pedestrian detection," 2020. [Online]. Available: <https://bit.ly/3C14eyn>
- [25] F. B. Tesema, H. Wu, M. Chen, J. Lin, W. Zhu, and K. Huang, "Hybrid channel based pedestrian detection," *Neurocomputing*, vol. 389, pp. 1–8, 2020. [Online]. Available: <https://doi.org/10.1016/j.neucom.2019.12.110>
- [26] C. Kyrkou, "Yolopeds: efficient real time single shot pedestrian detection for smart camera applications," *IET Computer Vision*, vol. 14, no. 7, pp. 417–425, Oct 2020. [Online]. Available: <http://dx.doi.org/10.1049/iet-cvi.2019.0897>
- [27] J. Redmon and A. Farhadi, "Yolo9000: Better, faster, stronger," in *Proceedings of the IEEE Conference on Computer Vision and Pattern Recognition (CVPR)*, July 2017. [Online]. Available: <https://bit.ly/3nuycv1>
- [28] W. Liu, D. Anguelov, D. Erhan, C. Szegedy, S. Reed, C.-Y. Fu, and A. C. Berg, "SSD: single shot multibox detector," in *Computer Vision – ECCV 2016*, B. Leibe, J. Matas, N. Sebe, and M. Welling, Eds. Cham: Springer International Publishing, 2016, pp. 21–37. [Online]. Available: [https://doi.org/10.1007/978-3-319-46448-0\\_2](https://doi.org/10.1007/978-3-319-46448-0_2)
- [29] F. Chabot, Q.-C. Pham, and M. Chaouch, "Lapnet : Automatic balanced loss and optimal assignment for real-time dense object detection," 2020. [Online]. Available: <https://bit.ly/3FYZDPo>
- [30] K. Zhou, L. Chen, and X. Cao, "Improving multispectral pedestrian detection by addressing modality imbalance problems," 2020. [Online]. Available: <https://bit.ly/2Z6qKaV>
- [31] W. Wang, "Detection of panoramic vision pedestrian based on deep learning," *Image and Vision Computing*, vol. 103, p. 103986, 2020. [Online]. Available: <https://doi.org/10.1016/j.imavis.2020.10398>
- [32] I. Shopovska, L. Jovanov, and W. Philips, "Deep visible and thermal image fusion for enhanced pedestrian visibility," *Sensors*, vol. 19, no. 17, 2019. [Online]. Available: <https://doi.org/10.3390/s19173727>
- [33] J. Redmon, S. Divvala, R. Girshick, and A. Farhadi, "You only look once: Unified, real-time object detection," 2016. [Online]. Available: <https://bit.ly/3aWg3tO>
- [34] D. Heo, E. Lee, and B. Chul Ko, "Pedestrian detection at night using deep neural networks and saliency maps," *Journal of Imaging Science and Technology*, vol. 61, no. 6, pp. 604 031–604 039, 2017. [Online]. Available: <https://doi.org/10.2352/J.ImagingSci.Technol.2017.61.6.060403>
- [35] J. Redmon and A. Farhadi, "Yolov3: An incremental improvement," 2018. [Online]. Available: <https://bit.ly/30Lg81v>
- [36] G. Jocher, A. Stoken, J. Borovec, NanoCode012, A. Chaurasia, TaoXie, L. Changyu, V. Abhiram, Laughing, tkianai, yxNONG, A. Hogan, lorenzomamma, AlexWang1900, J. Hajek, L. Diaconu, Marc, Y. Kwon, oleg, wanghaoyang0106, Y. Defretin, A. Lohia, ml5ah, B. Milanko, B. Fineran, D. Khromov, D. Yiwei, Doug, Durgesh, and F. Ingham, "ultralytics/yolov5: v5.0 - YOLOv5-P6 1280 models, AWS, Supervise.ly and YouTube integrations," Apr. 2021. [Online]. Available: <https://doi.org/10.5281/zenodo.4679653>

- [37] D. Olmeda, C. Premebida, U. Nunes, J. M. Armingol, and A. de la Escalera, "Pedestrian detection in far infrared images," *Integrated Computer-Aided Engineering*, vol. 20, no. 4, pp. 347–360, 2013. [Online]. Available: <http://dx.doi.org/10.3233/ICA-130441>
- [38] Teledyne Flir. (2021) Free flir thermal dataset for algorithm training. Teledyne FLIR LLC All rights reserved. [Online]. Available: <https://bit.ly/2Xxe3F4>
- [39] NightOwls. (2021) About nightowls. NightOwls Datasets. [Online]. Available: <https://bit.ly/3pof6m9>
- [40] M. Everingham, L. Van Gool, C. K. I. Williams, J. Winn, and A. Zisserman, "The Pascal Visual Object Classes (VOC) Challenge," *International Journal of Computer Vision*, vol. 88, no. 2, pp. 303–338, Jun. 2010. [Online]. Available: <https://doi.org/10.1007/s11263-009-0275-4>



# A DEEP LEARNING APPROACH TO ESTIMATE THE RESPIRATORY RATE FROM PHOTOPLETHYSMOGRAM

## UN ENFOQUE DE APRENDIZAJE PROFUNDO PARA ESTIMAR LA FRECUENCIA RESPIRATORIA DEL FOTOPLETISMOGRAMA

Lucas C. Lampier<sup>1,\*</sup> , Yves L. Coelho<sup>1</sup> , Eliete M. O. Caldeira<sup>1</sup> ,  
Teodiano F. Bastos-Filho<sup>1</sup>

Received: 15-05-2021, Received after review: 18-08-2021, Accepted: 20-09-2021, Published: 01-01-2022

### Abstract

This article describes the methodology used to train and test a Deep Neural Network (DNN) with Photoplethysmography (PPG) data performing a regression task to estimate the Respiratory Rate (RR). The DNN architecture is based on a model used to infer the heart rate (HR) from noisy PPG signals, which is optimized to the RR problem using genetic optimization. Two open-access datasets were used in the tests, the BIDMC and the CapnoBase. With the CapnoBase dataset, the DNN achieved a median error of 1.16 breaths/min, which is comparable with analytical methods in the literature, in which the best error found is 1.1 breaths/min (excluding the 8 % noisiest data). The BIDMC dataset seems to be more challenging, as the minimum median error of the literature's methods is 2.3 breaths/min (excluding 6 % of the noisiest data), and the DNN based approach achieved a median error of 1.52 breaths/min with the whole dataset.

**Keywords:** Deep Neural Networks, Photoplethysmography, Respiratory Rate

### Resumen

Este trabajo presenta una metodología para entrenar y probar una red neuronal profunda (Deep Neural Network – DNN) con datos de fotopleletismografía (Photoplethysmography – PPG), con la finalidad de llevar a cabo una tarea de regresión para estimar la frecuencia respiratoria (Respiratory Rate – RR). La arquitectura de la DNN se ha basado en un modelo de inferencia de frecuencia cardíaca (FC) a partir de señales PPG ruidosas. Dicho modelo se ha optimizado a través de algoritmos genéticos. En las pruebas realizadas se han utilizado dos conjuntos de datos de acceso abierto (BIDMC y CapnoBase). Con CapnoBase, la DNN ha logrado un error mediano de 1,16 respiraciones/min, que es comparable con los métodos analíticos en la literatura, donde el mejor error es 1,1 respiraciones/min (excluyendo el 8 % de datos más ruidosos). Por otro lado, el conjunto de datos BIDMC aparenta ser más desafiante, ya que el error mediano mínimo de los métodos de la literatura es de 2,3 respiraciones/min (excluyendo el 6 % de datos más ruidosos). Para este conjunto de datos la DNN ha logrado un error mediano de 1,52 respiraciones/min

**Palabras clave:** Redes Neuronales Profundas, Fotopleletismografía, Frecuencia Respiratoria

<sup>1,\*</sup>Postgraduate Program in Electrical Engineering, Universidade Federal do Espírito Santo (UFES), Vitória-ES, Brazil  
Corresponding author ✉: lucas.lampier@hotmail.com.

Suggested citation: Lampier, L. C.; Coelho, Y. L.; Caldeira, E. M. O. and Bastos-Filho, T. F. "A Deep Learning Approach to Estimate the Respiratory Rate from Photoplethysmogram," *Ingenius, Revista de Ciencia y Tecnología*, N.º 27, pp. 96-104, 2022, DOI: <https://doi.org/10.17163/ings.n27.2022.09>.

## 1. Introduction

Respiratory Rate (RR) is an important indicator of a person’s physiological state, useful mainly to monitor pulmonary diseases. This physiological signal is traditionally measured by spirometry, pneumography or electromyography [1]. These methodologies are in general expensive and used mostly in medical environments. Photoplethysmography (PPG) is a cardiac signal usually measured using an oximeter, which is way cheaper than the traditional RR measurement methods, and recent studies have shown that it can be captured even remotely using a smartphone camera [2]. As respiration has an influence on the heart cycles, the RR information is also presented in the PPG signal [3].

Several methodologies in the literature had success on estimating the RR with a small error from the PPG signal [1], [4–8], however, attenuating noise is still a challenge to get robust predictions on low-quality PPG signals. This paper presents an alternative way to infer the Respiration Rate from PPG signals. Deep Learning techniques have been widely used in image problems, however it’s also a powerful tool in one dimensional (1D) problems, mainly limited by the size and quality of the dataset, and also by the computer power in the training process. As the quantity of data available on-line growing, as well as the hardware computing power, DNNs are being tried in a large variety of problems that before were dominated by analytical procedures.

Regarding the PPG processing, in [1], the authors showed that a DNN can be used to extract the RR signal from PPG signals. And in [9], the pulse rate is extracted from the PPG using a DNN.

This work proposes to use a DNN to extract reliable RR measurements from PPG signals, by using analytical approaches to extract secondary signals from PPG and using DNN to infer the RR.

### 1.1. Related Work

According to [10] the PPG-RR algorithms can be summarized in five steps:

- Respiratory signal(s) extraction: This step consists of finding variation in the PPG signal related to the respiration cycles.
- Fusion of respiratory signals: The different signals extracted can be combined to create a unique signal with greater noise robustness (optional).
- Estimate the RR from a window: A window of the generated signal is segmented and the RR is estimated from it.
- Combine estimations: The result of different windows may be used to generate a final estimation (optional).

- Quality filtering: A quality score may be assigned to the PPG window to exclude low-quality predictions (optional).

Some of the first approaches that estimate RR from PPG use a highpass and a lowpass second-order Butterworth filters with cutoff frequencies at 0.1 Hz and 5 Hz respectively to remove noise from the PPG. And then the respiratory signal is estimated by applying a 0.4 Hz lowpass filter on the PPG signal [11]. The authors from [12] applied Singular Value Ratio (SVR) to extract the respiratory periodicity from the PPG, and then, they used Principal Component Analysis (PCA) to estimate the respiratory activity from the first principal component. In another approach, proposed by [13], they captured a PPG signal using the smartphone camera, and then the RR was estimated by finding the frequency corresponding to the highest peak on the spectrum generated by the Welch periodogram [7].

In [4], five different methodologies were compared (including their own). The oldest one was proposed in [14], and consists in apply a 16<sup>th</sup> degree Bessel band-pass filter with cutoff frequencies of 0.13 Hz and 0.48 Hz (7.8 to 28.8 breaths/min). The second was proposed by [8], which consists in use a Fourier transform on the PPG signal and get the frequency with the highest amplitude in the bandwidth from 0.08 Hz to 0.4 Hz. In the methodology proposed by [5], auto-regressive (AR) models estimate a filter using the PPG signal, and, according to them, the frequency of the highest magnitude pole, inside the range of the RR bandwidth (0.08 Hz to 0.7 Hz), corresponds to the RR. Instead of using the PPG itself, in [6] three RR-related temporal features are estimated from it: Respiratory-Induced Intensity Variation (RIIV), Respiratory-Induced Amplitude Variation (RIAV), and Respiratory-Induced Frequency Variation (RIFV). Then, the power spectrum of each one is calculated and the RR is estimated by each one by taking the highest amplitude frequency in the RR frequency-band (0.067 Hz – 1.08 Hz) and calculating the mean of the three frequencies. Finally, the methodology proposed by [4] combines the AR modeling, proposed in [5] with the fusion of results of the three features proposed by [6].

The results presented in [4] show that for the CapnoBase dataset [15] the method that presented the lowest error was the method from [6] with a Median Absolute Error (MdAE) of 0.8 breaths/min using a 62 s window, however, 46 % of the PPG data were excluded due to noise. The second best in this dataset was the method from [5], which achieved a MdAE of 1.1 breaths/min and kept 92 % of the data. The BIDMC dataset appears to be more challenging, since the best MdAE was achieved by the method proposed by [8] (2.3 breaths/min), which was also one of the methods that kept most of the data (94 %).

A recent work has achieved even more accurate results [16], in which a method derives multiple waveforms from the PPG signal, and their quality are measured and then used as a weight to combine them using a Kalman Smoother. With this approach they achieved a median error of 0.2 breaths/min.

## 1.2. Deep Neural Networks (DNN)

According to [17], Deep Learning is an approach that can handle an important step in a machine layer problem: the features extraction. Its concept consists of concatenating multiple layers of simple models, where each model “learns” part of the problem-concepts, and so, a complex problem can be split into simpler ones to be better solved. An interesting point of this approach is that it performs the machine learning (classification, regression, clustering, etc.) and also the feature extraction part of the problem, in contrast with shallow techniques, in which the feature extraction step has to be done separately, in a previous stage, and demands domain knowledge. The limitation of the Deep Learning approach is the dataset. Normally, Deep learning models have a large number of weights to be adjusted, so, it needs a large amount of data to optimize them.

There are already some approaches that implemented Deep Learning techniques to solve problems related to physiological data. In [9], a DNN was implemented to estimate the Heart Rate (HR) having a PPG signal from a sensor worn on the user’s wrist as input data. The model was tested with a challenging dataset, in which, the PPG signal was captured during various physical activities, which inserts noise and artifacts on it. The architecture of the model consisted of two 1-D convolutional layers followed by two Long Short-Term Memory (LSTM) layers and finally a dense layer at the end, and it reached a Mean Absolute Error (MAE) of  $1.47 \pm 3.37$  Beats Per Minute (BPM).

A Deep Learning approach to extract the RR signal from the PPG is presented in [1]. Their model consists of several convolutional layers connected to several deconvolutional layers that transform the PPG signal into a respiratory signal, and then they calculate the RR from it. Their method was tested in two independent datasets, the CapnoBase and the Vortal [18] and reached a Mean Squared Error (MSE) of 0.262 in the first dataset and an error of 0.145 in the second one (which corresponds to a Root Mean Squared Error (RMSE) of approximately 3.1 breaths/min and 2.3 breaths/min respectively).

## 2. Materials and methods

### 2.1. Datasets

Two datasets were used in the tests: the CapnoBase benchmark dataset [15] and the BIDMC PPG and

Respiration Dataset [19]. The CapnoBase benchmark dataset [20], contains 42 recordings, with 8 min each, containing the PPG and the inhaled and exhaled carbon-dioxide (CO<sub>2</sub>) signal, both collected with a sampling frequency of 300 Hz. The BIDMC PPG and Respiration Dataset [21], contains 8 min PPG and CO<sub>2</sub> breath signal recordings from 53 volunteers collected at 125 Hz.

### 2.2. Photoplethysmogram Respiratory Features

Three signals related to the respiration were generated from PPG [6]:

1. Respiratory-Induced Intensity Variation (RIIV): As the amplitude of the PPG signal varies in synchrony with the respiratory cycle, this feature can be used to estimate the RR [3]. This series is estimated by taking the intensity value of each peak in the PPG signal [4].
2. Respiratory-Induced Amplitude Variation (RIAV): The breath-cycles induce an amplitude-variation in the PPG waves, which can be estimated by calculating the variation in the peak-valley difference in the PPG waves [6].
3. Respiratory-Induced Frequency Variation (RIFV): The HR variation is also highly linked to the inspiration and expiration events of breathing. The inspirations increase the HR and the expiration decreases it. This signal may be represented by the time interval between consecutive PPG peaks [6].

A graphic representation of the RIIV, RIAV and RIFV features is presented in Figure 1.

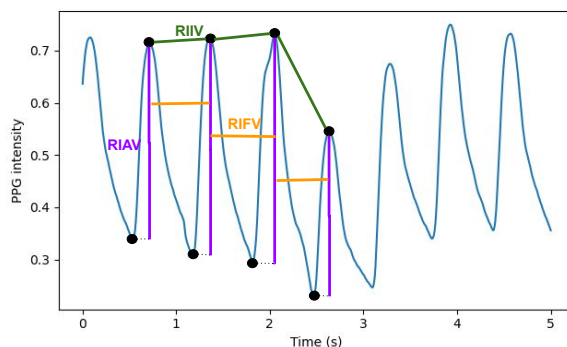


Figure 1. Extracted RR-related PPG features

### 2.3. Signal Quality Index (SQI)

The SQI quantifies the noise and artifact contamination in the analyzed PPG window. This index is used to exclude signals that do not reach a minimum

quality. In this work, the SQI is calculated targeting two points: “flat-lines” in the signal, and concordance between different peak detectors [4]. The “flat-lines” are defined as part of the PPG signal in which the difference between consecutive samples is near to zero. To detect it, the following method was performed:

1. Calculate the *StdDiff* signal as follows:

$$\text{StdDiff}[i-wdw] = \sigma(\text{diff}(\text{PPG}[i-wdw : i])),$$

for  $i = wdw, wdw + 1, wdw + 2, \dots, N$ .

Where  $\sigma(\cdot)$  is the standard deviation operation,  $\text{diff}(\cdot)$  is the first derivative operation, *PPG* is the PPG signal, *wdw* is the window length, that, in the case, is the integer part of  $1.5 \text{ s} \times \text{frequency sample}$  (1.5 s is the time interval between consecutive peaks on the minimum HR value, which is normally 40 BPM), and  $N$  is the number of samples in the PPG signal.

2. Initialize the  $Q$  array with ones and the same size as *PPG*:  $Q = \text{ones}(N)$

3. Calculate the threshold value:  $th = \mu(\text{StdDiff}) - \alpha \times \sigma(\text{StdDiff})$ , where  $\mu(\cdot)$  is the mean operation and  $\alpha$  is an adjustable parameter.

4. Set the values of  $k$  to zero in the corresponding locations where *StdDiff* is too low:

$$\text{for } i = wdw, wdw + 1, wdw + 2 \dots N : \{$$

$$\text{if } (\text{StdDiff}[i - wdw] < (th)) : \{$$

$$Q[i + wdw] = 0$$

$$\}}$$

5. The value of  $K$  is the proportion of one values in  $Q$  inside the analyzed PPG window, over the total size of it.

The concordance between the two peak-detectors was performed as following: if the difference between the position found by the detectors on the same peak is smaller than 150 ms, it is set that both detectors agree on that peak, therefore its position is correct, otherwise, the peak is considered a noise [4]. An F1-score is then applied to measure the concordance between the two peak-detectors on the analyzed segment of the signal. The peak detection methods were provided by two different *20* libraries: the *Neurokit2* [22], which implements the PPG peak detection algorithm provided in [23] and the *Heartpy* library [24], in which the authors implemented their own peak detection technique.

Finally the SQI is computed as:  $SQI = F1 \times K$ , where  $F1$  is the concordance between peaks and  $K$  is the “flat-line” proportion.

## 2.4. DNN Architecture

The architecture of the model was inspired on the CorNET [9], which has two convolution blocks, each containing a convolution layer (32 filters with a kernel size of 40), a batch normalization layer, a Rectified Linear Unit (ReLU) activation layer, and finally a max-pooling layer with a pool size of 4 (a Dropout layer with a drop rate of 0.1 was used for training). After the convolution blocks two LSTM layers are concatenated, each one with 128 units and the hyperbolic tangent (*tanh*) activation function. To predict the HR a single neuron with linear activation is used.

The architecture proposed to predict the RR is a result of genetic optimization on the CorNET’s parameters presented in Table 1. There is always an additional dense layer with one neuron with linear activation at the end of the model.

**Table 1.** Parameters tried in the DNN architecture

Parameter	Possibilities
# of convolution blocks	0/1/2
# of convolution filters/layer	128/64/32
Length of convolution filters	11/21/31
# of LSTM layers	1/2/3
# of LSTM units/layer	128/64/32
# of dense layers	0/1/2
# of neurons/layer	128/64/32/16

The parameters above are optimized, while the non-cited parameters are used as defined by default in the *Keras* library [25]. As the number of combinations is very large (2916), the parameters are optimized via genetic optimization. This strategy starts by defining a population of  $L$  models with random parameters and then all models are trained, tested, and sorted by the result. The  $M$  models with the best performance are kept while the others are discarded. The kept models set is called *parents*, then  $M - J$  new models are generated by taking values of three different models (one parent for the convolution parameters, one parent for the LSTM, and one for dense). Also, there is a chance of  $H$  % that the parameters of the new models change randomly (these changes are called mutations), these new models are called *offspring*. There is also generated  $J$  new completely random models. We give this set the name of *foreigners*. Then the *parents*, *offspring* and *foreigners* sets are united and a new interaction starts. The procedure is repeated for  $E$  epochs. The idea is that the parameters that decrease the estimation error will prevail in the *parents* set, and their combination may generate a model on the *offspring* set that overcomes its parents’ result. Also, new random parameters are inserted with the mutation and the *foreigners* set at each iteration. These

random additions give a chance for the population of models to get out of a sub-optimal local minimum.

For this experiment, the parameters of the genetic optimization were:  $L = 45$ ,  $M = 20$ ,  $J = 5$ ,  $E = 20$  and  $H = 20$ , this reduced the number of trained models from 2916 to 520 (25 new models/epoch  $\times$  20 epochs + the first 20 parents). And the best model found is a DNN with 2 convolution blocks with 32 filters and one MaxPooling-1D (kernel size of 2) on each convolution layer, a kernel size of 21, and ReLU activation. Then, one LSTM layer with 32 neurons, and finally, 2 dense layers, one with 32 neurons and ReLU activation and the last one with one neuron and linear activation. A summary of the final DNN architecture is presented on Figure 2.

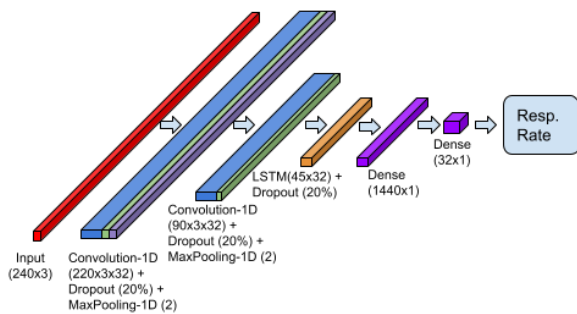


Figure 2. Selected Neural Network architecture

## 2.5. Training and Testing Procedure

To train and evaluate the model two datasets were used: the BIDMC [19] and the CapnoBase [15] datasets. The cross-validation method with four groups were used: for each database, their files were split into four groups, each group containing 25% of the data of each dataset. Then, the same procedure was performed on each group: first, the PPG peaks were found using the *Neurokit2* library [22]. Then using a sliding window of 64 s with step of 4 s, the three RR-related signals (RIIV, RIAV, and RIFV) were computed from it and then they were interpolated to an artificial sampling frequency of 4 Hz and the first 240 samples. As the peak will probably not start at the beginning and the end of the window, the interpolated signal may variate between 61 s to 64 s. (60 s) were extracted from the window generating a sample with 240 lines (temporal steps) and 3 columns (one for each: RIIV, RIAV, and RIFV). The final step is to normalize the data so each channel of the new sample has mean 0 and variance 1:  $Y = (X - \mu(X))/\sigma(X)$ , where  $Y$  is the normalized series,  $X$  the input series,  $\mu(\cdot)$  is the mean operation and  $\sigma(\cdot)$  is the standard deviation operation.

To get the reference value of RR, the peak of the  $\text{CO}_2$  correspondent signal of each sample is located using the Respiration module of *Neurokit2* and then, the Median RR of the 64 s sample is calculated by

taking the inverse of the median value of consecutive peaks time-interval.

The four groups of normalized samples are then split into the training and testing sets, where the training set has 3 groups and the test has 1. The training and testing procedures were repeated four times, so each group could be evaluated in the test set once. Each of the 4 models (one for each test group) was trained for 1400 epochs using the Adam optimizer with standard parameters from *Keras* [25]. The processing was made on a *Ryzen 5 3500X* computer with 16 GB of RAM memory and a *NVIDIA GeForce RTX 2060 SUPER* with 8 GB dedicated memory. The Mean Squared Error (MSE) metric was used to compute the loss for each epoch. The loss curve result is presented in Figure 3.

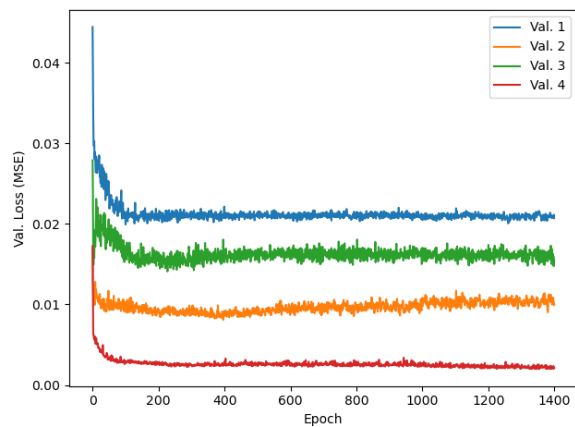


Figure 3. Ts curve of the 4 instances of the network

The validation groups 1 and 4 had a loss decreasing until epoch 1400, the validation group 2 has its minimum loss near the epoch 400 and validation group 3 had a minimum around epoch 200, then it decreased again after epoch 800. The graph was used to determine the number of epochs to train the DNNs, as half of the Validation groups still decreasing until epoch 1400 and the dropout layers seems to prevent overfitting on the other groups, since the loss do not increase to much after the minimums. We repeated the process shuffling the data and the groups, and training 4 DNNs (one for each train-test group) for 1400 epochs to perform the cross validation.

## 3. Results and Discussion

The Median Absolute Error (MdAE) and the standard deviation of the error (STD) for each dataset are presented in Table 2 and Table 3, as well as are presented the Root Mean Squared Error (RMSE), and the SQI threshold used to filter noisy samples. By testing different SQI values, it is possible to analyze the influence of the signal quality on the result.

**Table 2.** Error measurements of the DNN based RR prediction

BIDMC dataset				
SQI	N (%)	MdAE (bts/min*)	STD (bts/min)	RMSE (bts/min)
0.90	87	1.39	6.55	6.59
0.93	80	1.39	6.57	6.62
0.97	66	1.26	6.51	6.55
1.00	37	1.04	4.47	4.47
0.00	100	1.52	6.86	6.94

\* bts/min is equal to breaths/min

The MdAE results achieved by our model on the CapnoBase dataset are compatible with the ones from the best methodologies compared in [4], in which, the best MdAE for a 64 s window was 0.8 breaths/min, achieved using [6] method. However, the methodology excludes 36 % of samples that do not achieve the minimum SQI. The second best was the method from [5], achieving a MdAE of 1.1 breaths/min for 92 % of the best samples. For the same dataset, our method got a MdAE of 1.16 breaths/min (calculated concatenating the results of all four tests), and a MdAE of 1.11 breaths/min with 93% of the highest SQI samples. However, the RMSE of the proposed DNN model did not reach the error from the RespNET [1], which is 3.1 breaths/min, indicating that our model can still be refined to achieve better results.

**Table 3.** Error measurements of the DNN based RR prediction

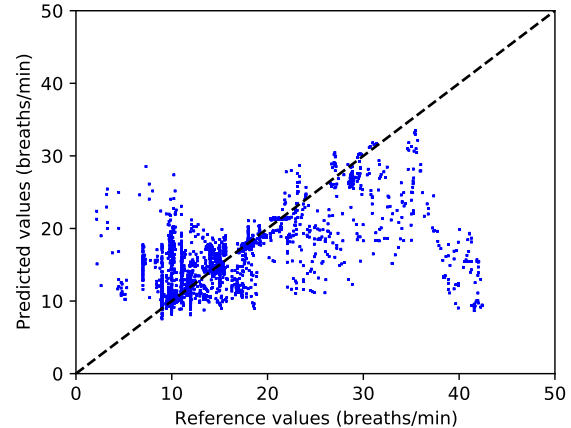
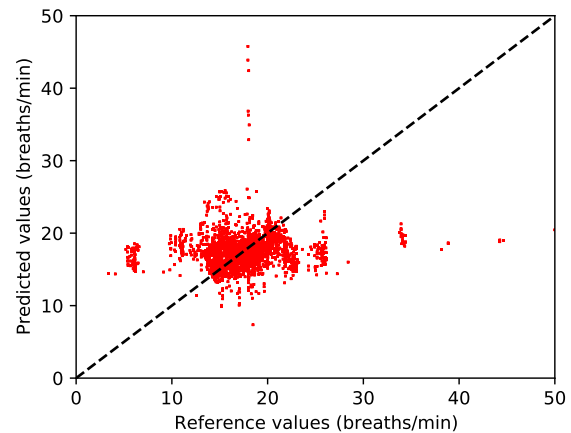
CapnoBase dataset				
SQI	N (%)	MdAE (bts/min*)	STD (bts/min)	RMSE (bts/min)
0.90	98	1.16	5.93	5.94
0.93	97	1.16	5.94	5.95
0.97	93	1.11	5.65	5.66
1.00	73	1.06	4.46	4.97
0.00	100	1.16	5.88	5.90

\* bts/min is equal to breaths/min

The proposed DNN model scored smaller errors on the BIDMC dataset than all other methods compared in [4]. With all samples, our method got a MdAE of 1.52 breaths/min in this dataset, while the smallest error found for this dataset in [4], was the methodology proposed by [8], with a MdAE of 2.3 breaths/min. This improvement in result shows the success in DNN methods to process physiological data. Where, with a dataset large enough and the right complexity, important information can be extracted from the data while noise and artifacts are discarded.

It is also notable in Table 2 and Table 3 that the MdAE by itself does not measure a good result. Besides having a low MdAE the results present a considerable RMSE, as it reinforces highly variation results and

the median computation does not take into account how much the extreme results deviate from the desired value, only the middle value(s) is(are) computed. This can be observed in the scatter plot of the predictions and true values presented in Figure 4, and Figure 5.

**Figure 4.** Scatter plot of the RR predictions and the true values of the CapnoBase dataset. The samples plotted have a SQI over 0.9**Figure 5.** Scatter plot of the RR predictions and the true values of the BIDMC. The samples plotted have a SQI over 0.9

To better compare the performance of our method against the researched literature, a summary of the results of each method is presented in Table 4. The best result presented in the Capnobase dataset was the method proposed by [16], which reached a MdAE of 0.2 breaths/min, whereas the previous benchmark methods on the same dataset achieved a minimum MdAE of 0.8 breaths/min (excluding 36% of the noisiest data). Our method, using the whole data, achieved a MdAE of 1.2 breaths/min. The BIDMC database seems more challenging, as the methods tested on this dataset presented a minimum MdAE of 2.3 breaths/min, and our

method achieved a MdAE of 1.5 breaths/min. The authors from [16] did not use the BIDMC dataset in their study, so, we are not able to compare the results with their method in this dataset.

**Table 4.** Error measurements of different methods presented in the literature. N is the percentage of PPG windows used, median absolute error (MdAE) and 25<sup>th</sup> and 75<sup>th</sup> percentiles (25TH - 75TH) Root Mean Squared Error (RMSE) and Mean absolute error (MAE) and Standard deviation (STD)

Method	Capnobase				BIDMC			
	N (%)	MdAE (25TH - 75TH)	RMSE	MAE (STD)	N (%)	MdAE (25TH - 75TH)	RMSE	MAE (STD)
Proposed	100	1.2 (0.4-3.4)	5.9	3.1 (5.0)	100	1.5 (0.6-3.6)	6.9	3.4 (6.0)
Khreis (2020)	100	0.2 (0.1-0.9)	-	-	-	-	-	-
Ravichandra (2019)	-	-	3.1	-	-	-	-	-
Pimentel (2017)	92	1.9 (0.3-3.4)	-	-	94	2.7 (1.5-5.3)	-	-
Shelley (2016)	92	2.2 (0.2-8.3)	-	-	94	2.3 (0.9-7.9)	-	-
Karlen (2013)	64	0.8 (0.3-2.7)	-	-	34	5.7 (1.5-9.7)	-	-
Fleming (2007)	92	1.1 (0.4-3.5)	-	-	94	5.5 (2.7-8.1)	-	-
Nilsson (2000)	92	10.2 (4.8-12.4)	-	-	94	4.6 (2.5-8.5)	-	-

## 4. Conclusions

This work presents a methodology to use a DNN approach to estimate RR using PPG signals. The model was inspired in a previous successful architecture, which was optimized to our problem using an adapted genetic optimization. The inputs to the DNN are three RR-related respiratory signals extracted from the PPG, and the output is the corresponding RR-value. To test the methodology the files of two open-access datasets were split into 4 folds, keeping the same proportion of each dataset files in each folder. A training-test procedure was repeated 4 times each one with 3 folds for training and 1 for testing, so every fold was used once as a test. The results achieved are comparable with the most of the benchmark analytical methodologies using the CapnoBase dataset, and the DNN overcame them in the more challenging BIDMC dataset, showing the success of the methodology to process physiological data.

Although successful, the performance of analytical methods is usually accompanied by heuristic thresholds or a large number of expertly-tuned free parameters, which could prevent generalization of the developed methodologies. However, DNN approaches are designed to generalize the data as much as possible and to have as less as preprocessing as possible.

## Acknowledgements

The authors thank CNPq (Conselho Nacional de Desenvolvimento Científico e Tecnológico), an agency of the Brazilian Ministry of Science, Technology, Innovations and Communications that supports scientific and technological development, FAPES (Fundação de Amparo à Pesquisa e Inovação do Espírito Santo), an agency of the State of Espírito Santo, Brazil, that supports scientific and technological development, and CAPES (Coordenação de Aperfeiçoamento de Pessoal de Nível Superior) for the financial support granted to this work.

## References

- [1] V. Ravichandran, B. Murugesan, V. Balakarthikeyan, K. Ram, S. P. Preejith, J. Joseph, and M. Sivaprakasam, "RespNet: A deep learning model for extraction of respiration from photoplethysmogram," in *2019 41st Annual International Conference of the IEEE Engineering in Medicine and Biology Society (EMBC)*, 2019, pp. 5556–5559. [Online]. Available: <https://doi.org/10.1109/EMBC.2019.8856301>
- [2] A. Floriano, L. Lampier, R. S. Rosa, E. Caldeira, and T. Bastos-Filho, "Remote vital sign mon-

- itoring in accidents,” *Polytechnica*, vol. 4, no. 1, pp. 26–32, Apr. 2021. [Online]. Available: <https://doi.org/10.1007/s41050-020-00027-1>
- [3] D. J. Meredith, D. Clifton, P. Charlton, J. Brooks, C. W. Pugh, and L. Tarassenko, “Photoplethysmographic derivation of respiratory rate: a review of relevant physiology.” *Journal of medical engineering & technology*, vol. 36, no. 1, pp. 1–7, Jan 2012. [Online]. Available: <https://doi.org/10.3109/03091902.2011.638965>
- [4] M. A. Pimentel, A. E. Johnson, P. H. Charlton, D. Birrenkott, P. J. Watkinson, L. Tarassenko, and D. A. Clifton, “Toward a robust estimation of respiratory rate from pulse oximeters,” *IEEE Transactions on Biomedical Engineering*, vol. 64, no. 8, pp. 1914–1923, 2017. [Online]. Available: <https://doi.org/10.1109/TBME.2016.2613124>
- [5] S. G. F. L. Tarassenko, “A comparison of signal processing techniques for the extraction of breathing rate from the photoplethysmogram,” *International Journal of Biological and Medical Sciences*, vol. 1, no. 6, pp. 366–370, 2007. [Online]. Available: <https://bit.ly/3Cprqqg>
- [6] W. Karlen, S. Raman, J. M. Ansermino, and G. A. Dumont, “Multiparameter respiratory rate estimation from the photoplethysmogram.” *IEEE transactions on bio-medical engineering*, vol. 60, no. 7, pp. 1946–1953, Jul 2013. [Online]. Available: <https://doi.org/10.1109/TBME.2013.2246160>
- [7] L. Nilsson, T. Goscinski, S. Kalman, L. G. Lindberg, and A. Johansson, “Combined photoplethysmographic monitoring of respiration rate and pulse: A comparison between different measurement sites in spontaneously breathing subjects,” *Acta Anaesthesiologica Scandinavica*, vol. 51, no. 9, pp. 1250–1257, 2007. [Online]. Available: <https://doi.org/10.1111/j.1399-6576.2007.01375.x>
- [8] K. H. Shelley, A. A. Awad, R. G. Stout, and D. G. Silverman, “The use of joint time frequency analysis to quantify the effect of ventilation on the pulse oximeter waveform.” *Journal of clinical monitoring and computing*, vol. 20, no. 2, pp. 81–87, Apr 2006. [Online]. Available: <https://doi.org/10.1007/s10877-006-9010-7>
- [9] D. Biswas, L. Everson, M. Liu, M. Panwar, B.-E. Verhoef, S. Patki, C. H. Kim, A. Acharyya, C. Van Hoof, M. Konijnenburg, and N. Van Helleputte, “Cornet: Deep learning framework for ppg-based heart rate estimation and biometric identification in ambulant environment,” *IEEE Transactions on Biomedical Circuits and Systems*, vol. 13, no. 2, pp. 282–291, 2019. [Online]. Available: <https://doi.org/10.1109/TBCAS.2019.2892297>
- [10] P. H. Charlton, D. A. Birrenkott, T. Bonnici, M. A. F. Pimentel, A. E. W. Johnson, J. Alastruey, L. Tarassenko, P. J. Watkinson, R. Beale, and D. A. Clifton, “Breathing rate estimation from the electrocardiogram and photoplethysmogram: A review,” *IEEE Reviews in Biomedical Engineering*, vol. 11, pp. 2–20, 2018. [Online]. Available: <https://doi.org/10.1109/RBME.2017.2763681>
- [11] L. G. Lindberg, H. Ugnell, and P. A. Oberg, “Monitoring of respiratory and heart rates using a fibre-optic sensor,” *Medical & Biological Engineering & Computing*, vol. 30, no. 5, pp. 533–537, 1992. [Online]. Available: <https://doi.org/10.1007/BF02457833>
- [12] K. V. Madhav, M. R. Ram, E. H. Krishna, K. N. Reddy, and K. A. Reddy, “Estimation of respiratory rate from principal components of photoplethysmographic signals,” *Proceedings of 2010 IEEE EMBS Conference on Biomedical Engineering and Sciences, IECBES 2010*, no. December, pp. 311–314, 2010. [Online]. Available: <https://doi.org/10.1109/IECBES.2010.5742251>
- [13] Y. Nam, Y. Kong, B. Reyes, N. Reljin, and K. H. Chon, “Monitoring of heart and breathing rates using dual cameras on a smartphone,” *PLoS ONE*, vol. 11, no. 3, Mar 2016. [Online]. Available: <https://doi.org/10.1371/journal.pone.0151013>
- [14] L. Nilsson, A. Johansson, and S. Kalman, “Monitoring of respiratory rate in postoperative care using a new photoplethysmographic technique,” *Journal of Clinical Monitoring and Computing*, vol. 16, no. 4, pp. 309–315, 2000. [Online]. Available: <https://doi.org/10.1023/A:1011424732717>
- [15] W. Karlen, “CapnoBase IEEE TBME Respiratory Rate Benchmark,” 2021. [Online]. Available: <https://doi.org/10.5683/SP2/NLB8IT>
- [16] S. Khreis, D. Ge, H. A. Rahman, and G. Carrault, “Breathing Rate Estimation Using Kalman Smoother with Electrocardiogram and Photoplethysmogram,” *IEEE Transactions on Biomedical Engineering*, vol. 67, no. 3, pp. 893–904, 2020. [Online]. Available: <https://doi.org/10.1109/TBME.2019.2923448>
- [17] I. Goodfellow, Y. Bengio, and A. Courville, *Deep Learning*. MIT Press, 2016. [Online]. Available: <https://bit.ly/3Eh4Twb>
- [18] P. H. Charlton, T. Bonnici, L. Tarassenko, D. A. Clifton, R. Beale, and P. J. Watkinson, “An assessment of algorithms to estimate respiratory

- rate from the electrocardiogram and photoplethysmogram.” *Physiological measurement*, vol. 37, no. 4, pp. 610–626, apr 2016. [Online]. Available: <https://doi.org/10.1088/0967-3334/37/4/610>
- [19] A. L. Goldberger, L. A. Amaral, L. Glass, J. M. Hausdorff, P. C. Ivanov, R. G. Mark, J. E. Mietus, G. B. Moody, C. K. Peng, and H. E. Stanley, “PhysioBank, PhysioToolkit, and PhysioNet: components of a new research resource for complex physiologic signals.” *Circulation*, vol. 101, no. 23, pp. e215–e220, jun 2000. [Online]. Available: <https://doi.org/10.1161/01.cir.101.23.e215>
- [20] CapnoBase. (2020) Capnobase is a collaborative research project that provides an online database of respiratory signals and labels obtained from capnography, spirometry and pulse oximetry. [Online]. Available: <https://bit.ly/3EjfHKm>
- [21] M. A. F. Pimentel, A. E. W. Johnson, P. H. Charlton, D. Birrenkott, P. J. Watkinson, L. Tarassenko, and D. A. Clifton, “Toward a robust estimation of respiratory rate from pulse oximeters,” *IEEE Transactions on Biomedical Engineering*, vol. 64, no. 8, pp. 1914–1923, 2017. [Online]. Available: <https://doi.org/10.1109/TBME.2016.2613124>
- [22] D. Makowski, T. Pham, Z. J. Lau, J. C. Brammer, F. Lespinasse, H. Pham, C. Schölzel, and S. H. A. Chen, “Neurokit2: A python toolbox for neurophysiological signal processing,” *Behavior Research Methods*, vol. 53, no. 4, pp. 1689–1696, Feb 2021. [Online]. Available: <https://doi.org/10.3758/s13428-020-01516-y>
- [23] M. Elgendi, I. Norton, M. Brearley, D. Abbott, and D. Schuurmans, “Systolic peak detection in acceleration photoplethysmograms measured from emergency responders in tropical conditions,” *PLOS ONE*, vol. 8, no. 10, pp. 1–11, 10 2013. [Online]. Available: <https://doi.org/10.1371/journal.pone.0076585>
- [24] P. van Gent, H. Farah, N. van Nes, and B. van Arem, “Heartpy: A novel heart rate algorithm for the analysis of noisy signals,” *Transportation Research Part F: Traffic Psychology and Behaviour*, vol. 66, pp. 368–378, 2019. [Online]. Available: <https://doi.org/10.1016/j.trf.2019.09.015>
- [25] F. Chollet, “Keras: Deep learning for humans,” GitHub. Inc, 2015. [Online]. Available: <https://bit.ly/3dA0g57>



# D-BLAST MIMO PERFORMANCE ANALYSIS OVER SDR-USRP

## ANÁLISIS DEL RENDIMIENTO DE D-BLAST MIMO SOBRE SDR-USRP

Freddy Cárdenas<sup>1</sup> , Jairo Otáñez<sup>1</sup> , Juan Inga<sup>2,\*</sup> ,  
Esteban Inga<sup>3</sup> , Andrés Ortega<sup>4</sup>

Received: 13-05-2021, Received after review: 29-11-2021, Accepted: 08-12-2021, Published: 01-01-2022

### Abstract

This paper describes the implementation of the technique based on D-BLAST spatial multiplexing on Software Defined Radio (SDR) equipment. Specifically, the aim is to use Universal Software Peripheral Radio (USRP) Ettus Research x310 devices, to tackle the problem of spatial diversity of the MIMO Alamouti scheme which it is not able to increase the number of antennas of the transmitter with respect to the receiver. The simulation scenario was an indoor environment using LabVIEW Communications Software graphical programming tools, achieving a more robust coding design based on the nonlinearity of matrix equations, thus mitigating through the redundancy of information the effects of the interference due to the increase of the antennas of the transmitter. The experimental results evaluated were bit error rate (BER) and symbol error rate (SER) to determine the effectiveness of spatial diversity. The gain achieved was around 10dB and 7dB in MIMO 2×2 and MIMO 3×2, respectively, using the symmetric D-BLAST technique.

**Keywords:** Alamouti, D-BLAST, MIMO, SDR, USRP

### Resumen

Este artículo describe la implementación de la técnica basada en multiplexación espacial D-BLAST sobre equipos de radio definido por *software* (SDR) específicamente usando USRP Ettus Research x310; con el objetivo de afrontar el problema de la diversidad espacial que posee el esquema de MIMO Alamouti, al no poder incrementar el número de antenas del transmisor respecto al del receptor. El escenario de simulación fue en un ambiente *indoor* usando las herramientas de programación gráfica con el *software Labview Communications*, logrando un diseño más robusto de codificación basado en la no linealidad de ecuaciones matriciales, mitigando, de este modo, a través de la redundancia de información los efectos de la interferencia que genera el incremento propio de las antenas en el transmisor. Los resultados experimentales evaluados fueron la tasa de error de bit (BER) y la tasa de error de símbolo (SER) para determinar la efectividad de la diversidad espacial. La ganancia lograda fue alrededor de 10 dB y 7 dB en MIMO 2×2 y MIMO 3×2 respectivamente, usando la técnica D-BLAST simétrica.

**Palabras clave:** Alamouti, D-BLAST, MIMO, SDR, USRP

<sup>1</sup>Carrera de Ingeniería Electrónica / GITEL, Universidad Politécnica Salesiana, Cuenca, Ecuador.

<sup>2,\*</sup>Carrera de Telecomunicaciones / GITEL, Universidad Politécnica Salesiana, Cuenca, Ecuador.  
Corresponding author ✉: [jinga@ups.edu.ec](mailto:jinga@ups.edu.ec)

<sup>3</sup>GIREI, Universidad Politécnica Salesiana, Quito, Ecuador.

<sup>4</sup>Centro de Estudios y Desarrollo Sostenible (CEDS), Universidad Tecnológica ECOTEC, Guayaquil, Ecuador.

Suggested citation: Cárdenas, F.; Otáñez, J.; Inga, J.; Inga, E. and Ortega, A. "D-BLAST MIMO Performance Analysis over SDR-USRP," *Ingenius, Revista de Ciencia y Tecnología*, N.º 27, pp. 105-116, 2022, DOI: <https://doi.org/10.17163/ings.n27.2022.10>.

## 1. Introduction

The development of MIMO systems has gained increasing importance in recent years for standardization and implementation of modern communication systems. The challenges for obtaining high quality of service and high data rate are being exploited using MIMO techniques through multipath propagation, with the objective of increasing spectral efficiency in wireless channels. In this context, MIMO systems may also increase the capacity of the link exploiting channel diversity [1–5].

The spectrum is a scarce resource, and this is evident with spectral migration from LTE to 5G [2]. The mobile communication spectrum is already saturated in existing networks; consequently, the main benefits provided by MIMO techniques besides spatial diversity, are spatial multiplexing and current beamforming techniques deployed in intelligent antennas for spectral optimization.

A space-time coder such as Alamouti [6] scheme maximizes spatial diversity for an equal number of antennas at the transmitter and at the receiver. In spatial multiplexing, signals are transmitted and received simultaneously in the same frequency spectrum, at high data rates.

In this context, spatial diversity may be influenced in terms of Bit Error Rate (BER) by the number of antennas to the receiver. The experimental study reported in [6], demonstrates that the BER with fading channel is close to the ideal situation when the number of antennas in the receiver is increased. It should be also considered that the Alamouti space-time coder takes advantage of the spatial diversity presented by the multipath interference so that the receiver separates the received information symbols, which are mixed by the channel such that the energy of a symbol may be received by each of the receiver antennas. In the case of Alamouti, this may be achieved while the number of receiving antennas is equal to or larger than the number of transmitting antennas; however, this does not always occur.

### 1.1. D-BLAST Spatial Multiplexing

Spatial multiplexing (SM) by Space-Time layers known as BLAST (Bell Laboratories Layered Space-Time) are valid alternatives for MIMO data transmission. In addition, it should be indicated that spatial multiplexing known as D-BLAST enables the receiver to work in a MIMO scenario, where the number of transmitting antennas may be larger than the number of receiving antennas even though this would demand greater complexity in the design of the transmitter and the receiver [4], [7, 8]. According to this, the information symbols are demultiplexed in various layers each of which is transmitted independently. A rotation or di-

agonalization process of the information symbols is applied to achieve this, where each symbol corresponds to an independent data flow [9].

Consequently, it is necessary to consider that within BLAST architectures, D-BLAST proposes an architecture where the symbols to be transmitted are multiplexed by each of the antennas of the transmitter, i.e., at least in a time instant, an information symbol is transmitted by each of the transmitting antennas, which increases spatial diversity, an important factor to take advantage of MIMO. However, in contrast with other working formats such as Alamouti, D-BLAST enables considering the scenario where the number of antennas of the transmitter is greater than the number of antennas of the receiver, as previously mentioned [7, 8], [10, 11]. The MIMO D-BLAST system is chosen for this work due to its capacity to operate without knowledge of the state of the channel and its capacity to take advantage of spatial diversity [7], [12].

### 1.2. Implementation of MIMO techniques on SDRs

The Software Defined Radio (SDR) systems are radiocommunication systems that enable to implement modulations and physical layer transmission schemes through software [13]. In addition, the technological development of communication systems is marked by the design and use of FPGA prototyping systems [14] through Software Defined Radio (SDR) systems, where this hardware is controlled by means of different developing platforms. This gives flexibility to the evaluation of digital communication systems. In this development environment, many software platforms are enabling to access to the processing core of the FPGA with more flexibility, to handle digital signal processing (DSP) in the wireless communication system. Thus, the present work uses SDR equipment, concretely Universal Software Radio Peripheral (USRP) equipment [15, 16]. USRP programming has been carried out using graphical language, and they are increasingly taking control for parallel processing of signals in radio transmissions; LabVIEW Communications by National Instruments [16–18] was used for the development of this work.

For the case of MIMO systems, the scientific community has had much experimental development, being even able to test a MIMO with an array of 64 antennas [19]. This demands more hardware acquisition, and thus a higher implementation cost. For this reason, the development systems seek for platforms with more accessible costs for evaluating new technologies. For example, a  $2 \times 2$  MIMO STBC-Alamouti scheme is evaluated in [20] through the use of USRP-2920 equipment employing the Simulink/MATLAB platform; it is verified the proportionality between the increment of the spatial capacity and the number of antennas of the

receiver, thus converging to a reduction in the BER through spatial diversity. However, Alamouti does not consider the case in which the number of antennas of the transmitter is larger than the number of antennas of the receiver.

The case presented in [12] is another example of modeling and application of MIMO systems, showing a MIMO D-BLAST implementation for air traffic communication systems. In such scenario, possible wireless interferences are greater than in an outdoor, indoor scenario, adding the interference (jamming) effect, situation which is common in the proposed scenario. In this way, [12] shows a strategy to unblock or disinhibit antennas due to the wireless interference, taking advantage of a MIMO system and using a low-speed feedback system for identifying the channel state; this aspect is indeed enabled by D-BLAST when facing the use of space-time coders. However, it should be considered that it is not always possible to take advantage of channel feedback since it requires an additional channel, and the system implemented is not either in contrast with the space-time encoding technique.

On the other hand, the use of the NI-USRP 2920 device [16] for MIMO systems has demonstrated that it is able to increase the capacity of the link; however, the system has two drawbacks due to the hardware architecture itself, namely (i) the data transmission rate, since the devices use the TCP/IP communication protocol, and (ii) when the number of antennas increases, it is necessary to use more SDR devices either for transmitting or receiving, thus arising a synchronization problem between devices. Case (i) may be improved using devices in which MXI ports are available for direct connection with the computer motherboard through the PCI-Express module. In this sense, although the speed improvement may be significant regarding transmission bandwidth, it is still limited. Case (ii) may be solved through software, to generate time synchronization signals from the first device to the second establishing a connection in a master-slave architecture using the corresponding inputs and outputs to pass the clock signals from one device to the other.

The synchronization problem is not only related to software, it is a software-hardware compromise which may be very complex. For example, in [16] the devices were synchronized using a LAN network between radio systems interconnected by means of a LAN switch. However, as the number of devices increases, the transmission rate decreases due to the capacity provided by the TCP/IP and the complexity of configuring the synchronization of devices increases. It should be remarked that this synchronization refers to all devices that constitute the transmitter or the receiver, and not to the synchronization of the communication link, which in this work is solved using training symbols in the transmission frame. This is expanded in subsequent sections. As mentioned above, a simpler option but also of higher cost is to use a version that integrates

a MIMO array, as it is the case with the NI-USRP 2940R model equivalent to the devices USRP Series X300. This SDR model already implements a  $2 \times 2$  array of antennas, simplifying the system implementation process and enabling to concentrate in processing the baseband radio signals and the digital communication section of the communication system. In addition, this model integrates the MXI port to increase the communication bandwidth between the SDR and the computer.

If the number of devices is larger than two, it is simpler to solve the synchronization problem using an external clock signal controller, such as the GPS NI-CDA2990 device. Since this work evaluates communication systems where the number of transmitting antennas is greater than 2, external synchronization is used because more than two devices are being used in the transmitter; therefore, the use of the NI-CDA2990 device is important in the MIMO operation and, hence, evaluation. Figure 1 shows an image corresponding to the implementation of this work using the aforementioned devices, where it can be seen how the SDR devices are arranged. It should be also mentioned that the use of this external clock may limit the distance of the link if it is used both in the transmitter and in the receiver.

### 1.3. Object of study and hypothesis

The object of study is mainly focused on the design and implementation of the nonlinear matrix equations in the D-BLAST coder, using 3 methods to improve symbol detection in the receiver: (i) Average the symbols transmitted at the different positions of the columns where each symbol is repeated, since it is distributed diagonally with the interference of other symbols; (ii) Equal to method (i), but the interference is subtracted, and finally (iii) Knowing that the largest interference is at the medium column of the matrix, this column is neglected and the remaining columns are averaged, likewise the aforementioned methods. The objective is to compare through a practical implementation with SDR devices, the performance between MIMO schemes such as diagonal spatial multiplexing or D-BLAST and Alamouti space-time coder (STBC) implemented in a real indoor environment using USRP equipment, as opposed to what was implemented [21], where the BLAST spatial multiplexing is evaluated, but in vertical format.

The rest of the paper is structured as follows: section II carries out a review of works similar in the use of SDR devices. Section III analyzes the scheme and mathematical model of the D-BLAST space-time coder and describes the implementation process of the decoding algorithms used in the SDR devices. Section IV presents the results obtained, analyzing the figures of merit such as the bit error rate. The document end with the conclusions presented in section V.



Figure 1. Equipment implementation

## 2. Materials and methods

The equipment considered for implementing the MIMO system architecture are the USRP X310 devices of the Ettus Research company, due to the transmission rate flexibility of every radio device. This device model has a PCI-E port to transmit up to 1 Gbps; in addition, it has an external GPS disciplined oscillator (GPSDO) synchronization system, and using the NI-CDA2990 synchronization clock it is possible to expand up to 8 antennas in the transmitter and in the receiver. LabVIEW NI Communications was the software development platform, which facilitates the synchronization process for any communication system that requires more than two transmitting or receiving equipment. Thanks to synchronization, each of the devices may establish the same symbol, bit and/or sample time.

The CDA-2990 device enables to distribute a clock signal to connect up to 8 channels or SDR equipment. This device may externally generate a synchronization clock pulse by GPSDO or through a crystal that enables to generate input synchronization signals with pulse per second (PPS) precision. The configuration and connection used in this work is shown in Figure 2.

### 2.1. D-BLAST Spatial Multiplexing Architecture

It is an architecture that combines various equal or similar signals with low bandwidth to obtain a signal with larger bandwidth [22, 23]. In addition, similar to

how it occurs in space-time coding, data are transmitted simultaneously through each antenna and through each channel [4], [22]. However, D-BLAST spatial multiplexing uses flow of intertwined data symbols; it should be taken into account that symbols might have been obtained from a flow of bits to which any coding or forward error correction (FEC) technique was previously applied.

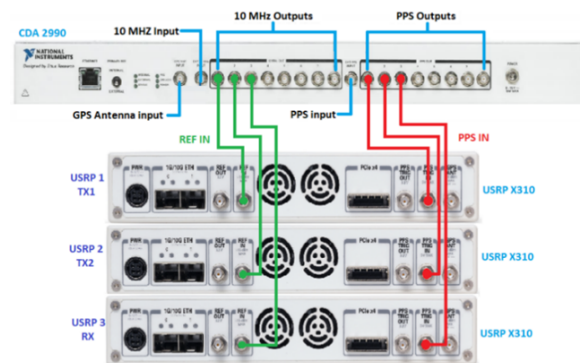


Figure 2. Connections of the CDA-2990, device used for the synchronization of NI-USRP radio devices

Based on this, it is first necessary to organize the information bits to be transmitted by means of a series/parallel converter according to the number of antennas of the transmitter. Then, time coding is applied to each flow obtained from the series/parallel conversion, and subsequently symbol mapping or linear modulation is used, as seen in Figure 3.

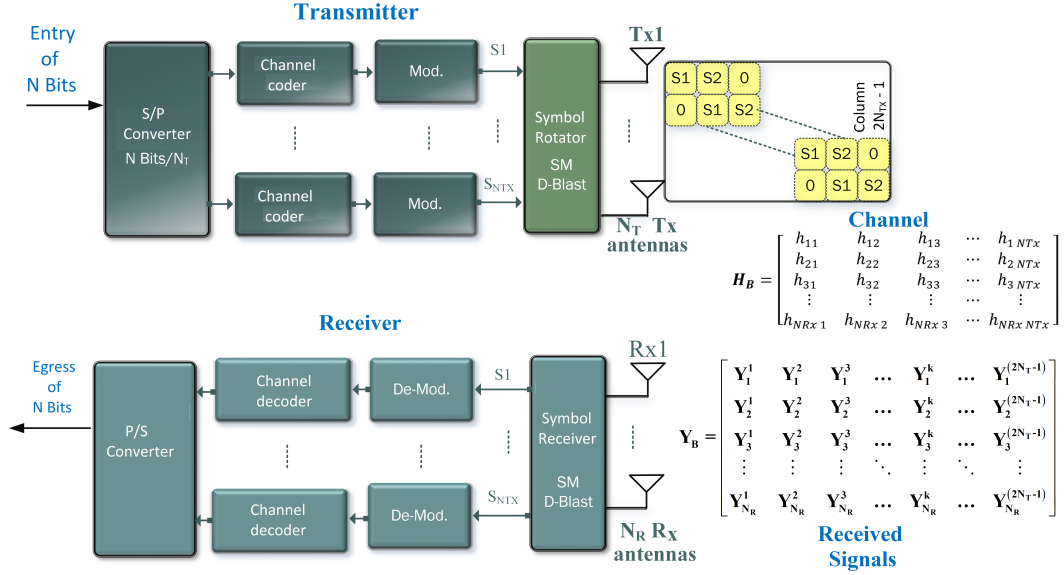


Figure 3. D-BLAST Spatial Multiplexing Architecture

In this way, independent frames are created for each antenna of the transmitter prior to the spatial multiplexing process, where these frames pass through a block that diagonally rotates the symbols of each flow [24] so that each symbol is transmitted at least one time through each of the antennas at the transmitter to ensure spatial diversity.

To illustrate this process, consider a transmitter with  $N_T = 3$  antennas; in this way it is assumed that prior to space-time multiplexing, i.e., at the input of the block that rotates the symbols, there will be one symbol for each flow generally represented as the  $i$ -th symbol that enters this rotator. On the other hand, the output will be represented by equation 1, where the positions filled with «0» correspond to time instants where no information is transmitted, i.e., signals with zero energy. In this way, each symbol hops from one antenna to the other at each transmission time  $T_k$ .

$$S_D = \begin{pmatrix} s_1^1 & s_2^2 & s_3^3 & 0 & 0 \\ 0 & s_1^1 & s_2^3 & s_3^4 & 0 \\ 0 & 0 & s_1^3 & s_2^4 & s_3^5 \end{pmatrix} \quad (1)$$

The columns of equation (1) represent each of the transmission instants or times, while the rows correspond to transmitting antennas. Thus,  $s_3^3$  corresponds to symbol 2 transmitted at time instant 3 or  $T_3$  and, in general,  $s_i^j$  represents symbol  $i$  that entered the rotator and will be transmitted at time  $j$ . Then, for a D-BLAST diagonal spatial multiplexing, the dimension of the resulting symbol rotation matrix at the transmitter will be  $N_T$  rows  $\times$   $2N_T - 1$  columns, understanding that each group of symbols enter and are mapped independently according to the space-time matrix applying the symbol rotation described in general

by equation (2).

$$S_D = \begin{pmatrix} s_1^1 & s_1^2 & \dots & s_{N_T}^{N_T} & 0 & \dots & 0 \\ 0 & 0 & \dots & s_{N_T}^{N_T-1} & s_{N_T+1}^{N_T} & \dots & 0 \\ 0 & 0 & \dots & s_{N_T}^{N_T-2} & s_{N_T+1}^{N_T-1} & \dots & 0 \\ \vdots & \vdots & \ddots & \vdots & \vdots & \ddots & \vdots \\ 0 & 0 & \dots & s_1^{N_T} & s_1^{N_T+1} & \dots & s_{N_T}^{2N_T-1} \end{pmatrix} \quad (2)$$

The matrix  $\mathbf{H}_B$  with channel coefficients is shown in equation (3) and the matrix of signals received is  $\mathbf{Y}_D$  obtained according to equation (4), which is a function of the  $\mathbf{H}_B$  channel of the  $\mathbf{S}_D$  symbols transmitted and of the noise of the channel represented by  $\mathbf{n}$ . For  $\mathbf{H}_B$ , the element  $h_{i,j}$  represents the impulse response of the channel between the transmitting antenna  $i$  and the receiving antenna  $j$ .

$$H_B = \begin{pmatrix} h_{11} & h_{12} & h_{13} & \dots & h_{1N_T} \\ h_{21} & h_{22} & h_{23} & \dots & h_{2N_T} \\ \vdots & \vdots & \vdots & \ddots & \vdots \\ h_{N_R \times 1} & h_{N_R \times 2} & h_{N_R \times 3} & \dots & h_{N_R \times N_T} \end{pmatrix} \quad (3)$$

$$\mathbf{Y}_D = \mathbf{H}_B \mathbf{S}_D + \mathbf{n} \quad (4)$$

For a continuous transmission, prior to applying the rotator a matrix is formed with the information symbols to be transmitted, where the number of rows is  $N_T$  and the number of columns is  $(R \cdot N)/N_T$ , where  $N$  represents the number of information bits and  $R$  is the FEC coding rate. In this way, according to the

mentioned example with  $N_T = 3$ , the second column that enters the rotator corresponds to symbols  $s_4$ ,  $s_5$  and  $s_6$ , which means that the rotator working matrix would use the following 5 transmission time instants under the matrix format given by equation (1) independent of the first three symbols.

Regarding reception, according to equation (4), for each symbol time it is received a linear combination of the symbols transmitted at time instant  $T_k$  through channel  $\mathbf{H}_B$  with elements  $h_{i,j}$ ; this means that each antenna of the receiver contains information of all symbols at such time instant  $T_k$ .

On the other hand, Table 1 shows the arrangement of symbols to be transmitted considering the  $2 \times 2$  MIMO case, presenting the rotation of D-BLAST symbols transmitted for each time instant and for each antenna for the first two transmission blocks; for the case of the D-BLAST  $2 \times 2$  MIMO reception, Table 2 shows the position of the symbols received for the first two blocks, identifying the corresponding symbol times.

**Table 1.** Arrangement of Symbols for TX with D-BLAST  $2 \times 2$  MIMO

	$T_1$	$T_2$	$T_3$	$T_4$	$T_5$	$T_6$
Antenna $T_{X1}$	$s_1^1$	$s_2^2$	$\mathbf{0}$	$s_3^4$	$s_4^5$	$\mathbf{0}$
Antenna $T_{X2}$	$\mathbf{0}$	$s_1^2$	$s_2^2$	$\mathbf{0}$	$s_3^5$	$s_4^6$
	First TX Block for $2 \times 2$ MIMO			Second TX Block for $2 \times 2$ MIMO		

**Table 2.** Arrangement of Symbols for RX with D-BLAST  $2 \times 2$  MIMO

	$T_1$	$T_2$	$T_3$	$T_4$	$T_5$	$T_6$
Antenna $R_{X1}$	$Y_1^1$	$Y_1^2$	$Y_1^3$	$Y_1^4$	$Y_1^5$	$Y_1^6$
Antenna $R_{X2}$	$Y_2^1$	$Y_2^2$	$Y_2^3$	$Y_2^4$	$Y_2^5$	$Y_2^6$
	First RX Block for $2 \times 2$ MIMO			Second RX Block for $2 \times 2$ MIMO		

Each of the symbols or signals received described in Table 2 correspond to signals exiting the channel, which are detailed in equations (5) to (10), where equation (5) corresponds to the signals received at the first-time instant for both antennas 1 and 2 of the receiver of the proposed example.

$$Y_1^1 = h_{11}s_1^1 + h_{12} \cdot 0 + n_1 \quad Y_2^1 = h_{21}s_1^1 + h_{22} \cdot 0 + n_2 \quad (5)$$

$$Y_1^2 = h_{11}s_2^2 + h_{12}s_1^2 + n_3 \quad Y_2^2 = h_{21}s_2^2 + h_{22}s_1^2 + n_4 \quad (6)$$

$$Y_1^3 = h_{11} \cdot 0 + h_{12}s_2^3 + n_5 \quad Y_2^3 = h_{21} \cdot 0 + h_{22}s_2^3 + n_6 \quad (7)$$

$$Y_1^4 = h_{11}s_3^4 + h_{12} \cdot 0 + n_7 \quad Y_2^4 = h_{21}s_3^4 + h_{22} \cdot 0 + n_8 \quad (8)$$

$$Y_1^5 = h_{11}s_4^5 + h_{12}s_3^5 + n_9 \quad Y_2^5 = h_{21}s_4^5 + h_{22}s_3^5 + n_{10} \quad (9)$$

$$Y_1^6 = h_{11} \cdot 0 + h_{12}s_4^6 + n_{11} \quad Y_2^6 = h_{21} \cdot 0 + h_{22}s_4^6 + n_{12} \quad (10)$$

## 2.2. D-BLAST using Software Defined Radio (SDR) Systems

The block diagram of the communication system implemented on Universal Software Radio Peripherals (USRP) is shown in Figure 4. The UHD architecture used is the one available for «LabVIEW Communication Design Suite». The devices used were the USRP Ettus X310 with the following specifications:

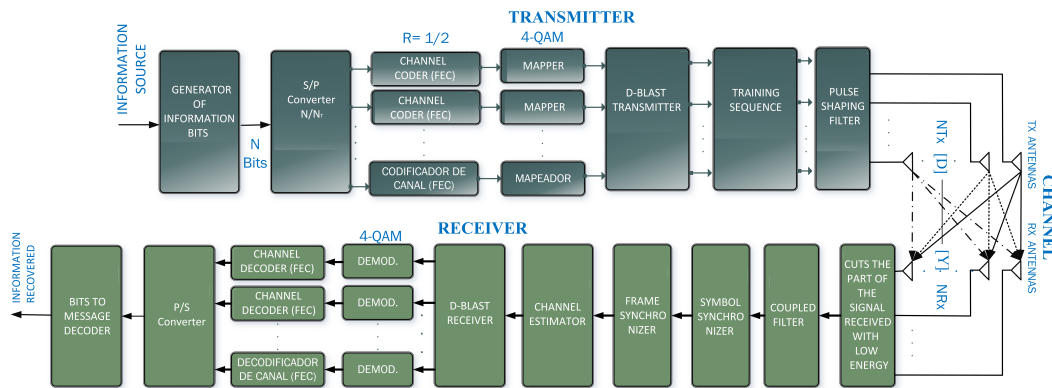


**Figure 4.** D-BLAST Implementation Architecture on SDR-USRP devices

- Bandwidth up to 40 MHz per channel (2 channels).
- The image loaded in the FPGA enables a 1 Gbps Ethernet connection to transmit 25Mega samples/s Full Duplex.
- Flexible clock architecture with configurable sampling frequency.

For MIMO implementation with SDR devices, the Alamouti 2×2, D-BLAST 2×2 and D-BLAST 3×2 configurations were used, where the information source is based on text, therefore, a source coder was implemented to obtain the appropriate flow of information bits. The first block of the transmitter in Figure 4 represents such source coder. In the case of application of the D-BLAST architecture, the flow of bits obtained from the information source is transformed from series to parallel according to the number  $N_T$  of transmitting antennas. For the case of this work,  $N_T = 2$  and  $N_T = 3$  and  $N_R = 2$  for both cases.

After obtaining multiplexed flows of bits, a channel coder with a structure similar to the one used in Alamouti and also the same 4-QAM modulation scheme were applied to each sub-flow, in order to make no difference when comparing the results. In this architecture, the time coding and modulation process is independent for each data sub-flow. D-BLAST is applied to these sub-flows.

Training symbols are inserted at the output of the D-BLAST transmission block so that the receiver may synchronize the data frames received in each sub-flow. The training symbols are transmitted sequentially by each of the antennas in the array, but the sequence of each sub-flow is transmitted individually. Therefore, for the case of the 3 × 2 example, the sub-flow consists of three parts, one constituted by symbols in the  $\pm \frac{1}{\sqrt{2}} \pm \frac{1}{\sqrt{2}}i$  range, and the other two correspond to symbols at zero ( $0 + 0i$ ). Then, the set of symbols that constitute the preamble of each sub-flow contained 528 symbols, where each of the parts previously described contains 176 symbols. The arrangement of these training symbols is presented in Table 3. This structure will enable that the training sequence of each data sub-flow does not interfere with another, and the communication is more stable.

**Table 3.** Distribution of the training symbols in the sub-flows

sub-flow 0	$\pm \frac{1}{\sqrt{2}} \pm \frac{1}{\sqrt{2}}i$	0+0i	0+0i	$S_D$
sub-flow 1	0+0i	$\pm \frac{1}{\sqrt{2}} \pm \frac{1}{\sqrt{2}}i$	0+0i	
sub-flow 2	0+0i	0+0i	$\pm \frac{1}{\sqrt{2}} \pm \frac{1}{\sqrt{2}}i$	
Total length = 528 symbols				

In the blocks shown at the receiver, five additional blocks are applied unlike the simulation diagram. According to this, the first receiver block in Figure 4 seeks to eliminate low energy samples that correspond to filling symbols set equal to zero. For this purpose, a threshold level is established to enable discarding samples with very low energy or simply noise. In this way, the threshold is the average energy of all possible values that may be obtained in a digital modulation. In the case of this work, it is the average of the four possible symbols transmitted with 4-QAM.

The second block is a coupled filter to maximize the Signal-to-Noise (SNR) of the signals captured. The third and fourth blocks of the receiver are in charge of synchronizing the symbol time and synchronizing a frame due to the signals captured by each of the antennas of the receiver. To achieve this, it is exploited that the receiver knows the training symbols, which are known by the receiver, and are eliminated at the output of the receiver. The mathematical model for each signal received before eliminating the synchronization symbols is presented in Table 4 and Table 5 for constructing the 2×2 MIMO and 3×2 MIMO, respectively; in both cases, these expressions result applying equation (4). Prior to using this third block of the receiver, the appropriate symbol sub-sampling is applied to pass from samples to symbols and, therefore, when finalizing the synchronization, the symbols that are ready for channel estimation are obtained at the output of the fourth block of the receiver.

The channel estimator block has a number of inputs equal to the number of transmitting antennas. In addition, to estimate the channel coefficients, it was decided to use an estimator of low computational complexity based on least squares (LS) [25, 26]. As mentioned above, the channel estimation used in this work requires that the receiver knows the symbols used for synchronization and has the objective function described by the equation  $\mathbf{h}_{LS} = \arg \min_h \|\mathbf{y} - \widehat{H}\mathbf{A}\|$  where the training symbols sequences transmitted are defined as  $\mathbf{A} \in \mathbb{R}^{N_{TX} \times L}$ , and the expression of the received matrix of training sequences is  $\mathbf{y}$ .

**Table 4.** Signals received for 2×2 MIMO considering the first layer of symbols for D-BLAST

	$\mathbf{T}_1$	$\mathbf{T}_2$	$\mathbf{T}_3$
$\mathbf{R}_{x1}$	$s_1 h_{11} + \mathbf{n}$	$s_1 h_{11} + s_1 h_{12} + \mathbf{n}$	$s_2 h_{12} + \mathbf{n}$
$\mathbf{R}_{x2}$	$s_1 h_{21} + \mathbf{n}$	$s_2 h_{21} + s_1 h_{22} + \mathbf{n}$	$s_2 h_{22} + \mathbf{n}$

**Table 5.** Signals received for 3×2 MIMO considering the first layer of symbols for D-BLAST

		$T_1$	$T_2$	$T_3$	$T_4$	$T_5$
$Y_B$	$R_{X1}$	$s_1 h_{11}$ + $\mathbf{n}$	$s_2 h_{11}$ + $s_1 h_{12}$ + $\mathbf{n}$	$s_3 h_{11}$ + $s_2 h_{12}$ + $s_1 h_{13}$ + $\mathbf{n}$	$s_3 h_{12}$ + $s_2 h_{13}$ + $\mathbf{n}$	+ $s_3 h_{13}$ + $\mathbf{n}$
	$R_{X2}$	$s_1 h_{21}$ + $\mathbf{n}$	$s_2 h_{21}$ + $s_1 h_{22}$ + $\mathbf{n}$	$s_3 h_{21}$ + $s_2 h_{22}$ + $s_1 h_{23}$ + $\mathbf{n}$	$s_3 h_{22}$ + $s_2 h_{23}$ + $\mathbf{n}$	+ $s_3 h_{23}$ + $\mathbf{n}$

In other words, the *LS* estimation algorithm seeks to find the  $\mathbf{h}_{LS}$  coefficients of the estimated channel  $\widehat{H}$  that minimize the quadratic error between the synchronization symbols received and the approximate version that uses the symbols known by the receiver. In addition, since the training symbols are known by the receiver, it is possible to pre-calculate matrix  $A^\dagger$  and store it in memory, and consequently the receiver does not calculate the pseudoinverse of  $\mathbf{A}$  every time the channel is re-estimated  $\widehat{H} = A^\dagger \mathbf{y} = (\mathbf{A}^H \mathbf{A})^{-1} \mathbf{A}^H \mathbf{y}$ .

At the output of the estimator, the training sequences are withdrawn and with the channel estimated and the symbols synchronized the received symbols are separated, because due to the channel multipath typical of a MIMO transmission, the information of each symbol transmitted during each transmission block (see Table 1) is now in all the received symbol flows.

### 2.2.1. D-BLAST Space-Time Decoder or Demultiplexer

To recover the symbols received, it is necessary to take into account that at the first receiving instant  $T_1$  there is a version of the first symbol transmitted, where each copy is affected by the corresponding channel component. It occurs similarly for the last transmission instant of a layer, where various copies of the last symbol transmitted will be present at the receiver such that each copy is modified by one channel component.

Likewise, from the second to the penultimate receiving instant, each new symbol that comes in will be modified by some copy of the symbols that entered in previous time instants; in addition, in the case of intermediate symbols, this interference will be more accentuated. According to this, at the third time instant it may be seen that the third symbol that enters is modified by the two previous symbols that already entered in the matrix for their demodulation process.

Then, the D-BLAST technique for the 2×2 MIMO system carries out an average of the diagonals 1 and 2 of the symbol matrix  $Y_B$ , which implies that the mean value between the signal received by antenna  $R_{X1}$  at receiving instant  $T_1$  and the signal received by antenna  $R_{X2}$  at receiving instant  $T_2$  enables decoding

symbol  $s_1$  according to equation 11. The symbol  $s_2$  is decoded determining the mean value between the signal received by antenna  $R_{X1}$  at receiving instant  $T_2$  and the signal received by antenna  $R_{X2}$  at receiving instant  $T_3$  according to equation 12.

$$s_i = \frac{(s_1 h_{11} + n) + (s_2 h_{21} + s_1 h_{22} + n)}{2} \quad (11)$$

$$s_{i+1} = \frac{(s_2 h_{11} + s_1 h_{12} + n) + (s_2 h_{22} + n)}{2} \quad (12)$$

This procedure was applied in the 3×2 MIMO scheme. The average to obtain the first three symbols that were sent and the sequence they keep, which are shown below, are of vital importance.

$$s_i = \frac{(s_1 h_{11} + n) + (s_2 h_{21} + s_1 h_{22} + n)}{2} \quad (13)$$

$$s_{i+1} = \frac{(s_2 h_{11} + s_1 h_{12} + n) + (s_3 h_{21} + s_2 h_{22} + s_1 h_{23} + n)}{2} \quad (14)$$

$$s_{i+2} = \frac{(s_3 h_{12} + s_2 h_{13} + n) + (s_3 h_{23} + n)}{2} \quad (15)$$

These symbols are considered as estimates since they are distorted by the effect of the channel. Therefore, the channel coefficients determined in the channel estimation are used to eliminate this effect, multiplying times the conjugate transpose of the matrix with the coefficients obtained from the channel estimator.

In all cases where the number of transmitting antennas is larger than the number of receiving antennas, it will be necessary to complete the channel matrix with as many columns as the difference between ( $N_{Tx} - N - Rx$ ) and dimension  $N_{Tx} \times N_{Rx}$ .

## 3. Analysis of Results

Due to the use of synchronization equipment, the distance between transmitter and receiver was around 3 meters, and to evaluate the behavior of the system, the power of the transmitter was modified with values from -30 dB to 15 dB preventing channel saturation. An additional radio equipment was used to generate a carrier with higher power to emulate the jamming effects in the transmission, to verify the operation for channel conditions such as great fading and multipath. The transmission frequency is 2.4 GHz, which coexists with the wifi network of the lab in which the experiments were carried out, thus producing continuous variations in the channel.

For the simulations carried out prior to the implementation, an indoor environment is considered where the distance effects are ignored to contrast it with the results obtained in the implementation. The evaluation of the simulation performance and experimentation

between spatial diversity and spatial multiplexing is described below. In addition, Table 6 summarizes the features of the equipment used in this implementation. It should be mentioned that the channel model used in the simulations corresponds to a channel with Rayleigh distribution, to consider the channel fading due to multipath; noise is also considered. The development of these simulations enabled establishing the processing of the radio signals to recover the message at the receiver.

**Table 6.** Parameters used in the implementation

Parameter	Value
Sampling rate IQ:	2,1 MSamples/s
Carrier Frequency:	2,4 GHz
Modulation:	4 QAM
Channel coder:	Convolutional, R=1/2
Transmitter gain:	15 dB
Receiver sensitivity:	10 dB
Types of Antennas Used:	Vertical Antennas for ISM band
Gain of Antennas:	6 dBi

Figures 5 and 6 show the disparity effect when  $N_{Rx} < N_{Tx}$ . When the system is symmetric MIMO (equal number of antennas), both the BER and SER are more optimal than when it is asymmetric. It was verified in a simulation environment, that a  $2 \times 2$  MIMO based on Alamouti enables to reduce the impact of the BER.

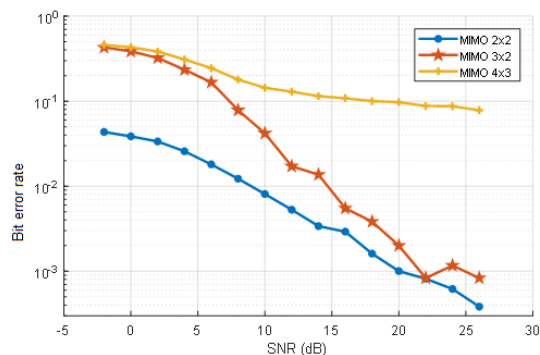


**Figure 5.** BER performance analysis in MIMO simulations

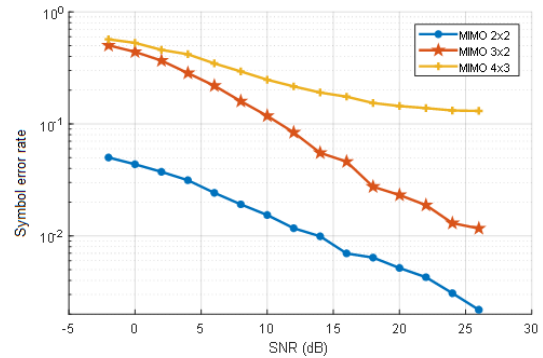


**Figure 6.** SER performance analysis in MIMO simulations

For the experimental approach, the same performance measures have been validated but with different techniques. Thus, in Figures 7 and 8 it may be compared the technique based on spatial diversity with Alamouti MIMO-10 vs. Spatial Multiplexing with D-BLAST MIMO.

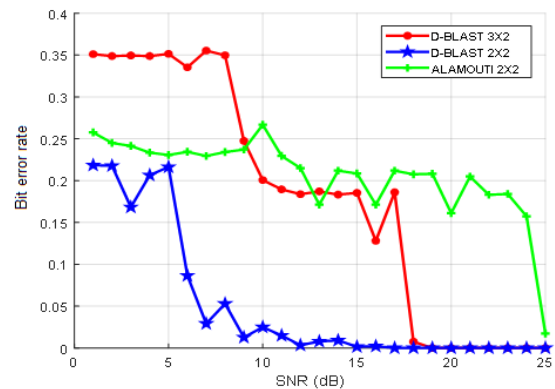


**Figure 7.** Experimental BER analysis between MIMO Alamouti and D-BLAST MIMO

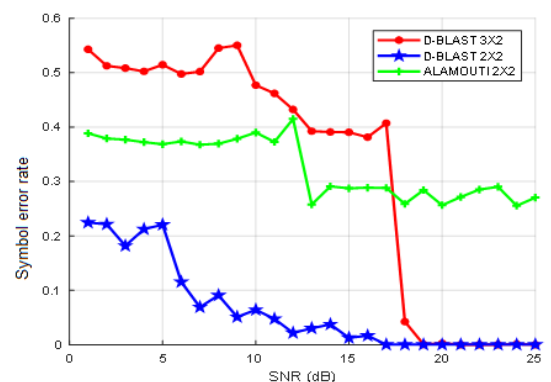


**Figure 8.** Experimental SER analysis between MIMO Alamouti and D-BLAST MIMO

Similarly, it may be observed that MIMO asymmetry deteriorates the system; nevertheless, the technique with BLAST Diagonal Matrices is better than traditional Alamouti space-time coding for MIMO in

around 10 dB. However, the symmetric and asymmetric D-BLAST MIMO systems are more robust than MIMO Alamouti; this is due to the mathematical treatment and the redundancy applied to the system to reduce the interference effects.

Another important point is that if the plots of all MIMO systems are compared, it may be observed that there is a higher symbol error rate than bit error rate for the same SNR value, which confirms the effectiveness of the convolutional coder despite the increased number of antennas. Nevertheless, it is clear that for larger MIMO systems, there is a higher probability of failure due to the complexity of the system even though the amount of data transmitted may be increased.

#### 4. Conclusions

At present, the use of SDR systems is very important, since they are capable of processing large data chains generating a parallel processing, whose internal architecture is in the FPGAs designed to overcome this problem. The implementation of the  $2 \times 2$  D-BLAST system (symmetric) was more efficient than the  $3 \times 2$  D-BLAST system (asymmetric), showing a less significant bit error rate in the different MIMO schemes analyzed. In addition, a symmetric D-BLAST provides better spatial diversity since both the number of transmitting and receiving antennas may be increased, unlike Alamouti scheme in which only the number of receiving antennas may grow.

To implement D-BLAST or any other type of space-time coding for MIMO systems, it is recommended to take into account each of the coding and decoding processes described in this document. One of these fundamental processes is channel estimation, since its coefficients are required for a good wireless communication, for any number of antennas required both in the transmitter and in the receiver.

In this sense, channel coefficients should be arranged and maintained in sequence as shown in this work. If these coefficients are not the correct ones, channel estimation will be wrong, which will produce a significant bit error rate in low noise level. For future works it is recommended to try another system for channel estimation.

Finally, it should be indicated that for data transmission using D-BLAST MIMO with  $N_T$  transmitting antennas, it will be necessary to transmit the symbols in  $2 \times (N_T - 1)$  symbol times, which should be analyzed for a large number of antennas if the D-BLAST operation does not come into conflict with the coherence time of the wireless channel. This is due to the fact that bandwidth is lost when redundancy is introduced in the symbol transfer.

#### References

- [1] S. Xu, S. Xu, and Y. Tanaka, "Dynamic resource reallocation for 5G with OFDMA in multiple user MIMO RoF-WDM-PON," 2016, pp. 480–484. [Online]. Available: <https://doi.org/10.1109/APCC.2015.7412561>
- [2] M. Danneberg, N. Michailow, I. Gaspar, M. Matthe, D. Zhang, L. L. Mendesy, and G. Fettweis, "Implementation of a 2 by 2 MIMO-GFDM transceiver for robust 5G networks," 2015, pp. 236–240. [Online]. Available: <https://doi.org/10.1109/ISWCS.2015.7454336>
- [3] N. Prasad and M. K. Varanasi, "Analysis and optimization of diagonally layered lattice schemes for MIMO fading channels," *IEEE transactions on information theory*, vol. 54, no. 3, pp. 1162–1185, 2008. [Online]. Available: <https://doi.org/10.1109/TIT.2007.915701>
- [4] B. Clerckx and Claude Oestges, *MIMO Wireless Networks*. Academic Press Publications, 2013. [Online]. Available: <https://doi.org/10.1016/C2010-0-66925-2>
- [5] Y. K. Chang, F. B. Ueng, and K. Z. Wu, "A novel MIMO-GFDM receiver for next generation communication," *Transactions on Emerging Telecommunications Technologies*, vol. 29, no. 6, pp. 1–15, 2018. [Online]. Available: <https://doi.org/10.1002/ett.3288>
- [6] M. Gupta and G. Murmu, "Experimental Study of Fading using Alamouti Space-Time Block Code," no. 1. IEEE, 2018, pp. 0–5. [Online]. Available: <https://doi.org/10.1109/SCEECs.2018.8546851>
- [7] A. Paulraj, R. Nabar, and D. Gore, *Introduction to Space-Time Wireless Communications*. Cambridge University Press, 2011, vol. 158. [Online]. Available: [https://doi.org/10.1007/978-1-4419-6111-2\\_2](https://doi.org/10.1007/978-1-4419-6111-2_2)
- [8] O. Shental, S. Venkatesan, A. Ashikhmin, and R. A. Valenzuela, "Massive BLAST: An architecture for realizing ultra-high data rates for large-scale MIMO," *IEEE WIRELESS COMMUNICATIONS LETTERS*, vol. 7, no. 3, pp. 404–407, 2017. [Online]. Available: <https://doi.org/10.1109/LWC.2017.2780079>
- [9] J. J. Mroczek, M. J. Gans, and L. L. Joiner, "Performance of frequency hopping d-blast mimo architecture using ldpc and bpsk," in *MILCOM 2015-2015 IEEE Military Communications Conference*. IEEE, 2015, pp. 860–865. [Online]. Available: <https://doi.org/10.1109/MILCOM.2015.7357553>

- [10] A. Sibille, C. Oestges, and A. Zanella, *MIMO: From Theory to Implementation*. Academic Press Publications, 2010. [Online]. Available: <https://bit.ly/3s2o9uk>
- [11] G. C. Daily and P. A. Matson, "Ecosystem services: From theory to implementation," *Proceedings of the National Academy of Sciences*, vol. 105, no. 28, pp. 9455–9456, 2008. [Online]. Available: <https://doi.org/10.1073/pnas.0804960105>
- [12] Y. Liu, B. Chen, J. J. Mroczek, J. E. Malowicki, and R. J. Michalak, "Robust mimo communications against antenna blockage and interference," in *MILCOM 2019-2019 IEEE Military Communications Conference (MILCOM)*. IEEE, 2019, pp. 7–12. [Online]. Available: <https://doi.org/10.1109/MILCOM47813.2019.9020916>
- [13] V. Garg, "Fourth generation systems and new wireless technologies," *en. Wireless Communications & Networking. Elsevier*, pp. 1–22, 2007.
- [14] N. T. Hieu, N. T. Tu, L. T. Danh, A. N. Duc, and B. H. Phu, "Design and implementation of MIMO-STBC systems on FPGA hardware," *International Conference on Advanced Technologies for Communications*, pp. 274–277, 2012. [Online]. Available: <https://doi.org/10.1109/ATC.2012.6404275>
- [15] J. Kaderka and T. Urbanec, "Time and sample rate synchronization of RTL-SDR using a GPS receiver," in *2020 30th International Conference Radioelektronika (RADIOELEKTRONIKA)*, 2020, pp. 4–7. [Online]. Available: <https://doi.org/10.1109/RADIOELEKTRONIKA49387.2020.9092398>
- [16] G. Soni, G. Kaur, and V. K. Banga, "Implementation & BER analysis of 2x2 MIMO Using USRP 2920- universal software radio peripheral," in *2016 Second International Conference on Computational Intelligence Communication Technology (CICT)*. IEEE, 2016, pp. 523–527. [Online]. Available: <https://doi.org/10.1109/CICT.2016.109>
- [17] V. S. Muradi, R. K. Paithane, A. Ahmed, and A. Pawar, "Spectrum sensing in cognitive radio using Labview and NI USRP," in *2018 2nd International Conference on Inventive Systems and Control (ICISC)*. IEEE, 2018, pp. 1316–1319. [Online]. Available: <https://doi.org/10.1109/ICISC.2018.8399019>
- [18] A. Yanza-Verdugo, C. Pucha-Cabrera, and J. Inga-Ortega, "Compressive Sensing Based Channel Estimator and LDPC Theory for OFDM using SDR," *Ingenius. Revista de Ciencia y Tecnología*, vol. 23, no. 1, pp. 74–85, 2020. [Online]. Available: <https://doi.org/10.17163/ings.n23.2020.07>
- [19] N. Narukawa, T. Fukushima, K. Honda, and K. Ogawa, "64 x 64 MIMO antenna arranged in a daisy chain array structure at 50 Gbps capacity," in *2019 URSI International Symposium on Electromagnetic Theory (EMTS)*. URSI, 2019, pp. 2019–2022. [Online]. Available: <https://doi.org/10.23919/URSI-EMTS.2019.8931517>
- [20] R. Prieto, A. Abril, and A. Ortega, "Experimental Alamouti-STBC Using LDPC Codes for MIMO Channels over SDR Systems," in *2017 IEEE 30th Canadian Conference on Electrical and Computer Engineering (CCECE)*. IEEE, 2017, pp. 1–5. [Online]. Available: <https://doi.org/10.1109/CCECE.2017.7946842>
- [21] V. Soria, G. V. Arevalo, P. Avila, F. Tello, and C. G. Santamaria, "Performance comparison of 2x2 and 4x4 V-BLAST and Alamouti MIMO systems," in *2018 IEEE 3rd Ecuador Technical Chapters Meeting, ETCM 2018*, 2018, pp. 18–21. [Online]. Available: <https://doi.org/10.1109/ETCM.2018.8580317>
- [22] J. J. Anguís Horno, *Redes de Área Local Inalámbricas: Diseño de la WLAN de Wheelers Lane Technology College*. Escuela Superior de Ingenieros Universidad de Sevilla, 2008. [Online]. Available: <https://bit.ly/3IFbsM9>
- [23] M. Sellathurai and S. Haykin, *Space-Time Layered Information Processing for Wireless Communications*. Wiley & Sons, 2009. [Online]. Available: <https://bit.ly/3oPIjG3>
- [24] J. R. Hampton, *Introduction to MIMO communications*. Cambridge university press, 2013. [Online]. Available: <https://bit.ly/3DQyh2>
- [25] V. Puig Borrás, "Simulación computacional y paralelización de un sistema de comunicaciones inalámbrico MIMO: Estimación de canal y decodificación de señales," Master's thesis, Universidad Politécnica de Valencia, 2011. [Online]. Available: <https://bit.ly/3IWIWlc>
- [26] Y. S. Cho, J. Kim, W. Y. Yang, and C. G. Kang, *MIMO-OFDM Wireless Communications with MATLAB*. Wiley & Sons, 2010, vol. 11, no. 3. [Online]. Available: <https://bit.ly/3m3QgFN>



## GUIDELINES FOR PUBLICATION IN INGENIUS JOURNAL

### 1. General Information

INGENIUS is a scientific publication of the *Universidad Politécnica Salesiana* of Ecuador, published since January 2007, with a fixed biannual periodicity, specialized in Mechanical Engineering, Electrical Engineering, Electronics, Computer Science and its integration in what is now known as Mechatronics; these lines of action strengthen areas such as automation, control, robotics, among others..

It is a scientific journal, which uses the peer-review system, under double-blind review methodology, according to the publication standards of the Institute of Electrical and Electronics Engineers (IEEE). Compliance with this system allows authors to guarantee an objective, impartial and transparent review process, which facilitates the publication of their inclusion in reference databases, repositories and international indexing.

INGENIUS is indexed in the directory and selective catalog of the Regional Online Information System for Scientific Journals of Latin America, the Caribbean, Spain and Portugal (Latindex), in the Directory of Journals of Open Access DOAJ, In the Information Matrix for the Analysis of Journals, MIAR, In the Ibero-American Network of Innovation and Scientific Knowledge, REDIB and in repositories, libraries and specialized catalogs of Latin America.

The journal is published in a double version: printed (ISSN: 1390-650X) and digital (e-ISSN: 1390-860X), in Spanish, each work being identified with a DOI (Digital Object Identifier System). The articles sent to INGENIUS magazine must comply with the following criteria:

### 2. Scope and policy

#### 2.1. Theme

Original contributions in Mechanical Engineering, Electrical and Electronic Engineering, Computer Science and its integration in what is now known as Mechatronics, as well as related areas: Automation, Control, Domotics, Robotics in their different fields of action and all those related disciplines with the same central theme.

All the work carried out by national or foreign researchers may be published once they meet the required scientific quality criteria.

#### 2.2. Contributions

INGENIUS Journal preferably publishes articles related to empirical research, and also reports of technological development, proposals for models and innovations, products for the elaboration of graduate and postgraduate thesis that contribute to the field of science and technology, as well as select revisions of literature. (state-of-the-art).

- **Research:** 5,000 to 6,500 words of text, including title, abstracts, descriptors, charts and references.
- **Reports:** 5,000 to 6,500 words of text, including title, abstracts, charts and references.
- **Reviews:** 6,000 to 7,000 words of text, including charts and references. Current, selective and justified references, would be specially valued from among 40 works

The INGENIUS Journal publishes original and unpublished works written in Spanish and English, they may not have been published

through any printed or electronic media, nor be in the process of arbitration or publication.

Every article will be subjected to a rigorous arbitration process; the evaluation of the article will be made according to criteria of originality, relevance, relevance, contributions, scientific rigor and compliance with established editorial guidelines.

Being an arbitrated publication, the Editorial Board approves its publication based on the concept of specialized pairs. The reception of a document does not imply commitment of publication.

It is essential to present a letter of presentation and grant of rights which can be downloaded from: [urlhttps://goo.gl/ZNkMRD](https://goo.gl/ZNkMRD).

Contributions must be exclusively sent and through the OJS (Open Journal System) <https://goo.gl/JF7dWT>. In which all authors must previously register as a user. For any consultation of the procedure you should contact:

[revistaingenius@ups.edu.ec](mailto:revistaingenius@ups.edu.ec),  
[jjcalle@ups.edu.ec](mailto:jjcalle@ups.edu.ec) ó  
[mquinde@ups.edu.ec](mailto:mquinde@ups.edu.ec).

### 3. Presentation and structure of the manuscripts

For those works that are empirical investigations, the manuscripts will follow the IMRDC structure (Introduction, Materials and Methods, Results and Discussion and Conclusions), being optional the Notes and Supports. Those papers that, on the contrary, deal with reports, studies, proposals and reviews may be more flexible in their epigraphs, particularly in material and methods, analysis, results, discussion and conclusions. In all typologies of works, references are mandatory.

Articles may be written on Microsoft Word (.doc or .docx) or L<sup>A</sup>T<sub>E</sub>X(.tex). The template to

be used can be downloaded from the journal's website, a, <https://goo.gl/gtCg6m>, while for L<sup>A</sup>T<sub>E</sub>X in <https://goo.gl/hrHzzQ>, it is necessary that the file be anonymised in Properties of File, so that the author(s) ID is not displayed.

Figures, Graphs and/or Illustrations, as well as Charts shall be numbered sequentially including an explanatory description for each. The equations included in the article must also be numbered; the figures, charts and equations must be cited in the text.

Use space after point, commas and question marks.

Use “enter” at the end of each paragraph and title heading. Do not use .<sup>enter.anywhere</sup> else, let the word processor program automatically break the lines.

Do not center headings or subheadings as they should be aligned to the left.

Charts must be created in the same program used for the document body, but must be stored in a separate file. Use tabs, not spaces, to create columns. Remember that the final size of printed pages will be 21 x 28 cm, so the tables must be designed to fit the final print space.

#### 3.1. Structure of the manuscripts

##### 3.1.1. Presentation and cover letter

1. **Título (español) / Title (inglés):** Concise but informative, in Spanish on the front line and in English on the second, when the article is written in Spanish and vice versa if it is written in English.
2. **Authors and affiliations:** Full name and surname of each author, organized by order of priority and their institutional affiliation with reference to the end of the first sheet, where it must include: Dependency to which belongs within the

institution, Institution to which he/she belongs, country, ORCID. A maximum of 5 authors will be accepted, although there may be exceptions justified by the complexity and extent of the topic.

3. **Abstract (Spanish) / Abstract (English):** It will have a maximum extension of 230 words, first in Spanish and then in English. : 1) Justification of the topic; 2) Objectives; 3) Methodology and sample; 4) Main results; 5) Main conclusions.
4. **Keywords (Spanish) / Keywords (English):** 6 descriptors must be presented for each language version directly related to the subject of the work. The use of the key words set out in UNESCO's Thesaurus will be positively valued.
5. **Presentation (Cover Letter):** A statement that the manuscript is an original contribution, not submission or evaluation process in another journal, with the confirmation of the signatory authors, acceptance (if applicable) of formal changes in the manuscript according to the guidelines and partial assignment of rights to the publisher, according to the format established in: <<https://goo.gl/ZNkMRD>>

### 3.1.2. Manuscript

1. **Título (español) / Title (inglés):** Concise but informative, in Spanish on the front line and in English on the second, when the article is written in Spanish and vice versa if it is written in English.
2. **Authors and affiliations:** Full name and surname of each author, organized by order of priority and their institutional affiliation with reference to the end of the first sheet, where it must include: Dependency to which belongs within the institution, Institution to which he/she belongs, country, ORCID. A maximum of 5 authors will be accepted, although

there may be exceptions justified by the complexity and extent of the topic.

3. **Abstract (Spanish) / Abstract (English):** It will have a maximum extension of 230 words, first in Spanish and then in English. : 1) Justification of the topic; 2) Objectives; 3) Methodology and sample; 4) Main results; 5) Main conclusions.
4. **Keywords (Spanish) / Keywords (English):** 6 descriptors must be presented for each language version directly related to the subject of the work. The use of the key words set out in UNESCO's Thesaurus will be positively valued.
5. **Introduction:** It should include the problem statement, context of the problem, justification, rationale and purpose of the study, using bibliographical citations, as well as the most significant and current literature on the topic at national and international level.
6. **Material and methods:** It must be written so that the reader can easily understand the development of the research. If applicable, it will describe the methodology, the sample and the form of sampling, as well as the type of statistical analysis used. If it is an original methodology, it is necessary to explain the reasons that led to its use and to describe its possible limitations.
7. **Analysis and results:** It will try to highlight the most important observations, describing, without making value judgments, the material and methods used. They will appear in a logical sequence in the text and the essential charts and figures avoiding the duplication of data.
8. **Discussion and Conclusions:** It will summarize the most important findings, relating the observations themselves to relevant studies, indicating contributions

and limitations, without adding data already mentioned in other sections. It should also include deductions and lines for future research.

9. **Supports and acknowledgments (optional):** The Council Science Editors recommends the author (s) to specify the source of funding for the research. Priority will be given to projects supported by national and international competitive projects.
10. **The notes (optional):** will go, only if necessary, at the end of the article (before the references). They must be manually annotated, since the system of footnotes or the end of Word is not recognized by the layout systems. The numbers of notes are placed in superscript, both in the text and in the final note. The numbers of notes are placed in superscript, both in the text and in the final note. No notes are allowed that collect simple bibliographic citations (without comments), as these should go in the references.
11. **References:** Bibliographical citations should be reviewed in the form of references to the text. Under no circumstances should references mentioned in the text not be included. Their number should be sufficient to contextualize the theoretical framework with current and important criteria. They will be presented sequentially in order of appearance, as appropriate following the format of the IEEE.

### 3.2. Guidelines for Bibliographical references

#### *Journal articles:*

- [1] J. Riess, J. J. Abbas, "Adaptive control of cyclic movements as muscles fatigue using functional neuromuscular stimulation". IEEE Trans. Neural Syst. Rehabil. Eng

vol. 9, pp.326–330, 2001. [Online]. Available: <https://doi.org/10.1109/7333.948462>

#### *Books:*

- [1] G. O. Young, "Synthetic structure of industrial plastics" in *Plastics*, 2nd ed., vol. 3, J. Peters, Ed. New York: McGraw–Hill, 1964, pp. 15–64.

#### *Technical reports:*

- [1] M. A. Brusberg and E. N. Clark, "Installation, operation, and data evaluation of an oblique–incidence ionosphere sounder system," in "Radio Propagation Characteristics of the Washington–Honolulu Path," Stanford Res. Inst., Stanford, CA, Contract NOBSR–87615, Final Rep., Feb. 1995, vol. 1

#### *Articles presented in conferences (unpublished):*

- [1] Vázquez, Rolando, Presentación curso "Realidad Virtual". National Instruments. Colombia, 2009.

#### *Articles of memories of Conferences (Published):*

- [1] L. I. Ruiz, A. García, J. García, G. Taiboadá. "Criterios para la optimización de sistemas eléctricos en refinerías de la industria petrolera: influencia y análisis en el equipo eléctrico," IEEE CONCAPAN XXVIII, Guatemala 2008.

#### *Thesis:*

- [1] L.M. Moreno, "Computación paralela y entornos heterogéneos," Tesis doctoral, Dep. Estadística, Investigación Operativa y Computación, Universidad de La Laguna, La Laguna, 2005.

#### *Guidelines:*

- [1] IEEE Guide for Application of Power Apparatus Bushings, IEEE Standard C57.19.100–1995, Aug. 1995.

#### *Patents:*

- [1] J. P. Wilkinson, "Nonlinear resonant circuit devices," U.S. Patent 3 624 125, July 16, 1990.

*Manuals:*

- [1] Motorola Semiconductor Data Manual, Motorola Semiconductor Products Inc., Phoenix, AZ, 1989.

*Internet resources:*

- [1] E. H. Miller, "A note on reflector arrays" [Online]. Available. <https://goo.gl/4cJkCF>

**3.3. Epigraphs, Figures and Charts**

The epigraphs of the body of the article will be numbered in Arabic. They should go without a full box of capital letters, neither underlined nor bold. The numbering must be a maximum of three levels: 1. / 1.1. / 1.1.1. At the end of each numbered epigraph will be given an enter to continue with the corresponding paragraph.

The charts must be included in the text according to order of appearance, numbered in Arabic and subtitled with the description of the content, the subtitle should go at the top of the table justified to the left.

Figures can be linear drawings, maps or black and white halftone or color photographs in 300 dpi resolution. Do not combine photographs and line drawings in the same figure.

Design the figures so that they fit eventually to the final size of the journal 21 x 28 cm. Make sure inscriptions or details, as well as lines, are of appropriate size and thickness so that they are not illegible when they are reduced to their final size (numbers, letters and symbols must be reduced to at least 2.5 mm in height After the illustrations have been reduced to fit the printed page). Ideally, the linear illustrations should be prepared at about a quarter of their final publication size.

Different elements in the same figure should be spelled a, b, c, etc.

Photographs should be recorded with high contrast and high resolution. Remember that

photographs frequently lose contrast in the printing process. Line drawings and maps should be prepared in black.

The text of the figures and maps must be written in easily legible letters.

If the figures have been previously used, it is the responsibility of the author to obtain the corresponding permission to avoid subsequent problems related to copyright.

Each figure must be submitted in a separate file, either as bitmap (.jpg, .bmp, .gif, or .png) or as vector graphics (.ps, .eps, .pdf).

**4. Submission process**

The manuscript must be sent through the OJS system of the journal, <<https://goo.gl/JF7dWT>>, the manuscript should be uploaded as an original file in .pdf without author data and anonymized according to the above; In complementary files the complete manuscript must be loaded in .doc or .docx (Word file), that is to say with the data of the author (s) and its institutional ascription; Also the numbered figures should be uploaded in independent files according to the corresponding in the manuscript (as bitmap .jpg, .bmp, .gif, or .png or as vector graphics .ps, .eps, .pdf). It is also obligatory to upload the cover letter and grant of rights as an additional file.

All authors must enter the required information on the OJS platform and only one of the authors will be responsible for correspondence.

Once the contribution has been sent the system will automatically send the author for correspondence a confirmation email of receipt of the contribution.

**5. Editorial process**

Once the manuscript has been received in OJS, a first check by the editorial team of the following points:

- The topic is in accordance with the criteria of the journal.
- Must have the IMRDC structure.
- Must be in the INGENIUS format.
- Must use the IEEE citation format.
- All references should be cited in the text of the manuscript as well as charts, figures and equations.
- The manuscript is original; for this, software is used to determine plagiarism.

The assessment described above can take up to 4 weeks.

If any of the above is not complete or there is inconsistency, an email will be sent to the author to make the requested corrections.

The author will make the corrections and re-send the contribution through an email in response to the notification and will also upload the corrected manuscript into OJS supplementary files.

The editorial team will verify that the requested corrections have been incorporated, if it complies, the manuscript will start the second part of the process that may be followed by the author through OJS, otherwise the author will be notified and the manuscript will be archived.

The second phase of the process consists of the evaluation under the methodology of double-blind review, which includes national and foreign experts considering the following steps:

- The editor assigns two or more reviewers for the article.

- After reviewing the article, the reviewers will submit the evaluation report with one of the following results.

- Publishable
- Publishable with suggested changes
- Publishable with mandatory changes
- Non publishable

- The editor once received the evaluation by the reviewers will analyze the results and determine if the article is accepted or denied.

- If the article is accepted, the author will be notified to make corrections if required and the corresponding editorial process will be continued.

- If the article is denied, the author will be notified and the manuscript will be archived.

- In the two previous cases the result of the evaluation of the reviewers and their respective recommendations will be sent.

The second phase of the process lasts at least 4 weeks, after which they will be notified to the author giving instructions to continue with the process.

## 6. Publication

The INGENIUS Journal publishes two issues per year, on January 1st and July 1st, so it is important to consider the dates for sending the articles and their corresponding publication. Articles received until October will be considered for the January publication and those received until April for the July publication.

**UNIVERSIDAD POLITÉCNICA SALESIANA DEL ECUADOR**

Juan Cárdenas Tapia, sdb,  
Rector

©Universidad Politécnica Salesiana  
Turuhuayco 3-69 y Calle Vieja  
Postal code 2074  
Cuenca, Ecuador  
Teléfono: (+593 7) 205 00 00  
Fax: (+593 7) 408 89 58  
Email: srector@ups.edu.ec

**Exchange**

Exchange with other periodicals is accepted.

Address:

Secretaría Técnica de Comunicación  
Universidad Politécnica Salesiana  
Turuhuayco 3-69 y Calle Vieja  
Postal code 2074  
Cuenca, Ecuador  
Phone: (+593 7) 205 00 00 Ext. 1182  
Fax: (+593 7) 408 89 58  
Email: rpublicas@ups.edu.ec  
www.ups.edu.ec  
Cuenca – Ecuador

INGENIUS, Journal Science of Technology,  
Special Issue 27: Use of Engineering Techniques to Fight COVID-19  
january/june 2022  
John Calle Sigüencia, Editor in chief  
revistaingenius@ups.edu.ec

**Printed**

Centro Gráfico Salesiano: Antonio Vega Muñoz 10-68 y General Torres.  
Phone: (+593 7) 283 17 45  
Cuenca – Ecuador  
Email: centrograficosalesiano@lms.com.ec

OTHER PERIODIC PUBLICATIONS OF THE UNIVERSITY  
UNIVERSITAS, Journal of Social and Human Sciences.

LA GRANJA, Journal of Life Sciences.

ALTERIDAD, Journal of Education.

RETOS Journal of Administration Sciences and Economics.

UTOPIA, University Youth Ministry Magazine.

SOPHIA, Collection of Philosophy of Education.



ABYA  
YALA | UNIVERSIDAD  
POLITÉCNICA  
SALESIANA

